Studies on Spatial Dependence of Photocarrier Transport in Hybrid Perovskite based Devices and Applications

A Thesis Submitted in the Partial Fulfillment of the Requirements for the Degree of

Doctor of Philosophy

By

Ganesh N.

Chemistry and Physics of Materials Unit

Jawaharlal Nehru Centre for Advanced Scientific Research

Bangalore - 560 064

Karnataka, INDIA

July 2021

DECLARATION

I hereby declare that the matter embodied in this thesis titled "**Studies on spatial dependence of photo-carrier transport in hybrid perovskite based devices and applications**" is the result of the work carried out by me under the supervision of Prof. K. S. Narayan, at Molecular Electronics Laboratory, in Chemistry and Physics of Materials Unit, Jawaharlal Nehru Centre for Advanced Scientific Research, Bangalore, India. It has not been submitted for the Award of any degree or diploma or associateship of any other university or institute.

In keeping with the general practice in reporting scientific observations, due acknowledgment has been made whenever the work described is based on the findings of other investigators.

(Ganesh N.)

Candidate

JAWAHARLAL NEHRU CENTRE FOR ADVANCED SCIENTIFIC RESEARCH
Jakkur, Bangalore 560064, India

K. S. NARAYAN
Professor
PHONE: 91 80 22082822
FAX: 91 80 22082766
e-mail: narayan@jncasr.ac.in
URL: www.jncasr.ac.in/narayan

5th July 2021

CERTIFICATE

I hereby certify that the matter embodied in the thesis entitled "**Studies on spatial dependence of photo-carrier transport in hybrid perovskite based devices and applications**" has been carried out by Mr. Ganesh N. at the Molecular Electronics Laboratory, Chemistry and Physics of Materials Unit, Jawaharlal Nehru Centre for Advanced Scientific Research, Bangalore, India, under my supervision and it has not been submitted elsewhere for the award of any degree or diploma.

Prof. K. S. Narayan

(Research Supervisor)

Dedicated to

My Parents and Teachers

ACKNOWLEDGEMENT

First and foremost, I would like to express my sincere gratitude to Prof. K.S. Narayan for being a constant source of support, encouragement and guidance. I am ever grateful to him for giving me an opportunity to pursue science and introducing me to the scientific community. He has provided me with utmost freedom to explore, while at the same time ensuring scientific rigor and accountability. His enthusiastic approach to research is infectious and motivational.

I thank Prof. K.L. Narasimhan for his valuable inputs and feedback. I've had many engaging discussions with him. He is a person who is capable of providing deep insights into seemingly straightforward observations. I sincerely thank him for his time and patience.

I would like to thank Prof. C.N.R. Rao for providing us with a beautiful campus.

I thank all my course instructors especially Prof. Vidyadhiraja, Prof. Umesh Waghmare, and Prof. Sushoban Avasthi. They were very approachable and I learnt a lot by discussing science with them. They were instrumental in making me appreciate the beauty of science and research.

I would like to acknowledge the Centre for providing me with the fellowship.

I also thank EPSRC project SUNRISE for giving me the opportunity to attend many meetings and interact with the international research community. I thank them for providing travel grants for my visit to the UK.

I would like to thank Dr. Ravichandran Shivanna and Prof. Richard Friend from the University of Cambridge, for helping with ultrafast measurements. I am deeply grateful to Ravi for his inputs, guidance and timely encouragement during my research. I thank him and his wife, Smt. Lakshmi for the hospitality they provided, during my visit to Cambridge.

I would like to thank Ms. Shrreya Krishnamurthy and Prof. Satishchandra Ogale from IISER Pune for providing high-quality perovskite single crystals. I would also like to thank Dr. Kelly Schutt, Dr. Pabitra Nayak and Prof. Henry Snaith from the University of Oxford for providing us with high quality, large-area perovskite samples.

I consider myself fortunate to be part of the Molecular Electronics Lab. I was lucky to work with many talented researchers and exchange ideas and perspectives in both academic and non-academic subjects. I would like to thank all the past and present lab members: Dr. Ravi, Dr. Ashar, Dr. Swathi, Dr. Prashant, Dr. Raaghesh, Dr. Suman Banerjee, Dr. Ishan, Dr. Manasa, Dr. Swanand, Dr. Kanti, Dr. Rahul, Rishav, Nisha, Apoorva, Anaranya, Sumukh, Sinay, Sukanya, Gaurav, Deepak, Abhijit, Anil Krishna, Abdul, Rahul Bharadwaj and Manish. I would like to especially thank Dr. Ashar, with whom I worked on my first successful project and learnt the basics of device fabrication, instrument handling and lab maintenance. I've had many discussions with seniors, especially with Dr. Prashant and Dr. Swathi, and learnt the nuances of experimentation. I would also like to thank Sumukh who is very proactive and takes extra care to ensure smooth functioning and maintenance of the lab. This makes it is so much easier to plan and execute experiments over a short period of time, in a hassle-free way.

I would like to acknowledge Rajkumar Sir and Sunoj for helping me with all the tools and instrumentation assistance in the workshop. Special thanks to Manjunath for helping with lab finances, purchases and shipments.

I would like to acknowledge my batchmates and friends with whom I had a lot of fun and a good time during my stay at JNC. I would like to especially mention Shivaram, Pradeep, Ravishankar, Anusha, Priyanka, Divya, Malay, Dheeraj, Rajender, Swati, Deepak, Premkumar, Madhulika, Abhiroop, Manoj, Divyesh, Adma, Ronak, Ramesh….. and many more. Heartfelt thanks to Anil Krishna for all the good and fun-filled memories that he gave us.

I would also like to thank my friends in IISc and elsewhere in Bangalore with whom I've had a memorable time. I am especially grateful to J. Aditya for being very patient with me and helping me understand the difficult concepts in physics, during my MSc. days.

I would like to thank all the staff at JNCASR for making our life easy, thereby helping us to focus on our research. I thank all the staff at the dining hall, library, admin, academic and hostel. I also thank the audio-visual team, hostel, garden staff, cleaning staff and security personnel.

I express my heartfelt gratitude to my Alma Mater: Sri Sathya Sai Institute of Higher Learning. I am grateful to the system and to the teachers who've devoted an enormous amount of time and effort to ensure our well-being. Special thanks to Ramamurthy Sir, Ravindranath Sir, Rangaswamy sir, Rajkumar Jain sir, Dr. Shiva Shankara Sai, Dr. Shailesh Srivastava, Vishwanathan brother and Harish brother.

Most importantly, I express my gratitude to my mother, father, sister and brother. My parents have stood by me as a pillar of love and encouragement. Heartfelt acknowledgement and appreciation to Charan and Chinmayi, who are always there to support me in my endeavour. My family had to bear with my irregular timings and haphazard schedule. I feel blessed to have had access to stay at home. Time with family always kept me in good spirits.

Finally, I pay my salutations to the source of all intelligence, wisdom and enlightenment, Sai…….

July 5th, 2021

JNCASR, Bengaluru Ganesh N.

LIST OF PUBLICATIONS

In this thesis:

1. **Ganesh, N.**, Anaranya Ghorai, Shreya Krishnamurthy, Suman Banerjee, K. L. Narasimhan, Satishchandra B. Ogale, and K. S. Narayan. "Impact of trap filling on carrier diffusion in MAPb Br 3 single crystals." *Physical Review Materials* 4, no. 8 (2020): 084602.

2. **Ganesh N.**, Ashar A. Z., Sumukh Purohit, K. L. Narasimhan, and K. S. Narayan. "Carrier transport regimes in lateral metal-perovskite-metal device structures" *Physical Review Applied* (manuscript under review)

3. **Ganesh N.**, Kelly Schutt, Pabitra K. Nayak, Henry J. Snaith and K. S. Narayan. "2D position-sensitive hybrid-perovskite detectors" *ACS Applied Materials and Interfaces* (manuscript under revision)**.**

4. **Ganesh, N.**, Ravichandran Shivanna, Richard H. Friend, and K. S. Narayan. "Wavelength-dependent charge carrier dynamics for single pixel color sensing using graded perovskite structures." *Nano letters* 19, no. 9 (2019): 6577-6584.

Miscellaneous:

5. Sett, Shaili, Subhamita Sengupta, **N. Ganesh**, K. S. Narayan, and A. K. Raychaudhuri. "Self-powered single semiconductor nanowire photodetector." *Nanotechnology* 29, no. 44 (2018): 445202.

6. Ashar, A. Z., **N. Ganesh**, and K. S. Narayan. "Hybrid Perovskite-Based Position-Sensitive Detectors." *Advanced Electronic Materials* 4, no. 2 (2018): 1700362.

7. Kumar, Prashant, **N. Ganesh**, and K. S. Narayan. "Electrospun fibers containing emissive hybrid perovskite quantum dots." *ACS applied materials & interfaces* 11, no. 27 (2019): 24468-24477.

8. Dhamaniya, Bhanu Pratap, Amit Kumar, **Ganesh N.**, Priyanka Chhillar, Anaranya Ghorai, Krishna Priya Ganesan, Suresh E. Puthanveettil, Narayan KS, and Sandeep Kumar Pathak. "Morphology and Crystallinity Amelioration of MAPbI3 Perovskite in Virtue of PbI2 Thermal Absorption Drifted Performance Enhancement in Planer n–i–p Solar Cells." *Advanced Engineering Materials* 23, no. 3 (2021): 2000990.

Synopsis

Hybrid organic inorganic perovskites (HOIP) have emerged as a promising semiconducting materials for optoelectronic applications. The excellent performance of these materials have been attributed to properties such as long carrier lifetime and diffusion lengths, high absorption coefficient and ease of solution processability. In a device architecture, the carrier transport properties is influenced by the spatial boundary conditions and the potential landscape. This thesis focuses on study of spatial signatures of carrier transport in hybrid perovskite based devices, and its applications.

The first part of the work deals with the impact of trap filling on carrier diffusion in Methyl Ammonium lead bromide ($MAPbBr_3$) single crystals. The use of millimeter sized single crystals overcomes the limitation of grain boundary recombination. Using the technique of spatial photocurrent scanning microscopy (SPCM), the effective carrier diffusion length, L_d was estimated, and this parameter was found to reduce upon the introduction of low intensity light bias, suggesting that the recombination dynamics are not monomolecular. This observation were then correlated with intensity dependent transient PL studies that reveal distinct dynamics corresponding to band recombination and trap emission. Intensity dependent analysis reveals that the sub-band-gap trap recombination influences carrier transport in the low-intensity excitation regime, while bimolecular recombination and transport dominate at high intensity.

The next part of the work, i.e. Chapter 3 presents the different regimes of carrier transport in a hybrid perovskite based lateral metal-semiconductor-metal device structures, with asymmetric electrodes. The device characteristics exhibit a cross-over from ohmic behavior to SCLC regime as function of inter-electrode distance and applied bias. In the observed device characteristics, the influence of carrier energetics at the metal-perovskite interface was studied using Kelvin Probe Force Microscopy (KPFM). KPFM on lateral MSM structures indicates the

presence of a transport-barrier at Al-perovskite and an ohmic contact at the Au-perovskite interface. Additionally, the potential map also points out to ineffective screening due to mobile ions, confirming the reliability of the observed SCLC behavior. The spatial behavior of photo-generated carriers were understood in response to the already present potential profile, using the technique of scanning photocurrent microscopy (SPCM). In the presence of an applied bias, the potential distribution profiles indicate constant electric field in the device, and the light response were understood in the context of drift-diffusion formalism.

Chapter 4 deals with the fabrication and demonstration of a 2 dimensional-position sensitive detector (2D- PSD). In these devices, the position detection functionality relies on geometrically asymmetric carrier transport upon photo-generation. Using mixed halide perovskite as the active layer, the PSD devices show a position sensitivity of ~ 50 μV/mm. In response to a single pulse of excitation, the devices exhibit a response time of ~ 1 μs, and these timescales extend as the excitation is translated away from the overlapping device area. These excitation-position dependent characteristics were understood in terms of equivalent circuit modelling, in combination with impedance spectroscopy measurements.

In Chapter 5, using 2D/3D graded bandgap perovskite based devices, single pixel color sensor is demonstrated. The excitation dependent transient photocurrent characteristics exhibit wavelength dependent temporal profiles. The observed polarity of the transient photocurrent switches as the excitation is spanned from the blue (450 nm) to the red (625 nm) part of the visible spectrum. Color sensing application is demonstrated utilizing detection schemes in the ultrafast excitation regime as well as steady-state light illumination. With the introduction of a temporal delay, interesting possibilities are proposed towards resolving the spectral components of a polychromatic source using sequential wavelength determination.

List of Contents

Synopsis ..... **xvii**

Abbreviations and Notations ..... **xxxiii**

Chapter 1: Introduction **1**

1.1 Overview of solution-processable electronics 1
1.2 Hybrid Organic-Inorganic Perovskites (HOIP) 2
1.2.1 Lattice structure 2
1.2.2 Bandgap Tunability 4
1.2.3 Optical properties 5
1.2.3.1 Absorption and PL 5
1.2.3.2 Binding energy 6
1.2.3.3 Photon recycling 7
1.2.4 Defects in Hybrid perovskites 8
1.3 Layered Perovskites. 10
1.4 Carrier transport and recombination 12
1.4.1 Drift diffusion formalism 12
1.4.2 Recombination Dynamics 14
1.5 Charge transport layers and Interfaces 17
1.5.1 Loss mechanism at the interface: 20
1.5.2 Metal-semiconductor interface. 23
1.6 Solution-processed electronic devices 25
1.6.1 Photovoltaics 26
1.6.2 Photo-detectors 28
1.7 Thesis outline. 33
References: 36

Chapter 2: Impact of trap-filling on carrier diffusion in $MAPbBr_3$ single crystals **43**

2.1 Introduction 43

2.2 Experimental Details 44
2.2.1 Materials 44
2.2.2 Sample Preparation 45
2.2.3 Measurements and Characterization 46
2.3 Results and Discussion 49
2.3.1 Scanning Photocurrent Microscopy (SPCM) 49
2.3.1.1 Diffusion Recombination Formalism 51
2.3.1.2 Diffusion mechanism in SPCM 53
2.3.1.3 Impact of Probe beam intensity variation 55
2.3.1.4 Impact of Light Bias 56
2.3.2 PL measurements 59
2.3.2.1 Recombination Kinetics 61
2.3.2.2 Time-Resolved Photoluminescence 63
2.3.3 Microscopic Picture 67
2.3.4 Influence of photon recycling on diffusion 72
2.4 Conclusion 73
References 75

Chapter 3: Visualization of carrier transport in lateral metal-perovskite-metal device structures. 79

3.1 Introduction 79
3.2 Experimental Details 80
3.2.1 Materials 80
3.2.2 Sample Preparation 81
3.2.3 Measurements and Characterization 83
3.3 Results and Discussion 85
3.3.1 Device operation 85
3.3.2 Carrier-transport regimes 87
3.3.3 Barrier estimates at metal-perovskite interface 92
3.3.4 Spatial Potential Mapping 95
3.3.5 Spatial Photocurrent Mapping 98
3.3.6 Bias-dependence 101
3.3.7 Drift-Diffusion Formalism 104

3.3.8 Photo-detector characteristics. 106
3.4 Conclusion 110
References 112

Chapter 4: 2-Dimensional Position-Sensitive Hybrid Perovskite based Detector 115

4.1 Introduction 115
4.2 Experimental Details 117
4.2.1 Materials 117
4.2.2 Sample Preparation 118
4.2.3 Measurements and Characterization 120
4.3 Results and Discussion 122
4.3.1 Characterization of perovskite films 122
4.3.2 Device structure for 2-D Position Detection 123
4.3.3 Spatial Photo-voltage Mapping 126
4.3.4 Position dependent photovoltage in inverted device structures 129
4.3.5 Dynamic Imaging 133
4.3.6 Position dependent Transient Photocurrent 137
4.3.7 Impedance Spectroscopy 140
4.4 Conclusion 143
References 144

Chapter 5: Single-pixel color sensing using graded-bandgap perovskite structures 147

5.1 Introduction 147
5.2 Experimental Details 149
5.2.1 Materials 149
5.2.2 Sample Preparation 150
5.2.3 Measurements and Characterization 152
5.3 Results and Discussion 154

5.3.1 Evidence of graded bandgap 154
5.3.1.1 PL and Confocal Microscopy 155
5.3.1.2 Transient Absorption 157
5.3.2 Asymmetric devices 158
5.3.2.1 Transient Photocurrent on Asymmetric devices 159
5.3.3 Symmetric hole-only devices 162
5.3.3.1 Transient Photocurrent on symmetric devices 162
5.3.3.2 Color-sensing scheme 166
5.3.4 Color sensing with steady-state illumination 168
5.3.4.1 Photo-response in Asymmetric devices 169
5.3.4.2 Equivalent circuit representation of off-cycle features in asymmetric devices. 171
5.3.4.3 Photo-response in symmetric devices 173
5.3.5 Use of graded band-gap devices for spectral resolution 176
5.4 Conclusion 178
References 180

Chapter 6: Summary and Future Directions 185

Appendix 1: Solution to transport equation based on drift-diffusion formalism. 189

A1.1 Carrier diffusion in the perovskite single crystal. 191

Appendix 2: Influence of photon recycling on carrier diffusion 193

Appendix 3: Representation of the SCLC current 197

Appendix 4: Thickness uniformity of mixed-phase perovskite films 199

List of Figures

***Figure 1. 1**: Schematic representation of organic-inorganic hybrid perovskite unit cell of the form ABX_3 where $A=CH_3NH_3$, B = Pb and X= I. The methylammonium ion is surrounded by the PbI_6 octahedral cage, with a coordination number of 12.....2*

***Figure 1. 2**: Schematic illustrating the mechanism of **(a)** carrier diffusion and **(b)** photon recycling.....7*

***Figure 1. 3**: Schematic expanding the distribution of band states, sub-bandgap states that form the shallow defects, and the deep trap states. The shallow defects have a low activation energy ~ k_BT, while the deep traps have higher activation energies.....9*

***Figure 1. 4**: Schematic illustrating the lattice ordering of 2D layered perovskites. The butyl-ammonium ions are interspersed between the different orders of octahedral stack layers. The $n = \infty$ corresponds to the bulk 3D perovskite. The bandgap of the 2D perovskite reduces for higher-order 2D perovskites. 11*

***Figure 1. 5**: Schematic illustrating the dominant carrier recombination pathways in a direct band-gap semiconductor. The band recombination is a direct radiative process. Trap-assisted recombination is given by the Shockley-Read-Hall (SRH) recombination dynamics. In the Auger recombination, upon the recombination of an electron-hole pair, either an electron is excited higher into the conduction band or a hole lower into the valence band. 15*

***Figure 1. 6**: Schematic illustrating the carrier generation and separation dynamics, with associated efficiencies, in a device with the configuration: electrode/HTL/HOIP/ETL/electrode. **(a)** depicts the process relating to the efficiency of photon absorption. **(b)** shows the process of exciton generation and dissociation to form free carriers **(c)** shows the charge transfer process to the charge transport layers. **(d)** depicts the charge collection to the respective electrodes, which forms the current in the external circuit.....18*

***Figure 1. 7**: **(a)** Schematic showing the energy levels and the band alignment across a metal-semiconductor interface before the formation of a contact. The scheme is represented for $\varphi_m < \varphi_s$. **(b)** shows the band bending after the formation of a contact, which results in an injection barrier across the interface. 24*

***Figure 1. 8**: Schematic depicting vertically stacked devices representing the **(a)** normal structure and **(b)** inverted structure. The abbreviations used are expanded here TCO: transparent conducting oxide, E(H)TL: electron (hole) transport layer, HOIP: hybrid organic-inorganic perovskite.....25*

***Figure 1. 9**: Schematic representation of the J-V characteristics of the solar cell. The inset shows the equivalent circuit model for a typical solar cell.....27*

***Figure 1. 10**: Schematic shows the device configuration for **(a)** Sandwich structure and **(b)** Lateral structure.....31*

***Figure 2. 1**: Schematic of SPCM experimental setup.....47*

***Figure 2. 2**: **(a)** The intensity profile as the knife edge is translated across the diameter of the focused beam spot. **(b)** The differential of the intensity profile gives the spot profile and the FWHM of the beam spot.....48*

***Figure 2. 3**: **(a)** Band alignment diagram depicting MSC-device used in SPCM experiments. **(b)** Schematic of Scanning Photocurrent Microscopy (SPCM) used for effective diffusion length measurement. The incident chopped probe-beam position is varied by translating the sample. The lock-in profile $I_{ph}(x)$ is utilized to estimate L_d. **(c)** $I_{ph}(x)$ shows I_{ph}-peak at the interface. Single exponential fit to the I_{ph} decay profile corresponds to the L_d of the corresponding carrier. The **inset** shows the image of the bulk single crystal. (Reprinted with permission from Ganesh, N., Ghorai, A., Krishnamurthy, S., Banerjee, S., Narasimhan, K. L., Ogale, S. B., & Narayan, K. S. (2020). Impact of trap filling on carrier diffusion in MAPb Br 3 single crystals. Physical Review Materials, 4(8), 084602. Copyright (2020) by American Physical Society)...50*

***Figure 2. 4**: (a) Schematic of the position-dependent TPC on the MSC device. The 355 nm pulsed laser, 1 ns pulse, 60 nJ/pulse was for excitation close to the interface and at the center of the crystal. (b) The TPC decay time shows a longer decay time for excitation close to the electrode when compared to excitation in the central region far from the electrodes. The long decay times reflect on the transit time of the un-extracted counter carrier. (Reprinted with permission from Ganesh, N., Ghorai, A., Krishnamurthy, S., Banerjee, S., Narasimhan, K. L., Ogale, S. B., & Narayan, K. S. (2020). Impact of trap filling on carrier diffusion in MAPb Br 3 single crystals. Physical Review Materials, 4(8), 084602. Copyright (2020) by American Physical Society)...54*

***Figure 2. 5**: **(a)** Plot of $I_{ph}(x)$ with variation in the 405 nm probe beam intensity in the absence of light bias. Solid lines indicate single exponential fits to obtain L_d. **(b)** Plot of L_d with respect to probe beam intensity indicates that L_d remains invariant with change in probe-beam intensity. (Reprinted with permission from Ganesh, N., Ghorai, A., Krishnamurthy, S., Banerjee, S., Narasimhan, K. L., Ogale, S. B., & Narayan, K. S. (2020). Impact of trap filling on carrier diffusion in MAPb Br 3 single crystals. Physical Review Materials, 4(8), 084602. Copyright (2020) by American Physical Society)...56*

***Figure 2. 6**: **(a)** $I_{ph}(x)$ variation on both ends of the MSC device with a 405 nm probe beam and 390 nm light bias. **(b)** Plot of variation of max. I_{ph} close to the electrode as a function of light bias intensity for 390 nm. The dashed horizontal lines correspond to the I_{ph} peak, in the absence of light bias. **(c)** Normalized $I_{ph}(x)$ profiles indicating sharp decay at higher light bias **(d)** L_d extracted with the exponential fitting of $I_{ph}(x)$-decay as a function of light bias. (Reprinted with permission from Ganesh, N., Ghorai, A., Krishnamurthy, S., Banerjee, S., Narasimhan, K. L., Ogale, S. B., & Narayan, K. S. (2020). Impact of trap filling on carrier diffusion in MAPb Br 3 single crystals. Physical Review Materials, 4(8), 084602. Copyright (2020) by American Physical Society)...58*

***Figure 2. 7**: Normalized absorption spectra of $MAPbBr_3$ single crystal.....59*

***Figure 2. 8**: (a) PL data depicts 545 nm and 575 nm peaks corresponding to PL measured in the reflection and transmission geometry respectively. (b)Comparison of PL spectra of $MAPbBr_3$ films and crystals. The films do not exhibit the low-intensity emission at 575 nm (c) Plot shows the increase in E-PLQE at higher excitation fluence (d) Schematic showing an illustration of band-to-band recombination and trap*

emission. (Reprinted with permission from Ganesh, N., Ghorai, A., Krishnamurthy, S., Banerjee, S., Narasimhan, K. L., Ogale, S. B., & Narayan, K. S. (2020). Impact of trap filling on carrier diffusion in MAPb Br 3 single crystals. Physical Review Materials, 4(8), 084602. Copyright (2020) by American Physical Society).....60

***Figure 2. 9**: intensity-dependent PL spectrum centered at **(a)** 545 nm, with PL measured in the reflection geometry and **(b)** 575nm, with PL measured in the transmission geometry on single crystals. **(c)** Integrated emission intensity exhibits linear and quadratic dependence on excitation for 545 nm and linear variation for the 575 nm emission. (Reprinted with permission from Ganesh, N., Ghorai, A., Krishnamurthy, S., Banerjee, S., Narasimhan, K. L., Ogale, S. B., & Narayan, K. S. (2020). Impact of trap filling on carrier diffusion in MAPb Br 3 single crystals. Physical Review Materials, 4(8), 084602. Copyright (2020) by American Physical Society)...62*

***Figure 2. 10: (a)** Time-resolved emission spectra on MSC upon pulsed excitation with a 405 nm source, 19 mW/cm^2. **(b)** TRPL at 545 nm and 575 nm shows a shorter band-recombination lifetime at 545 nm. (Reprinted with permission from Ganesh, N., Ghorai, A., Krishnamurthy, S., Banerjee, S., Narasimhan, K. L., Ogale, S. B., & Narayan, K. S. (2020). Impact of trap filling on carrier diffusion in MAPb Br 3 single crystals. Physical Review Materials, 4(8), 084602. Copyright (2020) by American Physical Society)...64*

***Figure 2. 11**: **(a)** TRPL depicting the decrease in the PL lifetime at high fluence illumination (545 nm) **(b)** TRPL for 575 nm depicts the constancy of lifetime for the range of excitation intensities. **(c)** Compilation of intensity-dependent lifetimes for 545 nm and 575 nm emission. For 545 nm emission, the lifetime is constant in the lower intensity (< 10^{15} photons/cm^2) and reduces at a higher intensity (> 10^{15} photons/cm^2). For the 575 nm emission, a uniform lifetime in the entire intensity regime. (Reprinted with permission from Ganesh, N., Ghorai, A., Krishnamurthy, S., Banerjee, S., Narasimhan, K. L., Ogale, S. B., & Narayan, K. S. (2020). Impact of trap filling on carrier diffusion in MAPb Br 3 single crystals. Physical Review Materials, 4(8), 084602. Copyright (2020) by American Physical Society).....65*

***Figure 2. 12**: Plot of recombination rate vs excess carrier density. The plot was fit to a quadratic equation to obtain A and B coefficients.....66*

***Figure 2. 13**: **(a)** The schematic describes the simulation of the SPCM experiment using the finite element method. The probe excitation (at x=0) is assumed to be a point source in addition to uniform dc light bias on the MSC sample. The blue line at x=0 in all the plots indicates probe excitation. **(b)** A linear fit to the plot of PL 1/τ vs excess carrier density. **Inset** shows the plot in semi-log scale **(c)** Plot of spatial carrier decay profile considering 1-D diffusion of probe-carriers. The decay profile changes with different intensities of light bias. **(d)** Shows the excess carrier lifetime at different dc light bias. The excess carrier lifetime depends on the background carrier density (shown in **(c)**). The dashed line indicates the lifetime of light-bias generated carriers. As excess probe-carriers diffuse in space and recombine, the excess carrier density decreases resulting in an increased excess-carrier lifetime. This results in a spatial dependence of the excess carrier lifetime. **(e)** Shows the effective diffusion length decreases with increasing light bias. The dashed line indicates L_{diff} of light bias generated carriers. Since the lifetime increases as the excess carriers diffuse away from x = 0, the effective*

diffusion length also increases. (Reprinted with permission from Ganesh, N., Ghorai, A., Krishnamurthy, S., Banerjee, S., Narasimhan, K. L., Ogale, S. B., & Narayan, K. S. (2020). Impact of trap filling on carrier diffusion in MAPb Br 3 single crystals. Physical Review Materials, 4(8), 084602. Copyright (2020) by American Physical Society)...69

***Figure 2. 14**: **(a)** Plot of φ_{PL} (internal luminescence efficiency) which depends on the background carrier density. Blue vertical lines in all the plots indicate the point of excitation. As the carriers diffuse away from x=0, the carrier density reduces resulting in a reduction of the lifetime (shown in **Figure 2.13(d)**). **(b)** The plot of excess carrier density profile shows a marginal increase considering photon recycling (PR). Consequently, due to the relative increase in the excess carrier density, the lifetime and diffusion length parameters show a marginal reduction as shown in **(c)** and **(d)** respectively. 73*

***Figure 3. 1**: Schematic of the procedure followed for the fabrication of the lateral asymmetric electrode MSM devices.....82*

***Figure 3. 2**: **(a)** Schematic of the lateral asymmetric electrode device, where l is the inter-electrode channel length and d is the thickness of the metal electrode. **(b)** Microscopy image of the asymmetric electrode lateral device, with l = 12 μm, captured in the reflection geometry. **(c)** Schematic of an asymmetric interdigitated electrode structure. The zoomed image is the microscopic image of the structure with an inter-electrode distance of 10 μm. 86*

***Figure 3. 3**: **(a)** Semi-log plot of J-V characteristics of the asymmetric electrode device for different values of l. **(b)** The plot of the J-V characteristics, normalized to J at 5 V bias. **(c)** The plot of the rectification ratio as a function of channel length shows that the rectification ratio increases for short channel devices.....87*

***Figure 3. 4**: **(a)** Schematic of the diagram representing the directionality of the applied bias. Here positive bias is applied to the Au electrode. **(b)** Log-log plot of the dark J-V data shows distinct ohmic ($\propto V^1$) and SCLC behavior ($\propto V^2$) for l = 4 μm and **(c)** 12 μm channel respectively. **(d)** Log-log J(V) plot for long-channel (l > 20 μm) asymmetric electrode devices, shows dominant ohmic behavior.....89*

***Figure 3. 5**: **(a)** Variation of dark current density at 5V as a function of channel length shows an ohmic behavior ($\propto l^{-1}$) for the long channel length and an SCLC behavior ($\propto l^{-3}$) for the short channel length. **(b)** Plot of current density, J' as a function of V^2/l^3 for short channel devices shows a single-exponent dependence, confirming SCLC behavior. 90*

***Figure 3. 6**: **(a)** Schematic of the diagram representing the directionality of the applied bias. Here positive bias is applied to the Al electrode. **(b)** Log-log plot of dark J(V) characteristics show single-exponent variation, representing the ohmic regime of operation for devices of different channel lengths, l.....91*

***Figure 3. 7**: Dark J(V) characteristics of Au/MAPI/Au symmetric electrode devices with a channel length of **(a)** 55 μm, **(b)** 10 μm, and **(c)** 5 μm. 92*

***Figure 3. 8**: Schematic shows the band alignment diagram across the Al/MAPI interface **(a)** before and **(b)** after the formation of the contact. The right-hand side shows the band-diagram across the Au/MAPI interface **(c)** before and **(d)** after the formation of the contact. 93*

***Figure 3. 9**: **(a)** Band alignment diagram of the asymmetric electrode MSM device. **(b)** The device in short-circuit condition shows an injection barrier at the metal-perovskite interface. A built-in potential, V_{bi} is developed at the metal-MAPI interface as a result of Fermi-level equilibration. 95*

***Figure 3. 10**: **(a)** Schematic of the KPFM experimental setup used for potential mapping. The measured contact potential difference (CPD) is used to measure the potential profile across the device. **(b)** 2D surface plots showing the morphology-KPFM correlation for asymmetric electrode device with l = 55 μm, in short-circuit condition **(c)** Line-scan of the CPD profile shows the presence of a significant potential drop at the Al-MAPI interface and also across the bulk of the device. The potential drop across the Au-MAPI interface is minimal. 97*

***Figure 3. 11**: **(a)** Schematic of Near-field scanning photocurrent microscopy (NSPM) setup. A tapered fiber-tip in near-field excitation is scanned across the lateral device. **(b)** $I_{ph}(x)$ line scan profiles of the NSPM scans on asymmetric electrodes in short-circuit condition for the inter-electrode channel length of 55 μm **(c)** 22 μm and **(d)** 13 μm. **(e)** Normalized $I_{ph}(x)$ profile as a function of channel length. For the short channel length devices, $I_{ph}(x)$ tends to a uniform distribution profile. 100*

***Figure 3. 12**: 2D surface plots showing the raw data of the CPD for bias-dependent KPFM measurement with **(a)** 5 V applied to the Al and **(b)** 5V applied to Au electrode. **(c)** shows the data for 5 V applied to Al with additional data processing by subtraction of a zeroth-order polynomial baseline to improve the contrast of the image. **(d)** shows the data for 5 V to Au electrode, with similar data processing. However, the raw data is utilized for all the analysis. 101*

***Figure 3. 13**: Plot of CPD and lateral electric field for asymmetric electrode devices with l = 56 μm for the case of **(a)** -5 V and **(b)** + 5 V. The dominant electric field at the Al-MAPI interface in the negative bias is indicative of the formation of a depletion zone. 102*

***Figure 3. 14**: **(a)** Schematic of the NSPM experimental setup in the presence of an external bias. **(b)** NSPM scans in the presence of external bias show the presence of an $I_{ph}(x)$ peak which shifts depending on the polarity of the bias. This indicates unbalanced carrier mobility. 103*

***Figure 3. 15**: **(a)** Simulation using the finite element method shows the decay of excess electrons and holes for excitation at x = 0, under conditions of 1-D drift-diffusion transport for different μ_e values. **(d)** The normalized J_{ph} profiles, simulated as a function of excitation position across the device, under 1 kV/cm electric field. The profiles indicate a shift in the $J_{ph}(x)$ peak in the case of unbalanced carrier mobility, which explains the feature observed in (**b**). 105*

Figure 3. 16**: **(a)** Voltage-dependent responsivity characteristics of the lateral devices for 532 nm illumination at 26 mW/cm^2. A short circuit I_{ph} is observed at 0 V. **(b)

Variation of the responsivity as a function of channel length under short circuit conditions and ± 5 V bias conditions. *106*

***Figure 3. 17**: Comparison of the dark and light (532 nm, 26 mW/cm^2) for channel lengths of **(a)** 4 μm, **(b)** 12 μm, **(c)** 25 μm, **(d)** 55 μm and **(e)** 122 μm.* *108*

***Figure 3. 18**: **(a)** Transient photocurrent measurement on lateral MSM devices with mixed-phase perovskite (FAMA) as the active layer. The bi-exponential fit reveals a fast response time of 11.8 ns followed by a slow component of ~ 100 ns. **(b)** Variation of photocurrent with respect to light-intensity (λ = 532nm), shows the LDR ~ 118 dB, spanning up to 6 orders of intensity variation.* *109*

***Figure 4. 1**: **(a)** Schematic of lateral photo signal measurement setup in bottom illumination mode. Sample mounted on an x-y stage is controlled at micron-scale precision. **(b)** Schematic of the PSD device and potential distribution as a result of non-uniform illumination in the active area of PSD. (Reprinted with permission from Ashar, A. Z., Ganesh, N., & Narayan, K. S. (2018). Hybrid Perovskite-Based Position-Sensitive Detectors. Advanced Electronic Materials, 4(2), 1700362. Copyright (2018) with John Wiley and Sons, Inc)* *116*

***Figure 4. 2**: Schematic of the photo-voltage scanning setup. A narrow laser beam is incident on the sample which translates in the x and y direction. The photo-voltage is mapped to the position of illumination.* *121*

***Figure 4. 3**: **(a)** SEM image shows uniform grains over a large area on the spin coated $FA_{0.83}Cs_{0.17}Pb(I_{0.9}Br_{0.1})_3$ films. The scale bar indicates 2 μm. **(b)** XRD data on $FA_{0.83}Cs_{0.17}Pb(I_{0.9}Br_{0.1})_3$ films. **(c)** Absorption and PL on these mixed-phase perovskite films.* *123*

***Figure 4. 4**: **(a)** Schematic of the device structure of a 2D-PSD. Intensity-modulated light excitation from the ITO side of the device. V_A, V_B, V_C, and V_D are the input signal measured with ITO as the ground reference. The differential voltage is measured using a lock-in amplifier (ac coupled, voltage input) across the opposite pair of electrodes: V_A-V_C and V_B-V_D. **(b)** Band alignment of different layers in the device. The ITO-HOIP interface allows for electron extraction to the back contact ITO electrode. **(c)** Normalized I(V) measured across Au-ITO electrodes, represented in a semi-log plot, under dark and illumination conditions, confirms the barrier for hole extraction at the ITO/HOIP interface. **Inset** shows I(V) in linear scale and the negative short-circuit current under illumination conditions indicates electron selective extraction at the ITO/HOIP interface. **(d)** Schematic showing the Schottky depletion width across the ITO/HOIP interface which is forward biased at the point of light excitation. The lateral photo-voltage is developed across the point of illumination and the electrode.* *125*

***Figure 4. 5**: **(a)** Spatial profile of differential photo-voltage $\Delta V_{A\text{-}C}$ across the electrodes A and C in **Figure 4.3(a)** and **(b)** $\Delta V_{B\text{-}D}$ across the electrodes B and D. **(c)** Variation of ΔV_{ph} as the light excitation is scanned between the electrodes A and C in the center of the active area. The **inset** shows the linear V_{ph} variation in the center of the device away from the electrodes. **(d)** Similar V_{ph} behavior across the other electrodes B and D.* *127*

***Figure 4. 6**: Plot of original and calculated positions showing the deviation from linear behavior for PSD measurement in **(a)** the x-axis and the **(b)** y-axis.....128*

***Figure 4. 7**: Variation of PSD linear response with **(a)** modulation frequency. The illumination power was maintained at 1 mW. **(b)** PSD response with a variation of excitation intensity. The modulation frequency was maintained at 119 Hz. 129*

***Figure 4. 8**: **(a)** Device schematic of inverted structure PSD. **(b)** Band alignment diagram shows the pathway for hole extraction to the PEDOT:PSS layer. In the above modified device, the PEDOT:PSS interlayer is utilized to improve charge separation efficiency to the ITO electrode.....130*

***Figure 4. 9**: $\Delta V_{ph}(x)$ scan for excitation translated between electrode A and C (**Figure S8a**) for **(a)** 0.4 cm, **(c)** 1.2 cm and **(e)** 2 cm. The shaded regions indicate the overlapping region due to the top Ag electrode. Correspondingly, the $V_{ph}(x)$ profiles for the different channel lengths away from the electrodes shows a linear behavior in the case of **(b)** channel length of l = 0.4 cm. However, these profiles deviate from linear behavior for the case of **(d)** l = 1.2 cm and **(f)** l = 2 cm.....131*

***Figure 4. 10**: Comparison of Transient Photocurrent (TPC) lifetimes of different PSD device types. The time decay of the photocurrent was measured in response to a pulsed excitation (532 nm, ~ 1 ns pulse width). Longer lifetimes in the inverted structure are reflective of a lower recombination rate and efficient carrier extraction. 133*

***Figure 4. 11**: Reconstructed light trajectory upon acquiring ΔV_{ph} from the two pairs of electrodes for **(a)** horizontal line, **(b)** vertical line, **(c)** diagonal, and a **(d)** square. Column 1 (blue) and column 2 (red) show the plot of $\Delta V_{ph}(x)$ and $\Delta V_{ph}(y)$ as the light moves in a particular trajectory. The black curve in all plots depicts the phase of the corresponding ΔV_{ph}. The last row depicts the ΔV_{ph} variation as the light beam traces a square pattern on the PSD.....135*

***Figure 4. 12**: **(a)** Transient photocurrent profiles $I_{ph}(t)$ collected across the Au and ITO electrodes as the point of excitation is translated away from the electrode. **(b)** Schematic showing the translation of a light beam with respect to the Au electrode. **(c)** Normalized features of $I_{ph}(t)$ obtained in **(a)** show an increase in decay lifetime as the beam illumination is farther away from the Au electrode. **Inset** shows the plot of decay time with respect to illumination position.....137*

***Figure 4. 13**: Plot of TPC showing consistent I_{ph} (t) profiles at a constant distance from the collecting electrode. The beam is translated perpendicular to a pair of PSD Au electrodes in the direction of the indicated arrow.....138*

***Figure 4. 14**: **(a)** Schematic illustrates single pulse measurement using differential transient photocurrent ΔI_{ph} measurement as the pulsed light beam is translated across the active channel length. **(b)** Transient $\Delta I_{ph}(t) = I_{ph}(1) - I_{ph}(2)$ profiles as a function of excitation position.....139*

***Figure 4. 15**: **(a)** Bode plot showing the variation of impedance and phase with driving frequency, with the variation of excitation intensity. **(b)** The corresponding Cole-Cole plot as a function of light intensity variation shows the semi-circle profiles. **(c)** Bode plots as a function of excitation-position translated away from the top Au electrode. **(d)** Cole-Cole plot of the device as the excitation position is translated away from the Au*

electrode. ***Inset*** *shows the equivalent circuit diagram and the variation of the* R_2 *parameter with excitation-translation. 141*

Figure 5. 1*: Schematic explaining the mechanism of color sensing using filter array in digital imaging. The wavelength information of the incoming light is discerned with the help of a dispersive color filter array. 149*

Figure 5. 2*: **(a)** Normalized absorbance of mixed Ruddlesden-Popper perovskite film spin-coated on a glass substrate using precursor having an initial stoichiometry of* $(BA)_2(FA)_4Pb_5I_{16}$ *and* $(BA)_2(MA)_4Pb_5I_{16}$*. The absorbance indicates the excitonic peaks corresponding to bandgaps of different quantum wells.* ***(b)*** *Photoluminescence of the perovskite film measured in the reflection geometry from both perovskite and substrate sides. Relatively high 2D/quasi-2D emissions are observed when measured from the substrate side.* ***(c)*** *z-stack of confocal images with 488 nm excitation. Reconstructed images with green and red color for emission below and above 640 nm respectively.* ***(d)*** *Transient absorption on layered perovskite showing predominant 3D GSB when probed from the perovskite side and* ***(e)*** *relatively high 2D/quasi-2D GSB from the substrate side at early times.* ***(f)*** *Kinetics of the GSB at 700-710 nm corresponding to the absorption of higher order QW's (n >50). The delayed growth of GSB when probed from the substrate side indicates the energy and charge funneling from lower order quantum wells to higher order (n > 50) perovskite.* ***(g)*** *Schematic showing the graded bandgap perovskite with higher order quantum wells and the 3D layer formed away from the substrate. (Reprinted with permission from Ganesh, N., Shivanna R, Friend R. H. and Narayan. K. S "Wavelength-dependent charge carrier dynamics for single pixel color sensing using graded perovskite structures." Nano letters 19, no. 9 (2019): 6577-6584, Copyright (2019) American Chemical Society).....156*

Figure 5. 3*: **(a)**Schematic of the asymmetric device, consisting of electron and hole extraction layers on either side of the graded HOIP layer.* ***(b)*** *J(V) of asymmetric device with graded bandgap perovskite as the active layer done in dark and under 1 sun solar-spectrum, which show PCE of 3.6%. (c) IPCE data on asymmetric devices across the UV-Vis spectrum. (Reprinted with permission from Ganesh, N., Shivanna R, Friend R. H. and Narayan. K. S "Wavelength-dependent charge carrier dynamics for single pixel color sensing using graded perovskite structures." Nano letters 19, no. 9 (2019): 6577-6584, Copyright (2019) American Chemical Society).....159*

Figure 5. 4*: **(a)** Graded bandgap perovskite asymmetric device structure (ITO/PEDOT:PSS/G-HOIP/PCBM/Ag) showing pathways for electron and hole transport.* ***(b)*** *Transient photocurrent response of asymmetric device upon excitation with a 150 fs pulse of different* λ *across the spectrum* ***(c)*** *Photocurrent peak time showing delay upon longer* λ *excitation.* ***(d)*** I_{ph} *decay lifetimes for different* λ *of excitation, shown in the log scale.* ***Inset*** *shows the steady increase of decay lifetime as a function of* λ*. (Reprinted with permission from Ganesh, N., Shivanna R, Friend R. H. and Narayan. K. S "Wavelength-dependent charge carrier dynamics for single pixel color sensing using graded perovskite structures." Nano letters 19, no. 9 (2019): 6577-6584, Copyright (2019) American Chemical Society).....161*

***Figure 5. 5**: **(a)** Schematic illustrating λ-dependent positive and negative currents in a symmetric hole-only device. Blue light generates and collects carriers at the PEDOT:PSS-perovskite interface giving rise to positive current while red light generates and collects carriers at perovskite-P3HT interface resulting in negative current. **(b)** $I_{ph}(t)$ profiles with the illumination of λ across the UV-Vis-NIR spectrum. Positive peaks are suppressed and negative peaks are enhanced upon increasing the λ of excitation. (Reprinted with permission from Ganesh, N., Shivanna R, Friend R. H. and Narayan. K. S "Wavelength-dependent charge carrier dynamics for single pixel color sensing using graded perovskite structures." Nano letters 19, no. 9 (2019): 6577-6584, Copyright (2019) American Chemical Society).....164*

***Figure 5. 6**: Ultrafast photocurrent on symmetric devices indicating intensity dependent photocurrent profile with illumination at **(a)** 480 nm **(b)** 550 nm and **(c)** 700 nm. (Reprinted with permission from Ganesh, N., Shivanna R, Friend R. H. and Narayan. K. S "Wavelength-dependent charge carrier dynamics for single pixel color sensing using graded perovskite structures." Nano letters 19, no. 9 (2019): 6577-6584, Copyright (2019) American Chemical Society).....166*

***Figure 5. 7**: **(a)** Photocurrent features (derived from **Figure 5.5(a)**), smoothed and normalized in the range [0, 1] show that the photocurrent minima appears earlier in case of longer wavelengths. **(b)** Slopes of photocurrent features showing an increased rate of charge extraction for lower wavelengths in the positive transients. The early arrival of I_{ph} minima is also reflected at the zero-crossing point. 167*

***Figure 5. 8**: **(a)** $I_{ph}(t)$ features (normalized in [0, 1]) determined by interpolation for λ in the interval between two experimentally acquired sets of data. $I_{ph}(t)$ were acquired at 550 nm and 600 nm. The intermediate features were obtained on linear interpolation. **(b)** The plot shows a good fit between the $I_{ph}(t)$ for 575 nm excitation and the feature obtained on interpolation.....168*

***Figure 5. 9**: **(a)** Pulsed response in an asymmetric device. The shaded region represents the light OFF-cycle part of the pulse. **(b)** λ-dependent off-cycle features on the asymmetric device. **(c)** Equivalent circuit diagram to model the photocurrent decay features obtained in (b). (Reprinted with permission from Ganesh, N., Shivanna R, Friend R. H. and Narayan. K. S "Wavelength-dependent charge carrier dynamics for single pixel color sensing using graded perovskite structures." Nano letters 19, no. 9 (2019): 6577-6584, Copyright (2019) American Chemical Society).....170*

***Figure 5. 10**: OFF-pulse $I_{ph}(t)$ profiles upon steady-state pulsing illumination in **(a)** blue **(b)** green **(c)** red and **(d)** NIR region of the visible spectrum. 171*

***Figure 5. 11**:**(a)** Simulated current profiles for light pulsing operation measured across digital signal analyzer (R_{DSO}) in **Figure 5.9(c)** for varying C_{bulk}, **(b)** C_{rec} and **(c)** C_{barr}. The shaded region represents the light OFF-cycle part of the pulse. 173*

***Figure 5. 12**: Steady-state light pulsing measurement of control (3-D) symmetric device in short-circuit mode, using a preamplifier and digital signal oscilloscope. The device configuration in this case was: ITO/PEDOT:PSS/3D-$MAPbI_3$/P3HT/Ag. The bright regions represent the ON part and the shaded regions represent the OFF part of the light pulse.....174*

Figure 5. 13*:*(a) *Short-circuit current its* ***(b)*** *normalised plot measured on the symmetric hole only devices with light pulsing at 10 kHz, showing polarity reversal for long-λ illumination. The shaded region represents the light OFF-cycle part of the pulse. The yellow highlighted region represents the off-cycle features* ***(c)*** *showing I_{ph} decay at different λ of illumination.* ***(d)*** *IPCE of the symmetric hole only device across the spectrum. (Reprinted with permission from Ganesh, N., Shivanna R., Friend R. H. and Narayan K. S. "Wavelength-dependent charge carrier dynamics for single pixel color sensing using graded perovskite structures." Nano letters 19, no. 9 (2019): 6577-6584, Copyright (2019) American Chemical Society).....175*

Figure 5. 14*: Schematic explaining the possibility of time-resolved wavelength identification by the single-pixel sensor using optical time division multiplexing (OTDM). (Reprinted with permission from Ganesh, N., Shivanna R, Friend R. H. and Narayan. K. S "Wavelength-dependent charge carrier dynamics for single pixel color sensing using graded perovskite structures." Nano letters 19, no. 9 (2019): 6577-6584. Copyright (2019) American Chemical Society).....178*

Abbreviations and Notations

HOIP	Hybrid organic inorganic perovskites
$MAPbI_3/Br_3/Cl_3$	Methyl ammonium iodide/bromide/chloride
MSC	Methylammonium bromide Single Crystal
PCE	Power conversion efficiency
V_{OC}	Open circuit voltage
J_{SC}	Short circuit current density
FF	Fill factor
I_{ph}	Photocurrent
I/J-V or I/J(V)	Current/current density-voltage characteristics
QFLS	Quasi Fermi-level splitting
PL	Photoluminescence
PLQY	Photoluminescence quantum yield
LED	Light emitting diode
E/HTL	Electron/Hole transport layer
V/CB	Valence/Conduction band
LUMO	Lowest Unoccupied Molecular Orbital
HOMO	Highest Occupied Molecular Orbital
PR	Photon Recycling
TPC	Transient Photocurrent
LDR	Linear Dynamic Range
EQE	External quantum efficiency
TRPL	Transient Photoluminescence
SRH	Shockley-Read-Hall
MSM	Metal-Semiconductor-Metal
AFM	Atomic Force Microscopy

KPFM	Kelvin Probe Force Microscopy
NSPM	Near-field Scanning Photocurrent Microscopy
SCLC	Space Charge Limited Current
ITO	Indium Tin Oxide
PSD	Position Sensitive Detector
LPV	Lateral Photovoltage
IS	Impedance Spectroscopy
G-HOIP	Graded-Hybrid Organic Inorganic Perovskite
TA	Transient Absorption
IPCE	Incident Photon to Current Efficiency
OTDM	Optical Time Domain Multiplexing
rr-P3HT	regioregular-poly3hexathiophene
PCBM-C70	Phenyl-C71-butyric acid methyl ester
Poly-TPD	Poly(N,N'-bis-4-butylphenyl-N,N'-bisphenyl)benzidine
PEDOT:PSS	Poly(3,4-ethylenedioxythiophene)-poly(styrenesulfonate)
λ	Wavelength
τ	Lifetime
μ	Mobility

Chapter 1: Introduction

1.1 Overview of solution-processable electronics

The class of solution-processable electronics has emerged as an alternative route for the fabrication of devices for optoelectronic applications. The ease of device fabrication using cost-effective techniques such as spin-coating, roll-to-roll deposition and inkjet printing have resulted in large-area fabrication of devices. The additional advantage of depositing on flexible substrates renders these devices suitable for integration with new-age smart technologies involving flexible display, detectors and memory circuits.

Amongst the different classes of solution-processable materials, hybrid perovskite has emerged as a promising semiconductor for optoelectronic applications. Unlike semiconducting polymers which form amorphous or semi-crystalline films, the hybrid perovskites are crystalline. This long-range order results in a conduction and valence band, with a characteristic direct-bandgap. In addition to the semiconductors, solution-processable buffer layers and metal electrodes play an important role towards selective carrier extraction and transport.

Depending on the preparation conditions, the size and dimensionality of hybrid perovskites can be varied over large length scales, from single crystals (≅ cm) to quantum dots (few nm). Additionally, the introduction of long-chain alkyl groups leads to planar stacking of PbI_6 octahedral sheets, resulting in 2D-perovskites. Depending on the dimensionality and the structural features of hybrid perovskite, the carrier transport is spatially modulated in the device structure to suit different optoelectronic

applications. These solution-processable techniques together with the advantage of bandgap tunability render this class of semiconductors useful for a host of interesting applications. Since the field is vast, this chapter presents only the necessary and relevant background for the problems undertaken in the thesis.

1.2 Hybrid Organic-Inorganic Perovskites (HOIP).

1.2.1 Lattice structure

Perovskites are compounds with the chemical composition ABX_3, where A and B are cations, and X is an anion. In the case of photo-active hybrid organic-inorganic perovskites (HOIP), A is a monovalent organic cation, B is a divalent heavy metal cation and X is a monovalent halide ion (I^-, Br^- or Cl^-). The lattice structure and equilibrium are maintained by ionic and hydrogen bonding, which make them soft materials compared to inorganic perovskites.[1] This class of semiconductors has superior device performance and many of the carrier transport properties are under exploration.

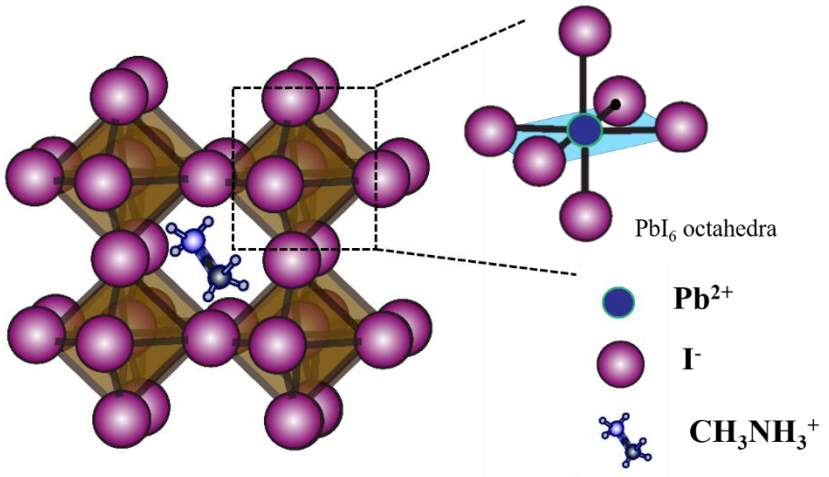

***Figure 1. 1**: Schematic representation of organic-inorganic hybrid perovskite unit cell of the form ABX_3 where $A=CH_3NH_3$, B = Pb and X= I. The methylammonium ion is surrounded by the PbI_6 octahedral cage, with a coordination number of 12.*

Figure 1.1 shows the typical perovskite lattice structure, where the BX_6 octahedra (B = Pb, and X = I) forms the corner-sharing points of the lattice, while the A-site cation ($CH_3NH_3^+$) occupies the center position, with a coordination number of 12. The selection rule for the formation of the 3D-perovskite phase is given by the Goldschmidt tolerance factor, *t*, described as follows: [2]

$$t = \frac{r_A + r_X}{\sqrt{2(r_B + r_X)}} \tag{1.1}$$

where r_A and r_B are the ionic radius of the A and B site cations respectively, and r_X is the ionic radius of the anion. The tolerance factor determines the ease of fitting the A-site cation within the octahedral surrounded cage. A tolerance factor of 1 indicates a perfect fit. For $0.8 \leq t \leq 1$, perovskites generally do form, although in the lower part of this range they may be distorted due to tilting of the BX_6 octahedra. If $t > 1$, this indicates the A-site cation is too large and generally precludes the formation of a perovskite; and if $t < 0.8$, the A cation is too small, again often leading to alternative structures. The monovalent organic cation such as methylammonium ($CH_3NH_3^+$, r_A ~ 2.16 Å) is suited for A-site cation, while at the B-site, heavy metal cations such as Pb^{2+} and Sn^{2+} is incorporated.[3] It is to be noted that the Goldschmidt tolerance is a selection rule for the 3D perovskite phase and is not valid for lower dimensional perovskites.

Despite the early discovery of hybrid perovskites[4, 5], the recent interest in this material is attributed to its facile solution processability. These materials are characterized by a high absorption coefficient (~ 10^5 cm^{-1})[6], requiring very thin (~ 200 nm) films to absorb most of the solar radiation. Upon bandgap tuning, the overlap of the low bandgap HOIP absorption spectrum and the solar spectrum can be maximized towards the Shockley-Queisser limit to achieve high efficiency in single-junction cells (~ 25 %)[7]. The superior absorption is complemented by efficient free carrier generation, owing to low exciton

binding energy (< 30 meV in $MAPbI_3$) in these materials[8]. In terms of carrier transport, these materials are characterized by high diffusion length (~ few μm) and long carrier lifetimes (> 10 ns)[9]. Additionally, the mobilities (> 10 cm^2V/s) are comparable to that of conventional inorganic semiconductors[9].

1.2.2 Bandgap Tunability

In HOIP systems, the bandgap can be tuned by both the cation as well as halide substitution. The underlying mechanism for the modification of the electronic structure is quite different. In the most studied case of $MAPbX_3$ perovskite, MA^+ can effectively stabilize the perovskite structure with a reasonable tolerance factor; however, the MA^+ cation does not have any significant contribution for the conduction and valence band states except for donating one electron to the Pb–I framework.[10] Here, the orientation of the MA^+ cation can indirectly play a role in determining the electronic properties of perovskites via distorting the PbI_6 octahedral cage.[11] Such molecular rotations result in a dynamical change of the band structure that may partially account for the $MAPbI_3$ perovskite's unique properties of slow carrier recombination and long diffusion lengths.[11]

The most commonly studied $MAPbI_3$ perovskite is characterized by a bandgap of ~1.6 eV [12] which is formed between the unoccupied Pb p-orbital and the occupied I p-orbital. Since the electronic structure of $MAPbX_3$ is related to the p-orbital of X and the p-orbital of Pb, the bandgap can generally be tuned by the p-orbital of X. In $MAPbX_3$ perovskite, the valence orbital of the halide changes from 3p to 4p to 5p when X changes from Cl to Br to I; the bandgap of the $MAPbX_3$ then decreases monotonically.[13] As previously mentioned, the cation can still affect the electronic structure of perovskites through the steric effect. Therefore, bandgap engineering is achieved by controlling the bond angles through the steric size of the cation molecule. This is

observed in the case of formamidinium lead iodide perovskite ($FAPbI_3$), which has a narrower bandgap compared to methylammonium lead iodide perovskite ($MAPbI_3$) due to the strong steric size of FA^+ molecular cation.[14] Accordingly the bandgap can be tuned in mixed cation perovskite by controlling the relative cation composition.[15] For larger cation, however, the tolerance factor $t > 1$; results in distortion of the perovskite structure. **Table 1.1** shows the bandgap of the commonly used hybrid perovskites, some of which are described in the thesis.

Table 1.1: *Bandgaps of commonly used hybrid perovskites.*

	Band gap (eV)
$MAPbI_3$	~1.6, (ref.[16])
$MAPbI_{3-x}Br_x$	1.6 - 2.3 (ref.[17])
$MAPbBr_3$	~ 2.3, (ref.[18])
$MAPbBr_{3-x}Cl_x$	2.3 - 2.9 (ref.[19])
$MAPbCl_3$	~ 2.9 (ref.[20])
$FAPbI_3$	~ 1.45 (ref.[21])
$FA_xMA_{1-x}Pb(I_yBr_{1-y})_3$	1.45 – 2.33 (ref.[15])

1.2.3 Optical properties

1.2.3.1 Absorption and PL

As described in **Table 1.1**, the perovskite materials are synthesized in various blends and colors covering the entire spectrum in the range ~ 1.5 eV to 3 eV. This class of materials exhibits high absorption coefficient reaching up to 10^5 cm^{-1}, allowing for most

of the incident light to be absorbed in 200-400 nm of the perovskite film. Additionally, photothermal deflection spectroscopy measurements show the presence of sub-bandgap or tail states well below the band-edges[6].

In addition to good absorption, HOIP materials are characterized by decent photoluminescence (PL) emission even at room temperature that results in high conversion efficiencies in solar cells [22, 23], and LEDs.[24, 25] It is observed that the emission quantum yield increases as a result of exciton confinement in layered perovskites and nanocrystals. This emission in these systems has been experimentally shown to originate from a direct band transition of the cold carriers that have relaxed to the band-edge.[26]

1.2.3.2 Binding energy

The fundamental species generated upon photoexcitation (either free charges, excitons, or a mixture of both) is largely dependent on the exciton binding energy E_b. This parameter is crucial for determining the mode of operation in optoelectronic devices. For instance, the methylammonium lead iodide, $MAPbI_3$ perovskites are characterized by low values of E_b (2–25 meV)[8, 27, 28], close to or smaller than the thermal energy at room temperature (k_BT = 25 meV), which leads to the generation of primarily free charges in the excited state. This feature serves as an advantage in solar cell devices.

On the other hand, the values of E_b for methylammonium lead bromide, $MAPbBr_3$ is slightly higher, in the range 15.3-150 meV depending on the type of sample (polycrystalline or single crystal).[29-31] As a result of E_b being slightly higher than the thermal energy, the free charges and excitons coexist, with their ratio depending on the excitation density.[32] Moreover, the crystal size, chemical nature, dielectric constant of the confined environment, and the dimensionality strongly affect E_b, which can increase

it up to 375 meV for small nanocrystals (NCs),[24, 30] Such high values of E_b >> 25 meV results in the photo-generation of excitons which leads to dominant radiative recombination. This property suits luminescent-based applications such as LEDs and lasers[33, 34].

1.2.3.3 Photon recycling

The twin properties of high absorption and decent emissive yield results in reabsorption and re-emission of light in the HOIP active layer, giving rise to photon-recycling effects. Previously, in inorganic semiconductors such as GaAs solar cells[35], the photon recycling effect was proposed to contribute to the high Voc since it allows the build-up of charge carriers in the active layer to increase the quasi-Fermi level splitting, resulting in the increase of power conversion efficiency (PCE) from 25 % to 29 %. The first experimental evidence for the photon recycling effect in $MAPbI_3$ polycrystalline thin films was reported which shows that the charge generation profile exhibits deviation from the Beer-Lamberts law[36]. Analysis of the spatially resolved PL reveals regions of charge generation as far as 50 μm from the point of initial light absorption.[36]

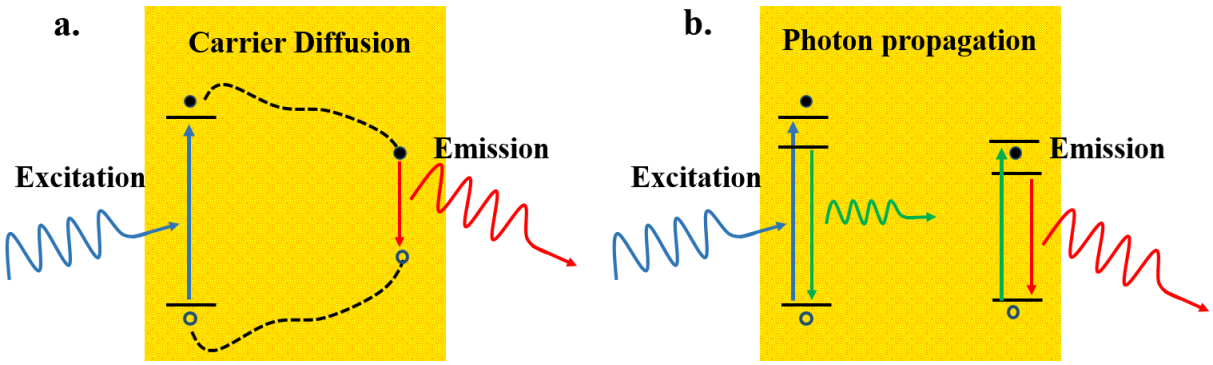

***Figure 1. 2**: Schematic illustrating the mechanism of **(a)** carrier diffusion and **(b)** photon recycling*

To quantify the effect of photon recycling on carrier generation and transport, Fang et.al developed a method to determine the efficiency of photon recycling by

differentiating the emitted and reabsorbed photons based on light polarisation[37]. It was found that in these systems, the efficiencies of photon recycling were less than 0.5%, showing negligible photon recycling effects under the solar cell working conditions (that is, close to 1 sun illumination intensity at room temperature). This low photon recycling efficiency is be attributed to the low photoluminescence quantum yield (PLQY) of the perovskite, especially under low photo-excitation intensity. In effect, the impact of photon-recycling on the device open-circuit voltage (V_{OC}) was estimated to be in the range of 40-80 mV.[38, 39]

1.2.4 Defects in Hybrid perovskites

Defects in crystalline semiconductors can be defined as either interruptions to an otherwise perfect crystal lattice, which leads to the formation of crystallographic defects, or, as foreign atoms in the lattice, which results in impurities. The spatially localized defect can lead to the formation of a defect state within the semiconductor bandgap, which acts as a carrier trap center. A schematic explaining the distribution of trap states is shown in **Figure 1.3**. The impact of trapping on carrier transport depends on the energy level of the defect state. The trapped electron (or hole) is likely to be de-trapped if the activation energy is small. On the other hand, if the activation energy is sufficiently large, the trapped carrier eventually recombines with the counter carrier, and the process is given by Shockley-Read-Hall (SRH) statistics, which is a loss mechanism in solar cells[40, 41]. This trap-related emission can be either radiative or non-radiative.

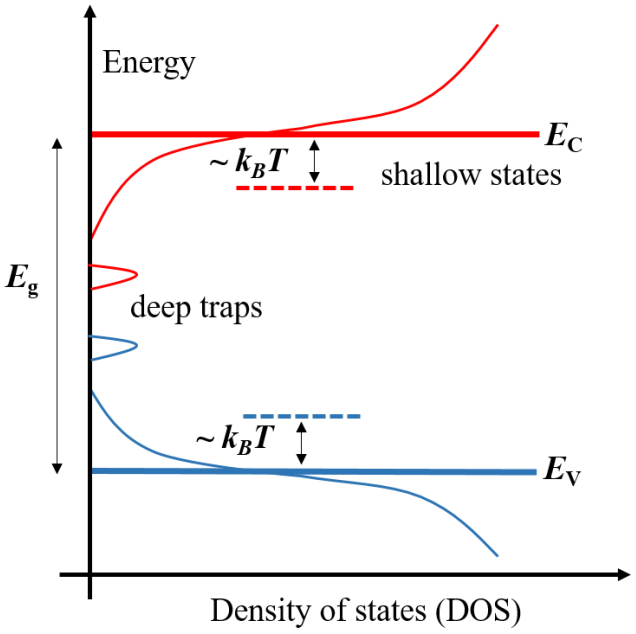

***Figure 1. 3**: Schematic expanding the distribution of band states, sub-bandgap states that form the shallow defects, and the deep trap states. The shallow defects have a low activation energy ~ k_BT, while the deep traps have higher activation energies.*

The trap-assisted non-radiative decay is of fundamental relevance to the solar-cell performance in the open-circuit condition. Upon steady-state excitation, the excess photo-generation of charge carrier results in the quasi Fermi-level splitting (QFLS) for the electrons and the holes. This difference in the QFLS results in the open-circuit voltage of the solar cells. The presence of additional non-radiative recombination at a faster rate results in the reduction of the excess charge carriers that contribute to QFLS, thereby reducing the difference in the QFLS levels. As a consequence, the device V_{OC} and the efficiency reduces. In other words, the external luminescent quantum efficiency (EQE_{EL}) in solar cells is directly related to the V_{OC} loss due to non-radiative recombination and is given by:[42].

$$\Delta V_{nr} = -\frac{k_B T}{e} \ln(EQE_{EL}) \tag{1.2}$$

where EQE_{EL} is related to both the radiative and non-radiative recombination rates (k_r and k_{nr} respectively), such that: $EQE_{EL} \propto \frac{k_r}{k_r+k_{nr}}$. In the ideal case considering $k_r = 0$ or $EQE_{EL} = 1$, $\Delta V_{nr} = 0$. However, in real devices, for every order reduction of EQE_{EL}, the V_{OC} reduces by 60 mV.

1.3 Layered Perovskites.

Unlike the 3D perovskites, layered 2D perovskites are formed upon introducing a long chain alkyl or aromatic moiety, which are supported by weak Van der Waals forces, into the PbI_6 octahedral layers. The order of the 2D or quasi-2D perovskites depends on the number of octahedral sheets that stack in every repeating unit. The layer-structured 2D perovskite materials follow stoichiometric relation given as:$(RNH_3)_2(ANH_3)_{n-1}M_nX_{3n+1}$ structure, where R is an alkyl or aromatic moiety larger than A, M is the heavy metal, X is the halide and n is the number of inorganic layers between the organic chains.[43, 44]. A schematic illustrating different ordering of the 2D perovskites is shown in **Figure 1.4**, where butyl ammonium cation (BA^+) is used as the organic linker. When $n \rightarrow \infty$, the structure converts to a 3D perovskite.

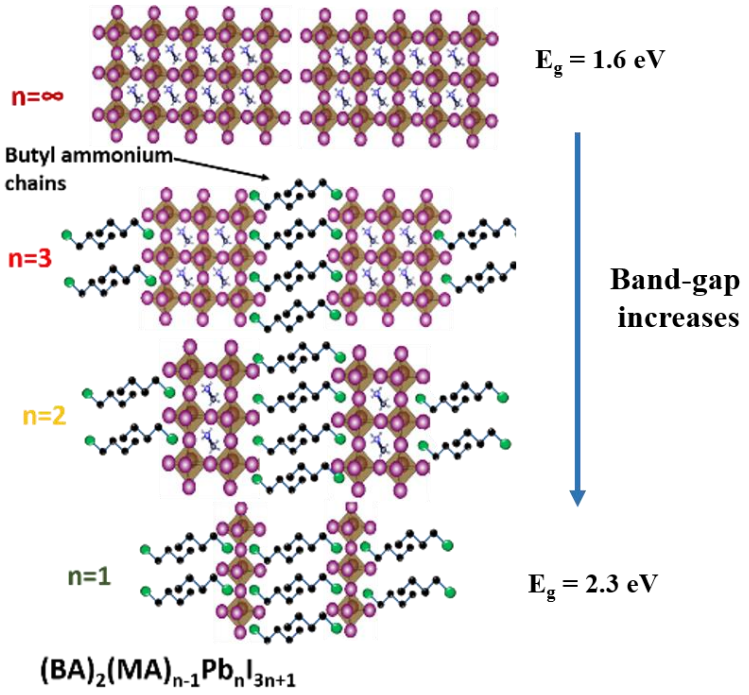

Figure 1. 4*: Schematic illustrating the lattice ordering of 2D layered perovskites. The butyl-ammonium ions are interspersed between the different orders of octahedral stack layers. The n = ∞ corresponds to the bulk 3D perovskite. The bandgap of the 2D perovskite reduces for higher-order 2D perovskites.*

The organic components, being either large aliphatic or aromatic ammonium cations, enhance hydrophobicity, thereby preventing moisture from penetrating and destroying the inorganic layers, improving operational stability[45]. Additionally, as a result of short-order periodicity and confinement due to the alkyl layers, the band-gap and the binding energy in these systems increase in the lower order 2D perovskites, indicating the excitonic nature of the photogenerated species[46]. This feature makes it a prospective material for optoelectronic applications such as LEDs where the spectral emission can be tuned[47, 48]. This property of bandgap tunability has been utilized in chapter 5 of the thesis, by the formation of a graded bandgap structure. The photocurrent output due to the wavelength-dependent absorption profile is utilized for color sensing application.

1.4 Carrier transport and recombination

1.4.1 Drift diffusion formalism

The long-range order and crystalline nature of perovskites allow for the application of drift-diffusion formalism to model carrier transport equations. Therefore, in a device structure, assuming predominant contribution of carrier transport in HOIP, to the observed current can be expressed as:

$$J_n = q\mu_n nE + qD_n \nabla n \tag{1.3}$$

$$J_p = q\mu_p pE - qD_p \nabla p \tag{1.4}$$

where q is the electronic charge, E is the applied electric field, n and p are electron and hole concentrations, $\mu_{n(p)}$ is the electron (hole) motilities that satisfy $\mu_{n(p)} = \frac{v_{n(p)}}{E}$ for the drift velocity $v_{n(p)}$ and, $D_{n(p)}$ is the electron (hole) diffusion constants, which satisfy the Einstein relation $D_{n(p)} = \mu_{n(p)} \frac{kT}{q}$.

The continuity equation for two carriers can be written as:

$$q\frac{\partial n}{\partial t} = \nabla J_n + q\,(G - R) \tag{1.5}$$

$$q\frac{\partial p}{\partial t} = \nabla J_p + q\,(G - R) \tag{1.6}$$

Where G and R are the carrier generation and recombination rate.

Electric field due to carrier concentration can be expressed by the Poisson's equation as:

$$\varepsilon.\nabla E = q(p - n + N_d) \tag{1.7}$$

Where, ε is the (homogeneous) permittivity of the medium and N_d is the concentration of any dopants, impurities, or trapped carriers, weighted by their relative charges.

Using **equations 1.5**, **1.6** and **1.7** and $E = -\nabla\phi$ where ϕ is the electrostatic potential, the ambipolar transport equations can be expressed as:

$$D'\nabla^2 n + \mu' E\nabla n + G - R = \frac{\partial n}{\partial t} \tag{1.8}$$

Where $D' = \frac{\mu_n n D_p + \mu_p p D_n}{\mu_n + \mu_p}$ is the ambipolar diffusion coefficient and, $\mu' = \frac{\mu_n \mu_p (p-n)}{\mu_n + \mu_p}$ is the ambipolar mobility. In the case of minority excess carrier transport and assuming the simplest case of 1-D transport, **equation 1.8** reduces to:

$$D_n \frac{\partial^2 n}{\partial x^2} + \mu_n E \frac{\partial n}{\partial x} + G - R = \frac{\partial n}{\partial t} \tag{1.9}$$

for excess electrons, and

$$D_p \frac{\partial^2 p}{\partial x^2} - \mu_p E \frac{\partial p}{\partial x} + G - R = \frac{\partial p}{\partial t} \tag{1.10}$$

for excess holes. It has to be noted that the second term, representing drift, indicates an opposite sign for the case of excess holes (**Eq. 1.10**). This follows that the sign of the drift term depends on the charge of the particle. Holes drift in the direction, and electrons opposite to the direction of the electric field.

Using **equations 1.9** and **1.10**, carrier transport with necessary boundary conditions is elaborated in Chapter 2 and Chapter 3, described under conditions of diffusion and drift

dominant photocurrents. The following conditions provided in **Table 1.2** is useful for further equation simplifications.[49]

Table 1.2: *Common equation simplification conditions*.

Specification	Effect
Steady-state carrier generation	$\frac{\partial n}{\partial t} = 0$
Uniform distribution of carriers	$D_n \frac{\partial^2 n}{\partial x^2} = 0$
Zero electric field	$E \frac{\partial n}{\partial x} = 0$
No excess carrier generation	$G = 0$
No carrier recombination (infinite carrier lifetime)	$R = 0$

1.4.2 Recombination Dynamics

The recombination dynamics play a crucial role and influences carrier transport and device performance. In terms of carrier transport, the diffusion length, L_{diff}, a parameter which indicates the efficiency of transport, depends on carrier recombination lifetime (τ) as, $L_{diff} = \sqrt{D\,\tau}$, where D is the diffusion coefficient. As a consequence, carrier recombination and transport are coupled processes that decide the efficiency of device operation.

The principle of detailed balance for carrier generation and recombination processes requires that photons must be continuously exchanged between a semiconductor and its

environment[50]. In other words, to maintain steady-state photo-carrier generation, radiative recombination is necessary. However, photogenerated carriers also recombine through additional trap-assisted pathways. The dominant mechanism of recombination however depends on factors such as excitation intensity and temperature. The schematic shown in **Figure 1.5** illustrates the various recombination mechanisms that occur in semiconductors.

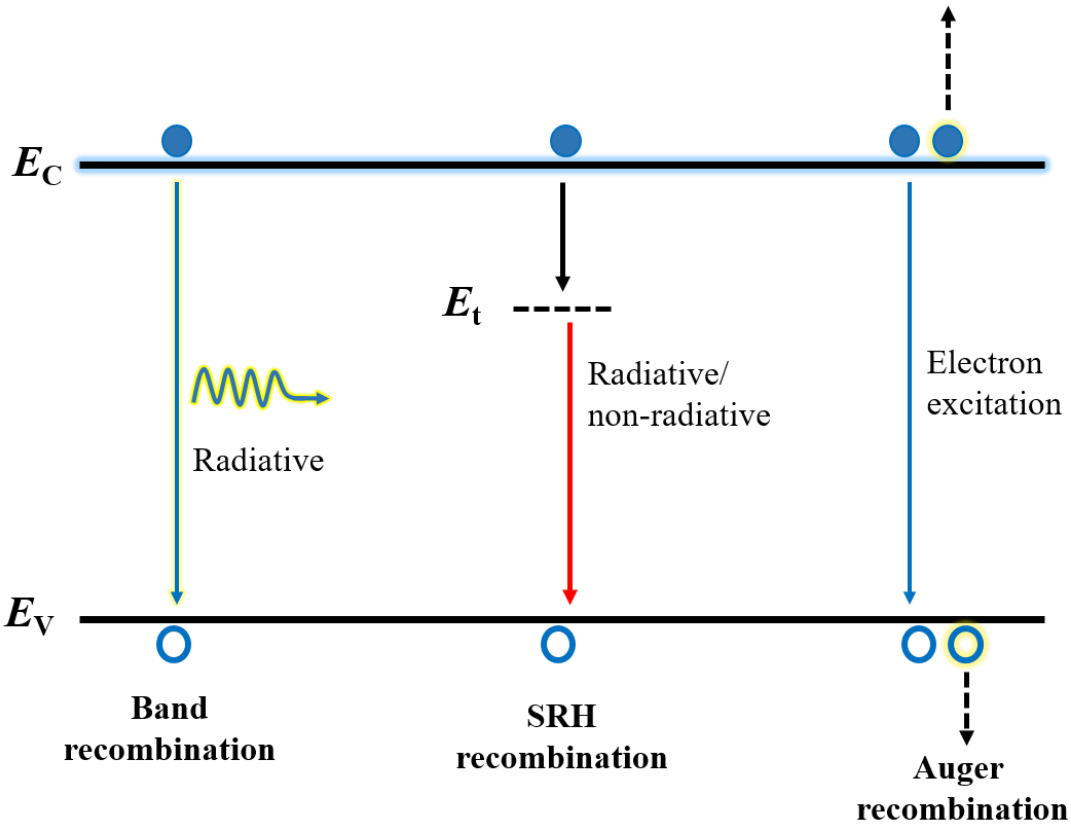

***Figure 1. 5**: Schematic illustrating the dominant carrier recombination pathways in a direct band-gap semiconductor. The band recombination is a direct radiative process. Trap-assisted recombination is given by the Shockley-Read-Hall (SRH) recombination dynamics. In the Auger recombination, upon the recombination of an electron-hole pair, either an electron is excited higher into the conduction band or a hole lower into the valence band.*

As shown in **Figure 1.5**, recombination of photo-generated carrier occurs through mainly three processes:

(i) *Band recombination*: Radiative recombination of free carriers.

(ii) *Trap-assisted recombination*: This could be either radiative or non-radiative and the recombination is given by Shockley-Read-Hall (SRH) statistics.

(iii) *Auger recombination*: This is a non-radiative process involving three carriers. When an electron-hole pair recombines, an electron is either excited higher into the conduction band or a hole lower into the valence band.

In this thesis, recombination dynamics are studied with excitation intensities in the low and intermediate-range (< 10^{17} photons/cm^2). The Auger mechanism of recombination is therefore not considered, since it is relevant only at high-intensity excitation.

Upon photo-carrier generation, the efficiency of either of the above recombination pathways depends on both the rate of recombination and the density of states or species available for recombination. Therefore, the effective recombination lifetime, τ_{eff} depends on radiative band recombination lifetime (τ_R) and trap recombination lifetime (τ_{SRH}) and is represented as:

$$\frac{1}{\tau_{eff}} = \frac{1}{\tau_{SRH}} + \frac{1}{\tau_R} \tag{1.11}$$

The auger recombination component which becomes prominent at high excitation fluence (> 10^{17} photons/cm^2) is neglected. $1/\tau_R$ can then be expressed as

$$\frac{1}{\tau_R} = B\ (N_A + \ \delta n)\ and\ \frac{1}{\tau_{SRH}} = R_{SRH}.N_T \tag{1.12}$$

where, δn is the excess carrier density, B the radiative constant, and N_A the background doping concentration, R_{SRH} is the non-radiative constant, and N_T is the trap density. The radiative recombination rate is given as:

$$\frac{\delta n}{\tau_R} = A_R \delta n + B\ (\delta n)^2 \tag{1.13}$$

where, $A_R = B.N_A$. It has to be noted in the first term on the right-hand side refers to monomolecular recombination and it varies linearly with excess carrier density and the second term, which refers to bi-molecular recombination depends quadratically on carrier density. At low excitation densities, the photoexcited population decays through interactions with the background carriers and defect states with a monomolecular rate. As the photo-carrier density increases, the monomolecular decay channels saturate and the bimolecular band to band recombination increasingly determines the overall recombination rate. A detailed investigation of dependence on recombination lifetime on excitation intensity and its influence on effective diffusion length is presented in chapter 2.

1.5 Charge transport layers and Interfaces

The efficiency of the photon to electron conversion, η in an optoelectronic device can be expressed as:

$$\eta = \left(\frac{charges\ at\ external\ circuit}{incident\ photons}\right) = \eta_A \eta_{CS} \eta_{CT} \eta_{CC} \tag{1.14}$$

where, η_A, η_{CS}, $\eta_{CT,}$ and η_{CC} represents the efficiency of photon absorption, charge separation, charge transfer, and charge collection, respectively. These mechanisms are shown in **Figure 1.6**.

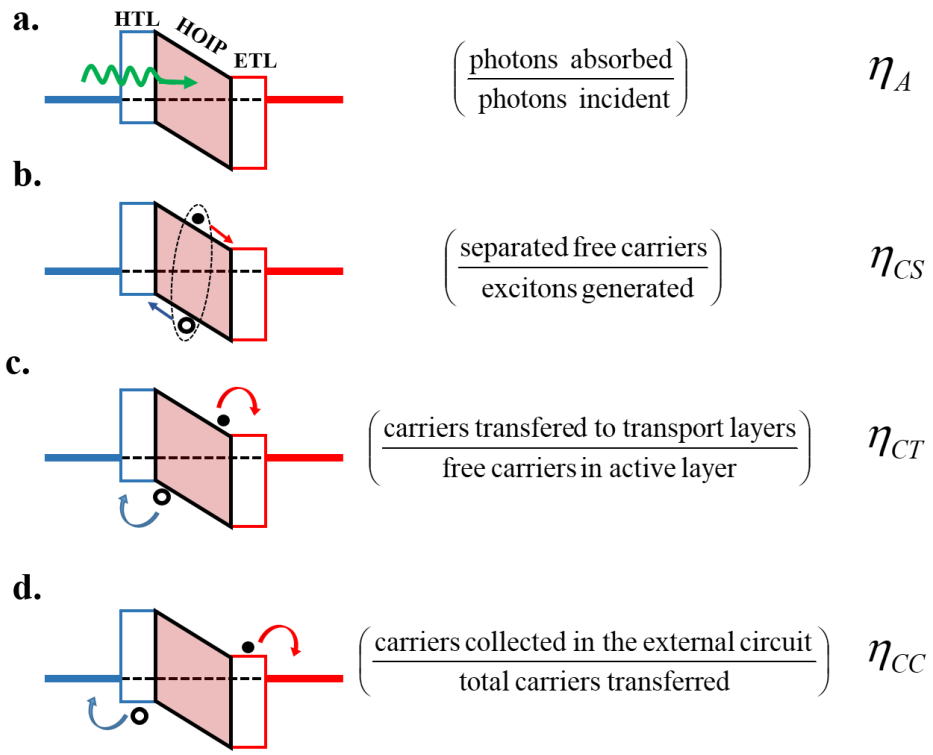

Figure 1. 6*: Schematic illustrating the carrier generation and separation dynamics, with associated efficiencies, in a device with the configuration: electrode/HTL/HOIP/ETL/electrode.* ***(a)*** *depicts the process relating to the efficiency of photon absorption.* ***(b)*** *shows the process of exciton generation and dissociation to form free carriers* ***(c)*** *shows the charge transfer process to the charge transport layers.* ***(d)*** *depicts the charge collection to the respective electrodes, which forms the current in the external circuit.*

As illustrated in **Figure 1.6**, the initial two processes of absorption (discussed in section 1.2.3) and exciton dissociation and transport (discussed in section 1.4) occurs in the active semiconductor layer. The next two processes of charge transfer and charge collection are determined by the charge transfer layers and the interfaces. Good interfaces and charge transport layers are characterized by low contact resistance, selective carrier mobility, the presence of an ohmic contact, and energy levels to facilitate efficient charge injection and extraction.

The method of solution-processable deposition of hybrid perovskites allows for the use of organic semiconductors as carrier transport layers. The organic semiconductors are π-conjugated organic molecules which can either be a polymer or a small molecule. The bandgap is defined as the energy gap between the lowest unoccupied molecular orbital (LUMO) and the highest occupied molecular orbital (HOMO)[51, 52]. The carrier mobility in these systems is relatively lower owing to strong localization effects[53]. Depending on the energy levels, these can be classified as hole transport layers (HTL) or donors, and electron transport layers (ETL) or acceptors. Essentially, with respect to device engineering, the energy levels of the selected material should facilitate the extraction of one carrier and block the counter carrier. Additionally, to improve the carrier mobility, the organic layers can also be extrinsically doped. These systems offer an additional advantage for device fabrication since most of the solvents for the organic layers have orthogonal solubility with HOIP based solvents. Some of the properties of the charge transport layers used in the thesis are tabulated in **Table 1.3.**

Table 1.3: *Properties of organic semiconductors used in this thesis.*

Charge transport layers	**Band gap (eV)**	**LUMO (eV)**	**HOMO (eV)**	**Mobility (hole) (cm^2/Vs)**
HTL				
P3HT	1.9	-3.0	-4.9	~ 10^{-4} (ref [54])
PEDOT:PSS (used from an aqueous dispersion)	1.7	-3.5	-5.2	~ 10^{-4} (ref [55])
Poly-TPD	2.9	-2.3	-5.2	~ 10^{-4} (ref [56])
ETL				**electron**
N2200	1.45	-3.95	-5.40	~ 0.45 - 0.8 (ref [57])
PCBM-C70	2.0	-3.9	-5.9	~ 10^{-3} (ref [58])

1.5.1 Loss mechanism at the interface:

The presence of lattice termination and the dangling bonds at the interface results in the formation of interfacial surface states that contribute to loss mechanisms, lowering device performance. Some of the main reasons for loss mechanisms are discussed below:

(i) ***Surface recombination***: One of the main loss mechanisms at the interface is due to surface recombination effects. The surface recombination loss-current *J*s of electrons at a hole contact is given as:[59]

$$J_S = qSn_0\, exp\left(\frac{\Delta E_F}{k_B T}\right) \quad (1.15)$$

where q is the unit charge, S is the surface recombination velocity, n_0 is the electron density at the hole contact in thermal equilibrium, ΔE_F the quasi-Fermi level splitting, and the thermal energy k_BT. It can be seen in **Equation 1.15** that Js increases proportionally with surface recombination velocities and charge densities. S is primarily dependent on the defect density that acts as centers for non-radiative recombination. n_0 on the other hand is dependent on the potential drop at the interface. A higher built-in field ensures lower accumulation of the n_0 (p_0) at the HTL (ETL) interface. Therefore, high defect density and improper energy level alignment results in major recombination losses[60]. In addition to surface states of the active perovskite surface, defect centers in the transport layers also contribute to charge accumulation processes, which reduces V_{OC} and FF (fill-factor) [61].

(ii) ***Ion accumulation***: The ionic lattice of perovskite which is characterized by low activation energies for ionic motion results in ion accumulation at the interfaces. The energy barrier, the defects, or charge/ion accumulation at perovskite/transport materials interfaces not only impedes charge collection efficiency but also affects hysteresis and long-term light soaking processes, since the mobile ions can screen the built-in potential, reducing the V_{OC} of the devices [62-64]. For example, it is demonstrated that under-coordinated halide ions on the surface of the organic-inorganic halide perovskite crystal reduces the cell performance by trapping positive charges at the perovskite/HTL interface [65].

(iii) ***Chemical instability***: In addition to the presence of intrinsic surface states, chemical reactions between adjacent contacts also create interface gap states[66,

[67]. Moreover, as a consequence of ion migration under the effects of light soaking or external electric fields, the accumulated halide ions at the electrodes have been found to cause corrosive effects[68]. These issues have been partially resolved using ionic liquids[69] that increase the activation energy for ion migration and passivation of interfacial buffer layers that block ion movements[70]. However, a major challenge would be to engineer buffer layers to match band-alignment and conductivity with the adjacent layers, thereby minimizing parasitic electrical losses[71].

In these systems, long-term operational stability is a bottleneck towards the commercialization of HOIP based devices. To overcome this, it is necessary to understand the perovskite degradation mechanism in working devices, in particular, fundamental processes due to light and electric field-assisted mechanisms at the interface and the bulk regions. Insight into defect formation dynamics, field triggered ion motion and light-induced phase segregation needs to be obtained. A precise characterization technique to study operational dynamics in devices to account for perturbations at grain boundaries in the material as well as the interfaces is needed.

With respect to this methodology, the application of tools such as Kelvin probe force microscopy (KPFM) and scanning photocurrent mapping have been presented in chapter 3 of the thesis. As an initial approximation of a solar cell device, lateral asymmetric electrode metal-semiconductor-metal (MSM) devices were used to understand the carrier transport in the bulk and across interfacial regions. This approach allows for the identification of physical mechanisms such as interface barrier heights and the degree of band-bending that are either beneficial or detrimental for the device operation.

1.5.2 Metal-semiconductor interface.

The metal junction in devices should ideally allow for unimpeded conduction of carrier, with the formation of an ohmic contact. However, due to the mismatch of the metal Fermi-level, a barrier for carrier injection is formed at the metal-semiconductor interface. **Figure 1.7(a)** shows the schematic explaining the band alignment across the metal-semiconductor interface. In this illustration, the metal is in contact with a p-doped semiconductor, with $\varphi_m < \varphi_s$, where φ_m and φ_s are the metal and semiconductor Fermi-levels respectively. **Figure 1.7(b)** shows, that in consistent with the vacuum level alignment (known as the Mott-Schottky limit), Fermi-level equilibration results in band bending at the interface. This gives rise to a Schottky injection barrier for electrons (φ_{bn}) and holes (φ_{bp}), and is given as:

$$\varphi_{bn} = \varphi_m - \chi \tag{1.16}$$

$$\varphi_{bp} = I.E - \varphi_m \tag{1.17}$$

where χ and *I.E* are the electron affinity and ionization energy of the semiconductor, respectively. Additionally, this band-banding results in the development of a built-in voltage (shown in **Figure 1.7(b)**) in the semiconductor and is given as

$$V_{bi} = \varphi_{bn} - \varphi_n \tag{1.18}$$

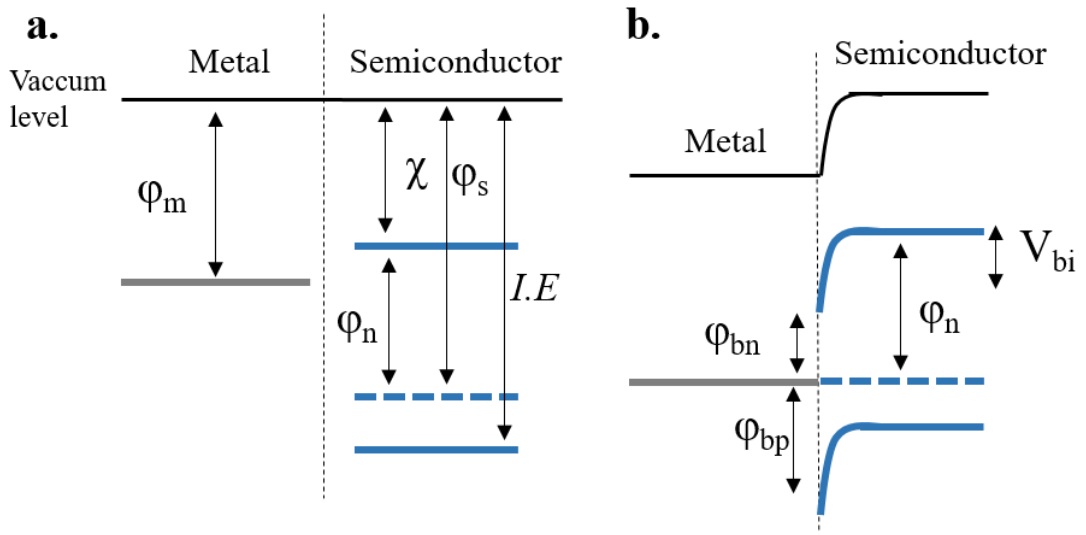

***Figure 1. 7**: **(a)** Schematic showing the energy levels and the band alignment across a metal-semiconductor interface before the formation of a contact. The scheme is represented for $\varphi_m < \varphi_s$. **(b)** shows the band bending after the formation of a contact, which results in an injection barrier across the interface.*

In the ideal condition of the formation of a Schottky diode, the injection current (for electrons) is given as:

$$J = J_{sT}\left[\exp\left(\frac{eV}{k_B T}\right) - 1\right] \tag{1.19}$$

where J_{sT} is the thermionic reverse saturation current and is given as:

$$J_{sT} = A^* T^2 \exp\left(-\frac{e\varphi_{bn}}{k_B T}\right) \tag{1.20}$$

where $A^* = \frac{4\pi e m_n^* k_B^2}{h^3}$ is the Richardson's constant for thermionic emission, with m_n^* and h being the effective electron mass and the Planck's constant respectively.

The above explanation considers the formation of an ideal Schottky contact assuming clean interfaces. However, instances of deviation from the Schottky behavior have been observed even in the case of well-functioning contacts. For example, the contact between copper (Cu) and cadmium sulphide (CdS), which was assumed to be a Schottky contact, was in fact a hetero-junction caused due to a chemical reaction that resulted in the formation of a p-type Cu_2S.[72, 73] In hybrid perovskites, the presence of surface states could alter the metal-perovskite interface, introducing interfacial trap states in addition to the charge injection barrier [74-76].

1.6 Solution-processed electronic devices

The end goal of solution-processed hybrid perovskite is to realize efficient, low-cost, and robust electronic devices. Most of the perovskite-based devices employ the sandwich architecture for charge separation and transport. **Figure 1.8** shows the two different architectures employed for device fabrication. In the normal structure, the n-i-p configuration, the electron transporting layer is positioned at the bottom electrode while in the inverted structure (p-i-n configuration) this convention is reversed.

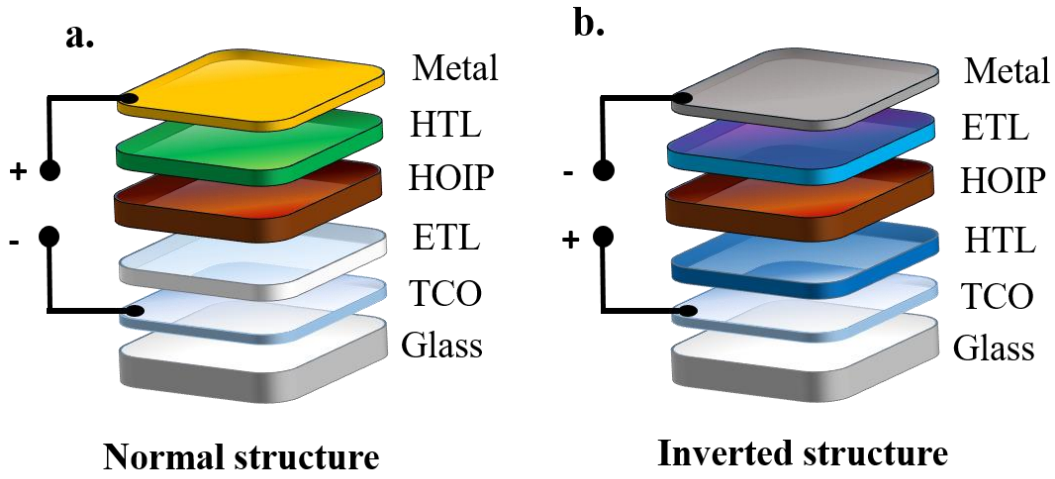

***Figure 1. 8**: Schematic depicting vertically stacked devices representing the **(a)** normal structure and **(b)** inverted structure. The abbreviations used are expanded here TCO:*

transparent conducting oxide, E(H)TL: electron (hole) transport layer, HOIP: hybrid organic-inorganic perovskite.

A plethora of devices has been realized using hybrid perovskites such as solar cells[77], photo-detectors[78], light-emitting diodes (LEDs)[79], x-ray imagers[80], neuromorphic circuits[81], lasers[82], and transistors[83]. From the perspective of the thesis, the following sections present the basic principles and working of solar cells and photo-detectors.

1.6.1 Photovoltaics

Hybrid perovskites have emerged as a promising material for solar cell applications. In 2009, Miyasaka and co-workers reported the $MAPbI_3$ and $MAPbBr_3$ based solar cells, with a small power conversion efficiency (PCE) of 3.8% for a $MAPbI_3$ based solar cell.[22, 84] In over a decade, the record efficiency of perovskite solar cells sky-rocketed to a certified efficiency of 25.2 %.[7]

In a hybrid-perovskite based solar cell, even at zero bias, a built-in electric field exists which assists in charge separation and drift. Upon photo-illumination, the photogenerated electron-hole pairs are swept out to produce a photocurrent I_L in reverse bias. Since the device is essentially a diode, the forward-bias voltage generates a forward-bias current I_F. Overall, the net *I-V* characteristics is expressed as:

$$I = I_L - I_F = I_L - I_0\left[\exp\left(-\frac{qV}{kT}\right) - 1\right] \qquad (1.21)$$

where I_0 is the reverse saturation current and V is the applied voltage. The plot of the current density, J-V in the dark and light is given in **Figure 1.9.**

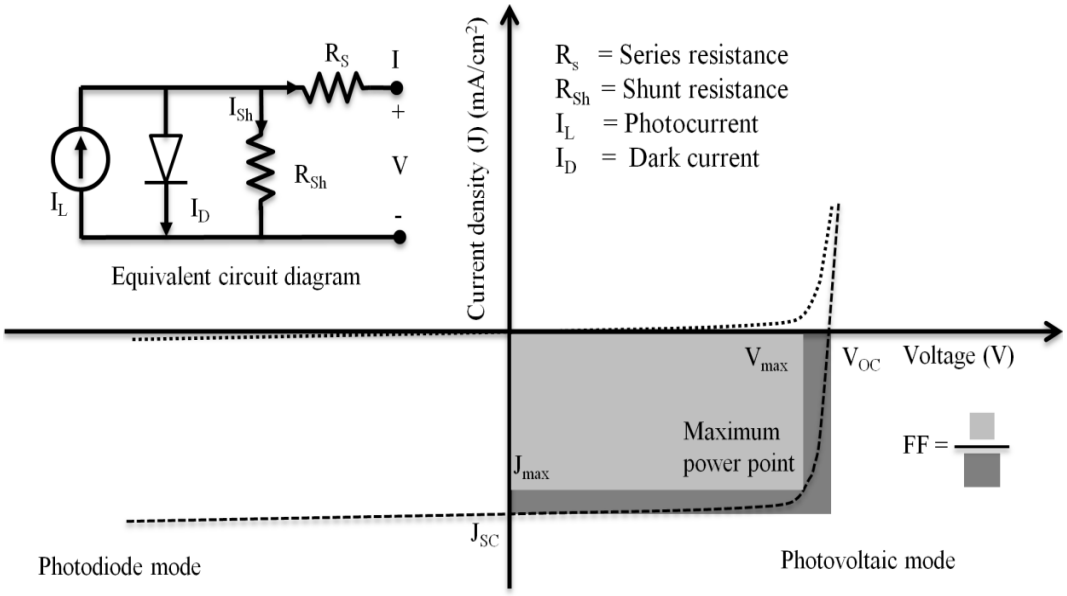

Figure 1. 9*: Schematic representation of the J-V characteristics of the solar cell. The inset shows the equivalent circuit model for a typical solar cell.*

Besides efficient light harvesting, a large absorption coefficient also contributes to a large open-circuit voltage (V_{OC}), because the material would require only a thin active layer to fully absorb light with energy above the band-gap, which can reduce the charge recombination induced reverse saturation dark current. This is described by the Shockley–Queisser model of the relationship between the film thickness and V_{OC}[85]:

$$V_{OC} = \frac{kT}{q} ln\left(\frac{J_{SC}}{J_0}\right) = \frac{kT}{q} ln\left(\frac{J_{SC} N_D \tau_{eff}}{q n_i^2 d}\right) \quad (1.22)$$

where k_B is the Boltzmann constant, T is the temperature, q is the elemental charge, J_{SC} is short-circuit current density, J_0 is initial current density, N_D is the doping concentration, τ_{eff} is the effective carrier recombination lifetime, n_i is the intrinsic carrier concentration and d is the thickness of the active layer. Due to the high absorption coefficient of the active layer, the thickness of most reported high-efficiency

HOIP solar cells is in the range of 0.3–0.6 μm[77, 86], whereas crystalline silicon solar cells are usually about 300 μm thick[87]. This advantage of HOIP results in a very low V_{OC} deficit (= E_g/q - V_{OC}) ~ 0.37 eV, in comparison to the silicon solar cells (~ 0.6eV)[88].

The inset of **Figure 1.9** shows the equivalent circuit model for a typical solar cell. The performance of a solar cell is characterized by four quantities, V_{OC}, short circuit current density (J_{Sc}), fill factor (FF) and power conversion efficiency (PCE).

$$FF = \frac{V_{max}J_{max}}{V_{OC}J_{SC}} \, , PCE = \frac{J_{max}V_{max}}{P_{in}} \tag{1.23}$$

The PCE of a photovoltaic cell is defined by the fraction of input optical power (P_{in}) delivered as electrical power at the output. The standard reference for measuring this parameter is AM 1.5G illumination (1 Sun = 100 mW/cm^2).

1.6.2 Photo-detectors

A photo-detector is a photo-active device that delivers an electric signal output which is proportional to the incident light intensity. The devices are also operated under bias conditions to ensure maximum charge extraction thereby improving the sensitivity. The performance of photo-detectors is characterized by the figure of merits, which are enumerated as follows:

(i) ***Responsivity***: Responsivity (R) is the ratio of the photocurrent generated per incident photon-power and is expressed as (A/W):

$$R(\lambda) = \frac{I_{ph}}{P(\lambda)} \tag{1.24}$$

where I_{ph} is the measured photocurrent and $P(\lambda)$ is the power of incident light of wavelength λ.

(ii) ***External Quantum Efficiency (EQE):*** It is expressed as the ratio of collected carriers to incident photons and it depends on the responsivity as follows:

$$EQE\ (\lambda) = \frac{n_{electrons}}{n_{photons}} \times 100 = \frac{R(\lambda) \times 1240}{\lambda} \times 100 \quad (1.25)$$

where λ is indicated in nm and EQE is expressed in %.

(iii) ***Linear Dynamic Range (LDR):*** It defines an optical power range in which the output current or voltage is linear with the input optical signal, and it can be calculated by:

$$LDR\ =\ 20\ \times log\left(\frac{P_{max}}{P_{min}}\right) \quad (1.26)$$

where P_{max} and P_{min} are the highest and the lowest detectable optical power with maintained responsivity.

(iv) ***Noise Equivalent Power (NEP):*** It represents the lowest light intensity that the photodetector identifies as electronic noise. It is defined as the input power of the optical signal with a signal-to-noise ratio equal to 1. It can be written as:

$$NEP\ =\ \frac{i_n}{R} \quad (1.27)$$

where i_n is the noise current in a particular frequency interval and R is responsivity. The NEP is measured in $W/Hz^{1/2}$

(v) ***Response time***: The response time is the ability of the photodetector to respond to a rapidly switching light signal. One of the methods to measuring the response speed of a photodetector is to analyze the rise and fall time of the photodetector using a transient photocurrent method. This response time also correlates to the frequency-dependent response. When the responsivity of the detector reduces by a factor of 2, the corresponding modulated frequency of light is noted as the f_{-3dB}. This frequency depends on the carrier transit time (τ_{tr}) in the device and the RC response time of the detector[89], and is given as:

$$(f_{-3dB})^{-2} = \left(\frac{3.5}{2\pi\tau_{tr}}\right)^{-2} + \left(\frac{1}{2\pi RC}\right)^{-2} \quad (1.28)$$

To improve the response speed, both the τ_{tr} and the RC lifetime of the device needs to be reduced. While τ_{tr} can be reduced by improving carrier mobility and the operating voltage, the RC lifetime can be reduced by implementing lateral structures that have low device capacitance.

The photo-detectors can be classified based on the device architecture: sandwich devices and lateral devices. A schematic of this is depicted in **Figure 1.10**

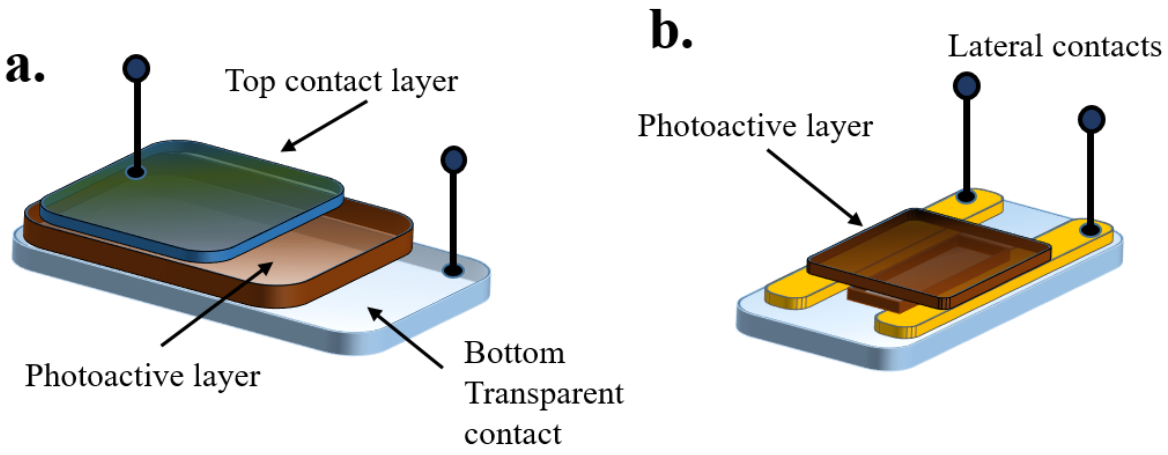

***Figure 1. 10**: Schematic shows the device configuration for **(a)** Sandwich structure and **(b)** Lateral structure*

The two architectures are utilized for specific applications. Sandwich structures are utilized for large area detectors with high responsivity at low operating voltage. Lateral structures on the other hand find a use for applications that require a high-speed response and small-signal detection.

Depending on the mode of operation, the photodetector devices can be classified into 3 types:

(i) ***Photoconductors***: Photoconductors are generally operated under applied bias, with high photoconductive gain, to even detect small signals. Here $\tau_{tr} < \tau_{rec}$ i.e., the carrier transit times (τ_{tr}) can be reduced to lower than the recombination time (τ_{rec}). This allows for multiple recirculation of the carriers. Efficiency higher than 100% may be obtained when more than one electron flows as a result of an absorbed single photon.[90, 91]

(ii) ***Photodiodes***: Photodiodes generally possess a vertical structure with the active area sandwiched by electrodes. The active layer thickness can be tuned for small signal detection which reduces the NEP, resulting in a large

LDR. In the photovoltaic regime of operation, the incident photon can at best generate one electron-hole pair to generate one unit of current. The EQE of these devices, therefore, is less than 100% and depends on the efficiency of absorption, charge separation, charge transfer, and collection[92, 93]. The collection of photogenerated carriers is controlled by the built-in potential due to the different work functions of the two electrodes. An additional reverse bias is often applied to increase the charge collection efficiency. In particular, self-powered photodetectors can be achieved when photodiodes work at zero bias, which is similar to solar cells working under short circuit conditions. In addition, the response speed of photodiodes is determined by the transit time of carriers, rather than lifetime. In addition to the transit time, the speed of operation is also limited by the RC lifetime.

(iii) ***Phototransistors***: Phototransistors are three-terminal devices, with device configurations similar to a field-effect transistor. Bias voltage across the source-drain controls the current in the unipolar channel. The conductivity in the channel is dependent on the gate voltage. The channel conductance can be additionally enabled by light illumination.[94] Opto-electronically modulated gate-programmable semiconducting channels can aid or hinder charge transport and simultaneously provide gain, working as optoelectronic amplifying switches[95]. Both photoconductors and phototransistors can have high EQE exceeding 100%, resulting in high photocurrent and responsivity[96].

In the subsequent chapters, various types of photo-detectors are discussed. Chapter 2 presents lateral devices that exhibit high-speed operation. Chapter 5 on the other hand presents sandwich-type detectors that operate in the short circuit condition and is used

for color sensing application. In chapter 4, the position-sensitive detectors are fabricated combining both the sandwich and the lateral structures into a 5-terminal device geometry.

1.7 Thesis outline.

In this introduction chapter, the basic overview of hybrid perovskites, their properties, carrier transport mechanism, and device working were presented. This thesis focuses on the study of spatially dependent photo-carrier dynamics in various device structures. In chapter two of the thesis, we begin with the study of photocurrent profiles in a large-sized (~ mm) single crystal device. The photocurrent observed in this system is dominantly due to the diffusion of photocarriers. These I_{ph} profiles are associated with a decay profile which reflects the effective diffusion length (L_d) of the carriers. Additionally, this L_d parameter reduces upon introducing a low-intensity light bias, indicating the bi-molecular nature of recombination. These results are analyzed with the help of intensity-dependent PL lifetime studies which suggest distinct recombination dynamics corresponding to band recombination and trap emission. The spatial and transient measurements are correlated in the context of trap filling effects on the carrier diffusion in HOIP systems.

Chapter three deals with the study of carrier transport regimes in hybrid perovskite-based lateral metal-semiconductor-metal (MSM) devices. Dark J-V characteristics in the asymmetric electrode devices exhibit a cross-over from the ohmic to space charge limited current (SCLC) behavior as a function of applied bias and interelectrode channel length. Spatially resolved potential mapping in these devices using the technique of KPFM reveals the presence of a transport barrier at the metal-perovskite interface, which explains the non-linear J-V characteristics. Additionally,

the potential map also confirms the presence of an electric field in the bulk of the device, indicating negligible screening of mobile ions in the lateral structures. Spatial photocurrent mapping in these devices using near field excitation reveals dominant recombination and charge separation zones. In the presence of an applied bias, the potential distribution profiles indicate a constant electric field in the device, and the light response was understood in the context of drift-diffusion formalism. These lateral devices exhibit photodetector characteristics with a responsivity of 6.2 A/W at 5 V bias for short channel devices. Owing to the low device capacitance, the transient photocurrent indicates a fast response component of ~12 ns, which allows for high-speed operational applications.

Chapter four of the thesis presents the fabrication and the demonstration of a light excitation dependent 2D position-sensitive detector (PSD). This functionality is achieved by measuring the differential photo-voltage signal, whose output is dependent on the position of light excitation on the device active area. The origin of this trend is initiated by an asymmetric distribution of photogenerated electrons and holes, which results in the development of a lateral photo-voltage. The PSD devices demonstrate a position sensitivity of ~ 50 μV/mm. Position detection both in the x and the y axis allows for applications such as the quadrant detector. In response to a single pulse of excitation, the devices exhibit a response time of ~ 1 μs, and these timescales extend marginally as the excitation is translated away from the overlapping device area. These excitation-position-dependent characteristics were understood in terms of equivalent circuit modeling, in combination with impedance spectroscopy measurements.

In Chapter five, the 2D/3D graded bandgap perovskite was used for the fabrication and demonstration of single-pixel color sensors. Due to the vertical stacking of the different bandgaps in the active layer, the light absorption profile is unique to the

incident wavelength of light. These wavelength-dependent charge transport dynamics are reflected in the transient photocurrent features. This is further enhanced in symmetric device structures which demonstrate reversal of the photocurrent polarity as the wavelength of light is spanned across the visible region of the spectrum. Color sensing application is demonstrated utilizing detection schemes in the ultrafast excitation regime as well as steady-state light illumination. With the introduction of a temporal delay, interesting possibilities are proposed for resolving the spectral components of a polychromatic source using sequential wavelength determination.

In summary, this thesis presents the various aspects of carrier transport in different device structures corresponding to different length scales. Conversely, this variation of the device parameters and structures also influence the dominant transport mechanism. The transport mechanism in large-sized single-crystal based devices is dominantly diffusive, whereas, in the short channel and sandwich structures, carrier drift plays a significant role. The carrier transport is spatially modulated, by tweaking the device architecture as well as introducing a graded bandgap to realize application-specific optoelectronic devices such as the PSDs and color sensors. These studies provide insights towards designing devices for a host of different optoelectronic applications

References:

1. Walsh A. Principles of chemical bonding and band gap engineering in hybrid organic–inorganic halide perovskites. *The Journal of Physical Chemistry C* **119**, 5755-5760 (2015).
2. Goldschmidt V. The laws of crystal chemistry. *Naturwissenschaften* **14**, 477-485 (1926).
3. Travis W, Glover E, Bronstein H, Scanlon D, Palgrave R. On the application of the tolerance factor to inorganic and hybrid halide perovskites: a revised system. *Chemical Science* **7**, 4548-4556 (2016).
4. Weber D. CH3NH3PbX3, ein Pb (II)-system mit kubischer perowskitstruktur/CH3NH3PbX3, a Pb (II)-system with cubic perovskite structure. *Zeitschrift für naturforschung B* **33**, 1443-1445 (1978).
5. Mitzi D, Wang S, Feild C, Chess C, Guloy A. Conducting layered organic-inorganic halides containing< 110>-oriented perovskite sheets. *Science* **267**, 1473-1476 (1995).
6. Wenger B, Nayak PK, Wen X, Kesava SV, Noel NK, Snaith HJ. Consolidation of the optoelectronic properties of CH 3 NH 3 PbBr 3 perovskite single crystals. *Nature communications* **8**, 1-10 (2017).
7. NREL Golden C. Best Research-Cell Effiency Chart | Photovoltaic Research | NREL. *https://wwwnrelgov/pv/cell-efficiencyhtml*, (accessed 2021).
8. Galkowski K, *et al.* Determination of the exciton binding energy and effective masses for methylammonium and formamidinium lead tri-halide perovskite semiconductors. *Energy & Environmental Science* **9**, 962-970 (2016).
9. Chen Y, *et al.* Extended carrier lifetimes and diffusion in hybrid perovskites revealed by Hall effect and photoconductivity measurements. *Nature communications* **7**, 1-9 (2016).
10. Zhao Y, Zhu K. Organic–inorganic hybrid lead halide perovskites for optoelectronic and electronic applications. *Chemical Society Reviews* **45**, 655-689 (2016).
11. Motta C, El-Mellouhi F, Kais S, Tabet N, Alharbi F, Sanvito S. Revealing the role of organic cations in hybrid halide perovskite CH 3 NH 3 PbI 3. *Nature communications* **6**, 1-7 (2015).
12. De Wolf S, *et al.* Organometallic halide perovskites: sharp optical absorption edge and its relation to photovoltaic performance. *The journal of physical chemistry letters* **5**, 1035-1039 (2014).
13. Mosconi E, Amat A, Nazeeruddin MK, Grätzel M, De Angelis F. First-principles modeling of mixed halide organometal perovskites for photovoltaic applications. *The Journal of Physical Chemistry C* **117**, 13902-13913 (2013).
14. Filip MR, Eperon GE, Snaith HJ, Giustino F. Steric engineering of metal-halide perovskites with tunable optical band gaps. *Nature communications* **5**, 1-9 (2014).
15. Jacobsson TJ, *et al.* Exploration of the compositional space for mixed lead halogen perovskites for high efficiency solar cells. *Energy & Environmental Science* **9**, 1706-1724 (2016).
16. Yang Y, *et al.* Observation of a hot-phonon bottleneck in lead-iodide perovskites. *Nature Photonics* **10**, 53-59 (2016).
17. Zhu W, *et al.* A halide exchange engineering for CH3NH3PbI3− xBrx perovskite solar cells with high performance and stability. *Nano Energy* **19**, 17-26 (2016).

18. Wenger B, Nayak PK, Wen X, Kesava SV, Noel NK, Snaith HJ. Consolidation of the optoelectronic properties of CH 3 NH 3 PbBr 3 perovskite single crystals. *Nature communications* **8**, 590 (2017).
19. Tang M-C, *et al.* Wide and Tunable Bandgap MAPbBr3− xClx Hybrid Perovskites with Enhanced Phase Stability: In Situ Investigation and Photovoltaic Devices. *Solar RRL* **5**, 2000718 (2021).
20. Caputo M, *et al.* Electronic structure of MAPbI 3 and MAPbCl 3: Importance of band alignment. *Scientific reports* **9**, 1-11 (2019).
21. Kim G, Min H, Lee KS, Lee DY, Yoon SM, Seok SI. Impact of strain relaxation on performance of α-formamidinium lead iodide perovskite solar cells. *Science* **370**, 108-112 (2020).
22. Kojima A, Teshima K, Shirai Y, Miyasaka T. Organometal halide perovskites as visible-light sensitizers for photovoltaic cells. *Journal of the American Chemical Society* **131**, 6050-6051 (2009).
23. Lee MM, Teuscher J, Miyasaka T, Murakami TN, Snaith HJ. Efficient hybrid solar cells based on meso-superstructured organometal halide perovskites. *Science* **338**, 643-647 (2012).
24. Lin K, *et al.* Perovskite light-emitting diodes with external quantum efficiency exceeding 20 per cent. *Nature* **562**, 245 (2018).
25. Cho H, *et al.* Overcoming the electroluminescence efficiency limitations of perovskite light-emitting diodes. *Science* **350**, 1222-1225 (2015).
26. Richter JM, *et al.* Direct Bandgap Behavior in Rashba-Type Metal Halide Perovskites. *Advanced Materials* **30**, 1803379 (2018).
27. Miyata A, *et al.* Direct measurement of the exciton binding energy and effective masses for charge carriers in organic–inorganic tri-halide perovskites. *Nature Physics* **11**, 582-587 (2015).
28. Even J, Pedesseau L, Katan C. Analysis of multivalley and multibandgap absorption and enhancement of free carriers related to exciton screening in hybrid perovskites. *The Journal of Physical Chemistry C* **118**, 11566-11572 (2014).
29. Tilchin J, Dirin DN, Maikov GI, Sashchiuk A, Kovalenko MV, Lifshitz E. Hydrogen-like Wannier–Mott excitons in single crystal of methylammonium lead bromide perovskite. *ACS nano* **10**, 6363-6371 (2016).
30. Hu M, *et al.* Distinct exciton dissociation behavior of organolead trihalide perovskite and excitonic semiconductors studied in the same system. *small* **11**, 2164-2169 (2015).
31. Kunugita H, *et al.* Excitonic feature in hybrid perovskite CH3NH3PbBr3 single crystals. *Chemistry Letters* **44**, 852-854 (2015).
32. Droseros N, Tsokkou D, Banerji N. Photophysics of Methylammonium Lead Tribromide Perovskite: Free Carriers, Excitons, and Sub-Bandgap States. *Advanced energy materials* **10**, 1903258 (2020).
33. Kumar P, Zhao B, Friend RH, Sadhanala A, Narayan K. Kinetic Control of Perovskite Thin-Film Morphology and Application in Printable Light-Emitting Diodes. *ACS Energy Letters* **2**, 81-87 (2017).
34. Zhang N, *et al.* All-optical control of lead halide perovskite microlasers. *Nature communications* **10**, 1-7 (2019).
35. Walker AW, Höhn O, Micha DN, Bläsi B, Bett AW, Dimroth F. Impact of photon recycling on GaAs solar cell designs. *IEEE Journal of photovoltaics* **5**, 1636-1645 (2015).

36. Pazos-Outón LM, *et al.* Photon recycling in lead iodide perovskite solar cells. *Science* **351**, 1430-1433 (2016).
37. Fang Y, Wei H, Dong Q, Huang J. Quantification of re-absorption and re-emission processes to determine photon recycling efficiency in perovskite single crystals. *Nature communications* **8**, 1-9 (2017).
38. Kirchartz T, Staub F, Rau U. Impact of photon recycling on the open-circuit voltage of metal halide perovskite solar cells. *ACS energy letters* **1**, 731-739 (2016).
39. Staub F, *et al.* Beyond bulk lifetimes: insights into lead halide perovskite films from time-resolved photoluminescence. *Physical review applied* **6**, 044017 (2016).
40. Hall RN. Electron-hole recombination in germanium. *Physical review* **87**, 387 (1952).
41. Shockley W, Read Jr W. Statistics of the recombinations of holes and electrons. *Physical review* **87**, 835 (1952).
42. Rau U. Reciprocity relation between photovoltaic quantum efficiency and electroluminescent emission of solar cells. *Physical Review B* **76**, 085303 (2007).
43. Dou L, *et al.* Atomically thin two-dimensional organic-inorganic hybrid perovskites. *Science* **349**, 1518-1521 (2015).
44. Gao P, Nazeeruddin MK. Dimensionality engineering of hybrid halide perovskite light absorbers. *Nature communications* **9**, 1-14 (2018).
45. Zhao Z, *et al.* Metal Halide Perovskite Materials for Solar Cells with Long-Term Stability. *Advanced Energy Materials* **9**, 1802671 (2019).
46. Blancon J-C, *et al.* Scaling law for excitons in 2D perovskite quantum wells. *Nature communications* **9**, 1-10 (2018).
47. Zhao B, *et al.* High-efficiency perovskite–polymer bulk heterostructure light-emitting diodes. *Nature Photonics* **12**, 783-789 (2018).
48. Zhang L, *et al.* High-performance quasi-2D perovskite light-emitting diodes: from materials to devices. *Light: Science & Applications* **10**, 1-26 (2021).
49. Neamen DA. *Semiconductor physics and devices: basic principles*. New York, NY: McGraw-Hill (2012).
50. Shockley W, Queisser HJ. Detailed balance limit of efficiency of p-n junction solar cells. *Journal of applied physics* **32**, 510-519 (1961).
51. Chamberlain G. Organic solar cells: A review. *Solar cells* **8**, 47-83 (1983).
52. Hertel D, Bässler H. Photoconduction in amorphous organic solids. *ChemPhysChem* **9**, 666-688 (2008).
53. Brabec CJ, Dyakonov V. Photoinduced charge transfer in bulk heterojunction composites. In: *Organic Photovoltaics* (ed^(eds). Springer (2003).
54. Baumann A, Lorrmann J, Deibel C, Dyakonov V. Bipolar charge transport in poly(3-hexyl thiophene)/methanofullerene blends: A ratio dependent study. *Appl Phys Lett* **93**, (2008).
55. Chang C-C, Tao J-H, Tsai C-E, Cheng Y-J, Hsu C-S. Cross-linked triarylamine-based hole-transporting layer for solution-processed PEDOT: PSS-free inverted perovskite solar cells. *ACS applied materials & interfaces* **10**, 21466-21471 (2018).
56. Thesen MW, *et al.* Hole-transporting host-polymer series consisting of triphenylamine basic structures for phosphorescent polymer light-emitting diodes. *Journal of Polymer Science Part A: Polymer Chemistry* **48**, 3417-3430 (2010).

57. Yan H, *et al.* A high-mobility electron-transporting polymer for printed transistors. *Nature* **457**, 679-U671 (2009).
58. Ebenhoch B, Thomson SAJ, Genevicius K, Juska G, Samuel IDW. Charge carrier mobility of the organic photovoltaic materials PTB7 and PC71BM and its influence on device performance. *Organic Electronics* **22**, 62-68 (2015).
59. Schulz P. Interface design for metal halide perovskite solar cells. *ACS Energy Letters* **3**, 1287-1293 (2018).
60. Tejedor C, Flores F. A simple approach to heterojunctions. *Journal of Physics C: Solid State Physics* **11**, L19 (1978).
61. Giordano F, *et al.* Enhanced electronic properties in mesoporous TiO 2 via lithium doping for high-efficiency perovskite solar cells. *Nature communications* **7**, 1-6 (2016).
62. Shao S, *et al.* Elimination of the light soaking effect and performance enhancement in perovskite solar cells using a fullerene derivative. *Energy & environmental science* **9**, 2444-2452 (2016).
63. Zhao C, Chen B, Qiao X, Luan L, Lu K, Hu B. Revealing underlying processes involved in light soaking effects and hysteresis phenomena in perovskite solar cells. *Advanced Energy Materials* **5**, 1500279 (2015).
64. Deng Y, Xiao Z, Huang J. Light-induced self-poling effect on organometal trihalide perovskite solar cells for increased device efficiency and stability. *Advanced Energy Materials* **5**, 1500721 (2015).
65. Noel NK, *et al.* Enhanced photoluminescence and solar cell performance via Lewis base passivation of organic–inorganic lead halide perovskites. *ACS nano* **8**, 9815-9821 (2014).
66. Wang QK, *et al.* Energy level offsets at lead halide perovskite/organic hybrid interfaces and their impacts on charge separation. *Advanced Materials Interfaces* **2**, 1400528 (2015).
67. Schulz P, Cahen D, Kahn A. Halide perovskites: is it all about the interfaces? *Chemical reviews* **119**, 3349-3417 (2019).
68. Kato Y, Ono LK, Lee MV, Wang S, Raga SR, Qi Y. Silver iodide formation in methyl ammonium lead iodide perovskite solar cells with silver top electrodes. *Advanced Materials Interfaces* **2**, 1500195 (2015).
69. Lin Y-H, *et al.* A piperidinium salt stabilizes efficient metal-halide perovskite solar cells. *Science* **369**, 96-102 (2020).
70. Bi E, *et al.* Diffusion engineering of ions and charge carriers for stable efficient perovskite solar cells. *Nature communications* **8**, 1-7 (2017).
71. Hou Y, *et al.* A generic interface to reduce the efficiency-stability-cost gap of perovskite solar cells. *Science* **358**, 1192-1197 (2017).
72. Shitaya T, Sato H. Single crystal CdS solar cell. *Japanese Journal of Applied Physics* **7**, 1348 (1968).
73. Singer J. Observations on the cuprous sulfide layer on single crystal cadmium sulfide. (1970).
74. Noel NK, *et al.* Interfacial charge-transfer doping of metal halide perovskites for high performance photovoltaics. *Energy & Environmental Science* **12**, 3063-3073 (2019).
75. Jiang X, Hoffman J, Stoumpos CC, Kanatzidis MG, Harel E. Transient sub-band-gap states at grain boundaries of CH3NH3PbI3 perovskite act as fast temperature relaxation centers. *ACS Energy Letters* **4**, 1741-1747 (2019).
76. Gallet T, Grabowski D, Kirchartz T, Redinger A. Fermi-level pinning in methylammonium lead iodide perovskites. *Nanoscale* **11**, 16828-16836 (2019).

77. Jiang Q, *et al.* Surface passivation of perovskite film for efficient solar cells. *Nature Photonics* **13**, 460-466 (2019).
78. Wang Y, *et al.* Solution-processed MoS2/organolead trihalide perovskite photodetectors. *Advanced Materials* **29**, 1603995 (2017).
79. Miao Y, *et al.* Stable and bright formamidinium-based perovskite light-emitting diodes with high energy conversion efficiency. *Nature communications* **10**, 1-7 (2019).
80. Wei W, *et al.* Monolithic integration of hybrid perovskite single crystals with heterogenous substrate for highly sensitive X-ray imaging. *Nature Photonics* **11**, 315-321 (2017).
81. Wang Y, *et al.* Photonic synapses based on inorganic perovskite quantum dots for neuromorphic computing. *Advanced materials* **30**, 1802883 (2018).
82. Qin C, *et al.* Stable room-temperature continuous-wave lasing in quasi-2D perovskite films. *Nature* **585**, 53-57 (2020).
83. Senanayak SP, *et al.* Understanding charge transport in lead iodide perovskite thin-film field-effect transistors. *Science advances* **3**, e1601935 (2017).
84. Gao P, Grätzel M, Nazeeruddin MK. Organohalide lead perovskites for photovoltaic applications. *Energy & Environmental Science* **7**, 2448-2463 (2014).
85. Jensen N, Hausner R, Bergmann R, Werner J, Rau U. Optimization and characterization of amorphous/crystalline silicon heterojunction solar cells. *Progress in Photovoltaics: Research and Applications* **10**, 1-13 (2002).
86. Yang WS, *et al.* Iodide management in formamidinium-lead-halide–based perovskite layers for efficient solar cells. *Science* **356**, 1376-1379 (2017).
87. Zhao J, Wang A, Green MA, Ferrazza F. 19.8% efficient "honeycomb" textured multicrystalline and 24.4% monocrystalline silicon solar cells. *Applied physics letters* **73**, 1991-1993 (1998).
88. Huang J, Yuan Y, Shao Y, Yan Y. Understanding the physical properties of hybrid perovskites for photovoltaic applications. *Nature Reviews Materials* **2**, 1-19 (2017).
89. Armin A, Hambsch M, Kim IK, Burn PL, Meredith P, Namdas EB. Thick junction broadband organic photodiodes. *Laser & Photonics Reviews* **8**, 924-932 (2014).
90. Zhang K, *et al.* Tellurophene-Based Random Copolymers for High Responsivity and Detectivity Photodetectors. *ACS applied materials & interfaces* **10**, 1917-1924 (2018).
91. Yuan Y, Huang J. Ultrahigh gain, low noise, ultraviolet photodetectors with highly aligned organic crystals. *Advanced Optical Materials* **4**, 264-270 (2016).
92. Xu X, *et al.* Enhanced photoresponse in metasurface-integrated organic photodetectors. *Nano letters* **18**, 3362-3367 (2018).
93. Dou L, *et al.* Solution-processed hybrid perovskite photodetectors with high detectivity. *Nature communications* **5**, 1-6 (2014).
94. Li F, *et al.* Ambipolar solution-processed hybrid perovskite phototransistors. *Nature communications* **6**, 1-8 (2015).
95. Jung JH, *et al.* High-Performance UV–Vis–NIR Phototransistors Based on Single-Crystalline Organic Semiconductor–Gold Hybrid Nanomaterials. *Advanced Functional Materials* **27**, 1604528 (2017).
96. Huang Y, *et al.* Van der Waals coupled organic molecules with monolayer MoS2 for fast response photodetectors with gate-tunable responsivity. *ACS nano* **12**, 4062-4073 (2018).

Chapter 2: Impact of trap-filling on carrier diffusion in $MAPbBr_3$ single crystals

2.1 Introduction

Hybrid organic-inorganic perovskites (HOIP) have demonstrated unprecedented potential for device applications such as solar cells, photodetectors, LEDs, and lasing [1-5]. Record high efficiencies, reaching 25.5 % [1, 6, 7] in HOIP single-junction solar cells can be attributed to properties such as high absorption coefficient, long diffusion lengths, decent mobility, and long-lived carrier lifetimes (τ)[8-10]. Especially, the long diffusion lengths (L_{diff}) in HOIP has been attributed to processes such as photon recycling, Rashba splitting, high bi-molecular recombination rates, and defect tolerance [11-15]. L_{diff} estimates in the range of 100 nm – 3 mm, spanning across four orders of magnitude have been reported [8, 16, 17]. This difference is partly due to different techniques such as transient photoluminescence (TRPL), transient photo-voltage (TPV), transient absorption, impedance spectroscopy and transient microwave conductivity (TRMC) to determine τ [8, 9, 18-20]. Additionally, techniques such as space charge limited current, time of flight, Hall Effect, TRMC, and terahertz conductivity are employed to determine carrier mobility (μ) [8, 10, 17, 19, 21]. Therefore, the determination of diffusion length (L_{diff}), a parameter indicative of efficient carrier transport, relies on twin measurements of τ and μ. It has been shown that long L_{diff} is characteristic of good quality films and improves with large grain size. Therefore carrier-recombination at the grain boundaries limits the L_{diff} to grain size length scales [22].

In this study, towards estimation of effective diffusion length, to overcome grain size effects on L_{diff} studies, sizable (2-3 mm) methylammonium lead bromide ($MAPbBr_3$) single crystals (MSC) were utilized. Hybrid perovskite single crystals have superior optoelectronic properties such as low trap density, high $L_{diff,}$ and high sub-bandgap absorption and are evolving as suitable solar cell candidates, reaching efficiencies of 21 % [21, 23, 24]. Applications based on their emission and optoelectronic properties are also emerging [25].

In this chapter, the results of the direct spatial estimation of effective diffusion length (L_d) on single crystals as a function of light bias intensity using scanning photocurrent microscopy (SPCM) are initially presented. Subsequently, the results are analyzed with the help of emission characteristics using time-resolved PL recombination lifetimes. These studies were carried out to gain perspective regarding the numerous reports to understand the nature of long carrier-diffusion lengths and extended lifetimes observed in hybrid perovskites. The emission studies were undertaken to understand the impact of band recombination and trap emission processes on carrier transport. Additionally, the use of low-intensity light bias dependent photocurrent mapping was implemented to gain insight into the trap-assisted carrier transport, which points to the defect-tolerance capability in HOIP systems.

2.2 Experimental Details

2.2.1 Materials

For the preparation of the single crystals, the perovskite precursors, Lead(II) bromide ($PbBr_2$, 98%, 367gm/mol), Methylammonium bromide (MABr, 111.97gm/mol) and solvent N,N-Dimethylformamide (DMF, anhydrous 98.9%, 73.09gm/mol) were obtained from Sigma Aldrich. Hole transporter, poly(N,N'-bis-4-butylphenyl-N,N'-

bisphenyl)benzidine (Poly-TPD) and electron transporter, phenyl-C71-butyric acid methyl ester ($PC_{71}BM$) were obtained from Lumtec Corporation, Taiwan. The solvent Chlorobenzene (anhydrous, 99.8 %) was also obtained from Sigma Aldrich.

2.2.2 Sample Preparation

The $MAPbBr_3$ single crystals were prepared by Prof. Satishchandra Ogale's group (at Indian Institute of Science Education and Research, Pune, India) using the following procedure:

The crystals were prepared by the technique of inverse temperature crystallization[19]. A 5 ml vial was used for the crystal growth containing 1M solution of $PbBr_2$ and MABr, using DMF (anhydrous 98.9%, Sigma Aldrich, mol. wt: 73.09gm/mol) as the solvent. The ratio of $PbBr_2$: MABr used was 1:1. The solution was kept in an oil bath wherein the temperature was gradually increased till the inverse temperature of crystallization (~80°C) was reached. The seeds ($MAPbBr_3$) formed were further transferred to a new solution for larger crystal growth and the process was repeated to achieve crystals of the desired size.

The crystals were shipped to our laboratory for the preparation of the device. Quality and integrity of the single crystals were ensured during the shipping process.

The crystal device was prepared by drop-casting $PC_{71}BM$ (Lumtec Corp.) and Poly-TPD (Lumtec Corp.) on opposite sides of the bulk single crystal. 3 mg/ml solution of PCBM and Poly-TPD in anhydrous Chlorobenzene (Sigma Aldrich) was drop-cast in a controlled manner with a micro-pipette. After each drop-casting, the layer was left to anneal by placing the coated crystal on a hot-plate at 60° C for 30 min. This was

followed by coating Ag (~ 150 nm) on the PCBM layer and Au (~ 40 nm) on the Poly-TPD layer by thermal evaporation.

2.2.3 Measurements and Characterization

Absorption on single crystals.

The steady-state absorption spectra was collected on the $MAPbBr_3$ single crystals using UV-Vis Helios Ultrafast Systems spectrophotometer and integrating sphere. The single crystal was mounted between grooved quartz plates and the spectrum was recorded in the reflectance mode.

PL on single crystals

The Photoluminescence (PL) measurements on the single crystals were carried out both in the reflection as well as in the transmission geometry. A 405 nm diode laser was used to excite the single crystal. In the reflection geometry, using a lens, the emitted light from the crystal, after passing through a 450 nm long-pass filter was collected into the fiber-coupled Mini Spectrometer (Hamamatsu, C10083CA).

In the transmission geometry, maintaining the angle of incidence of the excitation light, PL was measured with the help of suitable collection optics.

For PL measurements, that involved high intensity laser excitation over extended periods, care was taken to repeat measurements on new crystals to minime the effects of burn spots on the measurements.

PL Quantum Efficiency (PLQE):

PL measurements were carried out with samples placed in the integrating sphere to determine the external PLQE. A 405 nm laser with calibrated intensity was used as the illumination source and a fiber-coupled mini-spectrometer (Hamamatsu, C10083CA)

was used to collect the excitation and emission spectra. Measurements were carried out with both the reference slide (glass) and the bulk single crystal placed on the glass slide. Suitable optics was utilized to collimate the beam with a spot size smaller than the crystal size. The obtained spectrum was normalized with the responsivity of the detector and the integrated intensity of the excitation (I_{exc}) and emission (I_{em}) was used to determine the PLQE:

$$External\ PLQE\ = \frac{I_{em}(\text{crystal}) - I_{em}(\text{ref})}{I_{exc}(\text{ref}) - I_{exc}(\text{crystal})}$$

***Scanning Photocurrent Microscopy (SPCM)*:**

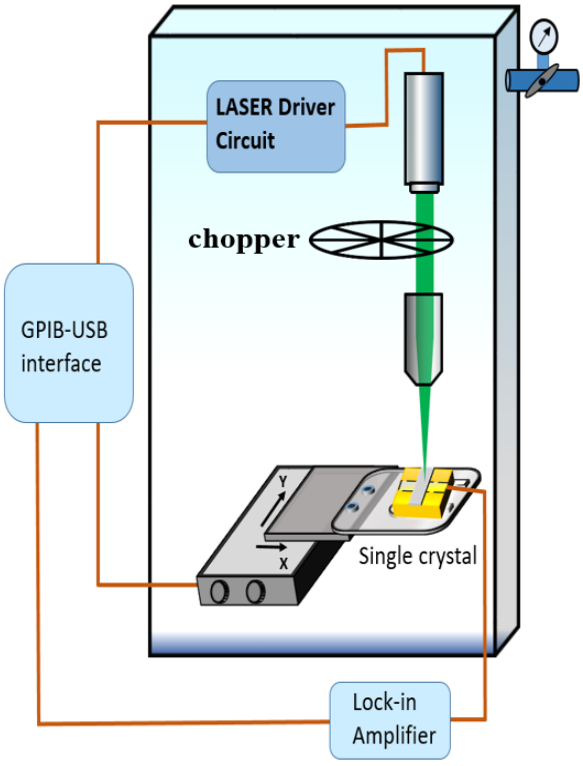

***Figure 2. 1**: Schematic of SPCM experimental setup*

The schematic explaining the SPCM scanning setup is shown in **Figure 2.1**. A modulated laser light (119 Hz) is focused using a microscope objective (50x, 0.7 NA)

on the MSC device. As the device translates, the short circuit I_{ph} is measured using an amplifier (SRS 830), locked-in to the modulating frequency of the laser driver. Additionally, a dc light bias is introduced by an LED ring-illumination to have uniform constant illumination. The intensity of the light bias was controlled by varying the current sourced to the LEDs. The intensity of the light bias was measured using a calibrated photodiode. The experiments were carried out using a GPIB-USB interfaced program.

The spot size of the excitation was determined using the knife-edge scanning technique, wherein a knife-edge is translated across the focused beam in the line of the light incident on the detector. As the knife-edge translates, the intensity of light on the detector varies as shown in **Figure 2.2(a)**. The differential plot of the intensity indicates the beam profile shown in **Figure 2.2(b),** which is used to estimate the spot size. In our experimental setup, we were able to improve the resolution up to a FWHM ~ 3.8 μm spot size.

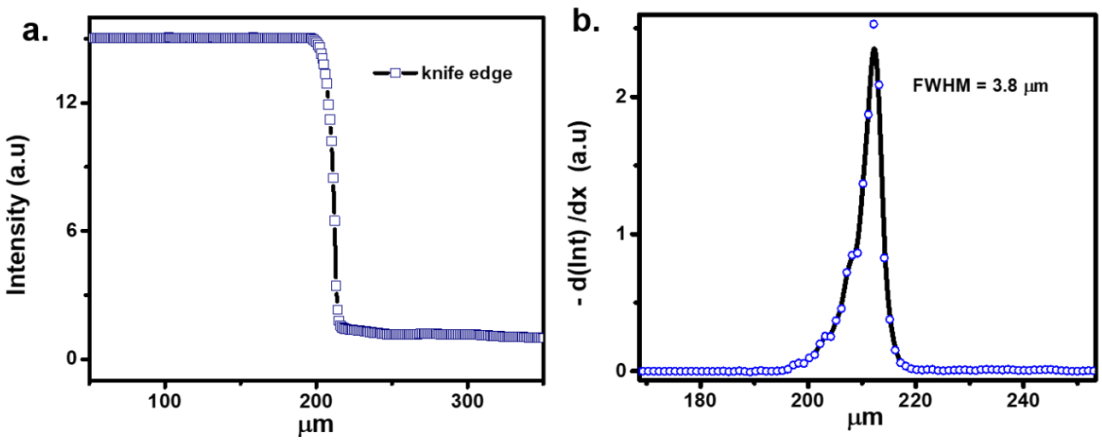

***Figure 2. 2**: **(a)** The intensity profile as the knife edge is translated across the diameter of the focused beam spot. **(b)** The differential of the intensity profile gives the spot profile and the FWHM of the beam spot.*

Time-resolved Photoluminescence (TRPL)

Time-Resolved Photoluminescence measurements were carried out using a custom-built Time Correlated Single Photon Counting (TCSPC) instrument with a temporal resolution of ~250 ps. A Picoquant LDH-P-C-405M laser source, with center wavelength 405 nm and pulse width of 90 ps, was operated using a Picoquant PDL 800-B laser diode driver to excite the crystal. A Tektronix AFG1024 arbitrary Function Generator was used to control the repetition rate and the laser was driven at 800 kHz. The emission profile was recorded using a single photon counter (Picoquant PMA-C-192-M) coupled to Zolix Omni 1300 monochromator. Time tagging of the data was done using the Picoquant TimeHarp 260 Nano data acquisition card. The time-resolved decay profiles were obtained for the wavelength range 500 nm to 700 nm. The time-resolved emission spectra (TRES) were derived using MATLAB.

2.3 Results and Discussion

2.3.1 Scanning Photocurrent Microscopy (SPCM)

To determine the effective carrier diffusion length (L_d), the technique of Scanning Photocurrent Microscopy (SPCM) was employed on $MAPbBr_3$ single crystal (MSC) devices. In these MSC-based devices, for efficient collection of photogenerated carriers, selective contact layers were deposited: Poly-TPD followed by Au for hole collection and $PC_{71}BM$ followed by Ag electrode for electron extraction. This is evidenced by the band alignment diagram shown in **Figure 2.3(a).** The energy levels indicated in Figure 2.3(a) are based on literature reports as provided **Table 1.3**.

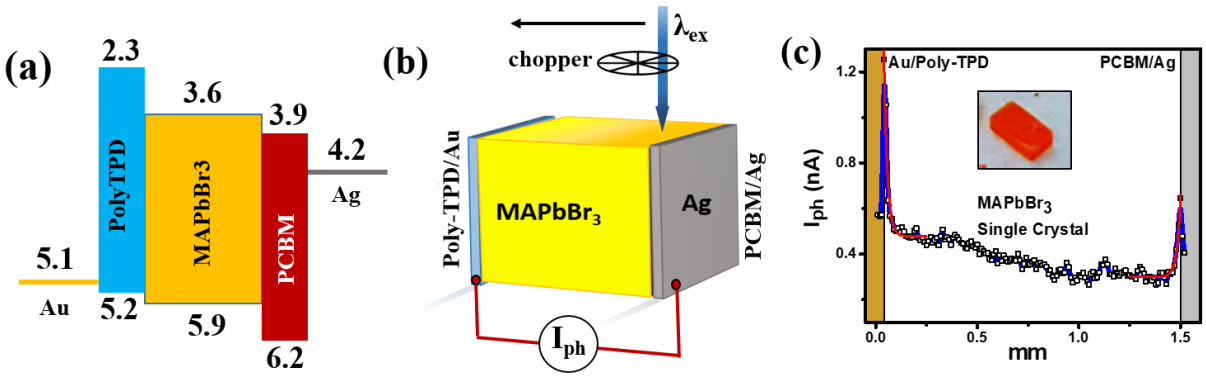

***Figure 2. 3**: **(a)** Band alignment diagram depicting MSC-device used in SPCM experiments. **(b)** Schematic of Scanning Photocurrent Microscopy (SPCM) used for effective diffusion length measurement. The incident chopped probe-beam position is varied by translating the sample. The lock-in profile $I_{ph}(x)$ is utilized to estimate L_d. **(c)** $I_{ph}(x)$ shows I_{ph}-peak at the interface. Single exponential fit to the I_{ph} decay profile corresponds to the L_d of the corresponding carrier. The **inset** shows the image of the bulk single crystal. (Reprinted with permission from Ganesh, N., Ghorai, A., Krishnamurthy, S., Banerjee, S., Narasimhan, K. L., Ogale, S. B., & Narayan, K. S. (2020). Impact of trap filling on carrier diffusion in MAPb Br 3 single crystals. Physical Review Materials, 4(8), 084602. Copyright (2020) by American Physical Society)*

Figure 2.3(b) shows the schematic of the setup used for SPCM, with the MSC being the device under consideration. An intensity-modulated laser beam (405 nm, ~ 27 mW/cm^2), normally incident on the MSC, is translated laterally between the two contacts. Simultaneously, the short-circuit photocurrent is measured using a lock-in amplifier, to obtain the spatial photocurrent profile, $I_{ph}(x)$ shown in **Figure 2.3(c).** It can be observed that the maxima in $I_{ph}(x)$ profile corresponds to light-excitation at electrode positions at either end. In these devices, due to the presence of charge-selective interfacial layers, the contact resistance at the electrodes is estimated to be negligible, resulting in the built-in voltage (V_{bi}) falling entirely along the inter-electrode

crystal length. In the present case of undoped sizable MSC (d ~ 1-2 mm, **inset Figure 2.3(c)**), this built-in electric-field, $E_{bi} = V_{bi}/d$ is negligible (< 6 V/cm). This results in dominant diffusion contribution to the observed photocurrent (I_{ph}), which indicates a decay profile, for excitation away from the electrode-MSC interface.

2.3.1.1 Diffusion Recombination Formalism

The determination of effective diffusion length, L_d from the $I_{ph}(x)$ measurement, shown in **Figure 2.3(c)** can be arrived at by solving the transport equation. The transport equation for a single type of excess carrier is given as[26]:

$$\frac{\partial \delta n}{\partial t} = D\frac{\partial^2 \delta n}{\partial x^2} + \mu E\frac{\partial \delta n}{\partial x} + G - \frac{\delta n}{\tau} \qquad (2.1)$$

The generation rate G is given by delta-function, $G = G_0\ \delta(x\text{-}x_0)$ where $x=x_0$ is the region of illumination. The estimated built-in field of ≈ 6 V/cm can be assumed to be negligible such that $\mu E \frac{\partial \delta n}{\partial x} << D\frac{\partial^2 n}{\partial x^2}$. A detailed analysis accounting for drift and diffusive effects on carrier distribution is presented in Appendix 1. Section A1.1 further shows simulated carrier profiles for different cases of electric fields. **Figure A1.1** clearly shows that the low value of the electric field (6 V/cm) has a negligible effect on the carrier distribution profiles. It is estimated that the magnitude of drift-assisted carriers is about an order of magnitude lower in comparison to the diffused carriers for excitation close to the electrodes. Therefore, under the conditions of steady-state illumination ($d\delta n/dt = 0$), negligibly small electric field ($E \approx 6$ V/cm) and $x \neq x_0$ diffusion-recombination equation can be written as:

$$D\frac{\partial^2 \delta n}{\partial x^2} = \frac{\delta n}{\tau} \quad (2.2)$$

With the diffusion length defined as $L_{diff} = \sqrt{(D\tau)}$, by solving the above equation we obtain,

$$\delta n(x) = \delta n_0 \exp(-\frac{x}{L_{diff}}) \quad (2.3)$$

For x > 0, is the distance between the collection electrode and the point of generation. δn_o is the generation density at the point of excitation.

The obtained I_{ph} as a result of diffusion is given as:

$$I_{ph}(x) = -eD\ \frac{\partial \delta \mathrm{n}}{\partial \mathrm{x}} \quad (2.4)$$

Since L_{diff} is not a constant and has a dependence on $\delta n(x)$, the $I_{ph}(x)$ can be expressed as:

$$\boldsymbol{I_{ph}(x) = I_0 \exp(-\frac{x}{L_d})} \quad (2.5)$$

Where L_d is the effective diffusion length and $L_d \propto L_{diff}$ (x) = $(kT\mu\tau/e)^{1/2}$, here τ depends on excess carrier density.

It must be noted that effective diffusion length, L_d is different from minority carrier diffusion length, L_{diff}. L_{diff} is the microscopic quantity related to the diffusion coefficient (D) and expressed as $(D\tau)^{1/2}$, where τ is the carrier lifetime. In disordered or amorphous systems, owing to the dispersive nature of transport, L_d and L_{diff} can differ appreciably [27, 28]. However, L_d is a representative of the long-lived carriers corresponding to states in the tail distribution, in organic and polymeric semiconductors [28, 29]. The L_d parameter in the present case of HOIP single crystals is expected to be a

closer representation of L_{diff} owing to the dominant band transport [30]. In the present case of SPCM on MSC devices, it has to be noted that the L_d parameter is obtained upon fitting over the entire decay range and accounts for additional factors such as finite beam spot, 3D carrier diffusion, and ambipolar transport away from the electrodes.

2.3.1.2 Diffusion mechanism in SPCM

The $I_{ph}(x)$ response in **Figure 2.3(c)** can be qualitatively described as follows: Photo-excitation results in a point spread of electrons and holes via 3D diffusion – a fraction of which diffuse towards the electrodes. When the excitation is at a distance equivalent to many diffusion lengths from the contacts, the diffusing photo-carriers get (i) trapped in shallow states and also (ii) recombine, resulting in a low current. When the excitation beam is within L_d from the electrode, the current increases exponentially with the probe distance (**Equation 2.5**) enabling one of the carriers to be extracted leaving the other carrier in the perovskite to transit to the other electrode. The extraction of one carrier and the long lifetime associated with the displacement of the counter carrier, renders the extracted carrier as a minority, with excitation close ($x \leq L_d$) to the extraction electrode. This is additionally observed in position-dependent transient photocurrent (TPC) measurements. **Figure 2.4(a)** shows the experimental schematic of the TPC for excitation close to the electrode-MSC interface and the bulk of the crystal. Transient decay profiles shown in **Figure 2.4(b)**, indicating longer $\tau_{transit}$ for excitation near the electrodes compared to a bulk region confirms charge selective carrier extraction, leaving the other counter carrier in the bulk of the MSC device.

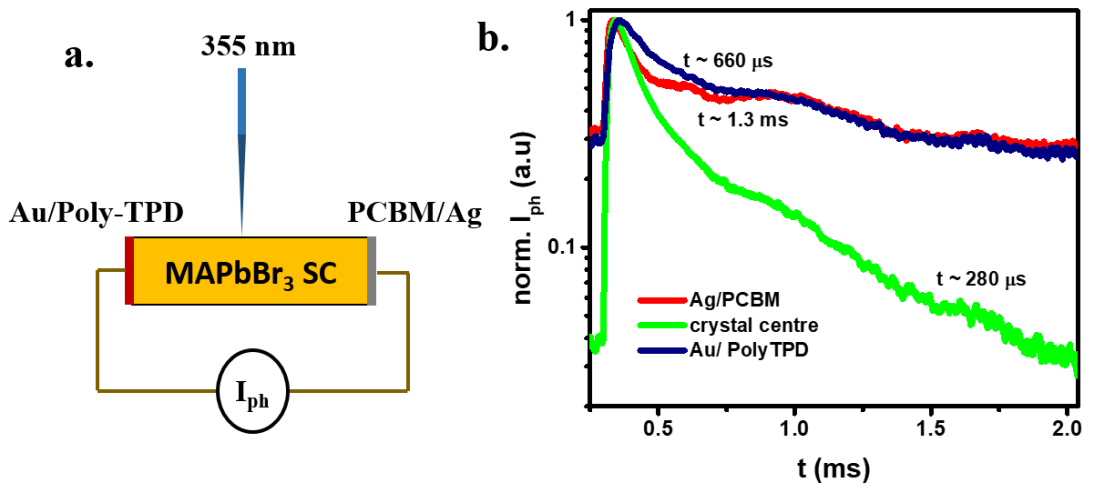

Figure 2. 4*: (a) Schematic of the position-dependent TPC on the MSC device. The 355 nm pulsed laser, 1 ns pulse, 60 nJ/pulse was for excitation close to the interface and at the center of the crystal. (b) The TPC decay time shows a longer decay time for excitation close to the electrode when compared to excitation in the central region far from the electrodes. The long decay times reflect on the transit time of the un-extracted counter carrier. (Reprinted with permission from Ganesh, N., Ghorai, A., Krishnamurthy, S., Banerjee, S., Narasimhan, K. L., Ogale, S. B., & Narayan, K. S. (2020). Impact of trap filling on carrier diffusion in MAPb Br 3 single crystals. Physical Review Materials, 4(8), 084602. Copyright (2020) by American Physical Society)*

Previous reports of SPCM have determined the "minority carrier diffusion length" using doped crystals and charge selective Schottky barrier [17, 31]. In the present case of MSCs, L_d corresponds to the selectivity of the extraction layer in undoped single crystal devices.

From the data in **Figure 2.3(c)** and **Equation 2.5**, L_d for electrons and holes was determined to be 13.3 ± 0.6 µm and 13.8 ± 0.5 µm respectively. In previous reports, intensity-dependent studies reveal that the carrier L_{diff} varies with excitation density. For example, Shi et.al[8], using TPV studies have estimated L_{diff} ~ 3 mm, at low-intensity

excitation [8, 10]. These studies of L_{diff} determination, however, rely on indirect estimation. To investigate the effect of intensity dependence on directly measured spatial L_d, intensity-dependent SPCM studies are carried out by:

(i) varying the intensity of the probe beam, and

(ii) Super-posing a uniform background illumination or dc light-bias using a 390 nm LED with the probe beam. (The optical absorption depth (~ 125 nm) of the 390 nm light is similar to the 405 nm probe beam [32].)

The effect of light-intensity dependence is useful to provide additional information to understand the scaling relation of transport parameters on photo-carrier density.

2.3.1.3 Impact of Probe beam intensity variation

Figure 2.5(a) shows $I_{ph}(x)$ profiles across the Ag/PCBM-MSC interface for probe-intensity variation in the SPCM measurement. The corresponding L_d values in **Figure 2.5(b)**, as a function of probe beam intensity, show that L_d is independent of probe beam intensity. The excess generated probe-photo carriers, δn_{probe} diffuse away from the point of generation and decays as $\delta n\,(x) = \delta n_{probe}(0).\exp\left(\frac{-x}{L_{diff}}\right)$. The invariance of L_d can be understood since the photo-carriers decay to background carrier concentration within ~ $3L_{diff}$.

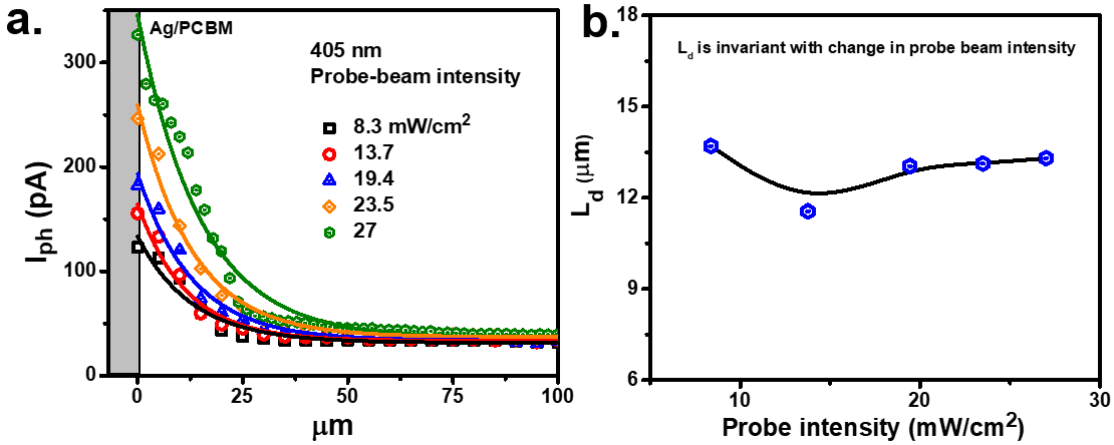

***Figure 2. 5**: **(a)** Plot of $I_{ph}(x)$ with variation in the 405 nm probe beam intensity in the absence of light bias. Solid lines indicate single exponential fits to obtain L_d. **(b)** Plot of L_d with respect to probe beam intensity indicates that L_d remains invariant with change in probe-beam intensity. (Reprinted with permission from Ganesh, N., Ghorai, A., Krishnamurthy, S., Banerjee, S., Narasimhan, K. L., Ogale, S. B., & Narayan, K. S. (2020). Impact of trap filling on carrier diffusion in MAPb Br 3 single crystals. Physical Review Materials, 4(8), 084602. Copyright (2020) by American Physical Society)*

2.3.1.4 Impact of Light Bias

The addition of light bias, on the other hand, maintains uniform charge generation across the transport length of the probe-carrier. It was ensured that the effects of light-induced halide redistribution and phase segregation are minimal by maintaining the MSC-device in dark under short-circuit conditions after each measurement, under a positive pressure of the inert atmosphere [33, 34]. It must be noted that the measurements were carried in the absence of applied bias, since one expects a sizeable ionic contribution under voltage bias[35].

Figure 2.6(a) depicts the $I_{ph}(x)$ profile at different dc-light bias intensity. The I_{ph} magnitude at the I_{ph} maxima, for excitation at the MSC-electrode interface, increases with the introduction of the light bias as indicated in **Figure 2.6(b)**. **Figure 2.6(c)** shows the normalized $I_{ph}(x)$ decay profiles at either end of the MSC-electrode interface. The steep decay of I_{ph} away from the electrode is evident under high light bias conditions. The L_d parameter is extracted by fitting the decay profile to **Equation 2.5**. The estimated L_d as a function of light bias-photon flux, presented in **Figure 2.6(d)** reveals the decrease of L_d with dc light-bias intensity. The extracted L_d parameter decreases by a factor of 3 for holes and a factor of ~ 2 for electrons upon increasing the light bias from zero to ~ 5×10^{15} photons/cm^2. It can be seen that beyond a certain high-intensity light bias, the I_{ph} magnitude reduces as shown in **Figure 2.6(b)** respectively. This reduction is attributed to the effects of light-soaking [36].

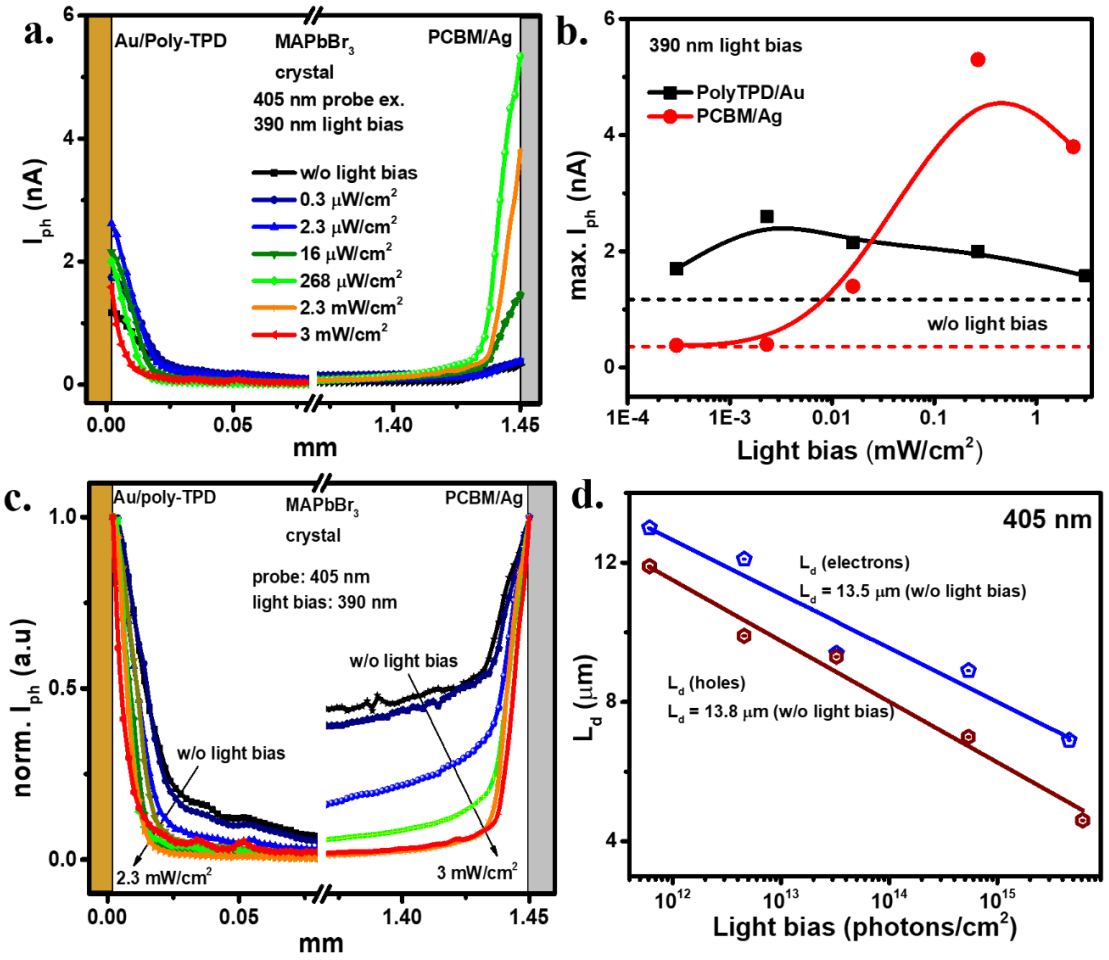

***Figure 2. 6**: **(a)** $I_{ph}(x)$ variation on both ends of the MSC device with a 405 nm probe beam and 390 nm light bias. **(b)** Plot of variation of max. I_{ph} close to the electrode as a function of light bias intensity for 390 nm. The dashed horizontal lines correspond to the I_{ph} peak, in the absence of light bias. **(c)** Normalized $I_{ph}(x)$ profiles indicating sharp decay at higher light bias **(d)** L_d extracted with the exponential fitting of $I_{ph}(x)$-decay as a function of light bias. (Reprinted with permission from Ganesh, N., Ghorai, A., Krishnamurthy, S., Banerjee, S., Narasimhan, K. L., Ogale, S. B., & Narayan, K. S. (2020). Impact of trap filling on carrier diffusion in MAPb Br 3 single crystals. Physical Review Materials, 4(8), 084602. Copyright (2020) by American Physical Society)*

The decrease of the L_d at high dc-light bias suggests that the recombination kinetics of the excess carriers is not monomolecular [37]. This was verified by photo-physical studies using intensity and time-dependent Photoluminescence (PL) measurements.

2.3.2 PL measurements

$MAPbBr_3$ is characterized by absorption in most of the UV-Vis spectral range as shown in **Figure 2.7**. Photo-thermal deflection spectroscopy and light transmission experiments have shown the presence of sub-bandgap states extending to ~ 2.0 eV [32, 38].

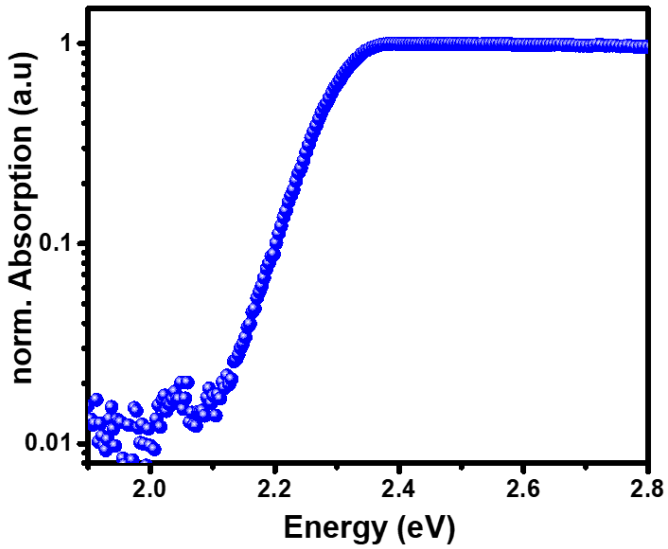

***Figure 2. 7**: Normalized absorption spectra of $MAPbBr_3$ single crystal.*

Figure 2.8(a) is the plot of PL spectra for 3 eV (405 nm) excitation in reflection and transmission geometry. In the reflection mode, the PL spectra exhibits a peak at 2.27 eV (545 nm) with a shoulder at 2.15 eV (575 nm). In the transmission mode, the 2.27 eV peak is masked due to self-absorption. The 2.27 eV peak is identified and attributed to the band-to-band transition (free carrier recombination). The 2.15 eV peak has been attributed to different mechanisms viz. radiative recombination from a defect level or to bound exciton recombination[38, 39]. The 2.15 eV is observed exclusively in crystals

and not in $MAPbBr_3$ thin films as can be seen in **Figure 2.8(b)**. Photo-induced absorption studies at different T of samples with different degrees of crystallinity can be used to attribute the 2.15 eV feature, in the present case, to long-range dipole-dipole interactions of defects in the bulk of single crystals [37, 40]. Without loss of generality and for simplicity of modeling and analysis, we identify the 2.15 eV (575 nm) emission as trap-mediated radiative emission in the bulk of MSC. This is shown schematically in **Figure 2.8(d)**.

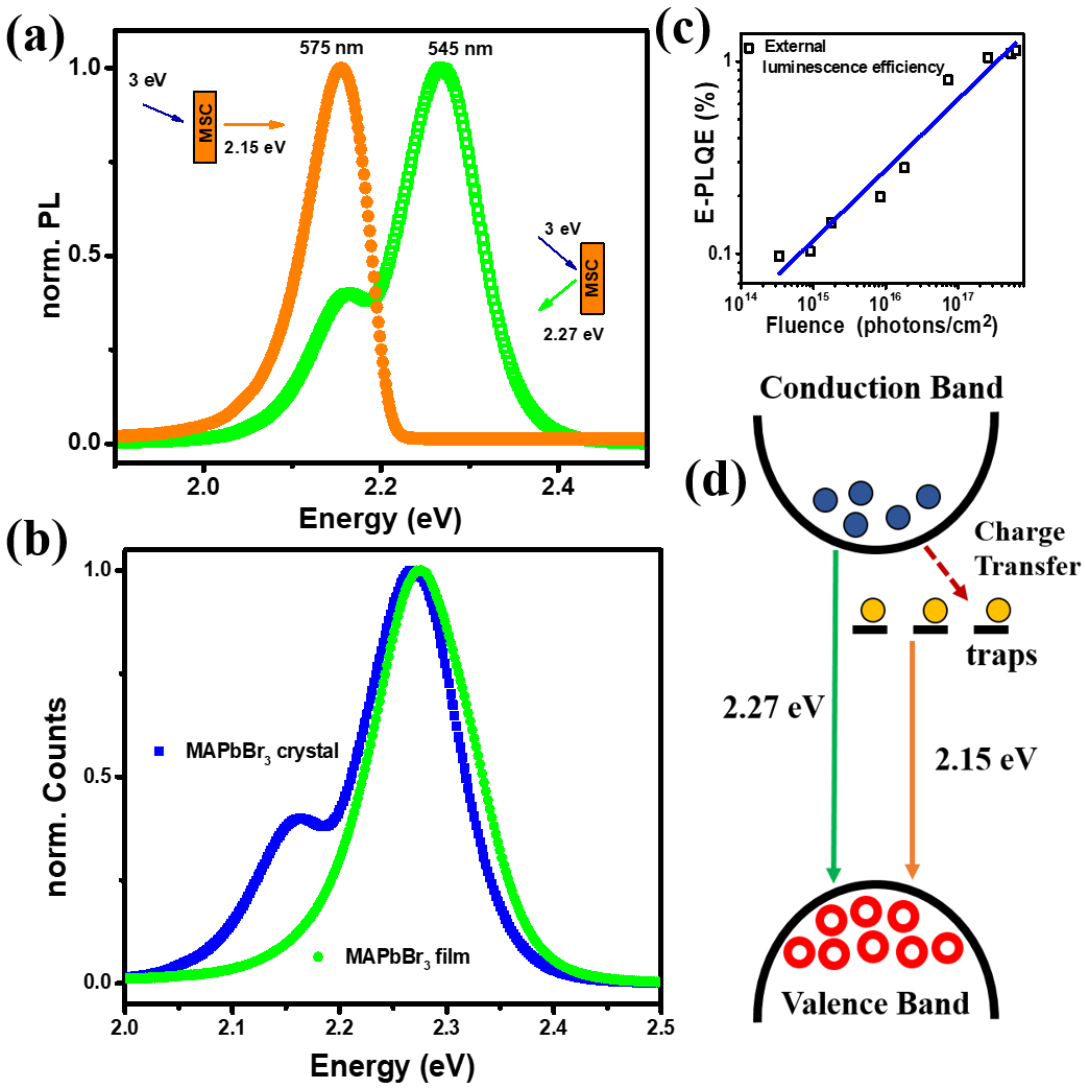

***Figure 2. 8**: (a) PL data depicts 545 nm and 575 nm peaks corresponding to PL measured in the reflection and transmission geometry respectively. (b)Comparison of*

PL spectra of $MAPbBr_3$ films and crystals. The films do not exhibit the low-intensity emission at 575 nm (c) Plot shows the increase in E-PLQE at higher excitation fluence (d) Schematic showing an illustration of band-to-band recombination and trap emission. (Reprinted with permission from Ganesh, N., Ghorai, A., Krishnamurthy, S., Banerjee, S., Narasimhan, K. L., Ogale, S. B., & Narayan, K. S. (2020). Impact of trap filling on carrier diffusion in MAPb Br 3 single crystals. Physical Review Materials, 4(8), 084602. Copyright (2020) by American Physical Society)

Additionally, the intensity dependence on External PL Quantum Efficiency (E-PLQE) is seen in **Figure 2.8(c),** which indicates that E-PLQE increases with excitation intensity. This indicates higher radiative efficiency at higher carrier generation. To understand this in detail, intensity-dependence on PL was studied for emissions at 545 nm as well as 575 nm.

2.3.2.1 Recombination Kinetics

Figure 2.9(a) and 2.9(b) shows the intensity dependence on excitation intensity for 545 nm and 575 nm respectively. **Figure 2.9(c)** shows the plot of integrated intensity dependence of emission on the excitation density for the 545 nm and 575 nm emission, which follows a power-law behavior: $\langle I_{PL} \rangle = \langle I_{ex} \rangle^x$ and is in agreement with previous observations [38, 41]. For the 545 nm peak (2.27eV), $x \approx 1$ at low intensity (blue shaded region), and ≈ 2 at high intensity. In contrast, the 575nm (2.15 eV) emission peak reveals a linear $x \approx 1$ response throughout.

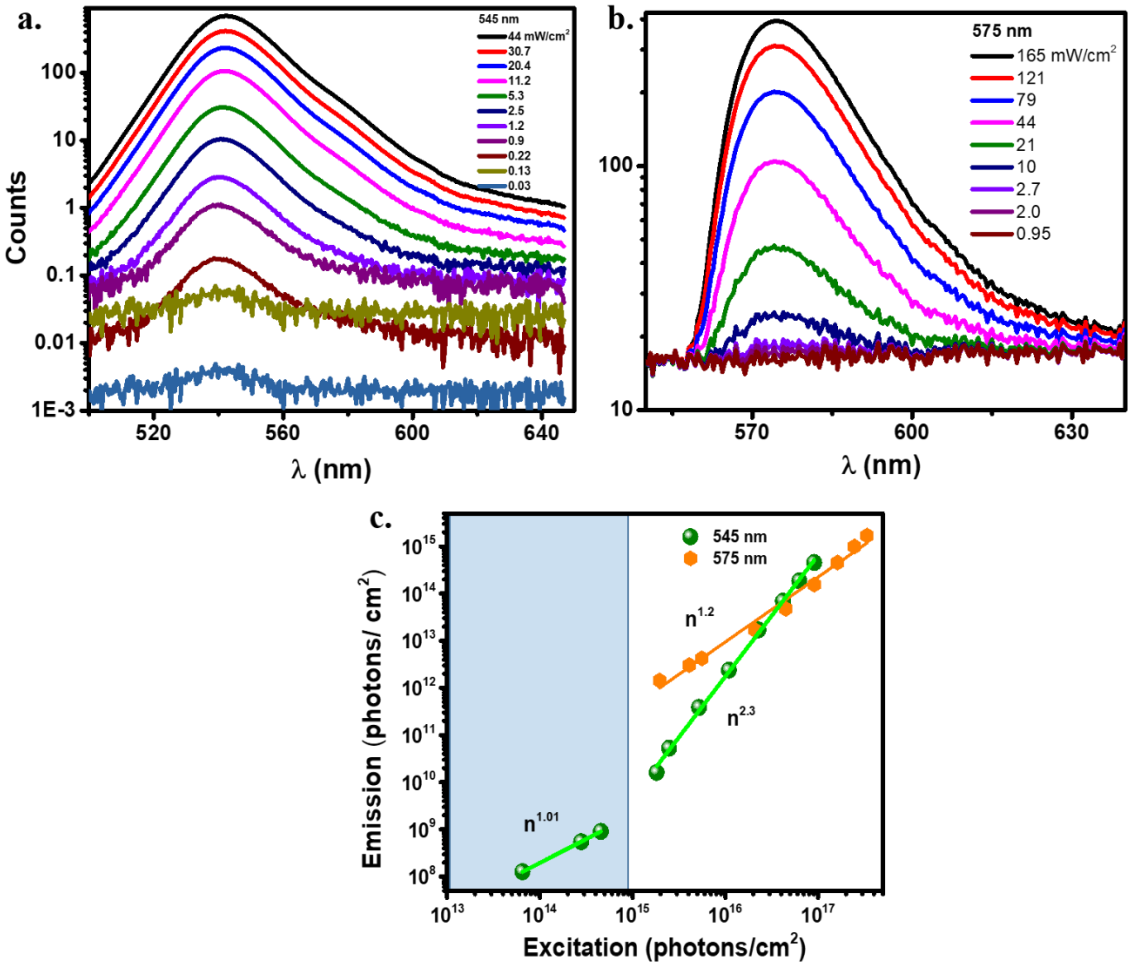

Figure 2. 9*: intensity-dependent PL spectrum centered at* ***(a)*** *545 nm, with PL measured in the reflection geometry and* ***(b)*** *575nm, with PL measured in the transmission geometry on single crystals.* ***(c)*** *Integrated emission intensity exhibits linear and quadratic dependence on excitation for 545 nm and linear variation for the 575 nm emission. (Reprinted with permission from Ganesh, N., Ghorai, A., Krishnamurthy, S., Banerjee, S., Narasimhan, K. L., Ogale, S. B., & Narayan, K. S. (2020). Impact of trap filling on carrier diffusion in MAPb Br 3 single crystals. Physical Review Materials, 4(8), 084602. Copyright (2020) by American Physical Society)*

These results can be understood from a simple physical model where the effective excess carrier lifetime (τ_{eff}) is expressed as $\frac{1}{\tau_{eff}} = \frac{1}{\tau_{SRH}} + \frac{1}{\tau_R}$, where τ_{SRH} is the trap mediated non-radiative recombination lifetime and τ_R is the radiative recombination

lifetime. The Auger recombination component which becomes prominent at high excitation fluence (> 10^{17} photons/cm^2) is neglected. $1/\tau_R$ can then be expressed as

$$\frac{1}{\tau_R} = B\ (N_A + \ \delta n)\ and\ \frac{1}{\tau_{SRH}} = R_{SRH}.N_T \tag{2.6}$$

where, δn is the excess carrier density, B the radiative constant, and N_A the background doping concentration, R_{SRH} is the non-radiative constant, and N_T is the trap density. The radiative recombination rate is given as:

$$\frac{\delta n}{\tau_R} = A_R \delta n + B\ (\delta n)^2 \tag{2.7}$$

where, $A_R = B.N_A$.

At low fluence, the radiative recombination rate increases linearly with the excitation and quadratically with fluence at a higher intensity. This explains the excitation dependence of the 545 nm peak. The 575 nm peak arises due to recombination from a shallow trap. If δn is smaller than the trap concentration, the emission rate is linearly dependent on the excitation intensity - in agreement with the observation in **Figure 2.8(c)**. This basic model satisfactorily accounts for the PL observations.

2.3.2.2 Time-Resolved Photoluminescence

Figure 2.10(a) shows the time-resolved emission spectra upon pulsed 405 nm excitation (19 mW/cm^2) on MSC. From the decay trends of the two peaks, it can be observed that 545 nm is characterized by a faster decay lifetime in comparison to the trap emission at 575 nm, as shown in **Figure 2.10(b)**.

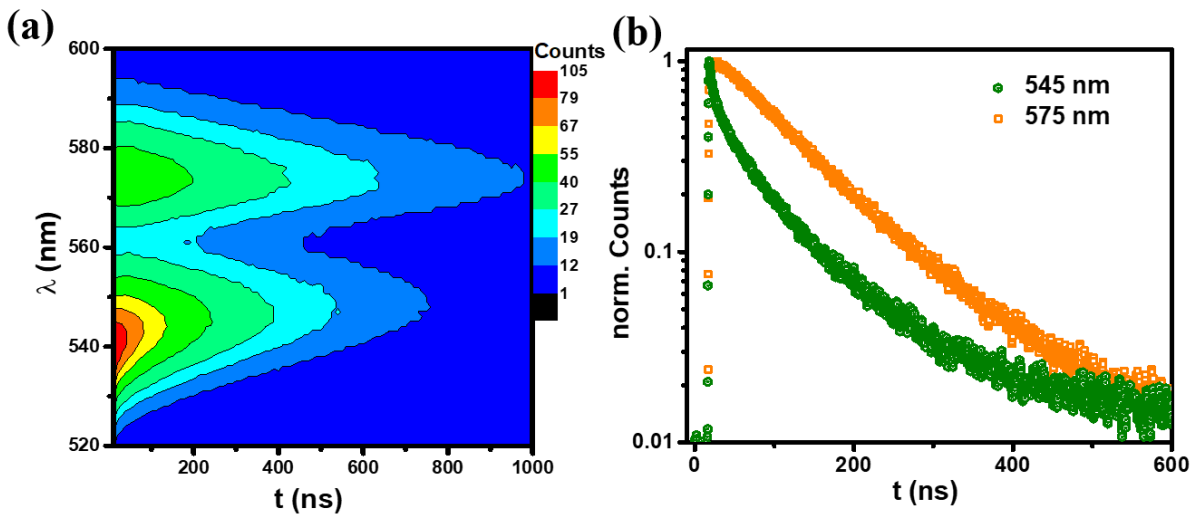

Figure 2. 10: (a) *Time-resolved emission spectra on MSC upon pulsed excitation with a 405 nm source, 19 mW/cm*^{2}*.* ***(b)*** *TRPL at 545 nm and 575 nm shows a shorter band-recombination lifetime at 545 nm. (Reprinted with permission from Ganesh, N., Ghorai, A., Krishnamurthy, S., Banerjee, S., Narasimhan, K. L., Ogale, S. B., & Narayan, K. S. (2020). Impact of trap filling on carrier diffusion in MAPb Br 3 single crystals. Physical Review Materials, 4(8), 084602. Copyright (2020) by American Physical Society)*

The PL-lifetimes were studied by varying the excitation intensity. **Figure 2.11(a)** and **2.11(b)** show the luminescence decay for both the 545 nm and the 575 nm respectively as a function of excitation power. The lifetime of the 545 nm emission decreases with an increase in excitation power. Since the shortest lifetime corresponds to the dominant recombination process, the initial decay lifetime associated with the transient PL is considered for analysis. Moreover, the initial decay lifetime provides a fair representation of the recombination process corresponding to the photogenerated carrier density. The results are summarized in **Figure 2.11(c)**. The lifetime measured in the TRPL corresponds to $\tau_{eff,}$ which is given as:

$$\frac{\delta n}{\tau_{eff}} = A\delta n + B\,(\delta n)^2 \qquad (2.8)$$

where, $A = B.N_A + R_{SRH}.\,N_T$.

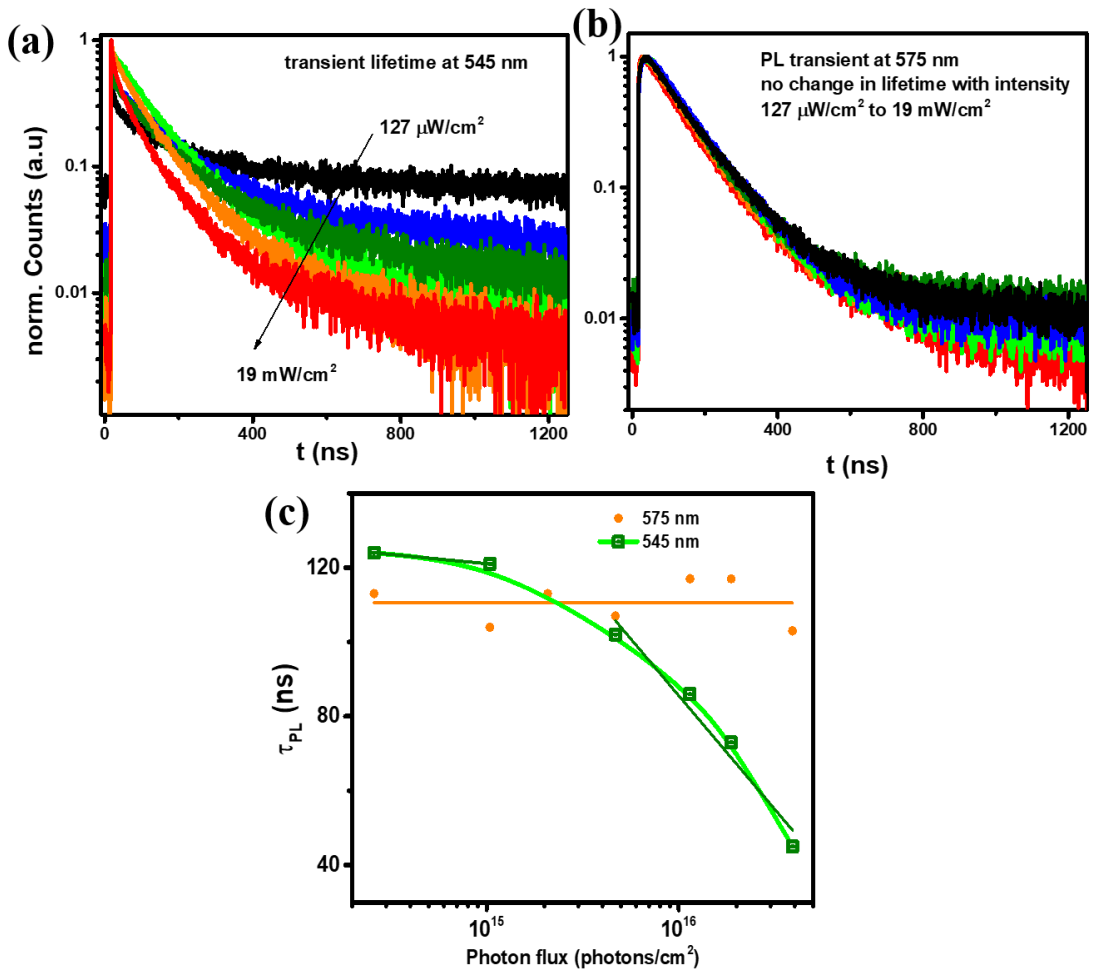

***Figure 2. 11**: **(a)** TRPL depicting the decrease in the PL lifetime at high fluence illumination (545 nm) **(b)** TRPL for 575 nm depicts the constancy of lifetime for the range of excitation intensities. **(c)** Compilation of intensity-dependent lifetimes for 545 nm and 575 nm emission. For 545 nm emission, the lifetime is constant in the lower intensity (< 10^{15} photons/cm^2) and reduces at a higher intensity (> 10^{15} photons/cm^2). For the 575 nm emission, a uniform lifetime in the entire intensity regime. (Reprinted with permission from Ganesh, N., Ghorai, A., Krishnamurthy, S., Banerjee, S.,*

Narasimhan, K. L., Ogale, S. B., & Narayan, K. S. (2020). Impact of trap filling on carrier diffusion in MAPb Br 3 single crystals. Physical Review Materials, 4(8), 084602. Copyright (2020) by American Physical Society)

The effective PL lifetime corresponding to 545 nm emission, marginally varies up to a fluence of 10^{15} photons/cm^2 and at higher fluence, decreases as $\tau_R \propto 1/B\delta n$. In contrast, for trap-emission at 575 nm, observed τ_{eff} is independent of excitation intensity, implying monomolecular emission.

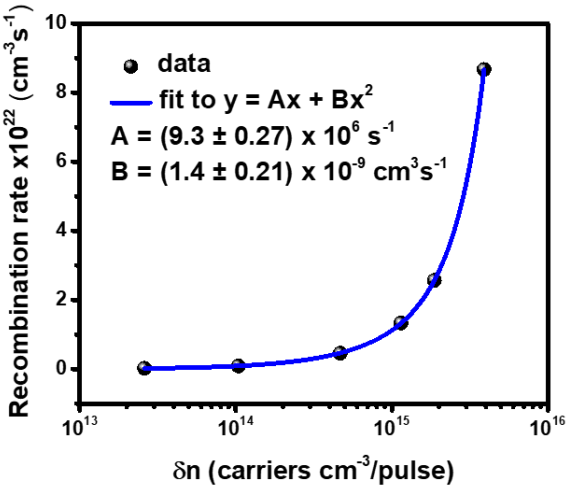

***Figure 2. 12**: Plot of recombination rate vs excess carrier density. The plot was fit to a quadratic equation to obtain A and B coefficients.*

Since the recombination rate is given as $\delta n/\tau$, with the τ values given in **Figure 2.11(c)**, the *A* and *B* constants (in **Equation 2.8**), which correspond to the monomolecular and bi-molecular recombination coefficients can be determined. **Figure 2.12** shows the plot of $\delta n/\tau$ vs δn, fit to the parabolic equation. The values of *A* and *B* were determined to be (9.3 ± 0.27) x10^6 s^{-1} and (1.4 ± 0.21) x10^{-9} cm^{3}s^{-1} respectively. These values are in good agreement with recombination rate constants for direct band-gap semiconductors

[32, 42]. Since the *E-PLQE* ~ $\tau_{eff}/\ \tau_R$, for a fluence > 10^{15}/cm^2, τ_R decreases with increasing fluence. The E-PLQE increases with increasing fluence, as shown in **Figure 2.8(c)**.

2.3.3 Microscopic Picture

We now correlate L_d to the PL-lifetime. In the absence of light bias, the tightly-focused probe beam (405 nm, 5×10^{16} photons/cm^2) in the SPCM studies generate a high concentration of electron-hole pairs, and correspondingly the excess carrier lifetime observed from the PL studies (**Figure 2.11(c)**) is small (< 28 ns). The excess carriers diffuse outside the illuminated zone and recombine gradually and the corresponding carrier lifetimes at these levels of concentration increase as observed in PL lifetime studies (545 nm, **Figure 2.11(c)**). As the modulated probe-carriers diffuse to the electrodes, they are also trapped in deep trapping states effectively reducing the photocurrent. When the probe beam is within a couple of diffusion lengths away from the electrode, an increasing number of carriers (for instance, electrons at the ETL contact) are collected and the holes diffuse to the HTL contact setting up a current in the external circuit. When the carrier concentration reduces sufficiently, the excess carrier lifetime converges to ~ 125 ns, and L_{diff} assumes the low-intensity value. The addition of dc light bias in the SPCM studies results in two effects:

1. DC light bias establishes a new dc equilibrium by populating the deep trapping states. This results in suppression of trapping along the pathway for the carriers generated by the modulated probe beam. The reduced trapping accounts for I_{ph} increase with light bias, explaining features in **Figure 2.6(b)**.

2. The magnitude of the dc light bias determines the lateral excess-carrier concentration. The excess carrier lifetime decreases to a limit which is set by the dc-

light bias magnitude. This scenario explains the decrease of L_d with increasing light bias.

The light-bias feature elicits the trap-assisted recombination processes[43]. Monomolecular recombination lifetime depends on radiative rate, SRH recombination rate, and trap density as shown in **Equation 2.6**. An estimated trap density of ~ 10^{15} traps/cm^3 [32, 37] significantly influences band recombination and their corresponding lifetimes. Loss of charge carriers to traps is reduced in the presence of bias light presumably since traps occupancy increases with bias light. Under light bias, a higher fraction of the probe carriers bi-molecularly recombines resulting in shorter τ and L_d.

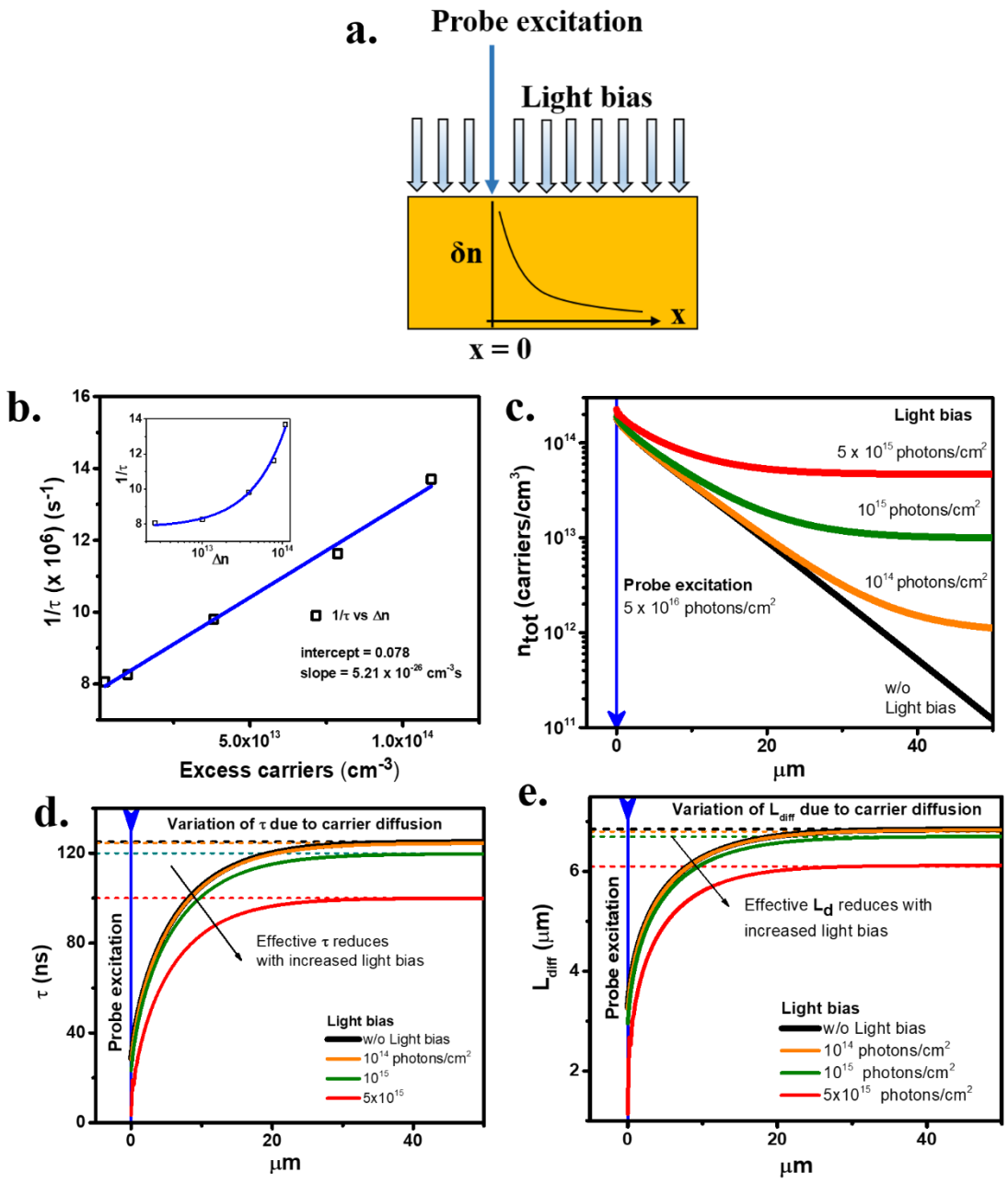

***Figure 2. 13**: **(a)** The schematic describes the simulation of the SPCM experiment using the finite element method. The probe excitation (at x=0) is assumed to be a point source in addition to uniform dc light bias on the MSC sample. The blue line at x=0 in all the plots indicates probe excitation. **(b)** A linear fit to the plot of PL 1/τ vs excess carrier density. **Inset** shows the plot in semi-log scale **(c)** Plot of spatial carrier decay profile considering 1-D diffusion of probe-carriers. The decay profile changes with different intensities of light bias. **(d)** Shows the excess carrier lifetime at different dc light bias.*

*The excess carrier lifetime depends on the background carrier density (shown in **(c)**). The dashed line indicates the lifetime of light-bias generated carriers. As excess probe-carriers diffuse in space and recombine, the excess carrier density decreases resulting in an increased excess-carrier lifetime. This results in a spatial dependence of the excess carrier lifetime. **(e)** Shows the effective diffusion length decreases with increasing light bias. The dashed line indicates L_{diff} of light bias generated carriers. Since the lifetime increases as the excess carriers diffuse away from x = 0, the effective diffusion length also increases. (Reprinted with permission from Ganesh, N., Ghorai, A., Krishnamurthy, S., Banerjee, S., Narasimhan, K. L., Ogale, S. B., & Narayan, K. S. (2020). Impact of trap filling on carrier diffusion in MAPb Br 3 single crystals. Physical Review Materials, 4(8), 084602. Copyright (2020) by American Physical Society)*

To understand the microscopic carrier diffusion dynamics, simulation of SPCM using the finite element method, incorporating 1-D carrier diffusion was carried out, results of which are presented in **Figure 2.13**. A probe excitation is introduced at x = 0 in addition to uniform dc-light bias on the MSC sample, as shown in the schematic **Figure 2.13(a)**. The probe generation (405 nm, 30 mW/cm^2) is at x=0 in addition to dc-uniform light bias on the MSC sample. The probe point excitation consisted of G (0) = 5 x 10^{16} photons/cm^2. Upon probe photo-excitation, the generation of excess carrier concentration, δn_{probe} is given as:

$$\delta n_{probe} = \alpha G_0 \tau \qquad (2.9)$$

α = 8 x 10^4 cm^{-1} is the absorption coefficient [32]. The lifetime for a given carrier density is obtained from the linear dependence of $1/\tau$ on excess carrier density shown in **Figure 2.13(b)**, derived from the trend observed in **Figure 2.11(c)**. The excess carrier

concentration, n_{tot}, due to both probe carrier diffusion and light bias generation, at each point is:

$$n_{tot}\,(x) = \delta n_{probe}(0).\exp\left(\frac{-x}{L_{diff}}\right) + n_{exc}\,(L.B) \qquad (2.10)$$

The first term on the RHS refers to probe carrier diffusion with the diffusion length $L_{diff} = (kT\mu\tau/e)^{1/2}$, where μ = 115 cm^2/Vs is the charge carrier mobility[21]. The second term corresponds to the excess carrier generated due to light bias such that, $n_{exc}\,(L.B) = \alpha\tau G_{L.B}$, where $G_{L.B}$ is the generation density of the light bias.

The plot of $n_{tot}(x)$ for different light bias conditions is given in **Figure 2.13(c)**. The photogenerated carriers diffuse from x=0 and also simultaneously recombine with lifetime τ which depends on excess carrier concentration as shown in **Figure 2.11(c)** and **Figure 2.13(b)**. As the excess probe-carriers diffuse away from x=0, the carrier density reduces, increasing τ. However, the effective τ reduces with increasing light bias as shown in **Figure 2.13(d)**. A similar trend is observed for the L_{diff}, as shown in **Figure 2.13(e)**. As the probe carriers diffuse from x=0, the increase in lifetime results in an increased value of L_{diff}. The effective L_{diff} reduces with increased light bias. The simulation results capture the observed trend of decreasing L_d (**Figure 2.6(d)**).

The other parameter, apart from lifetime, that determines L_d is the diffusion coefficient. Ščajev et.al has shown that the balancing effects of phonon scattering at low intensity and carrier scattering at high intensity were observed to have a marginal effect on D[30]. Therefore, the intensity-dependent factor that influences diffusion dynamics is determined largely by τ.

2.3.4 Influence of photon recycling on diffusion

Photon recycling in perovskites is an additional factor that contributes to the transport length in perovskite-based systems and devices [12, 44]. To study this effect, the carrier generation profile was simulated using the finite element method, accounting for photon recycling. The excess carrier diffusion and photon propagation upon point illumination at x=0 was simulated with finite element method using coupled equations. A detailed description of the formalism used for the simulation is given in Appendix 2. Results of the simulation is summarized in **Figure 2.14.**

Figure 2.14 (a) shows that the luminescent quantum efficiency away from the point of generation reduces, since only a fraction of photons are reemitted in every subsequent event of photon reabsorption. The excess carrier generation also follows the same trend. The simulated plot of excess carrier density with and without photon recycling is shown in **Figure 2.14(b)**. It can be observed that the change in the carrier density is very less and close to the illumination point. Similarly, as shown in **Figure 2.14(c)** and **Figure 2.14(d)** the change in the lifetime and L_{diff} values is marginal.

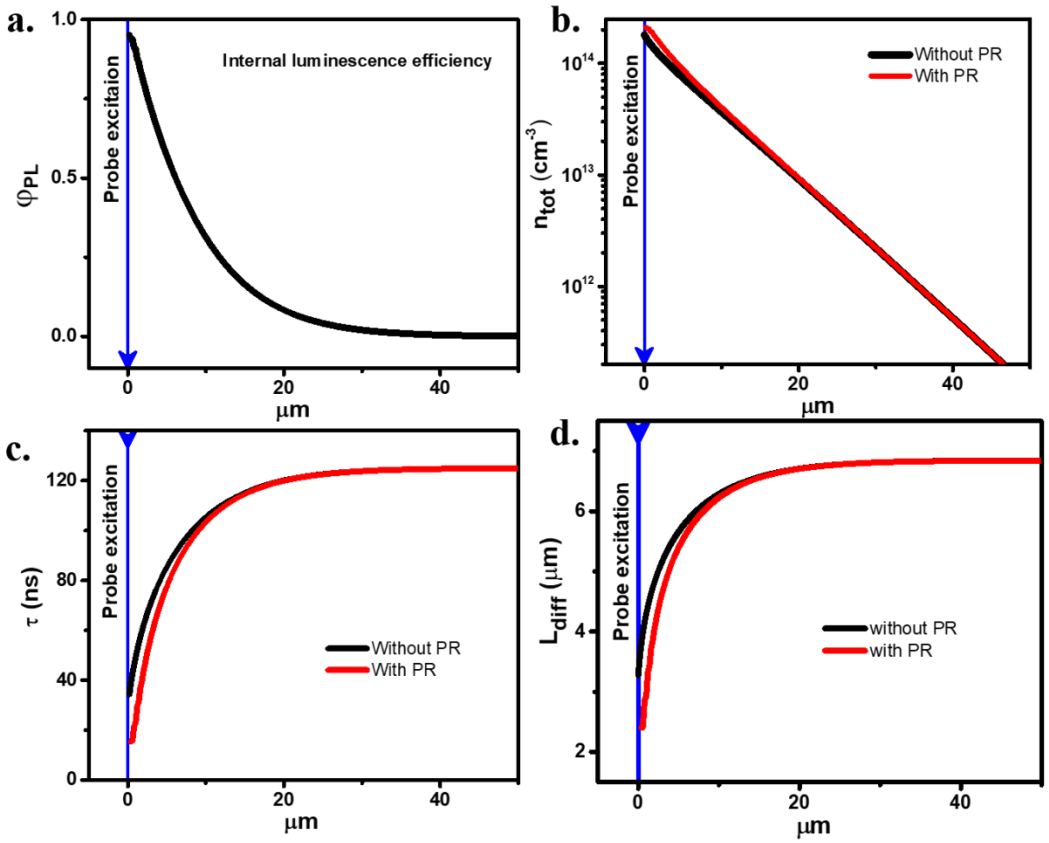

***Figure 2. 14**: **(a)** Plot of φ_{PL} (internal luminescence efficiency) which depends on the background carrier density. Blue vertical lines in all the plots indicate the point of excitation. As the carriers diffuse away from x=0, the carrier density reduces resulting in a reduction of the lifetime (shown in **Figure 2.13(d)**). **(b)** The plot of excess carrier density profile shows a marginal increase considering photon recycling (PR). Consequently, due to the relative increase in the excess carrier density, the lifetime and diffusion length parameters show a marginal reduction as shown in **(c)** and **(d)** respectively.*

2.4 Conclusion

This chapter presents experimental evidence showing the dependence of carrier generation density on the effective diffusion length and carrier lifetime in HOIP single crystal. Scanning photocurrent microscopy is used to extract the characteristic photocurrent I_{ph} decay-length parameter, L_d, which is a measure of effective carrier

diffusion. A marginal increase in uniform light bias ($\leq 5 \times 10^{15}$ photons/cm^2), which acts as a trap-filling mechanism, increases the modulated photocurrent magnitude and reduces the L_d parameter by a factor of two and three for electrons and holes respectively, indicating that the recombination is not monomolecular. This observation was correlated with PL lifetime studies which revealed the contribution of trap recombination dynamics in addition to free carrier dynamics. An elegant consistency is observed between the results of $I_{ph}(x)$ and PL measurements. Based on the trends of L_d and lifetime, it is inferred that the sub-band-gap trap recombination influences carrier transport in the low-intensity excitation regime, while bimolecular recombination and transport dominate at high intensity. These results provide an insight into the contribution of free carriers and trap emission dynamics to L_d. The sizable L_d in systems where carrier transport is trap mediated points to the defect-tolerant capability of HOIP based device structures.

References

1. Jiang Q, *et al.* Surface passivation of perovskite film for efficient solar cells. *Nature Photonics* **13**, 460-466 (2019).
2. Ding J, *et al.* Fully air-bladed high-efficiency perovskite photovoltaics. *Joule* **3**, 402-416 (2019).
3. Wang Y, *et al.* Solution-processed MoS2/organolead trihalide perovskite photodetectors. *Advanced Materials* **29**, 1603995 (2017).
4. Wu Y, Li X, Zeng H. Highly luminescent and stable halide perovskite nanocrystals. *ACS Energy Letters* **4**, 673-681 (2019).
5. Jia Y, Kerner RA, Grede AJ, Rand BP, Giebink NC. Continuous-wave lasing in an organic–inorganic lead halide perovskite semiconductor. *Nature Photonics* **11**, 784-788 (2017).
6. Yang WS, *et al.* Iodide management in formamidinium-lead-halide–based perovskite layers for efficient solar cells. *Science* **356**, 1376-1379 (2017).
7. Laboratory NRE. Best Research-Cell Efficiency Chart. (ed^(eds). NREL Golden, CO (2019).
8. Dong Q, *et al.* Electron-hole diffusion lengths> 175 μm in solution-grown CH3NH3PbI3 single crystals. *Science* **347**, 967-970 (2015).
9. Stranks SD, *et al.* Electron-hole diffusion lengths exceeding 1 micrometer in an organometal trihalide perovskite absorber. *Science* **342**, 341-344 (2013).
10. Jacobsson TJ, *et al.* Exploration of the compositional space for mixed lead halogen perovskites for high efficiency solar cells. *Energy & Environmental Science* **9**, 1706-1724 (2016).
11. Etienne T, Mosconi E, De Angelis F. Dynamical origin of the Rashba effect in organohalide lead perovskites: a key to suppressed carrier recombination in perovskite solar cells? *The journal of physical chemistry letters* **7**, 1638-1645 (2016).
12. Pazos-Outón LM, *et al.* Photon recycling in lead iodide perovskite solar cells. *Science* **351**, 1430-1433 (2016).
13. Wehrenfennig C, Eperon GE, Johnston MB, Snaith HJ, Herz LM. High charge carrier mobilities and lifetimes in organolead trihalide perovskites. *Advanced materials* **26**, 1584-1589 (2014).
14. Steirer KX, *et al.* Defect tolerance in methylammonium lead triiodide perovskite. *ACS Energy Letters* **1**, 360-366 (2016).
15. Huang H, Bodnarchuk MI, Kershaw SV, Kovalenko MV, Rogach AL. Lead halide perovskite nanocrystals in the research spotlight: Stability and defect tolerance. *ACS energy letters* **2**, 2071-2083 (2017).
16. Adhyaksa GW, Veldhuizen LW, Kuang Y, Brittman S, Schropp RE, Garnett EC. Carrier diffusion lengths in hybrid perovskites: processing, composition, aging, and surface passivation effects. *Chemistry of Materials* **28**, 5259-5263 (2016).
17. Semonin OE, *et al.* Limits of carrier diffusion in n-type and p-type CH3NH3PbI3 perovskite single crystals. *The journal of physical chemistry letters* **7**, 3510-3518 (2016).
18. Montcada NrF, *et al.* Analysis of photoinduced carrier recombination kinetics in flat and mesoporous lead perovskite solar cells. *ACS Energy Letters* **2**, 182-187 (2017).

19. Saidaminov MI, *et al.* High-quality bulk hybrid perovskite single crystals within minutes by inverse temperature crystallization. *Nature communications* **6**, 1-6 (2015).
20. Bi Y, Hutter EM, Fang Y, Dong Q, Huang J, Savenije TJ. Charge carrier lifetimes exceeding 15 μs in methylammonium lead iodide single crystals. *The journal of physical chemistry letters* **7**, 923-928 (2016).
21. Shi D, *et al.* Low trap-state density and long carrier diffusion in organolead trihalide perovskite single crystals. *Science* **347**, 519-522 (2015).
22. Xiao Z, Dong Q, Bi C, Shao Y, Yuan Y, Huang J. Solvent annealing of perovskite-induced crystal growth for photovoltaic-device efficiency enhancement. *Advanced Materials* **26**, 6503-6509 (2014).
23. Chen Z, *et al.* Thin single crystal perovskite solar cells to harvest below-bandgap light absorption. *Nature communications* **8**, 1-7 (2017).
24. Chen Z, *et al.* Single-crystal MAPbI3 perovskite solar cells exceeding 21% power conversion efficiency. *ACS Energy Letters* **4**, 1258-1259 (2019).
25. Fang Y, Dong Q, Shao Y, Yuan Y, Huang J. Highly narrowband perovskite single-crystal photodetectors enabled by surface-charge recombination. *Nature Photonics* **9**, 679-686 (2015).
26. Neamen DA. *Semiconductor physics and devices: basic principles*. New York, NY: McGraw-Hill (2012).
27. Scher H, Montroll EW. Anomalous transit-time dispersion in amorphous solids. *Physical Review B* **12**, 2455 (1975).
28. Kabra D, Shriram S, Vidhyadhiraja N, Narayan K. Charge carrier dynamics in organic semiconductors by position dependent optical probing. *Journal of applied physics* **101**, 064510 (2007).
29. Kabra D, Narayan K. Direct estimate of transport length scales in semiconducting polymers. *Advanced Materials* **19**, 1465-1470 (2007).
30. Ščajev P, *et al.* Two regimes of carrier diffusion in vapor-deposited lead-halide perovskites. *The Journal of Physical Chemistry C* **121**, 21600-21609 (2017).
31. Elbaz GA, *et al.* Unbalanced hole and electron diffusion in lead bromide perovskites. *Nano letters* **17**, 1727-1732 (2017).
32. Wenger B, Nayak PK, Wen X, Kesava SV, Noel NK, Snaith HJ. Consolidation of the optoelectronic properties of CH 3 NH 3 PbBr 3 perovskite single crystals. *Nature communications* **8**, 1-10 (2017).
33. DeQuilettes DW, *et al.* Photo-induced halide redistribution in organic–inorganic perovskite films. *Nature communications* **7**, 1-9 (2016).
34. Slotcavage DJ, Karunadasa HI, McGehee MD. Light-induced phase segregation in halide-perovskite absorbers. *ACS Energy Letters* **1**, 1199-1205 (2016).
35. Yuan Y, *et al.* Photovoltaic switching mechanism in lateral structure hybrid perovskite solar cells. *Advanced Energy Materials* **5**, 1500615 (2015).
36. Nie W, *et al.* Light-activated photocurrent degradation and self-healing in perovskite solar cells. *Nature communications* **7**, 1-9 (2016).
37. Wu B, *et al.* Discerning the surface and bulk recombination kinetics of organic–inorganic halide perovskite single crystals. *Advanced Energy Materials* **6**, 1600551 (2016).
38. He H, *et al.* Exciton localization in solution-processed organolead trihalide perovskites. *Nature communications* **7**, 1-7 (2016).
39. Shi J, *et al.* Identification of high-temperature exciton states and their phase-dependent trapping behaviour in lead halide perovskites. *Energy & Environmental Science* **11**, 1460-1469 (2018).

40. Grancini G, *et al.* Role of microstructure in the electron–hole interaction of hybrid lead halide perovskites. *Nature photonics* **9**, 695-701 (2015).
41. Schmidt T, Lischka K, Zulehner W. Excitation-power dependence of the near-band-edge photoluminescence of semiconductors. *Physical Review B* **45**, 8989 (1992).
42. Manser JS, Kamat PV. Band filling with free charge carriers in organometal halide perovskites. *Nature Photonics* **8**, 737 (2014).
43. Stranks SD, Burlakov VM, Leijtens T, Ball JM, Goriely A, Snaith HJ. Recombination kinetics in organic-inorganic perovskites: excitons, free charge, and subgap states. *Physical Review Applied* **2**, 034007 (2014).
44. Cho C, *et al.* The role of photon recycling in perovskite light-emitting diodes. *Nature Communications* **11**, 1-8 (2020).

Chapter 3: Visualization of carrier transport in lateral metal-perovskite-metal device structures.

3.1 Introduction

The excellent performance of Hybrid Organic-Inorganic Perovskite (HOIP) based devices is attributed to their outstanding bulk transport properties such as long diffusion length, extended carrier lifetimes, high absorption coefficient, and mobility [1-4]. However, interfacial charge transport dynamics, especially across the metal-perovskite interface are not widely understood. In spite of numerous reports related to devices based on metal-perovskite junctions, the transport dynamics have not been explored in detail [5-7]. Moreover, the study of carrier transport especially in the space charge regime is not conclusive[8]. One of the reasons for this discrepancy is due to the experimental studies are carried out on sandwich devices, where ionic motion affects carrier transport, even under equilibrium conditions[9]. The present study demonstrates that lateral structure are a suitable framework to separate the effects of carrier transport and ionic motion. In this chapter the carrier transport regimes in a HOIP based lateral metal-semiconductor-metal (MSM) device, as a function of inter-electrode distance and applied bias is studied. Additionally, the lateral geometry provides access to spatially probe the transport parameters such as the local potential and photocurrent across the device. These spatially resolved measurements were carried out along with the bulk device characteristics to provide a complete picture of the microscopic origins of carrier transport that affect the device response.

The transport studies were carried out on lateral back-contact MSM devices, with methylammonium lead iodide, $MAPbI_3$ (MAPI) as the hybrid-perovskite semiconductor. Unlike the widely used sandwich device architecture, lateral devices offer unique advantages such as: (i) Reduced light-absorption losses due to the absence of stack layers, (ii) lower dark current which is useful for small-signal detection, and (iii) low device capacitance which reduces RC lifetime, thereby rendering these devices suitable for high-speed applications[10].This work primarily investigates the transport characteristics in lateral asymmetric electrode devices, with dissimilar work-functions, i.e., Aluminum (Al) and Gold (Au). However, these results are correlated and compared with studies on symmetric electrode MSM devices. The choice of metal electrode work-functions, namely Al (φ_m = 4.1 eV) and Au (φ_m = 5.2 eV) in conjuction with MAPI, allows for selective extraction of the photogenerated electron and hole respectively.

3.2 Experimental Details

3.2.1 Materials

Pre-cleaned fused silica substrates and the photo-curable IP Dip photoresist for dip-in laser lithography were procured from Nanoscribe GmbH. For the preparation of the perovskite precursor solution, Lead (II) bromide ($PbBr_2$, 98%, 367 g/mol), Formamidium iodide (FAI, 99 %, 171.97 g/mol), Lead(II) chloride ($PbCl_2$, 99.999%, 278.11 g/mol), solvents N,N-Dimethylformamide (DMF, anhydrous 98.9%, 73.09gm/mol) and Dimethylsulfoxide (DMSO, anhydrous, 78.13 g/mol) were obtained from Sigma Aldrich. Lead (II) iodide (PbI_2, 99.9985 %,) was obtained from Alfa Aesar. Methylammonium iodide (MAI) and Methylammonium bromide (MABr) was obtained from Dyesol chemicals. For encapsulation, Poly (methyl methacrylate) (PMMA) was

obtained locally and solvent Chlorobenzene (anhydrous, 99.8 %) were obtained from Sigma Aldrich. All the materials were used as obtained

3.2.2 Sample Preparation

Fabrication of asymmetric metal electrodes:

The lateral metal-electrodes were deposited after 3D mask-printing (*Nanoscribe GmbH*). The masks were printed with 2-photon polymerization lithography technique using photo-curable resin (IP Dip) drop cast on fused silica substrates. After the development of the photoresist mask, Au metal was thermally evaporated. The resist was then removed by immersing in liquid N_2 for 30 s and then blow dry with air. The second mask corresponding to the channel length (and partially masking the edge of the Au electrode) was then printed using optical markers and then developed. This was followed by thermal evaporation of the Al electrode. Finally, the second mask was also removed to form the asymmetric electrode device. The thickness of the metal coating was in the range of 80-100 nm. This was followed by perovskite deposition. A schematic describing the fabrication process is given in **Figure 3.1**

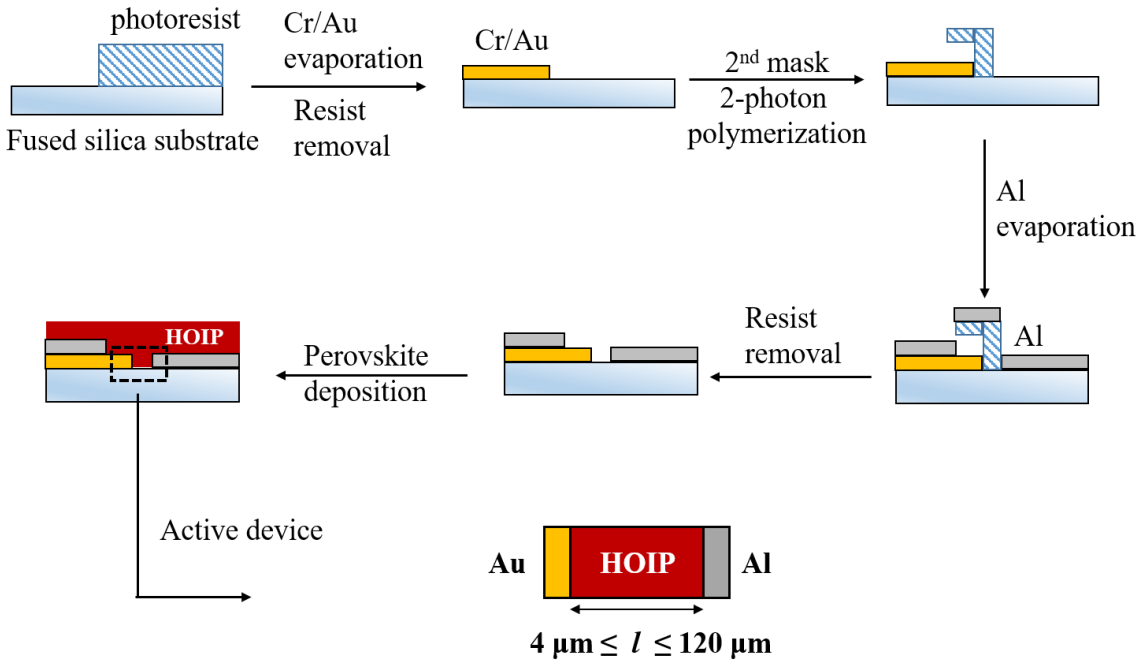

***Figure 3. 1**: Schematic of the procedure followed for the fabrication of the lateral asymmetric electrode MSM devices.*

Fabrication of lateral back contact devices.

The $MAPbI_3$ perovskite films was prepared according to the procedure given in ref.[11].The perovskite precursor was initially prepared using the following by dissolving 357 mg of methylammonium iodide (MAI, Dyesol), 204 mg lead chloride ($PbCl_2$, Sigma Aldrich) and 7 mg of lead iodide (PbI_2, 99.999 %, Sigma Aldrich) in 1 ml of DMF (N,N-Dimethylformamide, anhydrous) solution and stirred at high speed for at least 60 min. To render the substrates hydrophilic, they were plasma treated (using ultra high pure (UHP) nitrogen, 99.9995 %) for 2 min. The substrates were transferred to a glovebox maintained in an inert atmosphere. The perovskite precursor was dispensed onto the substrates and spin-coated at 3000 rpm for 80 s followed by 5000 rpm for 10 s. The substrates were then annealed in the following sequence: 20 °C for 15 min, 70 °C for 15 min, 100 °C for 90 min and 120 °C for 10 min. To encapsulate devices (for

J-V measurements), a layer of PMMA (250 mg/ml in chlorobenzene) was spin-coated at 2000 rpm for 60 s followed by annealing at 60 °C for 20 min.

For the preparation of mixed-phase perovskite films the procedure given in ref.[12] was followed. To prepare the mixed-phase perovskite precursor solution, 215 mg of FAI (Formamidium Iodide, Sigma Aldrich, > 99 %), 28 mg of MABr (Methylammonium bromide, Dyesol), 634 mg of PbI_2 (Lead(II) iodide, Alfa Aesar, 99.9985 %) and 92 mg of $PbBr_2$ (Lead Bromide, Sigma Aldrich, 98 %) was dissolved in 1 ml of 4:1 ratio of (Dimethylformamide : Dimethylsulfoxide) and stirred at 85 °C for about 30 min. 70 μL of the solution was then dispensed onto the substrates with lateral metal electrodes and spin-coated at 1000 rpm for 10 s followed by 6000 rpm for 35 s. In the last 7 s of the spin, 70 μL of Anisole was dynamically dispensed. The films were then annealed at 100 °C for 60 min.

3.2.3 Measurements and Characterization

I-V measurement on devices

The I-V measurements were carried out on devices using the Keithley Source Meter 2400. The scan on the voltage sweep was carried out at a rate of 0.5 V/s. the light responsivity measurements were carried out using a 532 nm excitation with an optical power of ~ 26 mW/cm^2.

Kelvin Probe Force Microscopy (KPFM)

Kelvin Probe measurements were carried out using the JPK Nanowizard-3 Atomic Force Microscopy instrument. The scans were performed using conductive Cr-Pt cantilever tips (BudgetSensors, Multi 75 EG) with a force calibration of 2 N/m. Calibration of the tip was initially done by measuring the contact potential difference (CPD) on the Au sample (100 nm of Au coated on glass slide). This was followed by a

measurement of the contact potential difference on the lateral devices. The thickness of the perovskite layer was reduced to ~ 150-180 nm to reduce masking effects due to the thick layer, and capture the potential profile of the active device. In short-circuit condition, both the Al and Au electrodes were grounded with respect to the Kelvin-Probe circuit. In the case of bias-dependent studies, an external bias was applied, in parallel to the lateral MSM device.

Near-field Scanning Photocurrent Microscopy (NSPM)

JPK Nanowizard-3 Atomic force microscope (AFM) in Near-field scanning optical microscopy (NSOM) mode was used to measure the local photocurrent in the channel region of the devices. A tapered optical fiber coated with Cr/Au and having aperture ~ 105 nm was raster-scanned using the piezo head of the AFM. The other end of the multi-mode fiber was coupled to a 532 nm laser using a 20x, N.A. = 0.4 microscope objective lens. The input laser power was maintained at 5mW during the measurement. Additionally, the laser intensity was modulated at 383 Hz using a mechanical chopper. Using a resonant-frequency based feedback system, the assembly consisting of the tuning fork and the fiber-tip was lowered to be in close proximity to the sample. When the fiber tip-to-sample distance is in the near-field approximation ($\leq \lambda_{ex}$), beyond Abbe's diffraction limit, spot sizes up to ~ 100 nm can be achieved. This was earlier verified in our laboratory[13, 14].

In synchronization with the excitation scanning, the photocurrent signal was measured using Stanford Research Systems SRS 830 lock-in amplifier and the read-out signal was fed to the JPK scanning probe module (SPM) control for data-sampling and storage. A calibrated photodetector was used to measure the transmitted light through the device. The transmission map of the device is used to correlate the local photocurrent value to discern the position of the metal electrodes. The ambient light

was completely blocked to avoid any external exposure to the sample. The measurements were performed in ambient air due to the practical limitations of mounting the instrument in a vacuum. During the measurements, desiccants were placed around the setup to reduce the moisture content in the ambient atmosphere.

Transient Photocurrent

Transient Photocurrent measurements were carried out by using a pulsed supercontinum laser (YSL Supercontinuum SC PRO 7, λ_{ex} ~ 400 – 2300 nm) with a pulse width of ~ 100 ps and energy ~ 1 μJ/pulse (with 100 kHz repetition rate), incident from the glass-substrate side on the lateral device. The device was operated at 5 V bias and the current was measured in series, using a digital oscilloscope (Tektronix MDO3024, 2.5 GS/s) with 50 Ω input coupling.

3.3 Results and Discussion

3.3.1 Device operation

The J-V characteristics on lateral MSM devices were initially carried out to study device operation. **Figure 3.2(a)** shows the schematic of the lateral asymmetric electrode MSM (metal-semiconductor-metal) device with $MAPbI_3$ (MAPI) perovskite as the active layer, in the back contact device geometry. Here, *l* is the inter-electrode channel length and *d* is the thickness of the metal electrode (~ 80 - 100 nm), and *w* is the width of the electrode. This work presents the study of device characteristics as a function of inter-electrode channel lengths (*l*) in the range of 4 μm ≤ *l* ≤ 120 μm. In these devices, the electrode width, *w* >> *l*, is in the range of ~ 2-4 mm. The effective area for charge conduction in these devices is given as ≈ *w* × *d*. **Figure 3.2(b)** shows the reflection-microscopy image of the asymmetric electrode device, with *l* ~ 12 μm. These devices

can be implemented to a larger area using inter-digitated electrode patterns, as shown in **Figure 3.2(c)**.

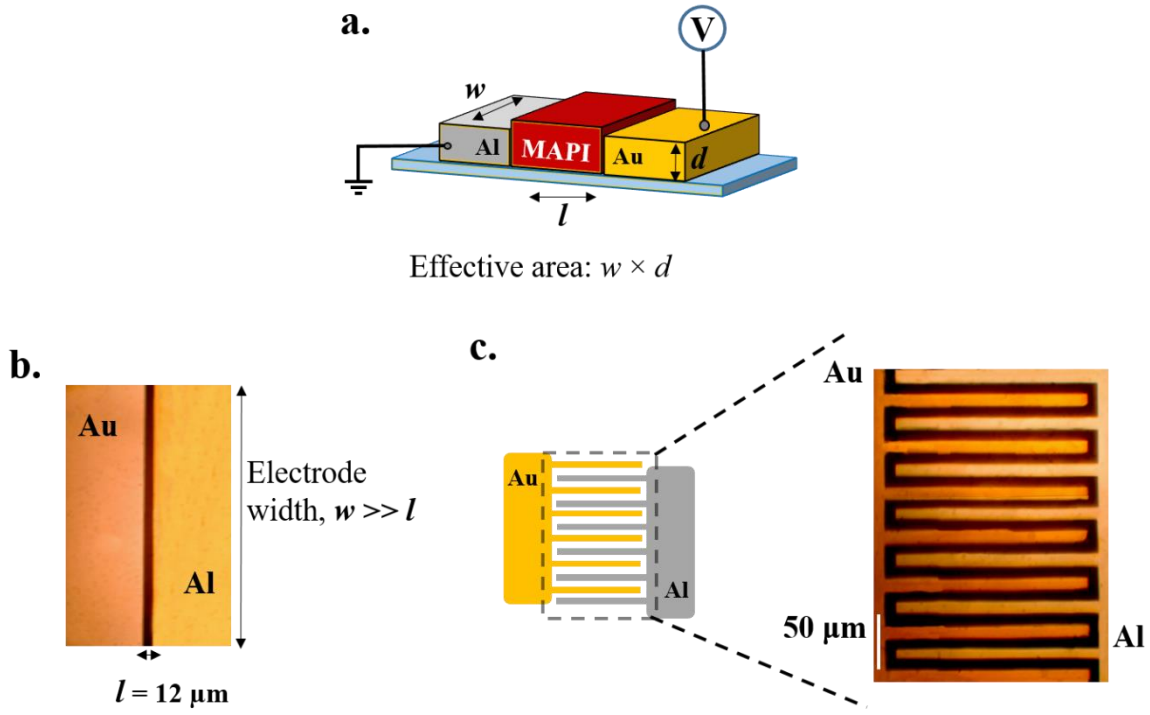

***Figure 3. 2**: **(a)** Schematic of the lateral asymmetric electrode device, where l is the inter-electrode channel length and d is the thickness of the metal electrode. **(b)** Microscopy image of the asymmetric electrode lateral device, with l = 12 µm, captured in the reflection geometry. **(c)** Schematic of an asymmetric interdigitated electrode structure. The zoomed image is the microscopic image of the structure with an inter-electrode distance of 10 µm.*

Figure 3.3(a) shows the dark J-V characteristics on asymmetric MSM devices for devices of different *l*. It is clear that the magnitude of the dark-J increases for the short-channel devices, owing to the higher electric field (~ V/*l*) in short channel devices. Further, it is also observed that the J-V curve tends to a rectification-like behavior for the case of short channel devices. This is clearly seen in **Figure 3.3(b)**, which shows the J-V plot normalized to the current value at 5 V. Likewise, the rectification ratio

$= \frac{J\,(5\,V)}{|J\,(-5\,V)|}$ in **Figure 3.3(c)** shows a sharp increase for the short channel devices reaching up to ~ 17 for l = 4 μm. To understand the non-linear nature of the observed current, a closer analysis of the J(V) characteristics is necessary.

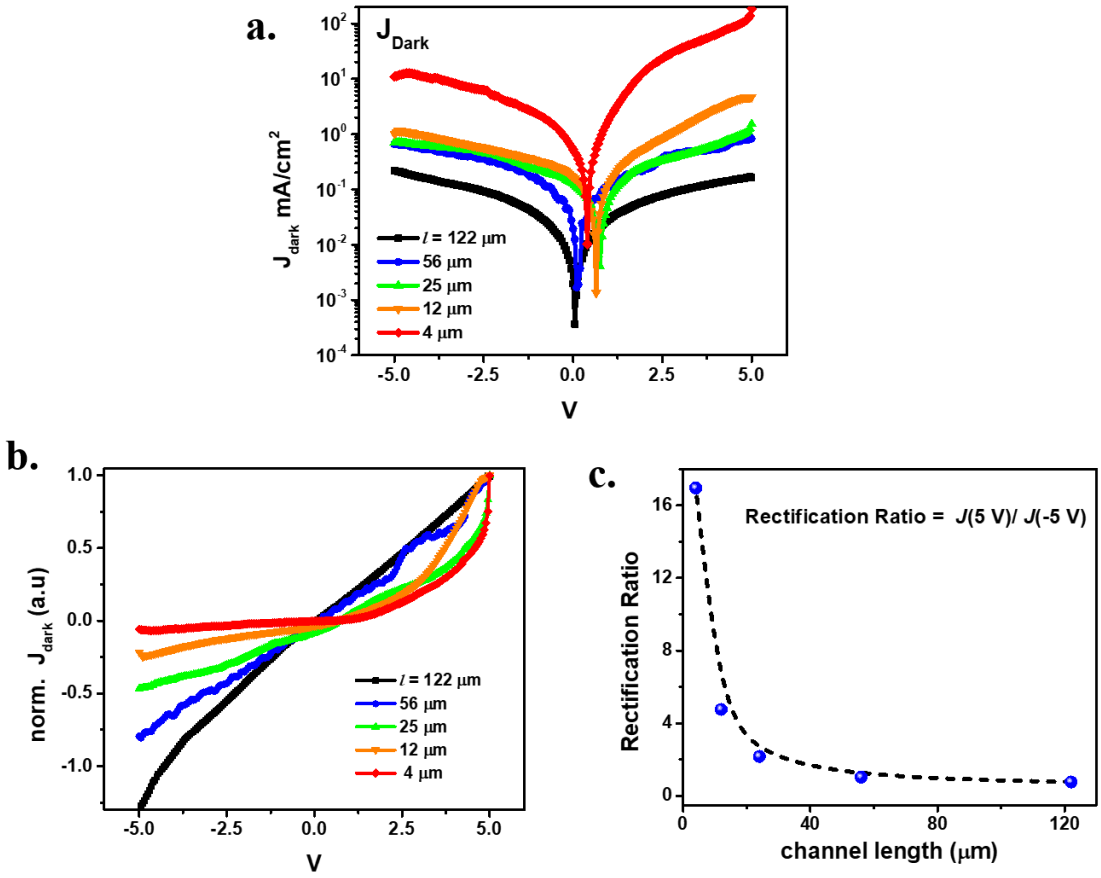

***Figure 3. 3**: **(a)** Semi-log plot of J-V characteristics of the asymmetric electrode device for different values of l. **(b)** The plot of the J-V characteristics, normalized to J at 5 V bias. **(c)** The plot of the rectification ratio as a function of channel length shows that the rectification ratio increases for short channel devices.*

3.3.2 Carrier-transport regimes

To understand the dominant transport mechanism, the J(V) characteristics are represented as a log-log plot. **Figures 3.4(b)** and **3.4(c)** show the log-log plots of the

J(V) characteristics for devices with l = 4 μm and 12 μm respectively, in the positive bias sweep (depicted in **Figure 3.4(a)**). The J-V characteristics are linear (ohmic) at low voltages, and is described by:

$$J_{ohmic} = \sigma \frac{V}{l} \tag{3.1}$$

Beyond a critical voltage, the current increases as V^2. This is suggestive of space charge limited current (SCLC) behavior and is described by:

$$J_{SCLC} = \frac{9}{8} \mu\theta \varepsilon_0 \varepsilon_r \frac{V^2}{l^3} \tag{3.2}$$

Where $\mu\theta$ and ε_r represent the SCLC mobility and the dielectric constant of the semiconductor, respectively. In the expression for the SCLC mobility: $\mu_{SCLC} = \mu\theta$, μ corresponds to the free carrier mobility and θ is the reduction factor due to the carrier-trapping effects[9]. For longer channel length devices, with l > 12 μm, **Figure 3.4(d)** shows that the J-V characteristic is linear

.

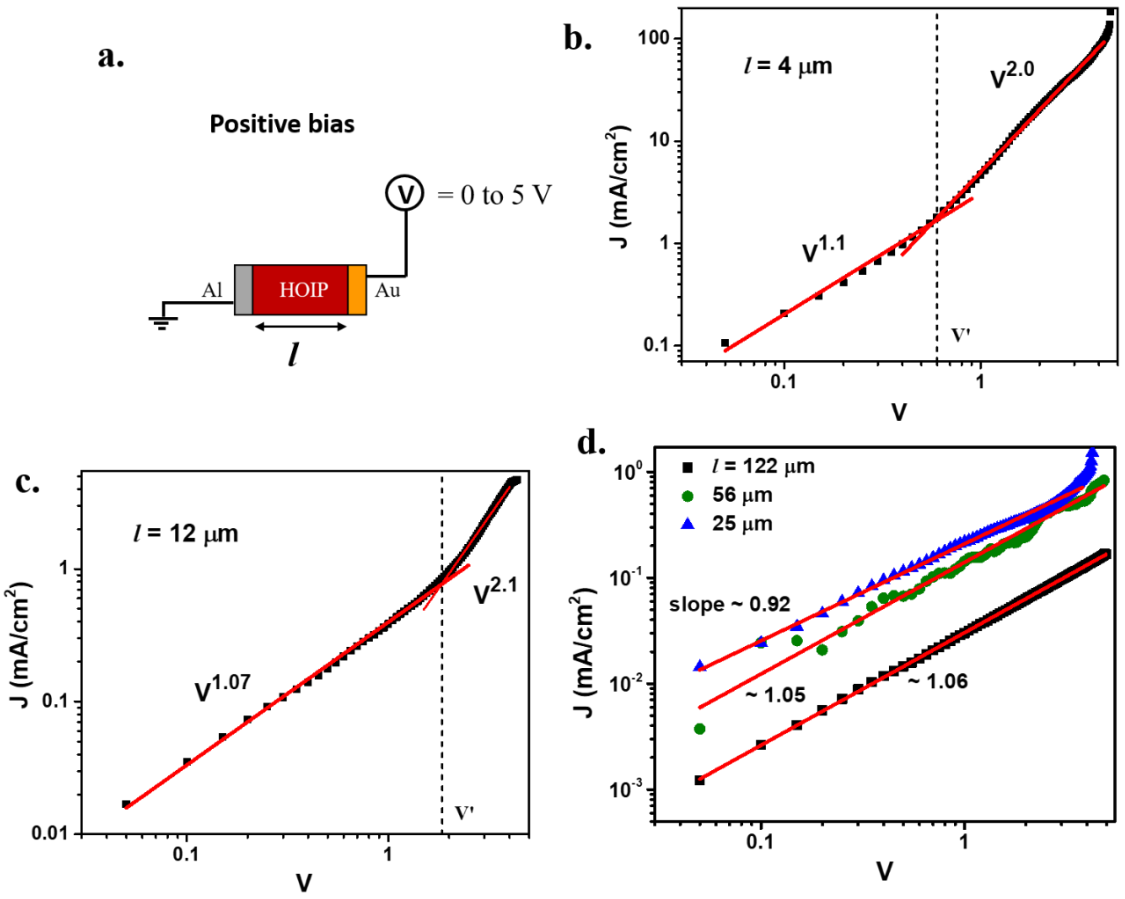

***Figure 3. 4**: **(a)** Schematic of the diagram representing the directionality of the applied bias. Here positive bias is applied to the Au electrode. **(b)** Log-log plot of the dark J-V data shows distinct ohmic ($\propto V^1$) and SCLC behavior ($\propto V^2$) for l = 4 μm and **(c)** 12 μm channel respectively. **(d)** Log-log J(V) plot for long-channel (l > 20 μm) asymmetric electrode devices, shows dominant ohmic behavior.*

It is observed that the onset voltage of SCLC, represented as V' reduces for the shorter channel devices. In addition to the quadratic dependence of J on the applied bias, **Figure 3.5(a)** represents the device current as a function of channel length, at a bias of 5 V. We observe the ohmic dependence of the channel length ($J \propto l^{-1}$) for the case of long channel devices (l > 24 μm) and SCLC behavior ($J \propto l^{-3}$) for the short-channel

devices. Effectively, if the transport is SCLC, then J should satisfy a scaling relation: $J = f(V^2/l^3)$. **Figure 3.5(b)** is a plot of J' vs V^2/l^3, indicating a linear variation (J' is the SCLC current, corrected for the ohmic contribution such that $J' = J_{total} - J_{ohmic}$ for V > V', further details in Appendix 3). The current in the SCLC region is similar for both the l = 4 μm and 12 μm samples. This confirms that the transport in these samples is SCLC.

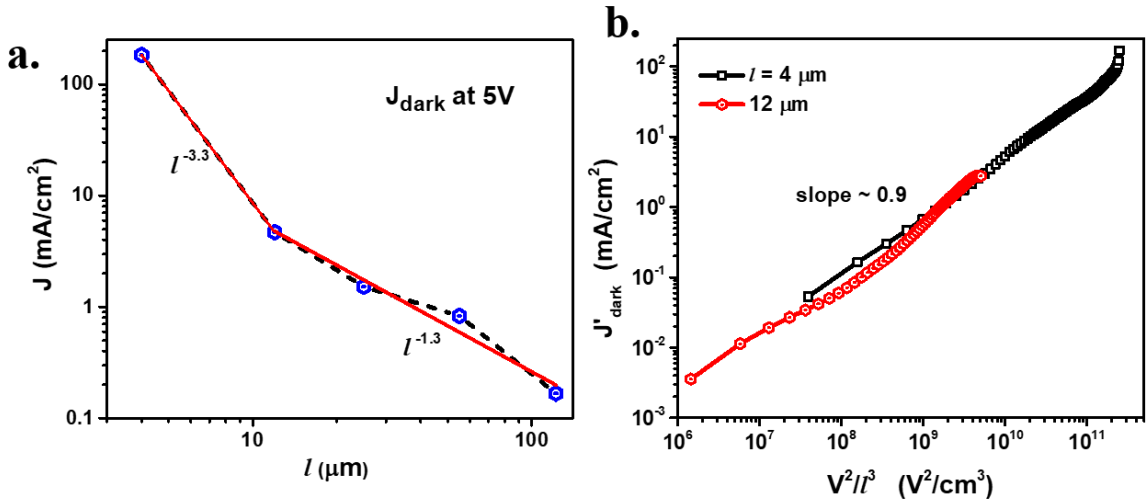

***Figure 3. 5**: **(a)** Variation of dark current density at 5V as a function of channel length shows an ohmic behavior ($\propto l^{-1}$) for the long channel length and an SCLC behavior ($\propto l^{-3}$) for the short channel length. **(b)** Plot of current density, J' as a function of V^2/l^3 for short channel devices shows a single-exponent dependence, confirming SCLC behavior.*

Using **Equation 3.2** and ε_r = 60,[15] the mobility is estimated to be μ_{SCLC} = 0.07 - 0.15 cm^2/Vs. These values are consistent with previous observations of mobility from contact-based measurements [9, 16-19]. The low mobility is attributed to lateral drift of carriers which is accompanied by scattering at the grain-boundaries in addition to carrier-trapping effects. The observed asymmetry in the J-V (for short channel devices)

in **Figure 3.3(b)** arises from the fact that Al does not make an ohmic contact with MAPI. This is consistent with the plot in **Figure 3.6(b)** which shows the linear J-V characteristics for positive potential sweep to Al electrode, for all the investigated values of the channel length.

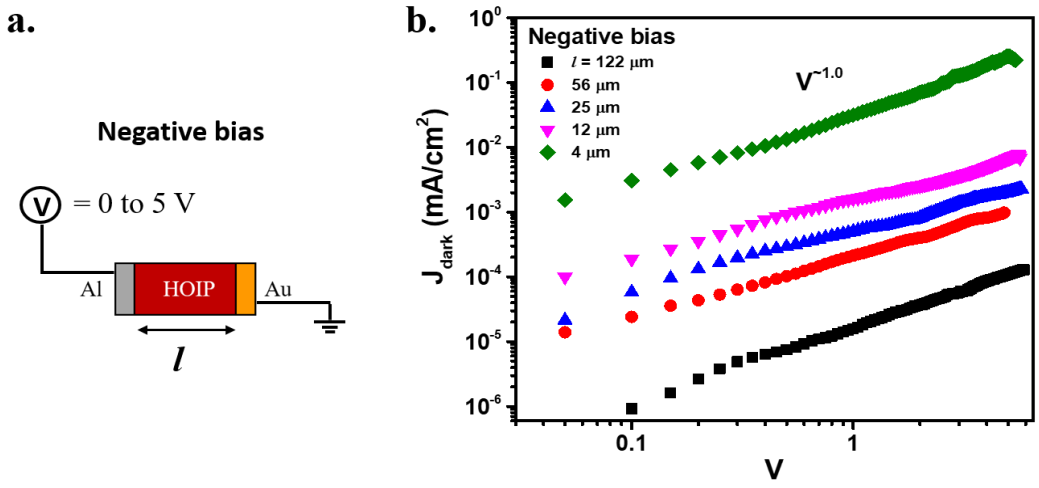

***Figure 3. 6**: **(a)** Schematic of the diagram representing the directionality of the applied bias. Here positive bias is applied to the Al electrode. **(b)** Log-log plot of dark J(V) characteristics show single-exponent variation, representing the ohmic regime of operation for devices of different channel lengths, l.*

It is noted that this rectification-like characteristic is not observed in the case of symmetric electrode devices as shown in **Figure 3.7**. The origin of the rectification-like characteristics is therefore attributed to the presence of an asymmetric charge-selective transport barrier across either of the metal-perovskite interface.

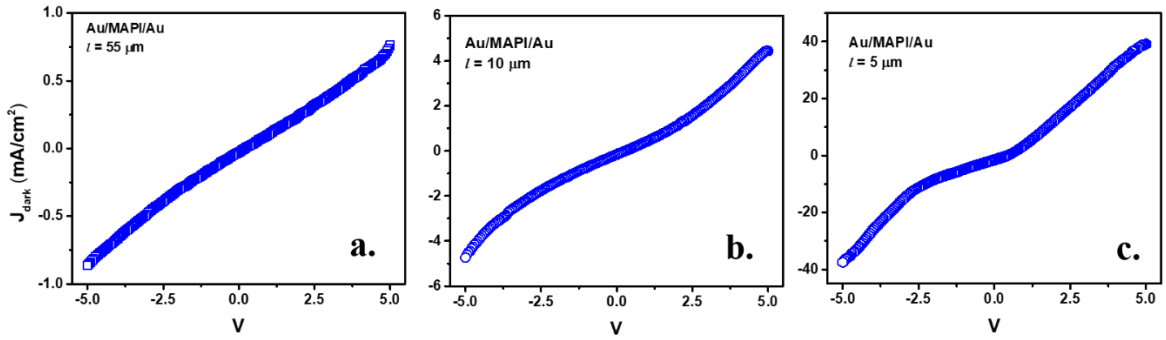

Figure 3. 7*: Dark J(V) characteristics of Au/MAPI/Au symmetric electrode devices with a channel length of* ***(a)*** *55 μm,* ***(b)*** *10 μm, and* ***(c)*** *5 μm.*

3.3.3 Barrier estimates at metal-perovskite interface

To investigate the origin of the non-linear J-V characteristics, the energy levels and band-bending dynamics across the metal perovskite interface is examined. **Figure 3.8** describes the energy levels and band-bending across the Al/MAPI (left-hand side of **Figure 3.8**) and Au/MAPI (right-hand side of **Figure 3.8**) interface. **Figure 3.8(a)** and **3.8(c)** show the Fermi-levels of the metals and the perovskite. The work-function of Al and MAPI were determined to be 4.1 eV and 5.1 eV respectively (Au as the reference) using Kelvin-Probe measurements. The higher work-function of MAPI (5.1 eV), attributing a p-type character is consistent with previous reports[20, 21], and the hole-carrier concentration is estimated to be ~ 10^{14} cm^{-3}.

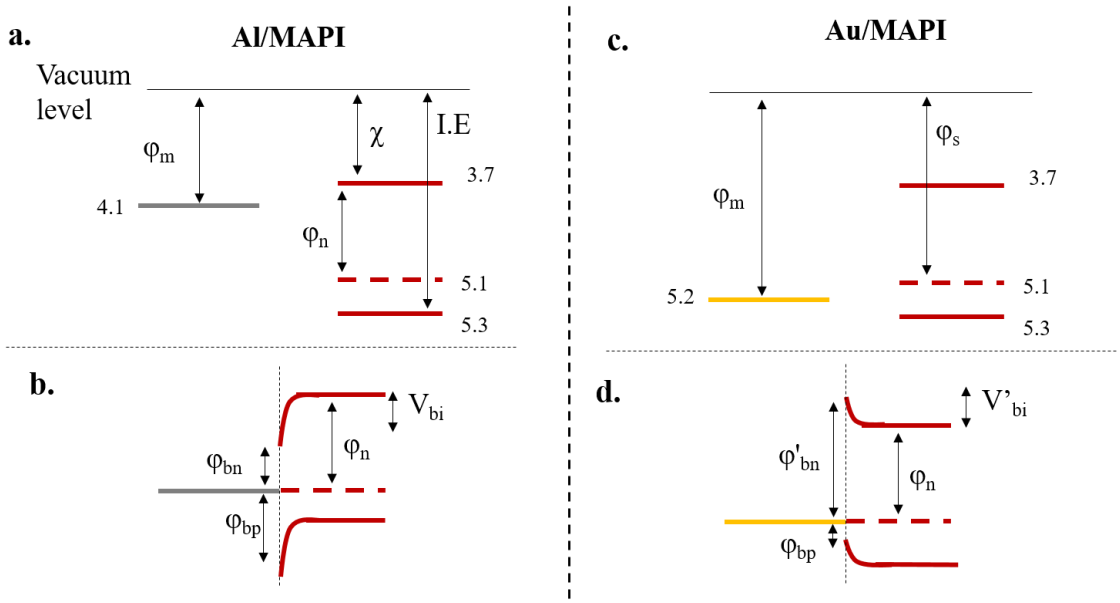

Figure 3. 8*: Schematic shows the band alignment diagram across the Al/MAPI interface* ***(a)*** *before and* ***(b)*** *after the formation of the contact. The right-hand side shows the band-diagram across the Au/MAPI interface* ***(c)*** *before and* ***(d)*** *after the formation of the contact.*

Upon the formation of contact in short-circuit condition, the fermi-level equilibrates, and band-bending at the metal-perovskite interface results in the formation of an injection barrier for both the electrons as well as the holes. From the description related to the formation of a transport barrier at the metal-semiconductor interface, discussed in section 1.5.2, the following estimates are presented:

At the Al/MAPI interface (**Figure 3.8(b)**), the carrier injection barrier is given as:

Electron barrier, $\varphi_{bn} = \varphi_m - \chi$ = 4.1 – 3.7 = 0.4 V

Hole barrier, $\varphi_{bp} = I.E - \varphi_m$ = 4.1 – 5.3 = 1.2 V

Built-in voltage (favoring electron extraction): $V_{bi} = \varphi_{bn} - \varphi_n$ = 0.4 – 1.4 = -1.0 V

At the Au/MAPI interface (**Figure 3.8(d)**), the carrier injection barrier is given as:

Electron barrier, $\varphi'_{bn} = \varphi_m - \chi$ = 5.2 – 3.7 = 1.5 V

Hole barrier, $\varphi'_{bp} = I.E - \varphi_m$ = 1.5 – 1.6 = 0.1 V

Built-in voltage (favoring hole extraction): $V'_{bi} = \varphi'_{bn} - \varphi_n$ = 1.5 – 1.4 = 0.1 V

The net built-in potential is given as: V'_{bi} (Au/MAPI) – V_{bi} (Al/MAPI) = **1.1 V**

The above-presented analysis indicates the presence of a finite injection barrier for both the carriers at Al-MAPI interface, while the injection barrier for the holes at Au-HOIP is very small (~ 0.1 eV) and can be assumed to be negligible. Additionally, a built-in potential is observed in the perovskite, represented as V_{bi} and V'_{bi} at Al-MAPI and Au-MAPI interface respectively that arise due to the band-bending dynamics. In the event of excess carrier generation, the built-in field facilitates electron and hole extraction to the Al and Au electrode respectively. The combined effect of band alignment and Fermi level equilibration in the asymmetric electrode device is schematically shown in **Figures 3.9(a)** and **3.9(b)** respectively.

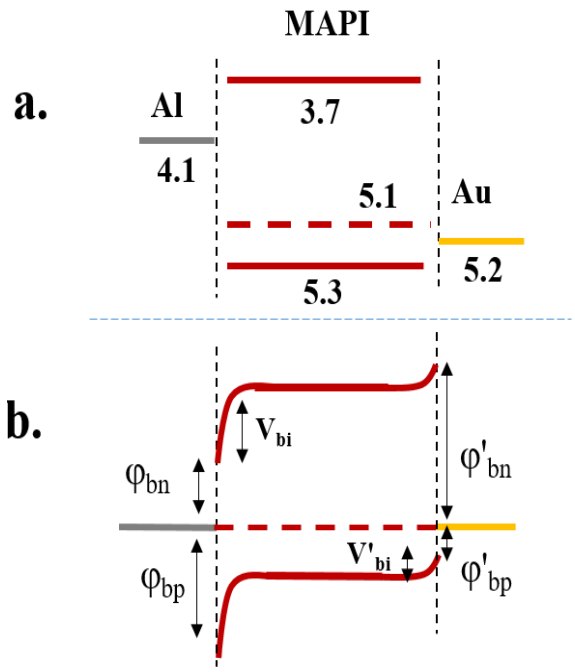

***Figure 3. 9**: **(a)** Band alignment diagram of the asymmetric electrode MSM device. **(b)** The device in short-circuit condition shows an injection barrier at the metal-perovskite interface. A built-in potential, V_{bi} is developed at the metal-MAPI interface as a result of Fermi-level equilibration.*

3.3.4 Spatial Potential Mapping

In addition to the above estimates, the spatial profile of the built-in potential helps to predict and analyze the dominant transport mechanism in the MSM devices. This is especially significant when the interface-induced effects are comparable to the bulk transport characteristics, especially in the instance of having short inter-electrode length devices. The lateral device structure offers the advantage to map the potential using the method of Kelvin Probe Force Microscopy (KPFM). The KPFM technique, depicted in **Figure 3.10(a)**, essentially consists of a conductive tip that is in intermittent contact with the sample. During the scan, a varied dc-potential with an overriding ac-bias is applied. At the point of fermi-level equilibration between the tip and the sample, the contact potential difference (CPD), which is proportional to the surface potential is

recorded. **Figure 3.10(b)** shows the 2D surface plots of the CPD for KPFM measurement probed across the device. In correlation with the metal work-function, the CPD depicts a higher value for the Al electrode and a low value for the Au electrode. **Figure 3.10(c)** shows the line scan profile of CPD across the device. The difference in the CPD value corresponding to the two electrodes is ~ 0.9 eV, which is in close agreement with the calculated value of 1.1 eV. Additionally, as estimated, a sharp potential drop across the Al-MAPI interface is observed, which indicates both the presence of a high V_{bi} as well as an injection barrier at this interface. In contrast, at the Au-HOIP interface, the potential drop is minimal indicating a pseudo-ohmic contact for the hole carriers. Interestingly, across the bulk of the device, a gradual reduction of the CPD reveals the presence of a built-in electric field, indicative of absence or negligible screening by mobile ions at the metal-perovskite interface. Any degrading process resulting from ion-accumulation during the short-circuit operation is minimal. Additionally, in presence of low bias and low field conditions, both degradation and ionic drifts are not significant. It is noted that in the KPFM measurements on back contact lateral devices, the CPD corresponding to the metal surface is modified due to the presence of a thin layer (~ 50 nm) of the MAPI perovskite, as depicted in **Figure 3.10(a)**. However, the spatial profile is indicative of the potential map across the lateral structure. This has also been verified by imaging the potential profile in the presence of an external bias.

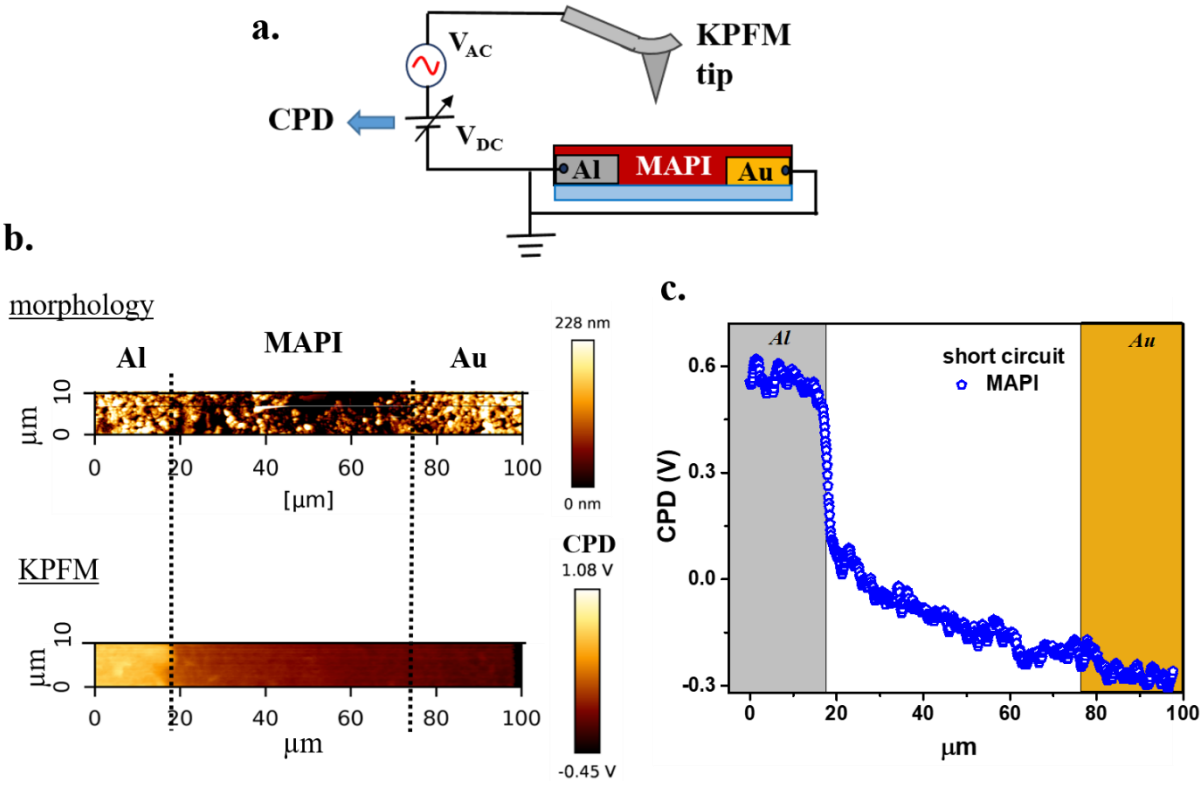

***Figure 3. 10**: **(a)** Schematic of the KPFM experimental setup used for potential mapping. The measured contact potential difference (CPD) is used to measure the potential profile across the device. **(b)** 2D surface plots showing the morphology-KPFM correlation for asymmetric electrode device with l = 55 µm, in short-circuit condition **(c)** Line-scan of the CPD profile shows the presence of a significant potential drop at the Al-MAPI interface and also across the bulk of the device. The potential drop across the Au-MAPI interface is minimal.*

The above-illustrated barrier dynamics explain the rectification-like behavior that is observed in these asymmetric electrode devices. Essentially, in the negative bias condition (positive voltage to Al), an injection barrier is present for the holes and electrons at Al-MAPI and Au-MAPI interface respectively. However, in the positive bias condition, the efficient injection of holes across the Au-MAPI interface results in a high forward bias current. Therefore the determined SCLC mobility corresponds to

the injected hole-carriers. The asymmetry in the J-V (for short channel devices) in **Figure 3.3(b)** arises then from the fact that Al does not make an ohmic contact with MAPI.

Previous reports on HOIP-based devices have shown that the classic SCLC formalism is invalid for systems with mobile ions [8, 22, 23]. The effect of ionic conduction is especially amplified in sandwich devices with an active layer thickness ~ 200- 300 nm. This results in a higher electric field (~ 10^5 V/cm) even in short-circuit condition[24, 25]. On the other hand, in lateral structures, finite electric field (~ 10^2 V/cm) across the bulk of the lateral device (**Figure 3.10(c)**) suggests the minimal influence of ion motion.

3.3.5 Spatial Photocurrent Mapping

The potential landscape in the lateral MSM structures influences device operation. However, in the presence of excess carrier generation, additional factors such as interfacial traps and carrier mobility influence the light response in these devices. In the context of device operation, the bulk light response depends on the cumulative response due to the different regions in the lateral device. The spatial dependence of photocurrent then provides additional information regarding the different regions that are associated with efficient charge separation, which is useful for device optimization. Lateral devices allow for spatially resolved studies using local excitation. Since the device dimensions are in the range of few ~ μm, a higher resolution of excitation spot-size is necessary. We employ the technique of Near-field Scanning Photocurrent Microscopy (NSPM), a schematic of which is shown in **Figure 3.11(a)**. The experimental setup consists of a tapered optical fiber-tip which is integrated with a tuning fork. Using the resonant-frequency based feedback system, the assembly consisting of the fiber-tip that is attached to a tuning fork is lowered to be in close proximity with to the device. With

the sample-to-fiber tip distance in the near-field approximation ($\leq \lambda_{ex}$), beyond Abbe's diffraction limit, spot sizes up to ~ 100 nm can be achieved[13, 14, 26].

Figures 3.11(b), 3.11(c) and **3.11(d)** show the line scan profiles of the short-circuit photocurrent (I_{ph}) for the asymmetric electrode device with l = 55 μm, 22 μm and 13 μm respectively. $I_{ph}(x)$ profile indicates regions of low I_{ph} for excitation close to the MAPI-Al interface and high I_{ph} at MAPI-Au interface. The higher I_{ph} close to the Au electrode is attributed to the efficient transport of the holes to the Au electrode. A model to understand the reduction of the I_{ph} close to the electrodes needs to be developed. It is to be noted that for local excitation, the magnitude of the I_{ph} is also controlled by the dark resistance of the channel region outside of the illumination zone. The interfacial contact resistance is expected to be relatively higher in the short channel devices[27]. Additionally, possible origins of the low I_{ph} close to the Al interface points to high recombination, presumably due to the presence of interfacial traps or a complex hetero-junction.

The influence on the $I_{ph}(x)$ profile is analyzed as a function of l, results of which are presented in a normalized plot shown in **Figure 3.11(e)**. For the case of longer l = 55 μm, the non-uniformity of the I_{ph} distribution is skewed towards the MAPI-Au interface. However for the case of shorter channel l = 13 μm, we see that the $I_{ph}(x)$-peak is at the center and the profile tends to a uniform spatial distribution. Additionally, the dashed line for l = 4 μm, is the $I_{ph}(x)$ estimated using interpolation, indicates a higher degree of spatial uniformity.

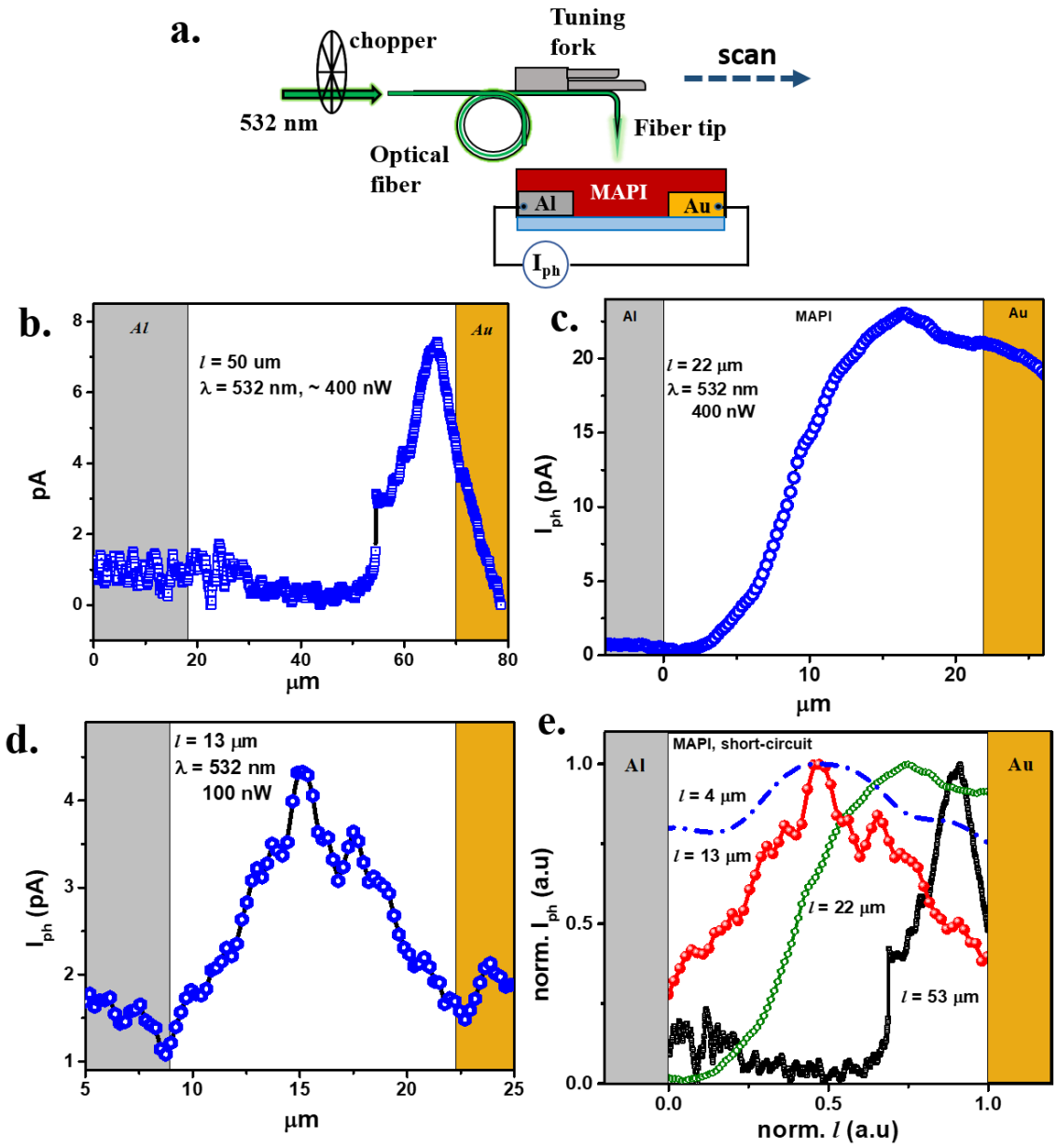

***Figure 3. 11**: **(a)** Schematic of Near-field scanning photocurrent microscopy (NSPM) setup. A tapered fiber-tip in near-field excitation is scanned across the lateral device. **(b)** $I_{ph}(x)$ line scan profiles of the NSPM scans on asymmetric electrodes in short-circuit condition for the inter-electrode channel length of 55 μm **(c)** 22 μm and **(d)** 13 μm. **(e)** Normalized $I_{ph}(x)$ profile as a function of channel length. For the short channel length devices, $I_{ph}(x)$ tends to a uniform distribution profile.*

3.3.6 Bias-dependence

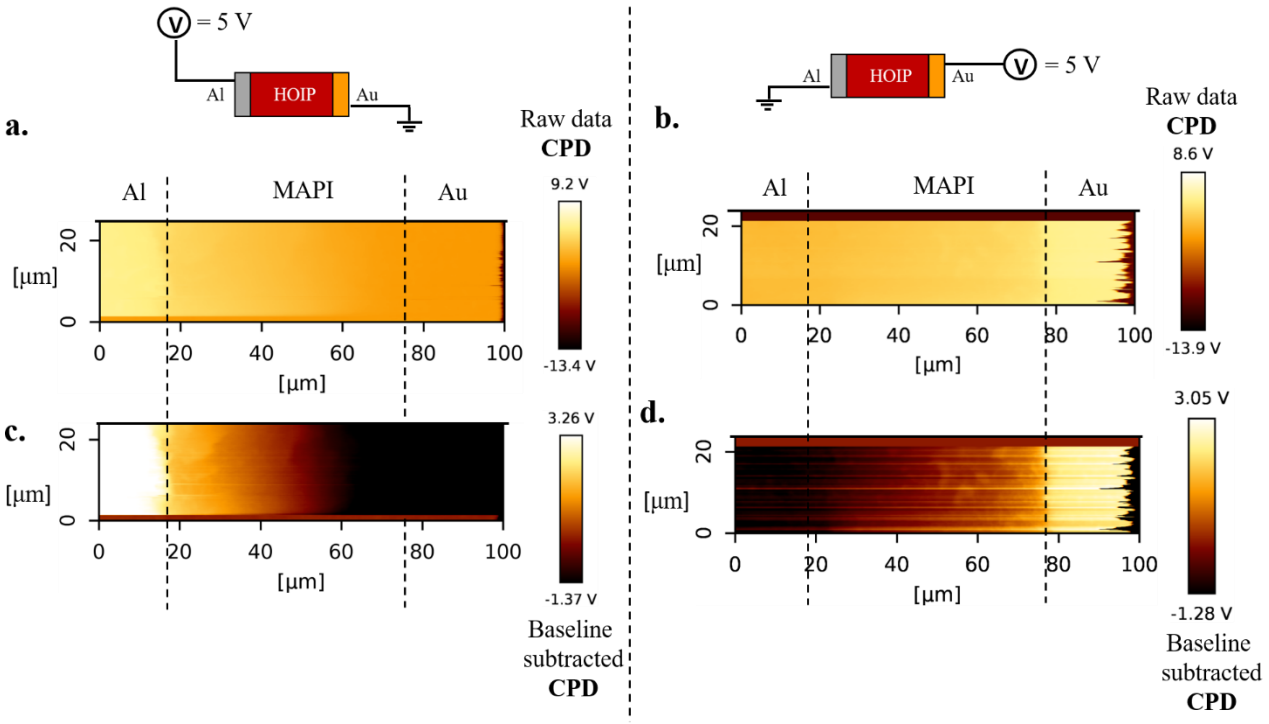

***Figure 3. 12**: 2D surface plots showing the raw data of the CPD for bias-dependent KPFM measurement with **(a)** 5 V applied to the Al and **(b)** 5V applied to Au electrode. **(c)** shows the data for 5 V applied to Al with additional data processing by subtraction of a zeroth-order polynomial baseline to improve the contrast of the image. **(d)** shows the data for 5 V to Au electrode, with similar data processing. However, the raw data is utilized for all the analysis.*

To understand the microscopic transport features in the entire regime of device operation, the potential profiles are mapped in the presence of an applied bias. **Figure 3.12** shows the 2D surface plots of the KPFM scan in the presence of 5 V bias alternatively to Au and Al electrode. The line scan profiles of the raw CPD data given in **Figure 3.13(a)** and **3.13(b)** shows the CPD profile for 5 V applied to the Al and Au electrode respectively. In the presence of 5 V applied to the Au electrode, the net potential difference across the electrodes is observed to be > 5 V, due to the added

contribution of the built-in voltage, i.e., 5 V + V_{bi}. On the other hand, for the case of 5 V to the Au electrode, the net potential difference across the electrodes is < 5 V or 5 V - V_{bi}.

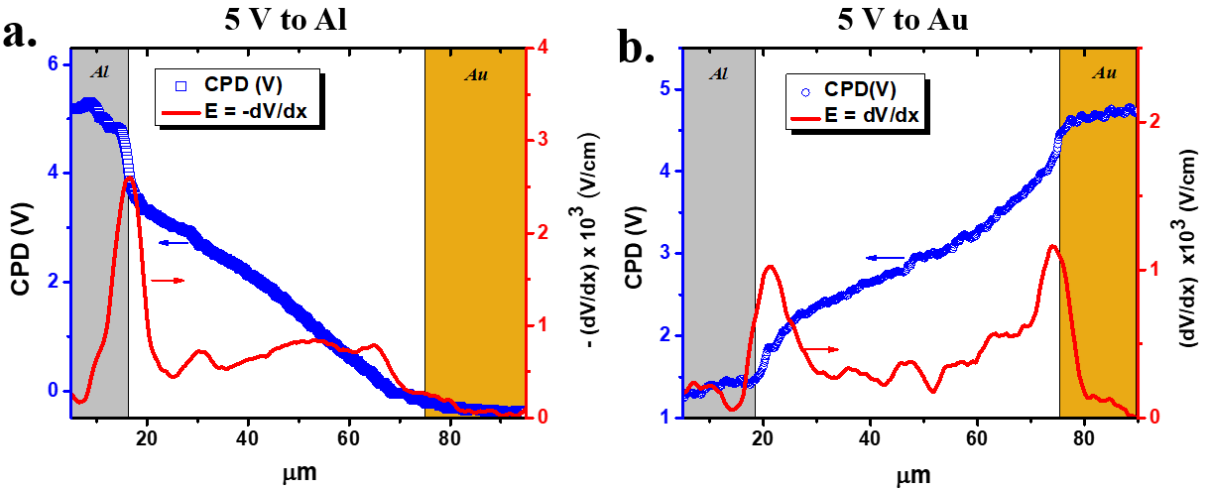

***Figure 3. 13**: Plot of CPD and lateral electric field for asymmetric electrode devices with l = 56 µm for the case of **(a)** -5 V and **(b)** + 5 V. The dominant electric field at the Al-MAPI interface in the negative bias is indicative of the formation of a depletion zone.*

Interestingly, the potential drop across the bulk of the device indicates a gradual reduction, suggesting a constant electric field. Additionally, in case of the negative bias (5 V to Al), we observe a considerable potential drop across the MAPI-Al interface, indicative of a depletion-barrier zone. The reduced dark-J in the reverse bias can be attributed to the inability of hole injection across this barrier. Previous works on lateral devices report dominant ion-migration effects under high electric field over long time scales[28, 29]. In our studies, experimental measurements have been performed under conditions of low electric field (< 10^4 V/cm) and shorter timescales.

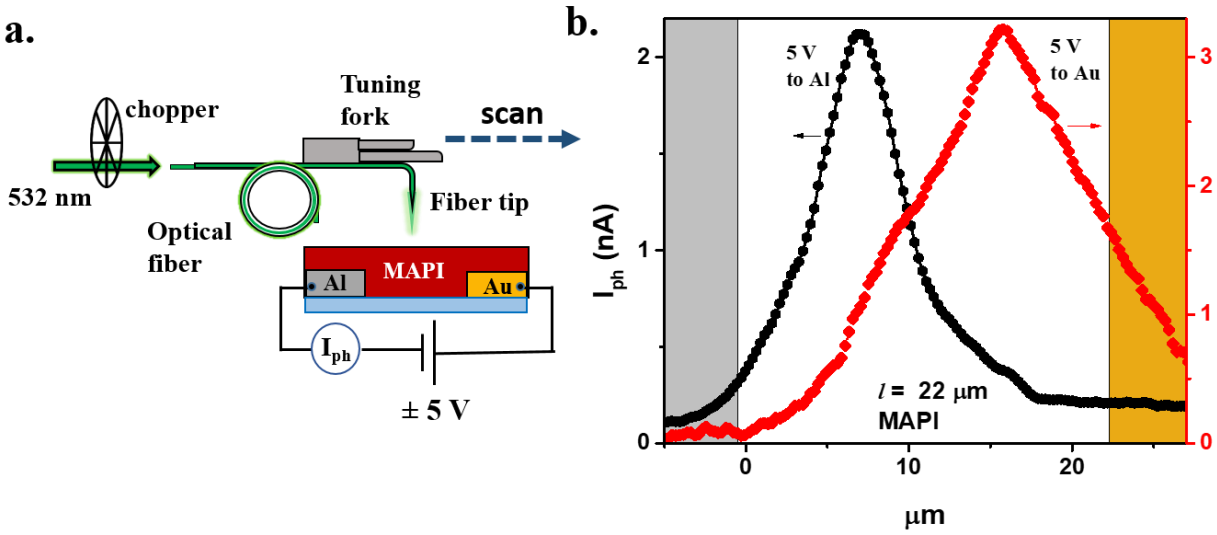

***Figure 3. 14**: **(a)** Schematic of the NSPM experimental setup in the presence of an external bias. **(b)** NSPM scans in the presence of external bias show the presence of an $I_{ph}(x)$ peak which shifts depending on the polarity of the bias. This indicates unbalanced carrier mobility.*

In the presence of an applied bias, the band-bending directionality allows for photo-carrier extraction to the respective electrodes. This photo-carrier extraction efficiency depends on the carrier mobility and the position of excitation from the collection electrode. **Figure 3.14(a)** shows the schematic of the NSPM experiment performed in the presence of an external bias. **Figure 3.14(b)** shows the $I_{ph}(x)$ profile obtained in the presence of 5 V applied alternatively to the Au and the Al electrode. The profile indicates a spatial asymmetry, where the I_{ph}-peak shifts towards the positively biased (or the electron extracting) electrode. This polarity-dependent $I_{ph}(x)$-asymmetry can be attributed to the unbalanced carrier mobility of the hole and the electron. This observation is explained using a simulation where the carrier decay profiles are analyzed as a function of unbalanced mobility.

3.3.7 Drift-Diffusion Formalism

To capture the microscopic picture of the carrier transport that results in the $I_{ph}(x)$ observed in **Figure 3.14(b)**, the transport is modeled based on the solution to the drift-diffusion equation.

$$\frac{\partial \delta n}{\partial t} = D\frac{\partial^2 \delta n}{\partial x^2} + \mu E\frac{\partial \delta n}{\partial x} + G - \frac{\delta n}{\tau} \tag{3.3}$$

The bias-dependent conditions are modeled considering an electric field of ~ 1 kV/cm. In concurrence with scanning photocurrent measurements, a steady-state point generation of photo-carriers is given as $G(x) = G_0\,\delta(x-x_0)$, where x_0 is the point of excitation. Considering 1D transport of carriers and carrier collection away from the point of generation ($x \neq x_0$), **Equation 3.3** reduces to the second-order homogeneous drift-diffusion equation given as:

$$D\frac{\partial^2 \delta n}{\partial x^2} + \mu E\frac{\partial \delta n}{\partial x} - \frac{\delta n}{\tau} = 0 \tag{3.4}$$

Here the initial conditions for the excess carrier concentrations are: $\delta n(x = 0) = \delta n(0) = \alpha G_0 \tau$, and $\delta n(x = \infty) = 0$. The detailed procedure for the solution of this equation is provided in Appendix 1. Additionally, it is noted that the excess electrons drift in the direction opposite to the electric field, $-E$. The excess carrier distribution is given as:

$$\delta n(x) = \delta n_0 \exp\left\{-\left(\frac{\sqrt{\left(\mu^2 E^2 + \frac{4D}{\tau}\right)} - \mu E}{2D}\right)x\right\} \tag{3.5}$$

The spatial profiles generated using the above expression for excess electrons and holes are given in **Figure 3.15(a)**, considering the hole mobility as μ_h = 100 cm^2/Vs,[4] recombination lifetime τ = 10 ns, an electric field, E = 1 kV/cm and a steady-state carrier

generation at x = 0 with a carrier density, δn_0. The electron distribution is simulated for different values of electron mobility, μ_e designated as a fraction of the hole mobility.

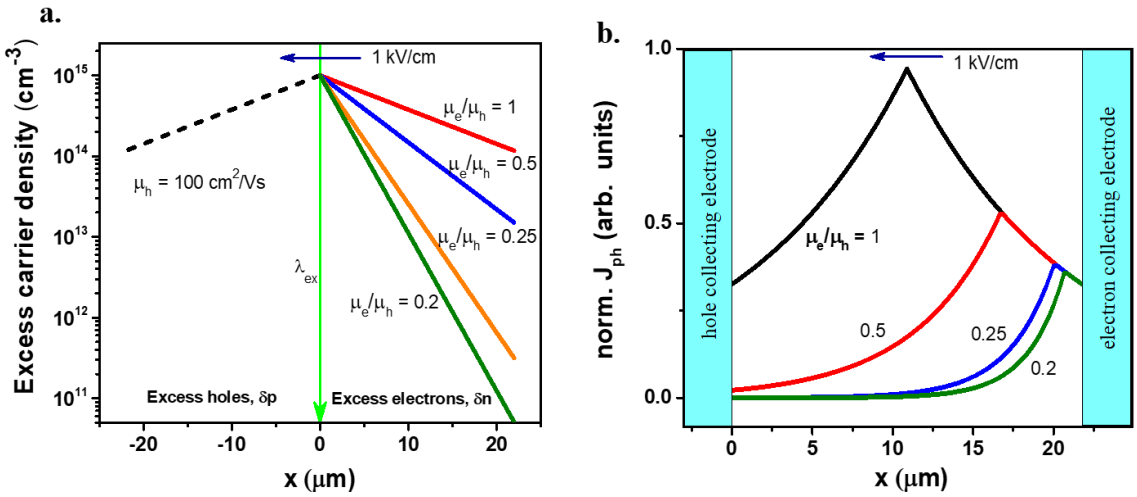

Figure 3. 15: **(a)** *Simulation using the finite element method shows the decay of excess electrons and holes for excitation at x = 0, under conditions of 1-D drift-diffusion transport for different μ_e values.* ***(d)*** *The normalized J_{ph} profiles, simulated as a function of excitation position across the device, under 1 kV/cm electric field. The profiles indicate a shift in the $J_{ph}(x)$ peak in the case of unbalanced carrier mobility, which explains the feature observed in* ***(b)****.*

The directionality of hole and electron decay profiles suggests that holes drift in the direction of the electric field, and the electrons drift and decay in the direction opposite to the electric field. As indicated in the electron distribution profiles, the spatial distribution indicates a longer decay length in the case of high μ_e. To simulate the NSPM experiment, the photocurrent due to carrier drift and diffusion is given as:

$$J_{ph}(x) = J_{drift} + J_{diffusion} = \delta n.\, e\mu E + eD\frac{\partial\, \delta n}{\partial x} \qquad (3.6)$$

The net photocurrent is considered to be equivalent to the excess carriers recombined in the external circuit. The spatial profile of externally recombined carriers is simulated, as shown in **Figure 3.15(b)** as a function of excitation position, for different ratios of

carrier mobilities. For the case of balanced mobility ($\mu_h = \mu_e$), the carriers that contribute to the I_{ph} (which is proportional to externally recombined carriers) is maximum for photo-excitation at the device center. In the case of unbalanced carrier mobility ($\mu e < \mu_h$), the I_{ph} peak shifts towards the electron-extracting electrode.

The results presented in **Figure 3.15** only shows the effect of unbalanced mobility on the $I_{ph}(x)$ profiles. Additionally, **Equation 3.5** indicates that the carrier lifetime (τ) also affects the distribution profile. Overall it is concluded that the asymmetry of the $I_{ph}(x)$, observed in **Figure 3.14(b)** points to the lower $\mu\tau$ product for the electrons ($\mu_e\tau_e < \mu_h\tau_h$). This conclusion is consistent with previous reports.[4, 30]

3.3.8 Photo-detector characteristics.

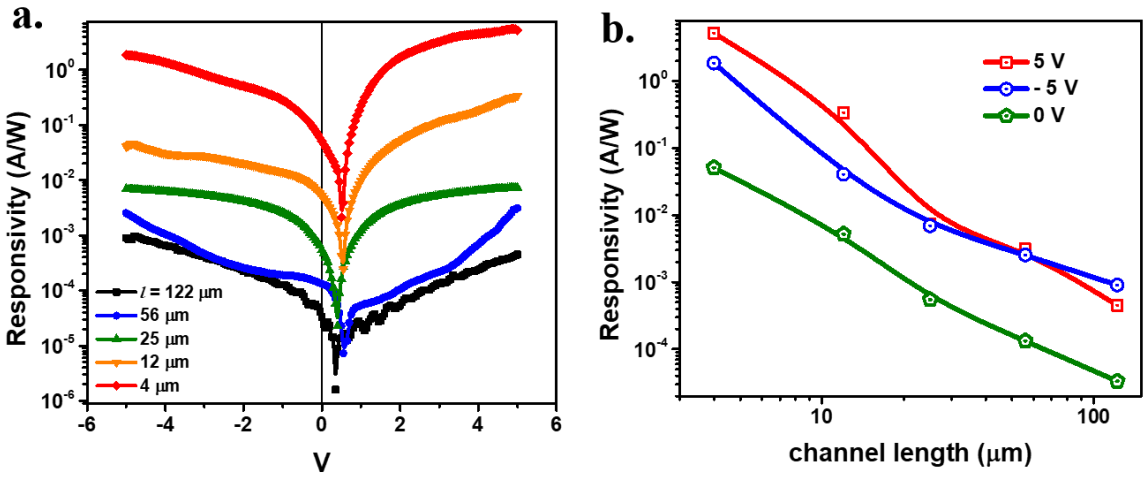

***Figure 3. 16**: **(a)** Voltage-dependent responsivity characteristics of the lateral devices for 532 nm illumination at 26 mW/cm^2. A short circuit I_{ph} is observed at 0 V. **(b)** Variation of the responsivity as a function of channel length under short circuit conditions and ± 5 V bias conditions.*

The light-dependent J-V characteristics on lateral MSM devices are shown in **Figure 3.16(a)**. The I_{ph} increases for the short-channel devices due to a higher electric field at a particular voltage. It can also be seen that a short-circuit I_{ph} is observed corresponding

to V = 0 (indicated in the vertical line). The directionality of the I_{ph} confirms the electron extraction to the Al electrode and holes to the Au electrode. **Figure 3.16(b)** shows the variation of the device responsivity with respect to the channel length. These devices exhibit a high responsivity of ~ 51 mA/W in the self-powered mode, and ~ 5.2 A/W under 5 V operational bias, for the l = 4 μm channel length. This corresponds to quantum efficiency, $QE = \frac{n_{carriers}}{n_{photons}} = \frac{R}{\lambda} \times 1240\ (W.nm/A)$ of 11.9 % and 1,212 % at 0 V and 5 V, respectively. The gain (I_{ph}/I_{dark}) observed in these devices is in the order of ~ 10^2, as shown in **Figure 3.17**. This device performance compares with lateral photo-detectors reported in the literature [6, 31, 32].

The high quantum efficiency of the device > 100% can be explained as a result of the difference in the transit timescales associated with the photogenerated holes and electrons. During the transport process of the photo-carrier, if one of the carriers (usually the minority carrier) either transits slowly or gets trapped, the counter carrier is collected at a faster rate at the opposite electrode. In order to preserve charge neutrality in the device, an excess of the majority counter carrier is injected into the device. This circulation of the majority carrier happens many times until the minority carrier is collected at the other end of the device. Thus one photon results in the circulation of more than one majority carrier in the external circuit resulting in over 100% quantum efficiency. This happens in the presence of an external power source and not under short-circuit conditions. Microscopically, the photo-responsive gain of a detector is inversely proportional to the carrier transit time. In the presence of an external bias, the carrier transit time reduces, resulting in higher quantum efficiency.

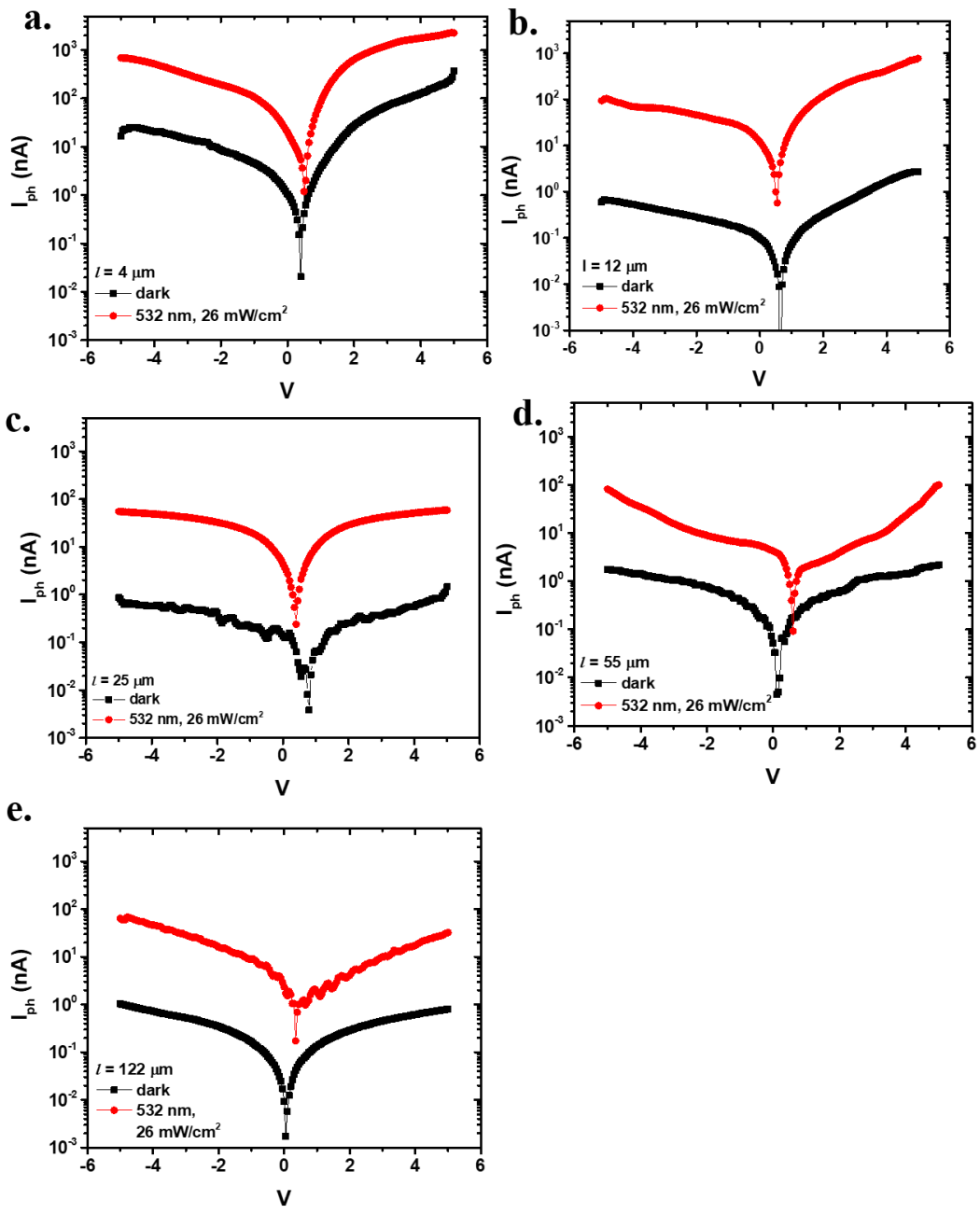

***Figure 3. 17**: Comparison of the dark and light (532 nm, 26 mW/cm^2) for channel lengths of **(a)** 4 μm, **(b)** 12 μm, **(c)** 25 μm, **(d)** 55 μm and **(e)** 122 μm.*

The lateral devices are characterized by low device capacitance owing to the tiny overlap area across the two metal electrodes. This results in a lower RC lifetime of the device, which reduces the overall response time of the device[33]. For example, device capacitance in the range of few ~ pF was observed for the lateral devices, which are

lower in comparison to typical sandwich structures (typically ~ 10 nF was observed for a 5 mm^2 active area). Photocurrent decay measurements on perovskite-based MSM devices have reported operational speeds in the range of ~ 40-90 ns. [34] Additionally, transient photocurrent on these devices reveals a fast decay component of ~ 12 ns, as shown in **Figure 3.18(a)**, with mixed-phase perovskite: $(FA_{0.82}MA_{0.18}Pb(I_{0.82}Br_{0.18})_3)$ (FA = Formamidium) as the active semiconductor. Such fast-response times allow for applications involving high-speed detectors.

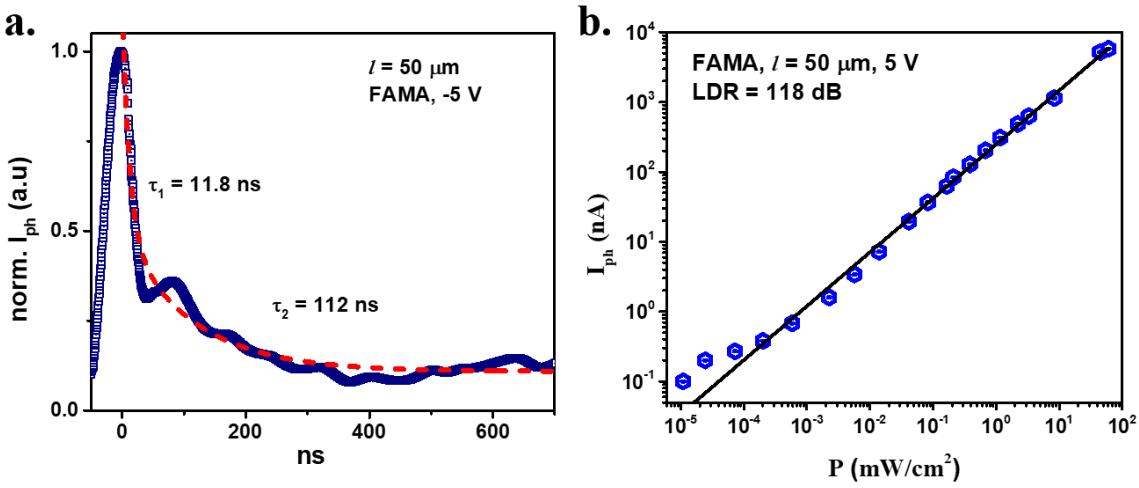

***Figure 3. 18**: **(a)** Transient photocurrent measurement on lateral MSM devices with mixed-phase perovskite (FAMA) as the active layer. The bi-exponential fit reveals a fast response time of 11.8 ns followed by a slow component of ~ 100 ns. **(b)** Variation of photocurrent with respect to light-intensity (λ = 532nm), shows the LDR ~ 118 dB, spanning up to 6 orders of intensity variation.*

The lateral device structure is characterized by low dark current in comparison to the widely used sandwich architecture. Dark currents of < 1 mA at 1 V bias (considering l ≈ 10 μm) were observed in lateral devices. This is lower when compared to sandwich devices, where a higher dark current ~ 10 mA/cm^2 (at 1 V bias) was observed. This feature of the lateral structures reduces the noise level of device operation and allows

for low signal detection, increasing the dynamic range in these devices. **Figure 3.18(b)** shows the linear dynamic range (LDR) of the lateral device with the mixed-phase perovskite ($FA_{0.82}MA_{0.18}Pb(I_{0.82}Br_{0.18})_3$) in the active layer. The device maintains linear response over a range spanning ~ 6 orders of intensity variation, resulting in a $LDR = 20\log\left(\frac{P_{max}}{P_{min}}\right)$, of 118 dB, where P_{max} and P_{min} correspond to the maximum and minimum light power, respectively, that is resolved with maintained responsivity.

3.4 Conclusion

The lateral asymmetric electrode MSM devices of $MAPbI_3$ exhibit distinct transport regimes as a function of both applied bias and inter-electrode distance. The transport shows ohmic behavior at low voltages and becomes space charge limited at high voltage, in short channel length devices, consistent with the SCLC scaling relation. The observed rectification-like J(V) characteristic is attributed to bias-direction dependent SCLC behavior, as a consequence of efficient hole injection across the Au-MAPI interface. These devices exhibit hysteresis behavior upon performing voltage sweeps in both directions. Also, a slight variation was seen in the SCLC threshold voltage is observed when compared across various devices. However, the rectification-like characteristics and the SCLC behavior are consistently observed in the short-channel asymmetric electrode devices.

The KPFM plots across the device indicate the presence of an electric field in the bulk, both in short-circuit and bias conditions, suggesting negligible ion-screening effects. In the presence of an applied bias, the spatial photocurrent profiles were understood in the context of drift-recombination formalism, which indicates unbalanced carrier transport. In terms of device application, the light response of the lateral devices demonstrates a high responsivity of ~ 5.2 A/W at 5 V operating bias in the short-channel structures.

The low device capacitance enables these devices for high-speed applications (up to ~GHz) in addition to the superior linear dynamic range of operation.

References

1. Chen Z, *et al.* Thin single crystal perovskite solar cells to harvest below-bandgap light absorption. *Nature communications* **8**, 1-7 (2017).
2. Chen Y, *et al.* Extended carrier lifetimes and diffusion in hybrid perovskites revealed by Hall effect and photoconductivity measurements. *Nature communications* **7**, 1-9 (2016).
3. Stranks SD, *et al.* Electron-hole diffusion lengths exceeding 1 micrometer in an organometal trihalide perovskite absorber. *Science* **342**, 341-344 (2013).
4. Dong Q, *et al.* Electron-hole diffusion lengths> 175 μm in solution-grown CH3NH3PbI3 single crystals. *Science* **347**, 967-970 (2015).
5. Yang SJ, *et al.* Visualization and Investigation of Charge Transport in Mixed-Halide Perovskite via Lateral-Structured Photovoltaic Devices. *Advanced Functional Materials* **28**, 1804067 (2018).
6. Ding J, *et al.* High-quality inorganic–organic perovskite CH 3 NH 3 PbI 3 single crystals for photo-detector applications. *Journal of Materials Science* **52**, 276-284 (2017).
7. Lin X, *et al.* Dipole-field-assisted charge extraction in metal-perovskite-metal back-contact solar cells. *Nature communications* **8**, 1-8 (2017).
8. Duijnstee EA, Ball JM, Le Corre VM, Koster LJA, Snaith HJ, Lim J. Toward understanding space-charge limited current measurements on metal halide perovskites. *ACS Energy Letters* **5**, 376-384 (2020).
9. Alvar MS, Blom PW, Wetzelaer G-JA. Space-charge-limited electron and hole currents in hybrid organic-inorganic perovskites. *Nature communications* **11**, 1-9 (2020).
10. Georgiadou DG, *et al.* 100 GHz zinc oxide Schottky diodes processed from solution on a wafer scale. *Nature Electronics* **3**, 718-725 (2020).
11. Sakai N, *et al.* Controlling Nucleation and Growth of Metal Halide Perovskite Thin Films for High-Efficiency Perovskite Solar Cells. *Small* **13**, 1602808 (2017).
12. Mahesh S, *et al.* Revealing the origin of voltage loss in mixed-halide perovskite solar cells. *Energy & Environmental Science* **13**, 258-267 (2020).
13. Mukhopadhyay S, Ramachandra S, Narayan K. Direct observation of charge generating regions and transport pathways in bulk heterojunction solar cells with asymmetric electrodes using near field photocurrent microscopy. *The Journal of Physical Chemistry C* **115**, 17184-17189 (2011).
14. Mukhopadhyay S, Das AJ, Narayan K. High-resolution photocurrent imaging of bulk heterojunction solar cells. *The journal of physical chemistry letters* **4**, 161-169 (2013).
15. Zhang M, Zhang X, Huang L-Y, Lin H-Q, Lu G. Charge transport in hybrid halide perovskites. *Physical Review B* **96**, 195203 (2017).
16. Petrovic M, Ye T, Chellappan V, Ramakrishna S. Effect of low temperature on charge transport in operational planar and mesoporous perovskite solar cells. *ACS applied materials & interfaces* **9**, 42769-42778 (2017).
17. Li D, *et al.* Size-dependent phase transition in methylammonium lead iodide perovskite microplate crystals. *Nature communications* **7**, 1-8 (2016).
18. Chin XY, Cortecchia D, Yin J, Bruno A, Soci C. Lead iodide perovskite light-emitting field-effect transistor. *Nature communications* **6**, 1-9 (2015).
19. Senanayak SP, *et al.* Understanding charge transport in lead iodide perovskite thin-film field-effect transistors. *Science advances* **3**, e1601935 (2017).

20. Harwell JR, *et al.* Probing the energy levels of perovskite solar cells via Kelvin probe and UV ambient pressure photoemission spectroscopy. *Physical Chemistry Chemical Physics* **18**, 19738-19745 (2016).
21. Zhou Y, Long G. Low density of conduction and valence band states contribute to the high open-circuit voltage in perovskite solar cells. *The Journal of Physical Chemistry C* **121**, 1455-1462 (2017).
22. Snaith HJ, *et al.* Anomalous hysteresis in perovskite solar cells. *The journal of physical chemistry letters* **5**, 1511-1515 (2014).
23. Tress W. Metal Halide Perovskites as Mixed Electronic–Ionic Conductors: Challenges and Opportunities□ From Hysteresis to Memristivity. *The journal of physical chemistry letters* **8**, 3106-3114 (2017).
24. Weber SA, *et al.* How the formation of interfacial charge causes hysteresis in perovskite solar cells. *Energy & Environmental Science* **11**, 2404-2413 (2018).
25. Wang H, Guerrero A, Bou A, Al-Mayouf AM, Bisquert J. Kinetic and material properties of interfaces governing slow response and long timescale phenomena in perovskite solar cells. *Energy & Environmental Science* **12**, 2054-2079 (2019).
26. McNeill CR, Frohne H, Holdsworth JL, Furst JE, King BV, Dastoor PC. Direct photocurrent mapping of organic solar cells using a near-field scanning optical microscope. *Nano Letters* **4**, 219-223 (2004).
27. Rao M, Narayan K. Evaluation of electrode-semiconductor barrier in transparent top-contact polymer field effect transistors. *Applied Physics Letters* **92**, 201 (2008).
28. Liu F, *et al.* 2D Ruddlesden–Popper Perovskite Single Crystal Field-Effect Transistors. *Advanced Functional Materials* **31**, 2005662 (2021).
29. Yuan Y, *et al.* Photovoltaic switching mechanism in lateral structure hybrid perovskite solar cells. *Advanced Energy Materials* **5**, 1500615 (2015).
30. Semonin OE, *et al.* Limits of carrier diffusion in n-type and p-type CH3NH3PbI3 perovskite single crystals. *The journal of physical chemistry letters* **7**, 3510-3518 (2016).
31. Liu Y, *et al.* A 1300 mm2 ultrahigh-performance digital imaging assembly using high-quality perovskite single crystals. *Advanced Materials* **30**, 1707314 (2018).
32. Yang B, *et al.* Ultrasensitive and fast all-inorganic perovskite-based photodetector via fast carrier diffusion. *Advanced Materials* **29**, 1703758 (2017).
33. Armin A, Hambsch M, Kim IK, Burn PL, Meredith P, Namdas EB. Thick junction broadband organic photodiodes. *Laser & Photonics Reviews* **8**, 924-932 (2014).
34. Liang FX, Wang JZ, Zhang ZX, Wang YY, Gao Y, Luo LB. Broadband, ultrafast, self-driven photodetector based on Cs-doped FAPbI3 perovskite thin film. *Advanced Optical Materials* **5**, 1700654 (2017).

Chapter 4: 2-Dimensional Position-Sensitive Hybrid Perovskite based Detector

4.1 Introduction

Over the past decade, optoelectronics applications utilizing hybrid organic-inorganic perovskites (HOIP) have gained enormous momentum. Apart from solar cells, numerous other applications such as LEDs[1], transistors[2], X-ray imagers[3], and neuromorphic devices[4] have been realized using hybrid perovskite as the active semi-conductor. The possibility of obtaining large-area high-quality films with suitable additives and treatments has further opened the range of applications such as light-position sensing detectors[5].

In an earlier report from our laboratory, 1-Dimensional (1-D) position-sensitive detector (PSD) has been fabricated and demonstrated, with HOIP as the active semiconductor[6, 7], schematic of which is shown in **Figure 4.1(a).** This 3-terminal device consists of a common ITO back electrode onto which the perovskite is coated followed by a charge transfer layer and top gold (Au) electrode-arms which serve as the boundary of the active channel. In these device structures, the differential photo-signal, ΔV_{ph} generated in the device as a function of excitation position was observed to have a linear dependence, a feature utilized for position determination.

The working principle of the 1D-PSD device is depicted **Figure 4.1(b)**. Upon photo-excitation at a point x, the charge selective Schottky barrier facilitates carrier extraction to the ITO electrode, locally forward biasing the device at the point of excitation. The

extracted photo-generated carriers are then distributed onto the equipotential ITO electrode, leaving the counter carriers in the bulk perovskite layer. This asymmetric distribution of carriers results in a lateral photo-voltage (LPV) which has linear spatial dependence, as elucidated by Schottky[8] and was initially implemented by Wallmark and others[9-12]. The enhanced optoelectronic properties such as high mobility in HOIP based PSDs allow for superior performance, with spatial sensitivity comparable to commercially available PSDs[7, 13]. These PSDs exhibit higher sensitivity in comparison with semiconducting polymers, and the ease of depositing on flexible substrates[14] find use in a variety of opto-electromechanical applications such as robotics, charged-particle detection, triangulation, imaging, displacement and vibration measurements[15-19].

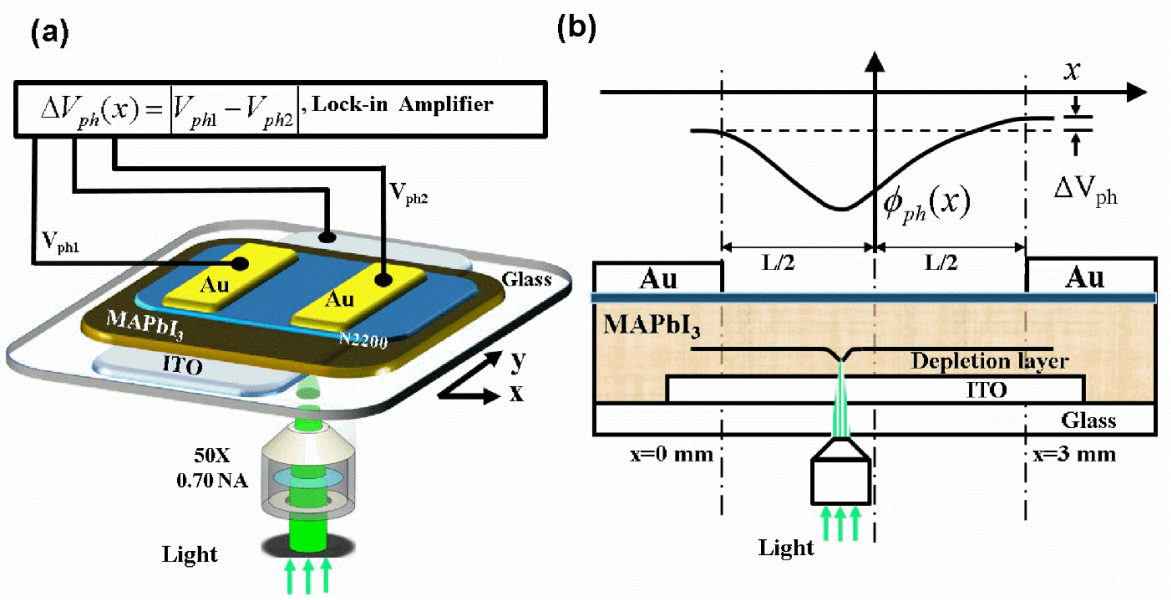

***Figure 4. 1**: **(a)** Schematic of lateral photo signal measurement setup in bottom illumination mode. Sample mounted on an x-y stage is controlled at micron-scale precision. **(b)** Schematic of the PSD device and potential distribution as a result of non-uniform illumination in the active area of PSD. (Reprinted with permission from Ashar, A. Z., Ganesh, N., & Narayan, K. S. (2018). Hybrid Perovskite-Based Position-*

Sensitive Detectors. Advanced Electronic Materials, 4(2), 1700362. Copyright (2018) with John Wiley and Sons, Inc)

The work presented in this chapter reports the first instance of position detection in 2-dimensions (2D), i.e., in the x and y-axis, utilizing HOIP as the active layer. The crucial pre-requite for large area devices requires uniform, smooth and pin-hole free films. Perovskite coating using single-step method invariably results in films with pin-holes. Introduction of additives improves crystallization kinetics, resulting in pin-hole free large area films, useful for applications such as large area PSDs[5, 20]. Extending the position-detection functionality in 2D allows for numerous applications such as optical tracking, charge particle detection, and quadrant detectors[21]. Incorporating serial detection of excitation position, dynamic imaging of a light beam trajectory is demonstrated. [22] In addition to steady-state photo-signal (V_{ph}) mapping, fast transient photocurrent lifetimes (~ 1 µs) in response to single-pulse excitation can be utilized for light trajectory imaging at the rate of ~ 1 MHz. Interestingly, the spatial dependence of the transient lifetimes (τ) reveals a proportional increase of τ with respect to the transport length of the carrier. These trends are analyzed with the help of complementary impedance spectroscopy (IS) results and circuit modeling, and the nature of carrier transport was interpreted to be dominantly resistive.

4.2 Experimental Details

4.2.1 Materials

Conducting transparent electrode, ITO (indium tin oxide) coated glass substrates (R_s = 8 Ωcm) were purchased from Xin Yan Technology Limited, China. For the perovskite precursors, Lead(II) bromide ($PbBr_2$, 98%, 367 g/mol), Formamidium iodide (FAI, 99 %, 171.97 g/mol), Cesium iodide (CsI, 99.9 %, 259.81g/mol) were obtained from

Sigma Aldrich. Solvents N,N-Dimethylformamide (DMF, anhydrous 98.9%, 73.09 g/mol), Dimethylsulfoxide (DMSO, anhydrous, 78.13 g/mol), and Chlorobenzene (anhydrous, 99.8 %) were obtained from Sigma Aldrich. Lead(II) iodide (PbI_2, 99.9985 %,) was obtained from Alfa Aesar. Hole transporter, poly(N,N'-bis-4-butylphenyl-N,N'-bisphenyl)benzidine (Poly-TPD) and electron transporter, phenyl-C71-butyric acid methyl ester ($PC_{71}BM$) were obtained from Luminescence Technology Corporation, Taiwan. Additionally, (Poly(3,4-ethylenedioxythiophene)-poly(styrenesulfonate)) PEDOT:PSS (Al 4083) was obtained from Ossila.

4.2.2 Sample Preparation

Preparation of $FACsPb(IBr)_3$ precursor:

The $FA_{0.83}Cs_{0.17}Pb(I_{0.90}Br_{0.10})_3$ films were prepared by adding 64.0 mg CsI, 80.0 mg $PbBr_2$, 207.0 mg FAI, and 568.0 mg PbI_2 to 1 mL solution (4:1 ratio of DMF:DMSO). The precursor solution was stirred for 15 min at 70 ℃ prior to use.

Substrate cleaning

ITO substrates were cleaned using wet cleaning procedure as described below,

I. 5 min Sonication in surfactant and de-ionized water at 50 ºC.
II. Rinsed and sonicated in de-ionized water for 10 min.
III. Rinsed and sonicated in acetone for 5 min.
IV. Rinsed and sonicated in isopropyl alcohol for 5 min
V. RCA treatment (5:1:1 ratio of DI water: ammonium solution (25 wt%): hydrogen peroxide) on the substrates for 20 min at 120 °C.
VI. Blow-dried using compressed air and treated in air plasma for 4 min.

Fabrication of PSD devices.

Deposition of mixed-phase perovskite on ITO substrates were prepared by Prof. Henry Snaith's group at University of Oxford, Oxford, UK; using the following procedure:

Spin coating was carried out in a dry box (purged with compressed dry air), with relative humidity below 20%. 35 µL of precursor solution was spread onto the substrates and then spin-coated at 6,000 rpm (2,000 rpm/s ramp) for 35 seconds. The films were "solvent quenched" with 100 µL of anisole, which was quickly dispensed when 10 seconds remained in the spin coating program. The films were then annealed at 100 ℃ for 15 minutes.

The perovskite coated substrates were shipped to our laboratory. The shipment was packed and maintained under inert conditions during the shipping process.

This was followed by spin-coating a thin layer of Poly(N,N'-bis-4-butylphenyl-N,N'-bisphenyl)benzidine (PolyTPD, Lumtec. Corp.), ~ 3 mg/ml in chlorobenzene, at 2000 rpm for 60 s and annealing at 90 °C for 20 min. The four top gold electrodes (~ 50 nm thickness) were then evaporation-deposited using shadow masks.

For the fabrication of inverted devices, a thin layer of PEDOT:PSS (Ossilla, Al-4083) was spin-coated at 3500 rpm for 80 s followed by annealing at 120 °C for 60 min. After the deposition of the perovskite layer, a 15 mg/ml solution of (6,6)-Phenyl C71 butyric acid methyl ester (PCBM, Lumtec Corp.) in chlorobenzene (Sigma Aldrich) was spin-coated at 2000 rpm for 60 s and annealed at 100 °C for 20 min. This was followed by thermal deposition of Ag electrodes using suitable shadow masks.

4.2.3 Measurements and Characterization

X-Ray Diffraction

XRD patterns on thin film samples were obtained with a Panalytical X'Pert Pro X-Ray diffractometer with a Cu k-alpha source (λ 1.54 Å).

Optical Characterization

The optical characterization were carried out on mixed-phase perovskite films.Absorption spectra were collected with a Varian Cary 1050 UV Vis spectrophotometer. Steady state photoluminescence was measured using a Horiba Fluorolog-3 with an InGaAs detector.

Scanning Elelctron Microscopy (SEM)

Thin film perovskite samples were imaged with the secondary electron detector in an FEI Quanta 600 FEG scanning electron microscope under an acceleration voltage of 5 kV.

***Photo-voltage Scanning*:**

The schematic of the photo-voltage scanning setup is given in **Figure 4.2**. A focused modulated laser light (532 nm) is incident from the ITO side of the device. Two sets of differential photo-voltage (opposite arms of the PSD constitute one pair) were measured and recorded with respect to the illumination position, as the sample translates in x and y-axis. Lock-in amplifiers (SRS 830) were used in differential voltage mode at high input impedance coupling (10 MΩ, 25 pF). The 2D photo-voltage mapping was obtained using GPIB-USB interfaced program.

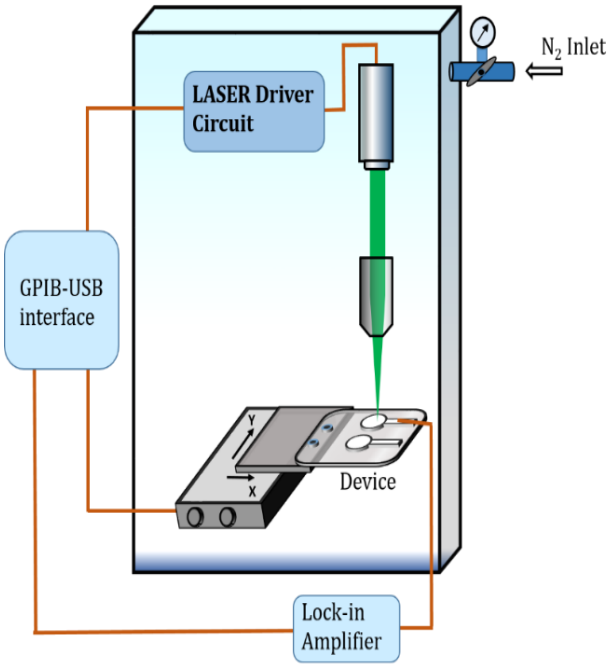

Figure 4. 2*: Schematic of the photo-voltage scanning setup. A narrow laser beam is incident on the sample which translates in the x and y direction. The photo-voltage is mapped to the position of illumination.*

Transient Photocurrent:

Transient Photocurrent experiment was carried out using a 532 nm pulsed laser source (ELFORLIGHT, SPOT 40-532), 1µJ/pulse, 1 ns pulse width, 1 kHz repetition rate. The focused light beam was incident on the device from the ITO side. As the device translates, the photocurrent is measured simultaneously. Photocurrent measurements were done in short-circuit condition across the Au-ITO electrodes. An Oscilloscope (Tektronix MDO3024, 2.5 GS/s) was used to sample the transient data with 50 Ω input impedance coupling in synchronization with the laser trigger.

Impedance Spectroscopy:

The impedance measurements were carried out using a Parameter Analyzer system (Keithley 4200-SCS). Both ends of the device (Au-ITO) were used as the electrical

contacts for the impedance measurements. Prior to measurements, impedance compensation were checked to reduce error in the high-frequency measurements. The obtained bode plots and Cole-cole plots were fit to the equivalent circuit (single parallel R-C with a series resistance) using impedance modelling software, ZView (Scribner Associates).

4.3 Results and Discussion

4.3.1 Characterization of perovskite films

The fabrication of large area PSDs require that the perovskite films maintain uniformity across the device active area. This crucial prerequisite of sizable area (~ cm^2) of uniform, pinhole-free films of mixed cation perovskite as the active layer was obtained using established methods[20, 23]. The film thickness was probed and was consistent across the large area (Details of thickness uniformity presented in Appendix 4). To characterize the perovskite films, the mixed-phase perovskite $FA_{0.83}Cs_{0.17}Pb(I_{0.9}Br_{0.1})_3$ (FA = Formamidium) was deposited on quartz slides. The uniformity of film formation is evident in the SEM image shown in **Figure 4.3(a)**. These films also shows good crystalline order which is reflected in the sharp XRD peaks in **Figure 4.3(b)**. The absorption profile and the PL data shown in **Figure 4.3(c)** reveal an absorption edge corresponding to ~1.5 eV. In mixed cation perovskites, the addition of small amounts of CsBr into the $FAPbI_3$ lattice renders the efficient transition to the photoactive α-phase[24, 25]. In comparison to the prototypical $MAPbI_3$ (MA = Methylammonium) perovskite, the mixed cation perovskites display increased stability and better tolerance to degradation factors such as oxygen and moisture[20].

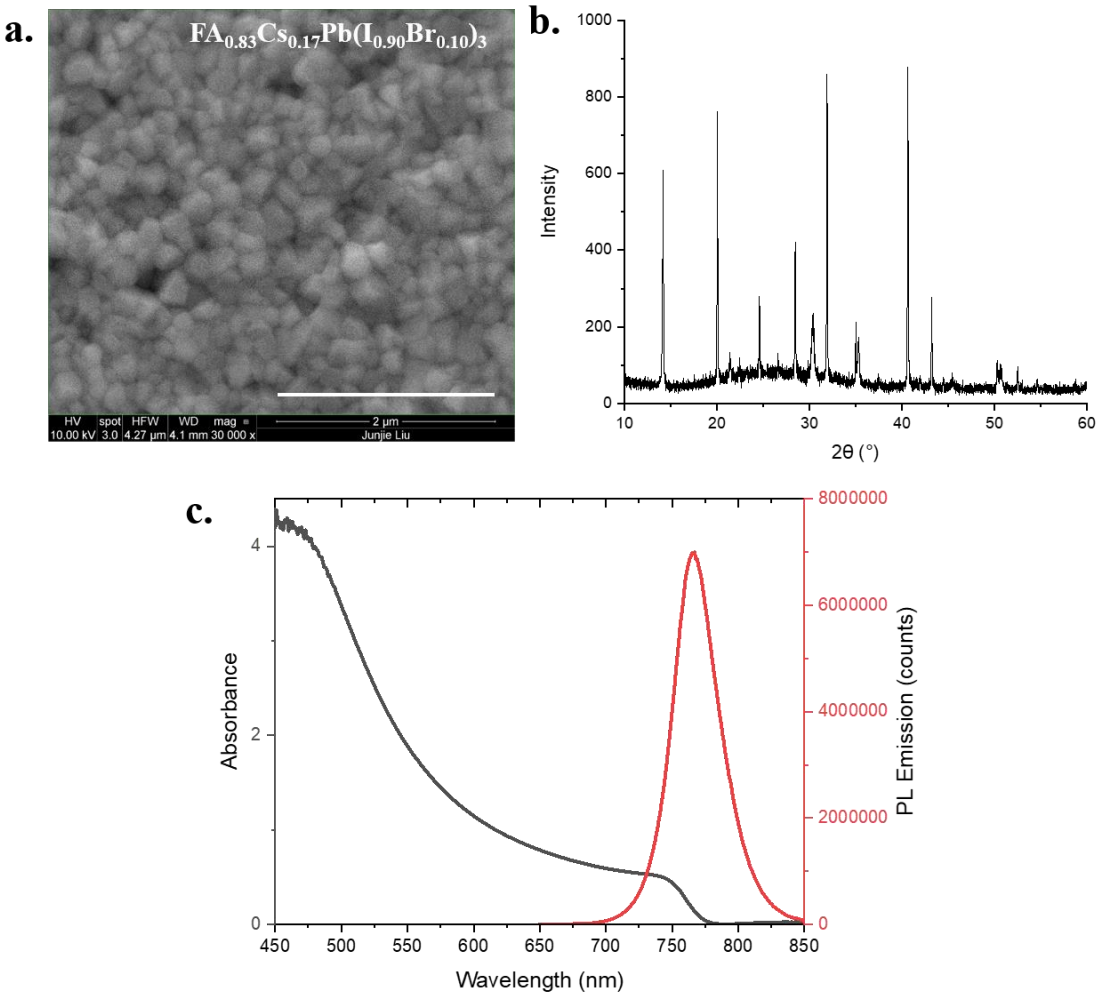

***Figure 4. 3**: **(a)** SEM image shows uniform grains over a large area on the spin coated $FA_{0.83}Cs_{0.17}Pb(I_{0.9}Br_{0.1})_3$films. The scale bar indicates 2 µm. **(b)** XRD data on $FA_{0.83}Cs_{0.17}Pb(I_{0.9}Br_{0.1})_3$ films. **(c)** Absorption and PL on these mixed-phase perovskite films.*

4.3.2 Device structure for 2-D Position Detection

The 2D PSD device is a 5- terminal device as shown in **Figure 4.4(a)** and consists of a common back Indium Tin Oxide (ITO) electrode onto which the semiconducting perovskite epi-layer was deposited. This was followed by the deposition of a hole transporting layer (Poly-TPD), for efficient charge transfer to the top four Au line-electrodes.

The Schottky barrier at the ITO-HOIP interface is utilized to generate the lateral photo-voltage (V_{ph})[26, 27]. **Figure 4.4(b)** shows the band alignment and energetics at the ITO-HOIP interface. The nature of the Schottky barrier at this interface allows for electron extraction across the interface to the back contact ITO-electrode. This is indicated in the I-V measurements across the Au-ITO electrodes (**Figure 4.4(c))** in dark and upon illumination, which shows a negative polarity of the photo-current (I_{ph}) in short-circuit. The PSD working principle in the current device is depicted in **Figure 4.4(d)**. Upon photo-excitation at a point x, the Schottky barrier facilitates electron extraction to the ITO electrode, leaving the counter carriers (holes) in the bulk perovskite layer. This asymmetric distribution of carriers results in a lateral photo-voltage (LPV). Our study of 2D-PSD operation was conducted employing spatial photo-voltage (V_{ph}) mapping of the devices at zero bias. Essentially, a modulated light beam (FWHM ~ 3 μm) is incident on the device, as it translates in the X and Y direction. In synchronization with the device translation, the differential photo-signal (ΔV_{ph}) is measured and recorded using a dual-port lock-in amplifier (SR830, 10 MΩ, 25 pF input impedance).

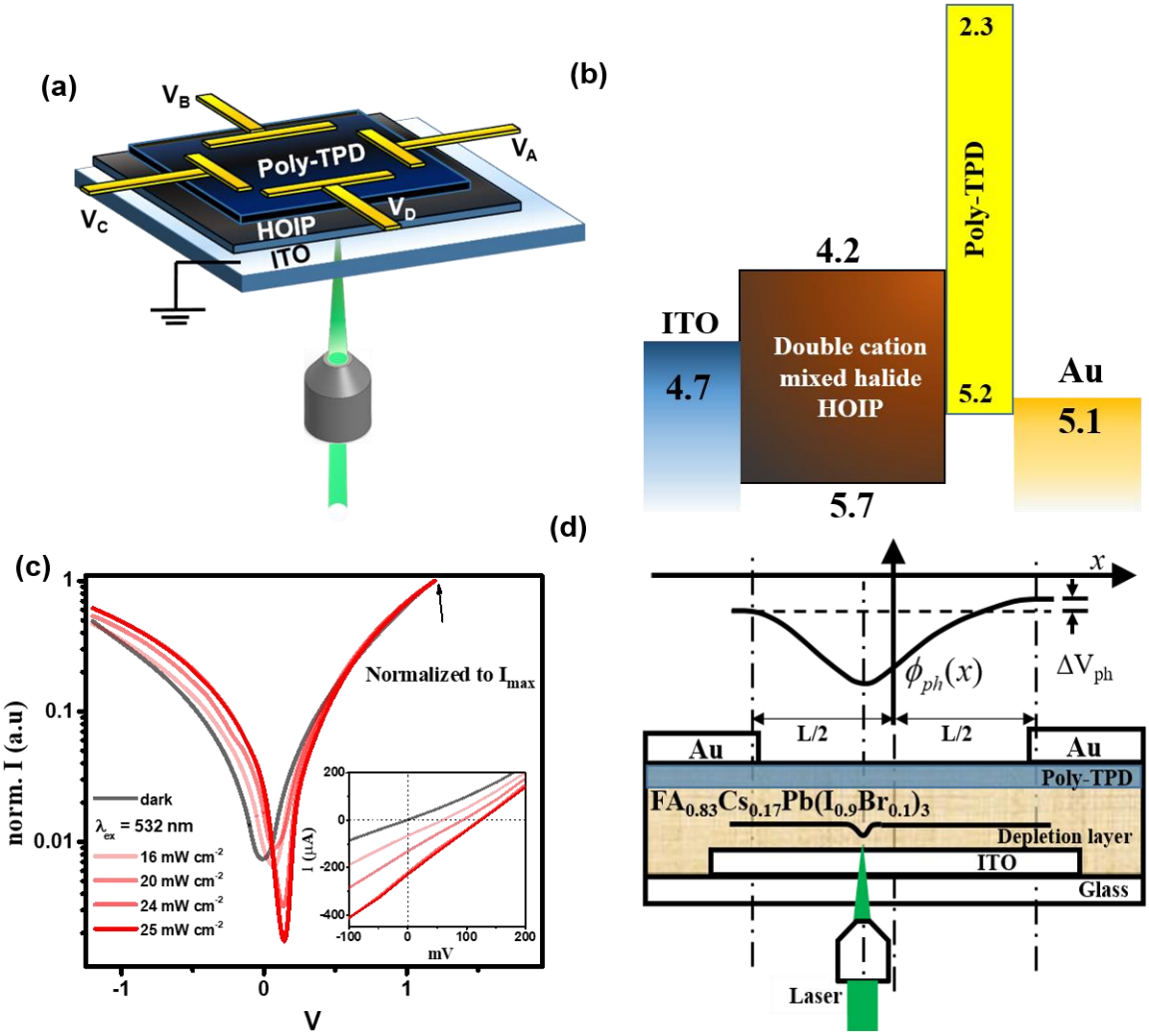

***Figure 4. 4**: **(a)** Schematic of the device structure of a 2D-PSD. Intensity-modulated light excitation from the ITO side of the device. V_A, V_B, V_C, and V_D are the input signal measured with ITO as the ground reference. The differential voltage is measured using a lock-in amplifier (ac coupled, voltage input) across the opposite pair of electrodes: V_A-V_C and V_B-V_D. **(b)** Band alignment of different layers in the device. The ITO-HOIP interface allows for electron extraction to the back contact ITO electrode. **(c)** Normalized I(V) measured across Au-ITO electrodes, represented in a semi-log plot, under dark and illumination conditions, confirms the barrier for hole extraction at the ITO/HOIP interface. **Inset** shows I(V) in linear scale and the negative short-circuit current under illumination conditions indicates electron selective extraction at the*

ITO/HOIP interface. ***(d)*** *Schematic showing the Schottky depletion width across the ITO/HOIP interface which is forward biased at the point of light excitation. The lateral photo-voltage is developed across the point of illumination and the electrode.*

4.3.3 Spatial Photo-voltage Mapping

The PSD operation requires that the observed photo-signal has a spatial dependence on the excitation position. **Figure 4.5(a)** (**4.5(b)**) shows the variation of ΔV_{ph} between the electrodes A (B) and C (D) (electrode configuration in **Figure 4.4(a)**), such that V_A-V_C = $\Delta V_{A\text{-}C}$ (similarly for $\Delta V_{B\text{-}D}$). The differential photo-voltage, $\Delta V_{A\text{-}C,}$ and $\Delta V_{B\text{-}D}$ are considered as $\Delta V_{ph}(x)$ and $\Delta V_{ph}(y)$ respectively. It is observed that ΔV_{ph} profiles maintain the linearity in the detection plane of a defined span around the central region resulting in higher V_{ph}[28-30]. **Figure 4.5(c)** and **4.5(d)** shows the line scan of $\Delta V_{ph}(x)$ and $\Delta V_{ph}(y)$ across the device-center respectively. The region close to the Au-electrodes reveals a steep exponential ΔV_{ph}(x and y) response, which is attributed to device edge effects and dominant carrier diffusion. At distances beyond the decay-length from the top electrode, encompassing the central region, the variation of $\Delta V_{ph}(x)$ and ΔV_{ph} (y) is linear on either side as shown in the **insets, Figure 4.5(c)** and **4.5(d)** respectively. Beyond the length scales of carrier diffusion effects, LPV is dominant. The superior transport features in HOIP such as higher mobility results in higher LPV, thereby allowing large-area structures to enable a wide spatial zone for light-position tracking. Ignoring the edge effect features, the active area used for PSD in the center of the device is in the range of ~ 3 mm, in either direction. It is to be noted that the plots indicate the magnitude, $|\Delta V_{ph}|$. In the lockin measurements, the corresponding phase shows a reversal of ~ *pi* radian for excitation on either side of the device center (details related to phase information of the signal presented in section 4.3.5).

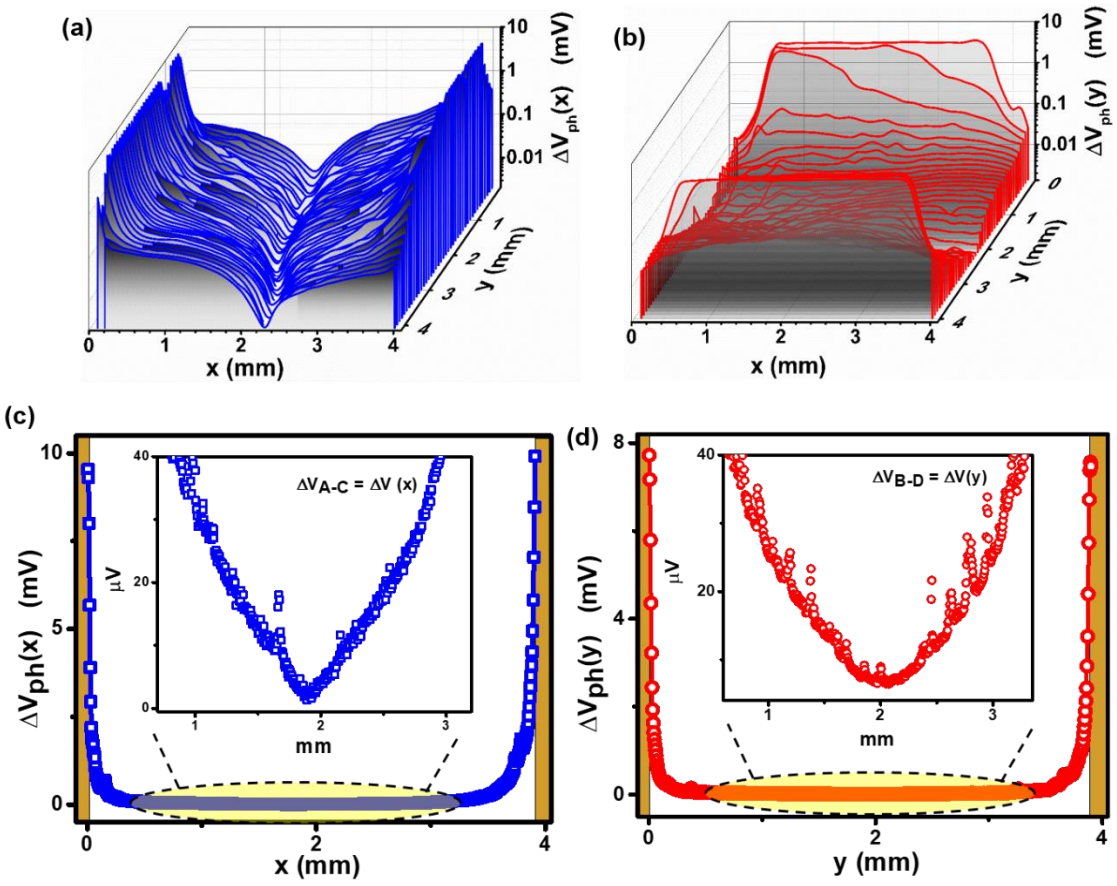

***Figure 4. 5**: **(a)** Spatial profile of differential photo-voltage $\Delta V_{A\text{-}C}$ across the electrodes A and C in **Figure 4.3(a)** and **(b)** $\Delta V_{B\text{-}D}$ across the electrodes B and D. **(c)** Variation of ΔV_{ph} as the light excitation is scanned between the electrodes A and C in the center of the active area. The **inset** shows the linear V_{ph} variation in the center of the device away from the electrodes. **(d)** Similar V_{ph} behavior across the other electrodes B and D.*

The sensitivity of position detection (η) values in both the x and y-axis are equivalent (η ~38 µV/mm, **inset of Figure 4.5(c), (d)**). Sensitivities in the range of ~ 50 µV/mm were observed for many devices.

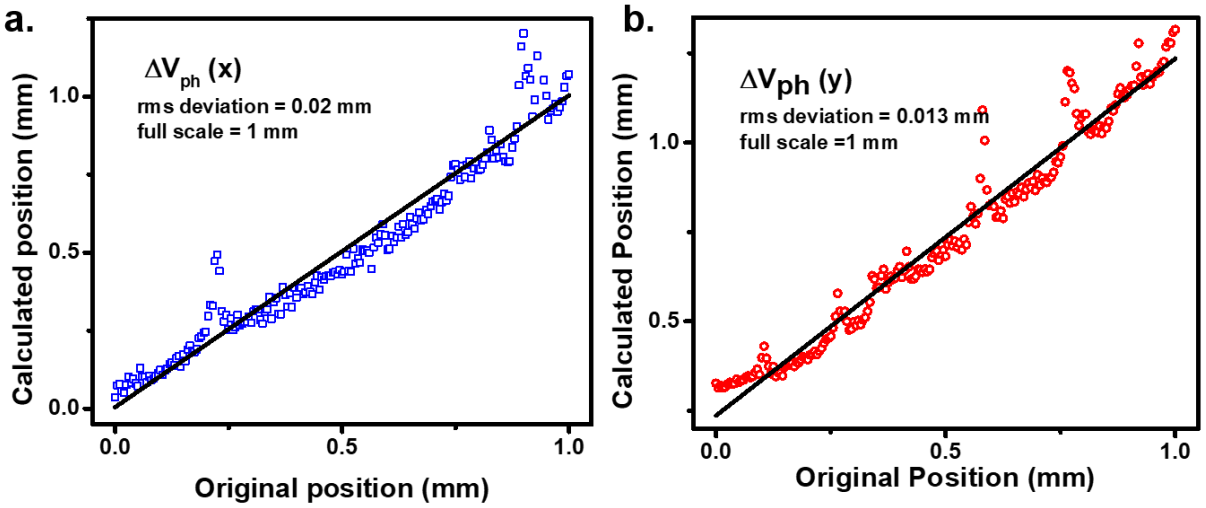

Figure 4. 6*: Plot of original and calculated positions showing the deviation from linear behavior for PSD measurement in* ***(a)*** *the x-axis and the* ***(b)*** *y-axis.*

It is observed in many PSD systems that the variation of $\Delta V_{ph}(x,y)$ gradually assumes a non-linear behavior away from the center. The non-linearity of HOIP 2D-PSDs given as the position detection error δ :[31, 32]

$$\delta = \frac{2 \times \ rms\ deviation}{Measured\ full\ scale} \tag{4.1}$$

Figure 4.6 (a) and **(b)** shows the plot of real vs calculated position using the PSD in the x-axis and y-axis respectively. The value of was δ was determined to be 2.1 % and 1.3 % in the x and y-axis, respectively, considering a channel length of 1 mm from the device center. The low values of δ indicate that the position detection characteristics can be considered linear and are comparable to commercial 2-D PSDs[33]. The optimum dimensions for defining the linear zone rely on a host of parameters including bulk-microscopic HOIP properties as well as interfacial features. In practice, the detection range can be extended to several centimeters covering a large area, employing methods used in commercial PSDs[34]. The PSD response is expected to exhibit linearity over a

wide range of intensity and spectra (300 nm – 800 nm). However, the sensitivity depends on the modulation frequency and excitation intensity as shown in **Figure 4.7(a)** and **(b),** respectively. The dependence of sensitivity to the excitation intensity is attributed to a higher signal-to-noise ratio, resulting in higher LPV[35].

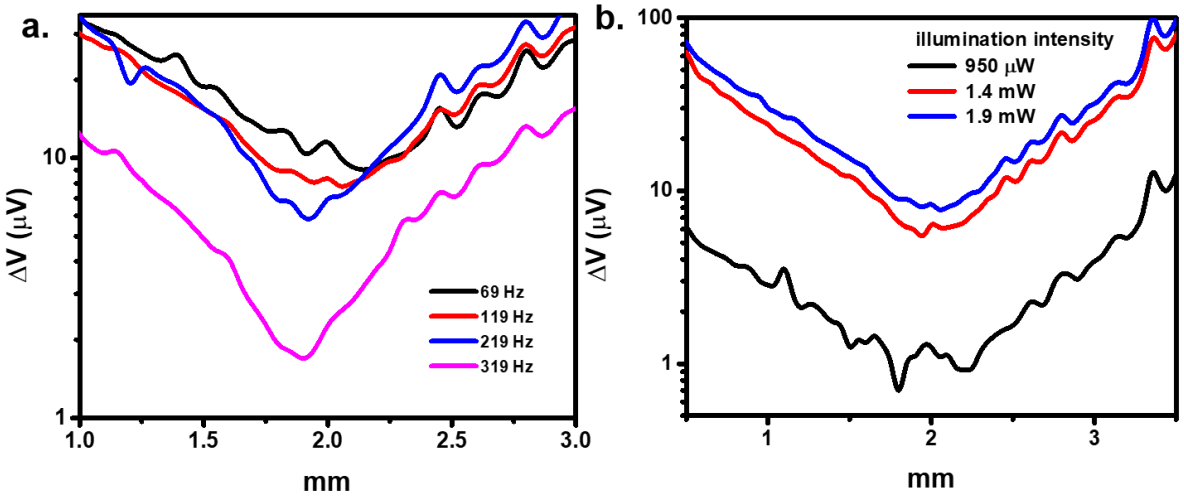

***Figure 4. 7**: Variation of PSD linear response with **(a)** modulation frequency. The illumination power was maintained at 1 mW. **(b)** PSD response with a variation of excitation intensity. The modulation frequency was maintained at 119 Hz.*

4.3.4 Position dependent photovoltage in inverted device structures

In the above-described scenario (with respect to device structure in **Figure 4.4**), the barrier at the ITO-HOIP interface is utilized to facilitate charge separation. This magnitude of the photo-signal can be increased upon having a charge selective layer instead of the metal-perovskite interface. An improved charge separation is achieved in inverted devices upon introducing a PEDOT-PSS hole extraction layer, as shown in the device schematic in **Figure 4.8(a).** This layer assists in hole extraction to the ITO bottom electrode as shown in the band-alignment diagram, **Figure 4.8(b)**. The PSD devices, in this configuration with dimensions of ~ (4 mm × 4 mm), exhibit an increase in the linear sensitivity up to > 80 μV mm^{-1}, as shown in **Figure 4.9(b)**.

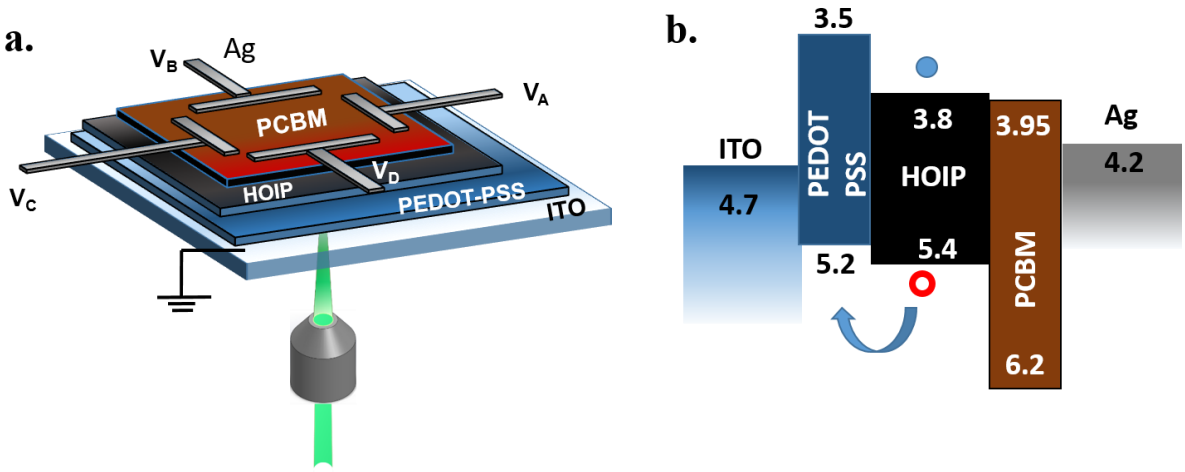

***Figure 4. 8**: **(a)** Device schematic of inverted structure PSD. **(b)** Band alignment diagram shows the pathway for hole extraction to the PEDOT:PSS layer. In the above modified device, the PEDOT:PSS interlayer is utilized to improve charge separation efficiency to the ITO electrode.*

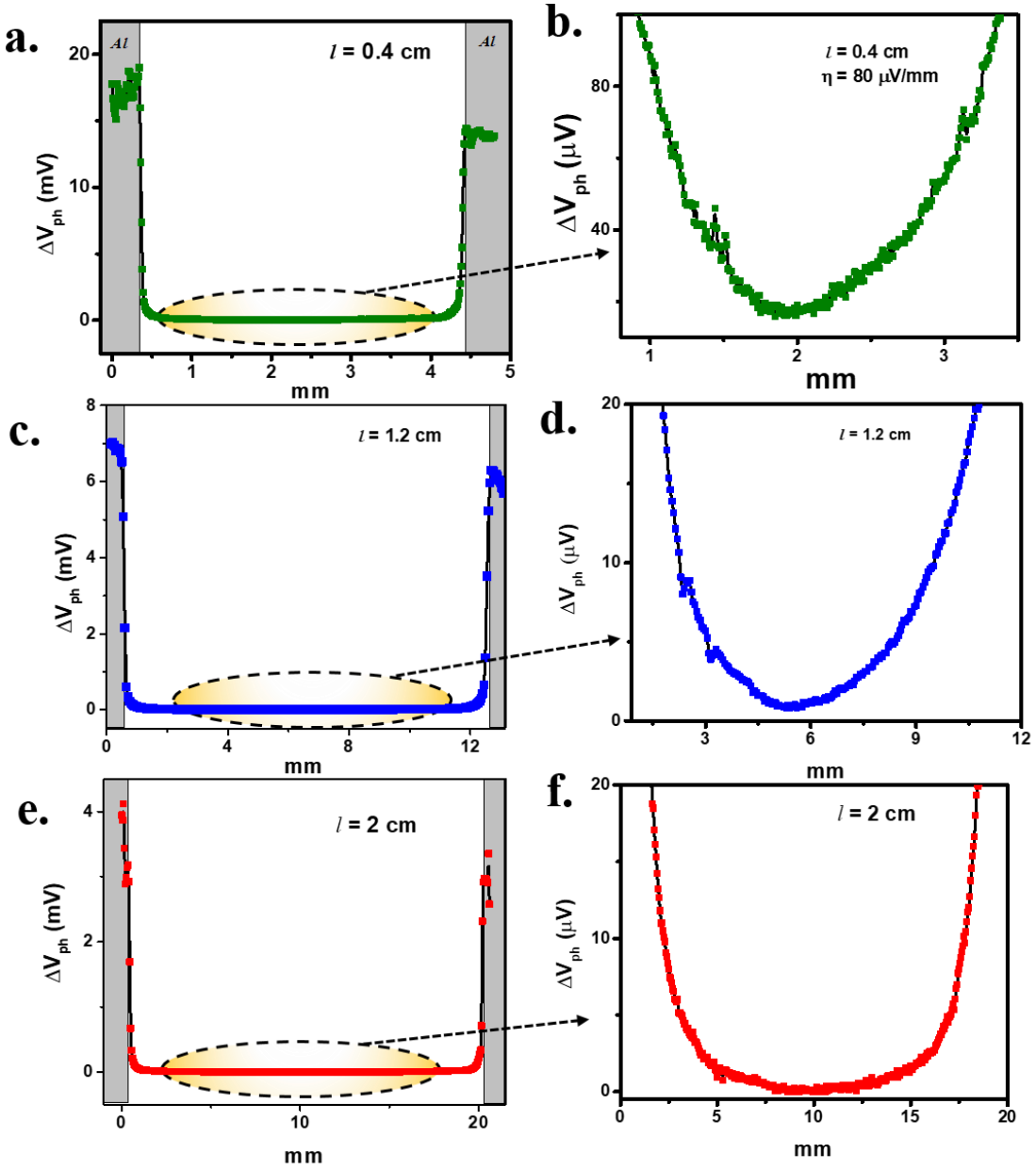

***Figure 4. 9**: $\Delta V_{ph}(x)$ scan for excitation translated between electrode A and C (**Figure S8a**) for **(a)** 0.4 cm, **(c)** 1.2 cm and **(e)** 2 cm. The shaded regions indicate the overlapping region due to the top Ag electrode. Correspondingly, the $V_{ph}(x)$ profiles for the different channel lengths away from the electrodes shows a linear behavior in the case of **(b)** channel length of l = 0.4 cm. However, these profiles deviate from linear behavior for the case of **(d)** l = 1.2 cm and **(f)** l = 2 cm.*

For device dimensions > 1 cm, deviation from the linear spatial behavior of the ΔV_{ph}(x and y) is observed. **Figure 4.9(d)** and **Figure 4.9(f)** show the ΔV_{ph}(x) trend for 2D-based devices with an active length of 1 cm and 1.8 cm, respectively. The observed non-linear spatial profile can be attributed to the efficient charge separation, lower carrier recombination, and the electron blocking nature of the PEODT-PSS interlayer. It is speculated that the high work-function and the electron blocking nature of the PEDOT-PSS layer improves the carrier separation due to the vertical electric field, resulting in the suppression of carrier recombination. Longer transient photocurrent decay time, shown in **Figure 4.10** is indicative of the longer-dwell time of the electron transport in bulk in comparison to the ITO-HOIP based devices where the e-h recombination zone stretches across the length of the device. As a result, the effect of the vertical electric field, lateral photovoltage is suppressed, resulting in an exponential profile of the spatial photosignal. Nevertheless, the ΔV_{ph}(x and y) of large-area inverted PSDs can still be utilized using an algorithm noting the non-linear response in terms of multiple polynomial fits spanning the device that is symmetric about the central 2-D axis.

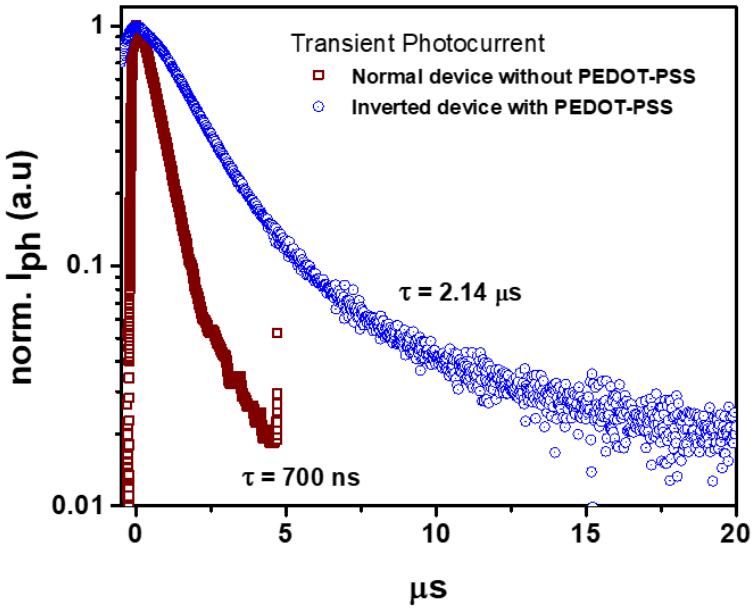

***Figure 4. 10**: Comparison of Transient Photocurrent (TPC) lifetimes of different PSD device types. The time decay of the photocurrent was measured in response to a pulsed excitation (532 nm, ~ 1 ns pulse width). Longer lifetimes in the inverted structure are reflective of a lower recombination rate and efficient carrier extraction.*

It is noted that the improvement of photo-signal in the presence of an interlayer, comes at the cost of linearity in position detection. The lower photosignal in the previously discussed device structure without the interlayer (depicted in **Figure 4.4**) can be compensated with externally integrated amplifier circuits. The following sections presents results related to the dynamic light imaging and position dependent measurements on PSD devices, in the absence of interlayer (i.e., without PEDOT:PSS, as described in **Figure 4.4**)

4.3.5 Dynamic Imaging

The 2D PSD functionality can utilized to realise a quadrant detector, to identify the incident-beam position. The lock-in based measurement utilizes both the magnitude,

$|V_{ph}|$, and the corresponding phase for every excitation position. If the spatial sensitivity of position detection is η, the coordinates (x, y) of light excitation is reconstructed as:

$$x = \begin{cases} -\eta.\Delta\mathrm{Vph(x)}, & \text{if phase} > 0 \\ \eta.\Delta\mathrm{Vph(x)}, & \text{if phase} < 0 \end{cases} \quad (4.2)$$

$$y = \begin{cases} -\eta.\Delta\mathrm{Vph(y)}, & \text{if phase} > 0 \\ \eta.\Delta\mathrm{Vph(y)}, & \text{if phase} < 0 \end{cases} \quad (4.3)$$

This procedure provides unique identifying (x,y) coordinates of the narrow-beam position on the active-device area. In the case of beam motion, the trajectory can be dynamically imaged at high definition. Utilizing a PSD with η = 37 µV/mm, a light beam trajectory that is projected onto the device area is reconstructed. A 532 nm laser excitation (1.9 mW, ~ 5 µm spot) is used to trace different geometrical patterns, while the ΔV_{ph} was simultaneously recorded. The pattern of light trajectory was reconstructed, with values of $\Delta V_{ph}(x)$ and $\Delta V_{ph}(y)$ corresponding to each point, using **Equation 4.2** and **Equation 4.3. Figure 4.11** shows the values of $\Delta V_{ph}(x)$, $\Delta V_{ph}(y)$, and the pattern of reconstructed light trajectory. **Figure 4.11(a)** and **Figure 4.11(b)** represent the V_{ph} values and reconstructed pattern when the light beam was scanned in the horizontal and the vertical direction respectively. In **Figure 4.11(c)** the light beam was translated diagonally and in **Figure 4.11(d)**, the light beam traced a square pattern.

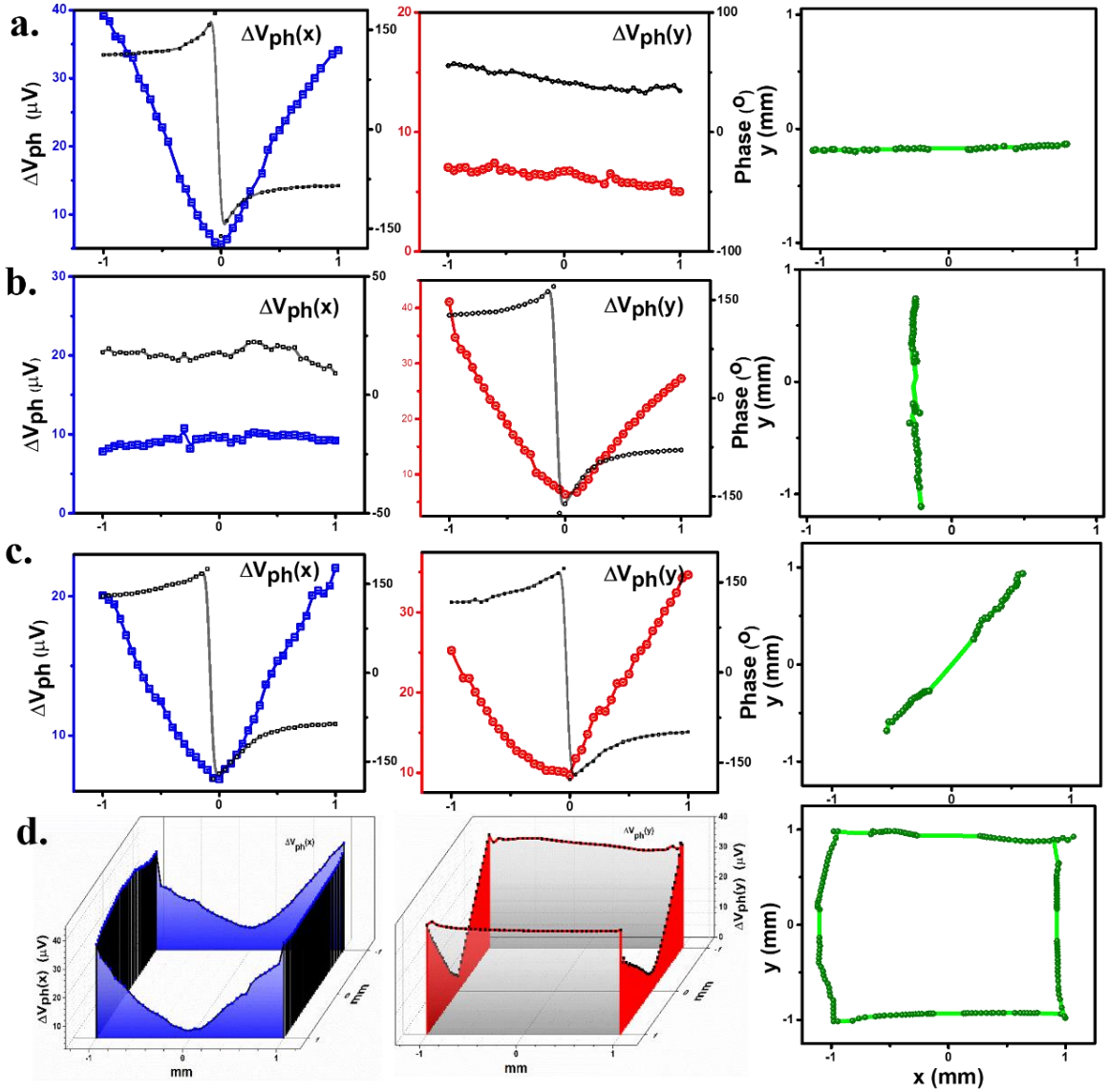

Figure 4. 11*: Reconstructed light trajectory upon acquiring ΔV_{ph} from the two pairs of electrodes for* ***(a)*** *horizontal line,* ***(b)*** *vertical line,* ***(c)*** *diagonal, and a* ***(d)*** *square. Column 1 (blue) and column 2 (red) show the plot of $\Delta V_{ph}(x)$ and $\Delta V_{ph}(y)$ as the light moves in a particular trajectory. The black curve in all plots depicts the phase of the corresponding ΔV_{ph}. The last row depicts the ΔV_{ph} variation as the light beam traces a square pattern on the PSD.*

As seen in **Figure 4.11(a)**, when the light trajectory traces in the x-axis, $\Delta V_{ph}(y)$ has the same value corresponding to the constant y-value. In the plot of $\Delta V_{ph}(x)$, we see a

symmetric variation of V_{ph} on either side of the center. The phase plot also shows a phase reversal on either side of the device center. Considering only $\Delta V_{ph}(x)$, $\Delta V_{ph}(y)$ (without the phase information), coordinates (x,y) has four equivalent points, one in each quadrant of the detector area. The phase information can be used to discern the quadrant corresponding to the point with coordinates(x, y). In our pattern reconstruction, we have observed and implemented the convention that a positive phase implies a negative scale of the corresponding axis and a negative phase implies a positive scale. As shown in the last column of **Figure 4.11,** the reconstructed pattern is in good resemblance with the light trajectory.

Considering only $\Delta V_{ph}(x)$, $\Delta V_{ph}(y)$ (without the phase information), coordinates (x,y) can be mapped to four equivalent points, one in each quadrant of the detector area. The additional phase information is useful to discern the quadrant corresponding to the excitation-position (using **Equations 4.2** and **4.3**). The above represents the dynamic imaging in the steady-state scheme of measurement. The speed of imaging can be improved using transient measurements, with timescales corresponding to photo-signal decay, in response to a single-pulse excitation. The Transient Photocurrent (TPC) studies on PSDs provide an estimate of the range for the dynamic response.

4.3.6 Position dependent Transient Photocurrent

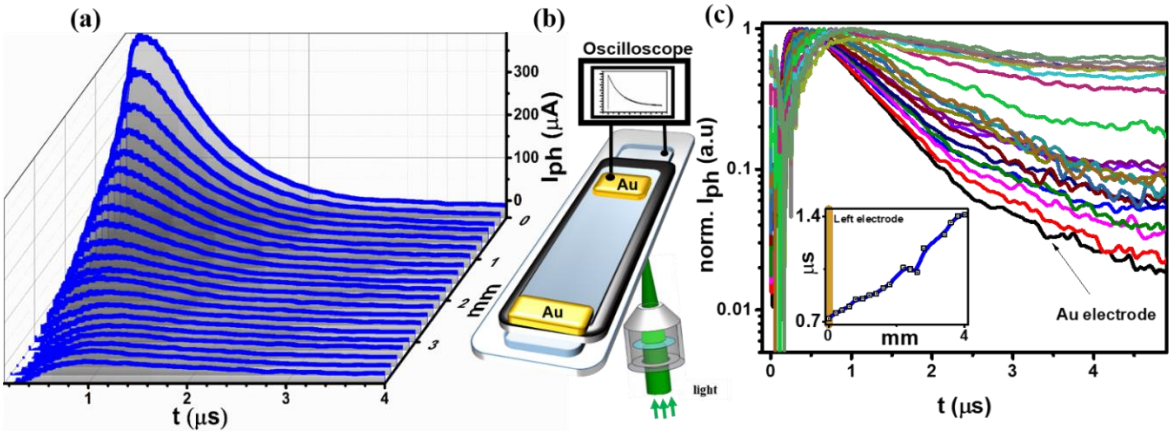

***Figure 4. 12**: **(a)** Transient photocurrent profiles $I_{ph}(t)$ collected across the Au and ITO electrodes as the point of excitation is translated away from the electrode. **(b)** Schematic showing the translation of a light beam with respect to the Au electrode. **(c)** Normalized features of $I_{ph}(t)$ obtained in **(a)** show an increase in decay lifetime as the beam illumination is farther away from the Au electrode. **Inset** shows the plot of decay time with respect to illumination position.*

Position dependent TPC measurements were carried out on the PSD devices, with pulsed-excitation translated away from the top Au-electrode, schematic of which is depicted in **Figure 4.12(b)**. **Figure 4.12(a)** shows TPC decay profiles on PSD devices, which reveal fast decay lifetimes ~ 700 ns, with excitation at the metal overlapping device (ITO/HOIP/Poly-TPD/Au). As the excitation is furthered away from the Au-electrode the reduction in I_{ph} magnitude (shown in **Figure 4.12(a)**) is accompanied by an increase in the decay lifetime, as is evident in the normalized plot, shown in **Figure 4.12(c)**. **Inset** of **Figure 4c** which shows the plot of decay time as a function of excitation position, indicates a monotonic increase in decay timescales up to ~ 1.4 μs for excitation at the other end of the device. It is noted that the decay lifetimes were observed to be independent of the relative position of the other two electrodes which

are parallel to the direction of beam translation. This is indicated in **Figure 4.13**, which shows the consistent I_{ph} decay profiles when measured from the third Au-electrode, as the beam translates between an opposite pair of Au-electrodes.

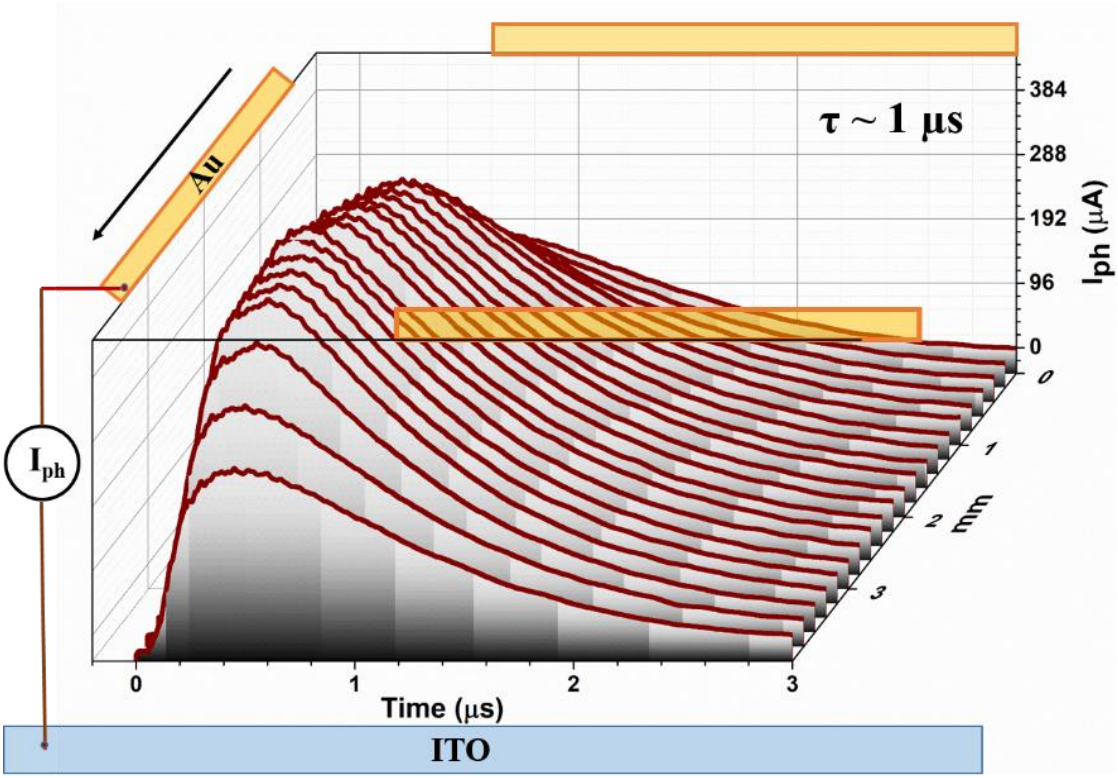

***Figure 4. 13**: Plot of TPC showing consistent I_{ph} (t) profiles at a constant distance from the collecting electrode. The beam is translated perpendicular to a pair of PSD Au electrodes in the direction of the indicated arrow.*

The position-dependent TPC characteristics can be utilized for position detection application employing the transient scheme of detection. For example, **Figure 4.14(b)** shows excitation position dependent differential photocurrent profiles, $\Delta I_{ph}(t) = I_{ph}1(t) - I_{ph}2(t)$ where $I_{ph}(1)$ and $I_{ph}(2)$ is the TPC at Au-electrode 1 and 2 respectively, shown in **Figure 4.14(a).** Assuming an average response time of ~ 1 µs, a dynamic-imaging rate in the range of ~ 1 MHz can, in principle, be achieved. The transient measurements

offer an additional method of position detection with improved speed and resolution of the reconstructed light beam trajectory.

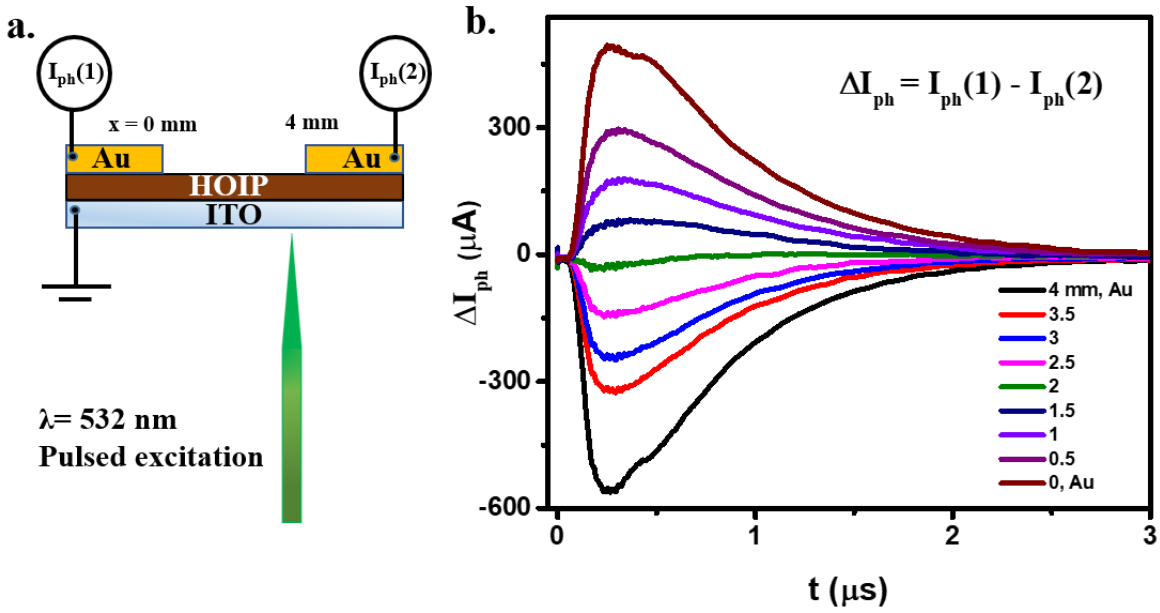

***Figure 4. 14**: **(a)** Schematic illustrates single pulse measurement using differential transient photocurrent ΔI_{ph} measurement as the pulsed light beam is translated across the active channel length. **(b)** Transient $\Delta I_{ph}(t) = I_{ph}(1) - I_{ph}(2)$ profiles as a function of excitation position.*

To understand the lifetime dependence on the excitation position (**Figure 4.12(c)**), it is necessary to investigate the nature of transport for photo-carrier generation away from the Au electrode. This transit-timescale depends on the effective mobility of the corresponding carrier. In a previous report, where circuit modelling of a polymer-based PSD was studied, the distance-dependent characteristics were based on the spreading impedance approach[29]. Essentially, the resistive contribution to lateral transport is attributed to the disorder scattering of charge carriers and the capacitive contribution is due to the deep trap states in the bulk of the active layer. In a similar line of approach, to estimate the resistive and capacitive contribution to the observed I_{ph}, excitation-

position dependent impedance spectroscopy (IS) measurements in combination with circuit modelling are carried out.

4.3.7 Impedance Spectroscopy

IS measurements were carried out using a small ac-signal input of 30 mV in the frequency range from 10 kHz to 1 MHz. **Figure 4.15(a)** and **(b)** show the Bode plot and the Nyquist plot (or Cole-Cole plot), respectively, on the PSD device as a function of intensity variation. The semi-circle trend in the Nyquist plot (**Figure 4.15(b)**) indicates that the device can be represented as a single RC circuit in series with a resistor, as shown in the **inset** of **Figure 4.15(d)**. Here R_1 represents the series resistance of the device while R_2 and C_1 represent the bulk resistance and capacitance, respectively. The Cole-Cole plots (**Figure 4.15(b)** and **(d)**) are utilized to analyze the real (Z´) and imaginary parts (Z´´) of the impedance using **Equations 4.4** and **4.5**. The calculated values of R and C are tabulated in **Table 4.1**.

$$Z' = R_1 + \frac{R_2}{1+(\omega C_1 R_2)^2}, \tag{4.4}$$

$$-Z'' = \frac{\omega C_1 {R_2}^2}{1+(\omega C_1 R_2)^2} \tag{4.5}$$

In the same line of approach, IS was studied as a function of excitation position (532 nm, 550 µW, 0.5 mm spot size), as the beam is translated away from the Au electrode of the PSD. **Figure 4.15(c)** and **4.15(d)** show the Bode and Nyquist plots, respectively, as the excitation-position is varied. **Figure 4.15(d)** shows that as the position of

excitation is furthered away from the electrode, the arc of the semicircle feature increases, indicating a higher R-C value.

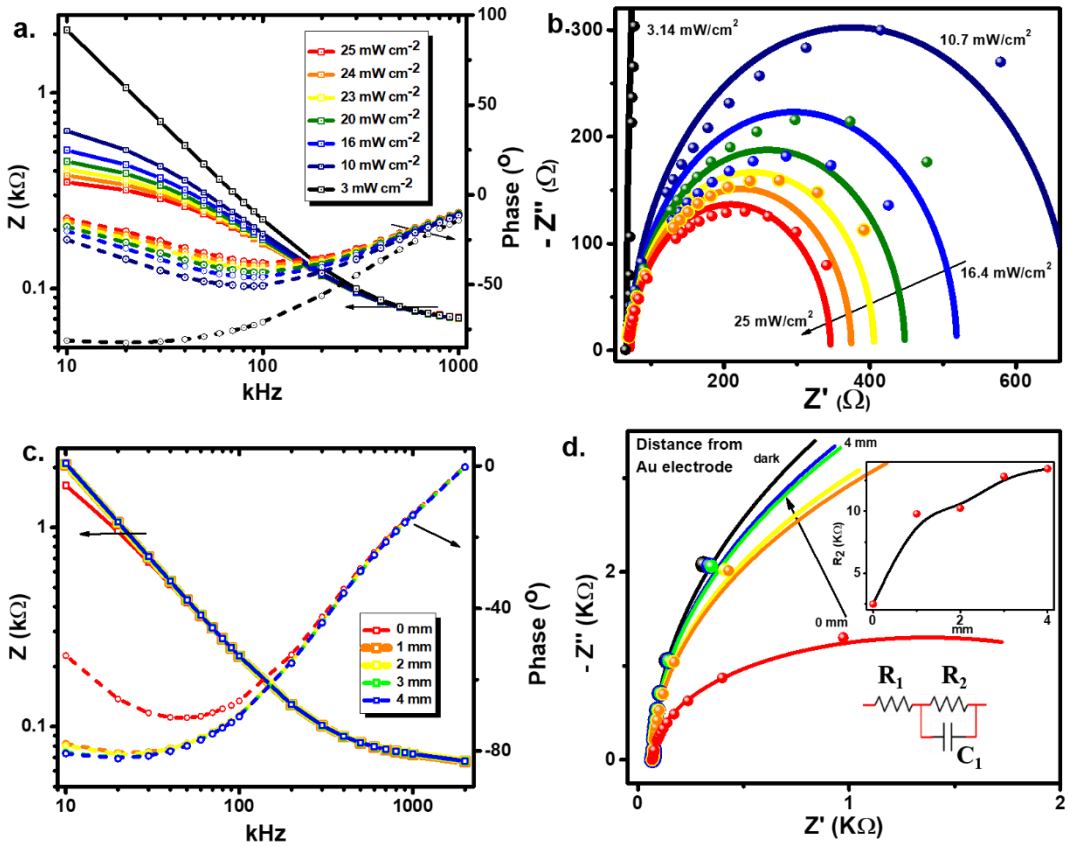

***Figure 4. 15**: **(a)** Bode plot showing the variation of impedance and phase with driving frequency, with the variation of excitation intensity. **(b)** The corresponding Cole-Cole plot as a function of light intensity variation shows the semi-circle profiles. **(c)** Bode plots as a function of excitation-position translated away from the top Au electrode. **(d)** Cole-Cole plot of the device as the excitation position is translated away from the Au electrode. **Inset** shows the equivalent circuit diagram and the variation of the R_2 parameter with excitation-translation.*

Table 4.1: *RC values from impedance data shown in* ***Figure 4.15(b)***

Intensity (mW/cm^2)	R1 (Ω)	R2 (Ω)	C1 (nF)
25	71.5	262.8	11.47
24	70.73	287.3	11.4
23	70.66	314.2	11.2
20	70.8	351.2	11
16	70.99	412	10.6
10	70.44	544	9.96
3	69.54	14011	7.6

Table 4.2: *RC values from impedance data shown in* ***Figure 4.15(d)***

Position (mm)	R_1 (Ω)	R_2 (kΩ)	C_1 (nF)
0	72	2.49	7.8
1	71.38	9.79	7.6
2	72	10.25	7.6
3	71.65	12.83	7.58
4	71.83	13.45	7.6
dark	73.28	15.43	7.56

The R-C values obtained after data fitting and tabulated in **Table 4.2** show no variation in the values of R_1 and C_1. On the other hand, the values of R_2, also shown in the **inset, Figure 4.15(d)** indicate an increasing trend with the excitation-position. These results indicate that the carrier transport length, and not the carrier trapping process is the limiting factor for efficient charge collection at the Au- electrode. Suitable strategies such as the incorporation of efficient charge separation layers and the introduction of

an external amplification circuit can be implemented for compensating for photo-signal losses.

4.4 Conclusion

The superior semiconducting properties of HOIP have been utilized to demonstrate the position detection functionality in 2-dimensions, using a process initiated by selective charge transfer across the metal-HOIP barrier-interface. The fabricated devices exhibit linear variation of photo-voltage over a long-range with spatial sensitivity in the range of ~ 50 µV mm^{-1}, which can be increased to ~ 80 µV mm^{-1} using inverted device structures. Using a continuous scheme of position-detection over the defined area of the PSD, the devices offer the possibility of dynamic imaging of the light-beam trajectory. Given the fast-transient decay time scales, the single pulse detection scheme can be utilized to improve the device's operational bandwidth to ~ 1 MHz. This functionality extends the utility of PSDs to a wide range of applications in microscopy and feedback sensors. The transient current and impedance studies provide an understanding and estimate of the limits of the operation. It should be possible to further optimize the 2-D PSD to realize the performance comparable to traditional semiconductors. The semi-transparent, thin-film, large-area, pixel-free 2D-PSD structure opens up an innovative design option to a host of applications.

References

1. Tian Y, *et al.* A Solution-Processed Organometal Halide Perovskite Hole Transport Layer for Highly Efficient Organic Light-Emitting Diodes. *Advanced Electronic Materials* **2**, 1600165-n/a (2016).
2. Senanayak SP, *et al.* Understanding charge transport in lead iodide perovskite thin-film field-effect transistors. *Science Advances* **3**, (2017).
3. Yakunin S, *et al.* Detection of X-ray photons by solution-processed lead halide perovskites. *Nat Photonics* **9**, 444-449 (2015).
4. Wang Y, *et al.* Photonic synapses based on inorganic perovskite quantum dots for neuromorphic computing. *Advanced Materials* **30**, 1802883 (2018).
5. Kumar P, Zhao B, Friend RH, Sadhanala A, Narayan KS. Kinetic Control of Perovskite Thin-Film Morphology and Application in Printable Light-Emitting Diodes. *ACS Energy Letters* **2**, 81-87 (2017).
6. D. Kabra, Th. B. Singh, Narayan KS. Semiconducting-polymer-based position-sensitive detectors. *Appl Phys Lett* **85**, 5073-5075 (2004).
7. Ashar A, Ganesh N, Narayan K. Hybrid Perovskite-Based Position-Sensitive Detectors. *Advanced Electronic Materials* **4**, 1700362 (2018).
8. Schottky W. On the origins of photoelectrons in Cu2 O-Cu photocells. *Phys Z* **31**, (1930).
9. Henry J, Livingstone J. A comparative study of position-sensitive detectors based on Schottky barrier crystalline and amorphous silicon structures. *Journal of Materials Science: Materials in Electronics* **12**, 387-393 (2001).
10. Fortunato E, Lavareda G, Vieira M, Martins R. Thin film position sensitive detector based on amorphous silicon p–i–n diode. *Review of Scientific Instruments* **65**, 3784-3786 (1994).
11. Qiao S, Feng K, Li Z, Fu G, Wang S. Ultrahigh, ultrafast and large response size visible-near-infrared optical position sensitive detectors based on CIGS structures. *Journal of Materials Chemistry C* **5**, 4915-4922 (2017).
12. Wallmark JT. A New Semiconductor Photocell Using Lateral Photoeffect. *Proceedings of the IRE* **45**, 474-483 (1957).
13. *Hamamatsu, 1D PSD, S8673*, (2017).
14. Babu V, *et al.* Improved stability of inverted and flexible perovskite solar cells with carbon electrode. *ACS Applied Energy Materials* **3**, 5126-5134 (2020).
15. Mäkynen A. PositionSensitive Devices and Sensor Systems for optical Tracking and Displacement Sensing Application [Dissertation]. *Finland: Faculty of Technology, University of Oulu*, (2000).
16. Castracane J, Tokranova N, Lydecker L. Self-balancing position sensitive detector. (ed^(eds). Google Patents (2017).
17. de Bakker M, Verbeek PW, Steenvoorden GK. Design considerations for a range image sensor containing a PSD-array and an on-chip multiplexer. In: *Proceedings. International Conference on Recent Advances in 3-D Digital Imaging and Modeling (Cat. No. 97TB100134)* (ed^(eds). IEEE (1997).
18. Kovačević K, Zadro M. Two-dimensional position sensitive silicon photodiode as a charged particle detector. *Nuclear Instruments and Methods in Physics Research Section A: Accelerators, Spectrometers, Detectors and Associated Equipment* **423**, 103-107 (1999).
19. Ivan IA, Ardeleanu M, Laurent GJ, Tan N, Clevy C. The metrology and applications of PSD (position sensitive detector) sensors for microrobotics. In:

2012 International Symposium on Optomechatronic Technologies (ISOT 2012) (ed^(eds). IEEE (2012).
20. Schutt K, Nayak PK, Ramadan AJ, Wenger B, Lin YH, Snaith HJ. Overcoming Zinc Oxide Interface Instability with a Methylammonium-Free Perovskite for High-Performance Solar Cells. *Advanced Functional Materials* **29**, 1900466 (2019).
21. Kiyanagi Y, Kamiyama T, Kino K, Sato H, Sato S, Uno S. Pulsed neutron imaging using 2-dimensional position sensitive detectors. *Journal of Instrumentation* **9**, C07012 (2014).
22. Ivan IA, Ardeleanu M, Laurent GJ. High dynamics and precision optical measurement using a position sensitive detector (PSD) in reflection-mode: application to 2D object tracking over a smart surface. *Sensors* **12**, 16771-16784 (2012).
23. Kumar P, Zhao B, Friend RH, Sadhanala A, Narayan K. Kinetic Control of Perovskite Thin-Film Morphology and Application in Printable Light-Emitting Diodes. *ACS Energy Letters* **2**, 81-87 (2017).
24. Saliba M, *et al.* Cesium-containing triple cation perovskite solar cells: improved stability, reproducibility and high efficiency. *Energy & environmental science* **9**, 1989-1997 (2016).
25. Yi C, *et al.* Entropic stabilization of mixed A-cation ABX 3 metal halide perovskites for high performance perovskite solar cells. *Energy & Environmental Science* **9**, 656-662 (2016).
26. Hu X, *et al.* High-performance flexible broadband photodetector based on organolead halide perovskite. *Advanced Functional Materials* **24**, 7373-7380 (2014).
27. Koh TM, *et al.* Formamidinium-containing metal-halide: an alternative material for near-IR absorption perovskite solar cells. *The Journal of Physical Chemistry C* **118**, 16458-16462 (2014).
28. Fortunato E, Lavareda G, Martins R, Soares F, Fernandes L. Large-area 1D thin-film position-sensitive detector with high detection resolution. *Sensors and Actuators A: Physical* **51**, 135-142 (1995).
29. Kabra D, Shriram S, Vidhyadhiraja NS, Narayan KS. Charge carrier dynamics in organic semiconductors by position dependent optical probing. *Journal of Applied Physics* **101**, 064510 (2007).
30. Ganesh N, *et al.* Impact of trap filling on carrier diffusion in MAPb Br 3 single crystals. *Physical Review Materials* **4**, 084602 (2020).
31. Yu C, Wang H. Large lateral photovoltaic effect in metal-(oxide-) semiconductor structures. *Sensors* **10**, 10155-10180 (2010).
32. Kawasaki A, Goto M. On the position response of a position-sensitive detector (PSD) irradiated with multiple light beams. *Sensors and Actuators A: Physical* **22**, 534-537 (1990).
33. Hamamatsu. 2D PSD S2044. *Hamamatsu, 2D PSD, S2044*, (2019).
34. Hamamatsu. Signal processing circuit for 2-D PSD C4674-01. *Signal processing circuit for 2-D PSD C4674-01, 2D PSD, S2044*, (2019).
35. Zhang Y, Zhang Y, Yao T, Hu C, Sui Y, Wang X. Ultrahigh position sensitivity and fast optical relaxation time of lateral photovoltaic effect in Sb 2 Se 3/p-Si junctions. *Optics express* **26**, 34214-34223 (2018).

Chapter 5: Single-pixel color sensing using graded-bandgap perovskite structures

5.1 Introduction

Intensive research on hybrid perovskites in the last decade has resulted in the development of a wide variety of perovskite structures such as quantum dots, nanocrystals, nanowires, etc[1-4]. One such class of hybrid perovskite which has displayed huge potential as a promising optoelectronic material is the layered Ruddlesden-Popper 2D-perovskite[5, 6]. Homologous 2D perovskites initially were explored for higher stability of opto-electronic devices[7]. The highest power conversion efficiency (PCE) of solar cells close to 20 % [8, 9] and the external quantum efficiency of the light emitting diodes > 20 %[10] has been achieved by 2D/3D mixed-phase perovskites. Ease of pinhole-free film formation from simple solution-processable techniques, tweaking precursor stoichiometric ratios to tune the bandgap and long-term stability [11, 12] make this system attractive for device fabrication and engineering.

The homologous 2D perovskites are formed by the introduction of long alkyl chain cations in the perovskite structure which self-assembles to form 2D/quasi-2D quantum well structures. Typical quantum wells comprise of inorganic PbI_6 octahedral sheets stacked alternately with the organic alkyl chains. The bandgap of a particular quantum well depends on the order of octahedral stacking and confinement due to the alkyl (Butyl Ammonium (BA) in this study) barrier layers[13, 14]. In these systems, the lower order quantum wells have a higher bandgap. As the order increases, the bandgap

reduces with $n \sim \infty$ having the lowest 3D bandgap. An illustration of layered perovskites is presented in **Figure 1.4**, with a brief introduction in the corresponding section 1.3.

In this work, the mixture of 2D/3D hybrid perovskite having a vertically graded bandgap structure formed using a hot-cast method and used as the active layer of the photodetector. The hot-cast method[11] for fabricating self-assembled graded structures is a facile attractive method as compared to conventional epitaxially constrained growth methods. In these films, the higher bandgap (lower-order) 2D quantum wells assemble towards the substrate, and the lower bandgap (higher-order) forms to the top of the film, away from the substrate[15, 16]. In such a graded bandgap hybrid organic-inorganic perovskite (G-HOIP), the spatial (vertical) distribution profile of the charge generation depends on the incident wavelength, λ. The short-λ incident light is absorbed in the high bandgap region, while the long-λ light propagates through the film and is absorbed in the low-bandgap backplane region. The photocurrent transient ($I_{ph}(t)$) which depends on the charge generation profile, transport rates and extraction efficiency, results in a characteristic temporal profile corresponding to the incident λ[17]. This λ-dependent $I_{ph}(t)$ profiles are utilized for color sensing application.

Light detection and color representation in digital imaging involves the quantification of two parameters: light intensity and wavelength. **Figure 5.1** shows the schematic illustrating the color reconstruction mechanism in typical CMOS-based image sensors. An array of color filters (CFA) is used as a mask, which absorbs a sizeable percentage of the incoming light prior to detection by a photodiode element. The color is then reconstructed through an interpolation demosaicing algorithm. This chapter presents a different methodology, where a temporal photo-detection scheme is implemented, which allows for resolving the wavelength and intensity information in the absence of optically dispersive elements. This is achieved using a single-pixel

detector with graded bandgap perovskite as the active layer. This chapter initially presents the results for the spectral and temporal response of the photocurrent in these structures and then explores the use of the characteristic $I_{ph}(t)$ response to extract the wavelength information.

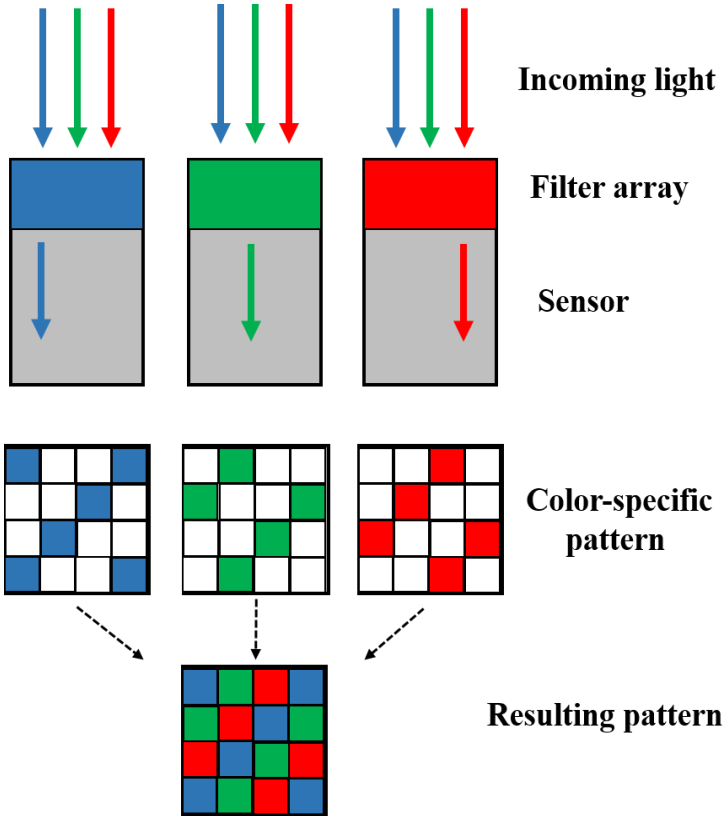

Figure 5. 1*: Schematic explaining the mechanism of color sensing using filter array in digital imaging. The wavelength information of the incoming light is discerned with the help of a dispersive color filter array.*

5.2 Experimental Details

5.2.1 Materials

Conducting transparent electrode, ITO (indium tin oxide) coated glass substrates (R_s = 8 Ω cm) were purchased from Xin Yan Technology Limited, China. For the perovskite precursors, Lead (II) iodide (PbI_2, 99.999%, 461 g/mol), Formamidium iodide (FAI, 99

%, 171.97 g/mol), Methylammonium iodide (MAI, Dyesol) and n-Butylammonium iodide (BAI, 98%, 201.05 g/mol) were obtained from Sigma Aldrich. Solvents N,N-Dimethylformamide (DMF, anhydrous 98.9%, 73.09 g/mol) and Chlorobenzene (anhydrous, 99.8 %) were obtained from Sigma Aldrich. Hole transporter, regioregular-poly3hexathiophene (rr-P3HT) and electron transporter, phenyl-C71-butyric acid methyl ester ($PC_{71}BM$) were obtained from Luminescence Technology Corporation, Taiwan. Additionally, (Poly(3,4-ethylene dioxythiophene)-poly(styrenesulfonate)) PEDOT:PSS (Al 4083) was obtained from Ossila.

5.2.2 Sample Preparation

***Preparation of graded perovskite films**:*

A 0.3M perovskite precursor was prepared by adding Butylammonium Iodide (BAI, Sigma Aldrich), Methylammonium Iodide (MAI, Dyesol) or (alternatively FAI), and Lead (II) Iodide (PbI_2, Sigma Aldrich) in 2:4:5 molar ratio respectively in N,N-Dimethylformamide (DMF, Alfa Aesar). The films were prepared by the hot-cast method. The glass substrates were first sonicated in Extran soap solution after which it was progressively cleaned with DI water, Acetone and IPA. These substrates were further treated with RCA solution which consists of solution in volumetric ratios of 6:1:1 of DI water, Ammonia solution (EMSURE) and Hydrogen Peroxide (SDFCL chemicals) respectively at 120°C for 20 min. This was followed by air plasma treatment for 5 min. The substrates were then transferred to the glove box in order to spin coat perovskite precursor solution under inert conditions. The substrates were first heated up to 150 °C for 10 min and then placed on the spin coater chuck onto which the hot perovskite precursor solution (60 °C) was dispensed immediately (~ 5 s) and spin-coated at 5000 rpm for 60 s.

Device Fabrication:

Using the 0.3M precursor solution, the graded bandgap devices were prepared using the hot- cast method. The patterned ITO coated glass substrates were sonicated in Extran soap solution and progressively cleaned with DI water, IPA and Acetone. The cleaned substrates were RCA treated at 120°C in a solution with volumetric ratios of 6:1:1 of DI water, Ammonia and hydrogen peroxide respectively followed by plasma treatment for 2 min. PEDOT:PSS (Ossila, PEDOT:PSS, AL 4083) solution was filtered using a 0.22 µm pore filter and spin coated onto ITO coated substrates at 4000 rpm for 60 s followed by annealing at 120 °C for 30 min. The ITO/PEDOT:PSS substrates were transferred to glovebox to spin coat the perovskite precursor under inert conditions. These substrates were heated for 10 min at 150 °C and transferred to the spin-coater chuck onto which the hot precursor solution was dispensed immediately (~5 s) and spin-coated at 5000 rpm for 60 s.

For the fabrication of *asymmetric electrode devices*, PCBM (Lumtec Corp.) was then spin-coated at 2000 rpm for 60 s from a 25 mg/ml solution in chlorobenzene (anhydrous, Sigma Aldrich). After annealing for 3 min at 100 °C, 100 nm of Ag was thermally evaporated using shadow masks to form the top electrode.

In the case of *symmetric electrode devices*, rr-P3HT (Lumtec Corp.) was spin-coated on the ITO/PEDOT:PSS/perovskite films at 2000 rpm for 60 s from a 14 mg/ml solution in chlorobenzene (anhydrous, Sigma Aldrich). After annealing for 3 min at 140 °C, both MoO_x (9 nm) and Ag (100 nm) were thermally evaporated using shadow masks to form the top electrode.

All the devices were encapsulated using UV-curable epoxy to reduce the effects of air and moisture-induced degradation.

5.2.3 Measurements and Characterization

Absorption Spectroscopy:

Thin-film absorption spectroscopy was performed using a UV/Vis/NIR spectrometer (PerkinElmer Lambda 750) in the transmission geometry. Graded perovskites spin-coated on glass slides were excited in the spectral range of 400 nm-850 nm and the absorption was measured simultaneously.

PL spectroscopy:

PL spectroscopy was performed on graded perovskite thin films. A 470 nm excitation laser source (PicoQuant GmbH LDH-P-C-470), operated using a laser driver (PicoQuant GmbH PDL 800-B), was incident on the sample and the reflected light after passing through a 500 nm long-pass filter was collected using a fiber-coupled mini spectrometer (Hamamatsu, C10083CA). The perovskite thin film coated on the glass slide was flipped to record the PL spectrum for light reflected from other side of the sample.

Photoluminescence Mapping:

Zeiss-700 confocal microscope is used to acquire the confocal images. A 488 nm laser diode was utilized to excite the sample. The emission spectra is collected using two different channels (PMTs) operating simultaneously. One of the channels had a long-pass 640 nm filter (red color used during image reconstruction) and the other had a short-pass 640 nm filter (green color used during image reconstruction). The two-channel measurements were then overlaid to construct the confocal maps. The pinhole used is 1 Airy unit.

Transient Absorption Spectroscopy:

Ultrafast measurements using femtosecond lasers were carried out in collaboration with Dr. R. Shivanna and Prof. R.H. Friend, University of Cambridge, UK.

For the transient absorption measurements, the fundamental output of a Ti:Sapphire amplifier system (Spectra-Physics Solstice) operating at 1 kHz (Pulse wavelength = 800 nm, pulse width = 90 fs) was split into two beams. One beam pulse was converted into the broadband visible probe by the home-built noncollinear optical parametric amplifier (NOPA). Another beam was passed through the second harmonic generation (SHG) beta barium borate crystal to generate the 400 nm pump pulse. 400 nm pump was used to excite the sample and visible broadband pulse is probed to observe the changes in the photo-induced absorption as a function of time. The pump and probe pulses are both incident from the same side of the sample. The delay between the pump and probe was obtained by the motorized translation stage. The pump and probe beams are overlapped onto the sample from the same side. The transmitted probe beam was collected with an InGaAs dual-line array detector (Hamamatsu G11608-512). The transmission difference was read out by a custom-built lock-in board from Stresing Entwicklungsbüro.

Transient Photocurrent:

The fundamental output of a Ti:Sapphire amplifier system (Spectra-Physics Solstice) operating at 1 kHz (Pulse wavelength = 800 nm, pulse width = 90 fs) was passed through the commercial optical parametric amplifier TOPAS (Light Conversion). The monochromatic light pulse (< 10 nm) from the TOPAS is incident on the device from the ITO side. The short-circuit photocurrent is measured across the 50 Ω resistor in series with the device. The data is acquired using Agilent Infiniium (DSO80304B, 40 GSa/s) oscilloscope.

Steady state pulsing measurements:

Steady-state measurements were performed on graded perovskite devices using commercially available LEDs. The LED was modulated using a function generator (Tektronix), and the same input was used as a trigger to sample the data from the graded perovskite device. The light was focused on the device area using an optical lens and the current was amplified using a pre-amplifier (Femto HCA-100M-50K-C, 50 kV/A, 100 MHz) before being input into the oscilloscope (LeCroy waveRunner 6100A, 1 GHz).

5.3 Results and Discussion

5.3.1 Evidence of graded bandgap

The Ruddlesden-Popper 2D-perovskites are synthesized by simple solution-processable techniques. The films prepared by spin coating the hot precursor solution on a hot substrate showed evidence of vertical phase separation. The degree of phase separation depends on the formation energy of the corresponding quantum well, the density of alkyl chains, and the temperature gradient during film formation[18, 19]. In agreement with earlier reports[10, 20], it is observed that the higher bandgap quantum well gets segregated towards the substrate and the low bandgaps segregate away from the substrate to form a graded-bandgap heterojunction structure. The film prepared by this method is effectively a mixed 2D/3D perovskite. Absorption for $BA_2FA_{n-1}Pb_nI_{3n+1}$ (FA = Formamidinium, BA = Butylammonium) and $BA_2MA_{n-1}Pb_nI_{3n+1}$ (MA = methylammonium) based 2D/3D systems in **Figure 5.2(a)** indicates features due to the presence of multiple order quantum wells along with 3D perovskite. Steady-state photoluminescence (PL) in **Figure 5.2(b)** measured in reflection geometry shows the difference in emission with the direction of illumination, due to the presence of graded

bandgap. When illuminated with a 470 nm source from the direction of the substrate, the relative emission from lower dimension quantum wells is higher in comparison to the emission when illuminated from the perovskite side, which is predominantly from the 3D phase.

5.3.1.1 PL and Confocal Microscopy

Bandgap gradation across the thickness of the film was also confirmed using confocal microscopy with 488 nm excitation. **Figure 5.2(c)** shows the z-stacking of reconstructed confocal images with green and red color indicating regions of emission below and above 640 nm emission respectively. Emission below 640 nm corresponds to emission from 2D and quasi-2D ($n < 4$) layers while the emission above 640 nm corresponds to higher order ($n > 4$) /3D perovskite emission. As can be observed from the vertical-stack images (**Figure 5.2(c)**), there is a gradual transition from the dominant 2D/ quasi-2D layer to dominant 3D layers indicating that the different layers in the film are not phase pure. However, the layers close to the substrate are predominantly 2D-type while the top layer is predominantly 3D-type.

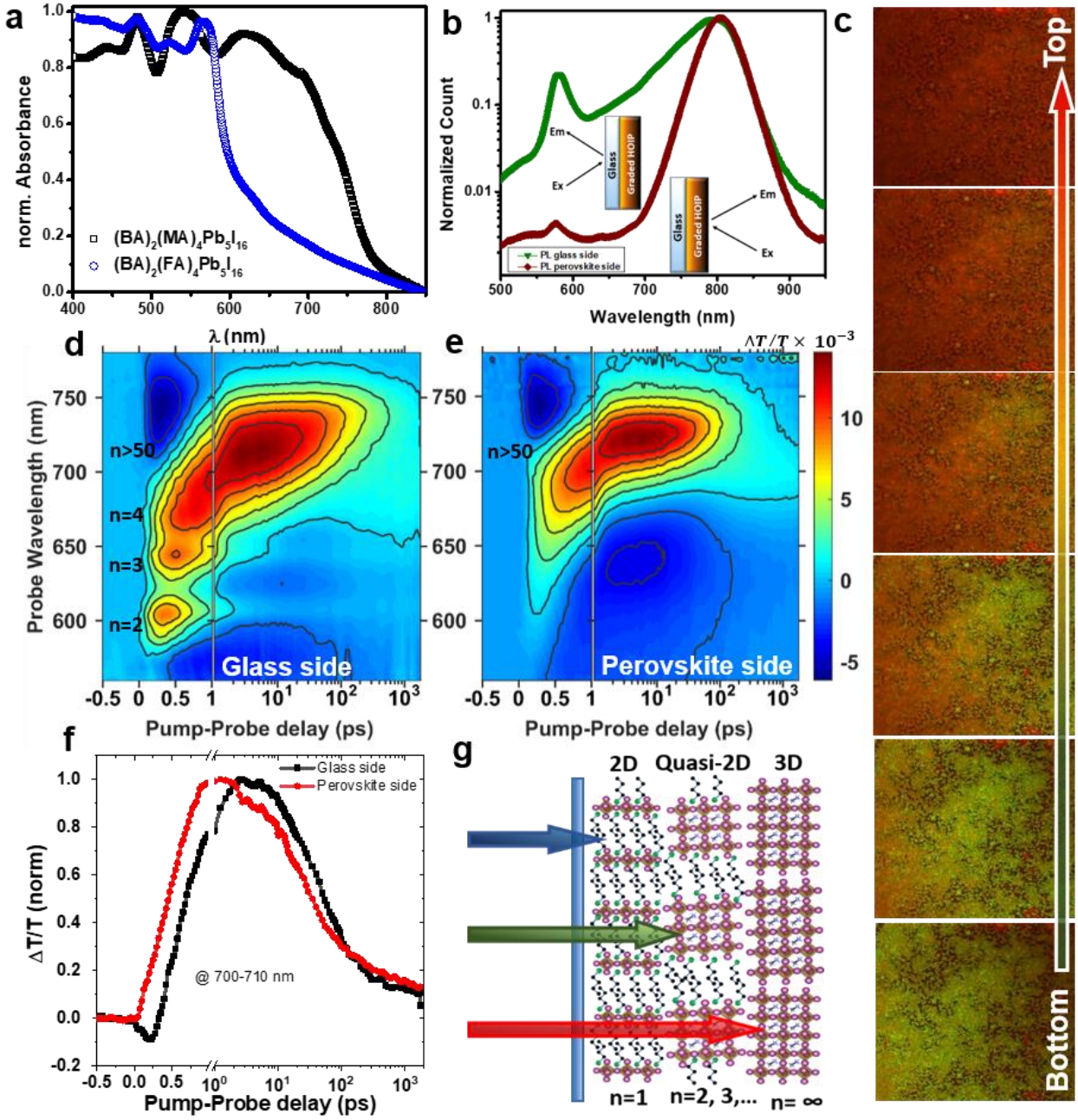

***Figure 5. 2**: **(a)** Normalized absorbance of mixed Ruddlesden-Popper perovskite film spin-coated on a glass substrate using precursor having an initial stoichiometry of $(BA)_2(FA)_4Pb_5I_{16}$ and $(BA)_2(MA)_4Pb_5I_{16}$. The absorbance indicates the excitonic peaks corresponding to bandgaps of different quantum wells. **(b)** Photoluminescence of the perovskite film measured in the reflection geometry from both perovskite and substrate sides. Relatively high 2D/quasi-2D emissions are observed when measured from the substrate side. **(c)** z-stack of confocal images with 488 nm excitation. Reconstructed*

images with green and red color for emission below and above 640 nm respectively. ***(d)*** *Transient absorption on layered perovskite showing predominant 3D GSB when probed from the perovskite side and* ***(e)*** *relatively high 2D/quasi-2D GSB from the substrate side at early times.* ***(f)*** *Kinetics of the GSB at 700-710 nm corresponding to the absorption of higher order QW's (n >50). The delayed growth of GSB when probed from the substrate side indicates the energy and charge funneling from lower order quantum wells to higher order (n > 50) perovskite.* ***(g)*** *Schematic showing the graded bandgap perovskite with higher order quantum wells and the 3D layer formed away from the substrate. (Reprinted with permission from Ganesh, N., Shivanna R, Friend R. H. and Narayan. K. S "Wavelength-dependent charge carrier dynamics for single pixel color sensing using graded perovskite structures." Nano letters 19, no. 9 (2019): 6577-6584, Copyright (2019) American Chemical Society)*

5.3.1.2 Transient Absorption

Ultrafast transient absorption (TA) spectroscopic measurements in the transmission geometry was performed to study the direction dependent charge carrier dynamics[15]. When the sample was pumped and probed from the glass substrate side, four distinct bleach-regions are observed spectrally at early time delay corresponding to the ground state bleaching (GSB) of quantum wells of different n's (n = 2, 3, 4, >50) as shown in **Figure 5.2(d)**. Bleach signal of lower order (n = 2, 3, 4) quantum wells (QW) rapidly recovers whereas the 3D/higher-order quantum wells QW's (n > 50) GSB increases over a few picoseconds, indicative of carrier/energy transfer from lower order QW's to higher order QW's. For comparison, the results of the same film when pump-probed from the perovskite side is shown in **Figure 5.2(e)**. The signal arising from GSB of the higher order QW's(n > 50) is dominated from an early time and GSB from the lower order QW's are merged in the signal. The kinetics of the GSB for higher

order QW's (700-710 nm), shown in **Figure 5.2(f)**, indicates a delayed growth when probed from the glass-side as compared to the perovskite-side. This direction dependent transient absorption measurement clearly indicates the graded structure of QW's of increasing order (or decreasing bandgap) perpendicular to the substrate plane (**Figure 5.2(g)**). This inference is consistent with the observed PL and confocal microscopic measurements. Therefore, the approximation of the 2D/3D perovskite film to graded bandgap sections where energy transfer processes are not dominant especially in a device structure is relevant to the λ-dependent I_{ph} analysis.

5.3.2 Asymmetric devices

Asymmetric perovskite devices were fabricated with electron and hole transporting layers to either side of the perovskite layer. Devices were fabricated on indium tin oxide (ITO) coated glass slides with deposition of PEDOT:PSS, followed by the MA-based graded perovskite layer ($BA_2MA_4Pb_5I_{16}$), then PCBM and finally deposition of silver as the top electrode. This structure (ITO/PEDOT:PSS/G-HOIP/PCBM/Ag), shown in **Figure 5.3(a)** is, referred to as an asymmetric device structure. The power conversion efficiency (PCE) and Incident Photon to electron Conversion Efficiency (IPCE) of these devices are about 4 % (**Figure 5.3(b)**) and 20 % (**Figure 5.3(c))** respectively. The low PCE can be attributed to the relatively lower mobility of the graded structure as compared to a pure 3D perovskite[21, 22].

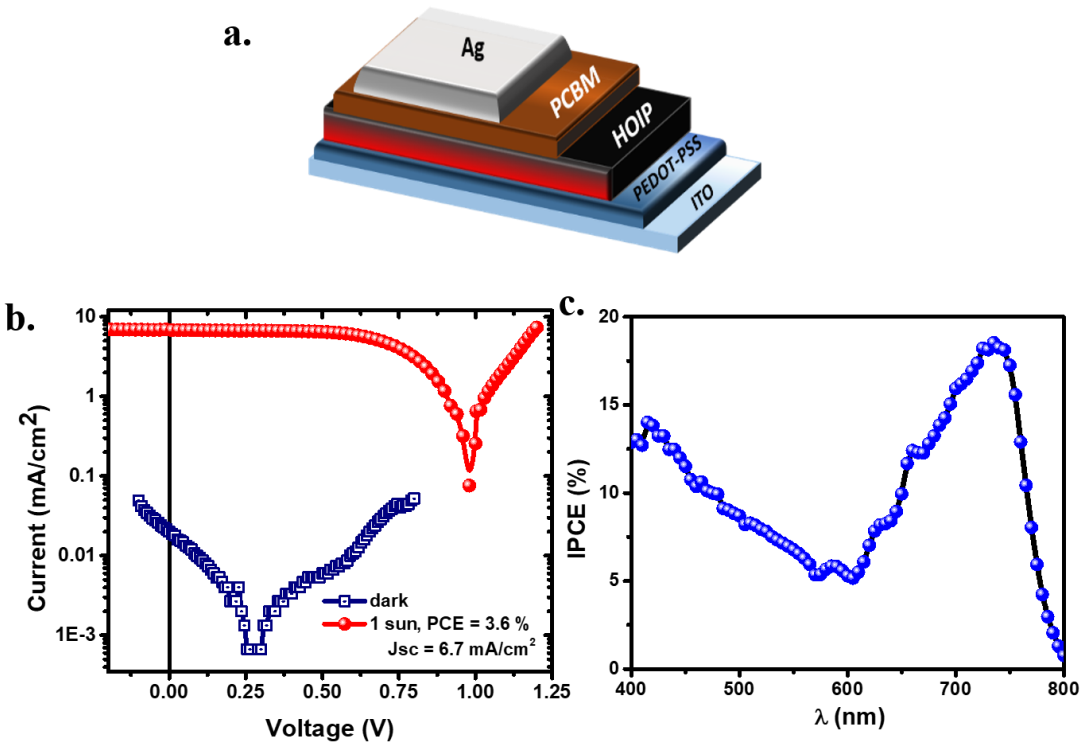

***Figure 5. 3**: **(a)**Schematic of the asymmetric device, consisting of electron and hole extraction layers on either side of the graded HOIP layer. **(b)** J(V) of asymmetric device with graded bandgap perovskite as the active layer done in dark and under 1 sun solar-spectrum, which show PCE of 3.6%. (c) IPCE data on asymmetric devices across the UV-Vis spectrum. (Reprinted with permission from Ganesh, N., Shivanna R, Friend R. H. and Narayan. K. S "Wavelength-dependent charge carrier dynamics for single pixel color sensing using graded perovskite structures." Nano letters 19, no. 9 (2019): 6577-6584, Copyright (2019) American Chemical Society)*

5.3.2.1 Transient Photocurrent on Asymmetric devices

Transient photocurrent measurements were performed for different λ of excitation using an ultrafast pulse (150 fs, 1 kHz rep rate, ~1 μJ/pulse), to study the carrier transport dynamics in the graded bandgap device (schematic in **Figure 5.4(a)**). The $I_{ph}(t)$ decay has similar profiles for different values of λ (450 nm < λ < 750 nm) as depicted in **Figure 5.4(b)**. A close analysis of the time associated with the rise-time and

peak in $I_{ph}(t)$ (**Figure 5.4(c)**), which corresponds to the response time of the carriers in the presence of the graded potential landscape, reveals that $I_{ph}(t)$ peaks for longer-λ excitation occur later than those corresponding to the short λ. Similarly, the $I_{ph}(t)$ decay lifetime increases with λ as shown in **Figure 5.4(d)** and **inset.** It was ascertained that the observed trend does not arise from inherent laser jitter whose timescales are orders of magnitude lower (< 1 ps) or delay in the incident light pulse. Since the observed delay is proportional to the distance of the charge generation plane to the hole collection layer (depicted in **Figure 5.4(a)**), the hole transit time is longer than the electron transit period. This inference is consistent with previous reports of unbalanced mobility with relatively higher electron mobility[23]. This observation is also congruent with previous transient spectroscopy measurements on these hierarchical systems, which have elegantly shown that the electron transfer rate is twice as fast as holes[15].

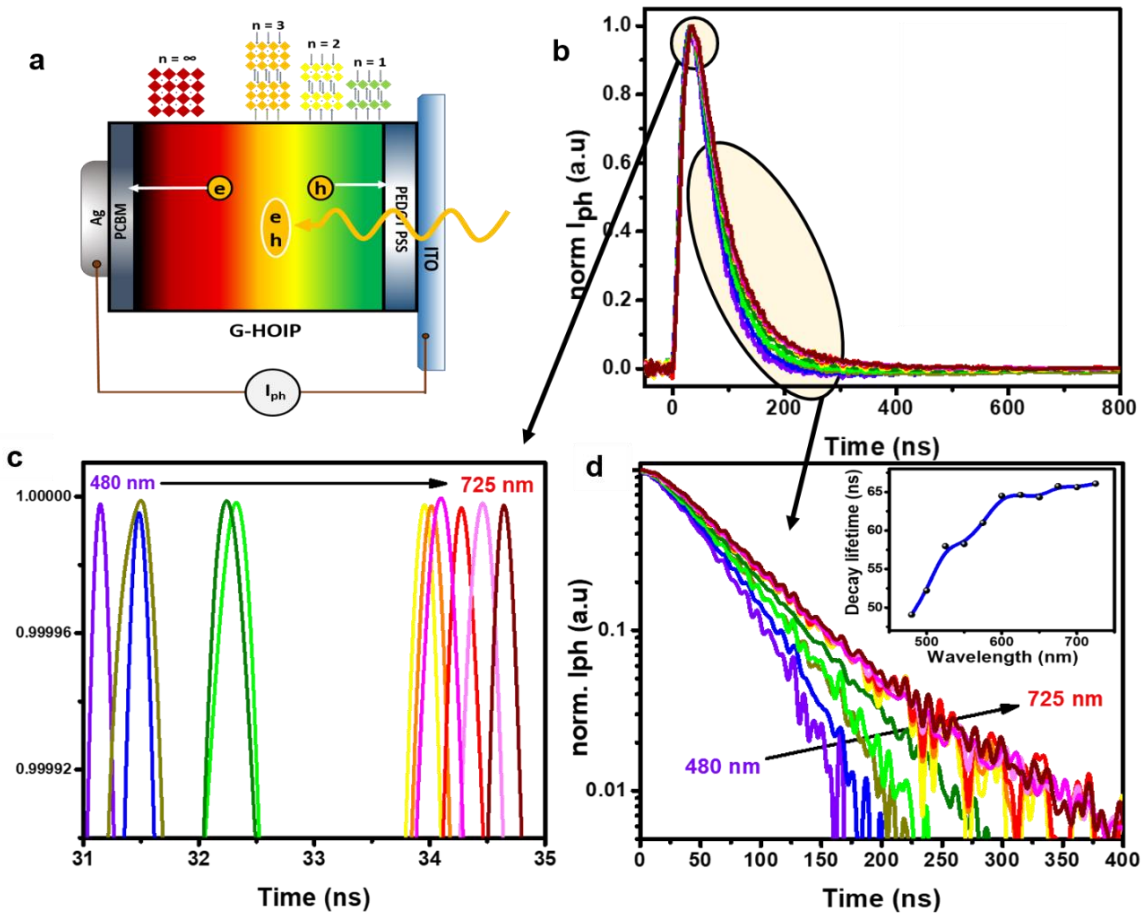

***Figure 5. 4**: **(a)** Graded bandgap perovskite asymmetric device structure (ITO/PEDOT:PSS/G-HOIP/PCBM/Ag) showing pathways for electron and hole transport. **(b)** Transient photocurrent response of asymmetric device upon excitation with a 150 fs pulse of different λ across the spectrum **(c)** Photocurrent peak time showing delay upon longer λ excitation. **(d)** I_{ph} decay lifetimes for different λ of excitation, shown in the log scale. **Inset** shows the steady increase of decay lifetime as a function of λ. (Reprinted with permission from Ganesh, N., Shivanna R, Friend R. H. and Narayan. K. S "Wavelength-dependent charge carrier dynamics for single pixel color sensing using graded perovskite structures." Nano letters 19, no. 9 (2019): 6577-6584, Copyright (2019) American Chemical Society)*

5.3.3 Symmetric hole-only devices

5.3.3.1 Transient Photocurrent on symmetric devices

Transient photocurrent measurements performed on a symmetric device reveals a complete reversal of the photocurrent-polarity (positive to negative) for two regimes of incident λ, corresponding to the highest and lowest band-gap levels in the graded structure. This feature is demonstrated by fabricating a hole-only device with PEDOT:PSS and poly(3-hexylthiophene-2,5-diyl) (P3HT) polymer, below and above the perovskite layer respectively, forming a symmetric hole-only device. **Figure 5.5(a)** shows the device schematic with the following configuration: ITO/PEDOT:PSS/G-HOIP/P3HT/MoO_x/Ag. Since the high bandgap region lies closer to the illumination plane (i.e., towards hole collecting ITO electrode) and the low bandgap region lies further into the backplane of the active layer, upon having only hole collection from either of the sides, the polarity or the direction of the extracted I_{ph} is reversed. This mechanism for charge extraction at short and long λ is also depicted in **Figure 5.5(a)**.

In the same line of reasoning, **Figure 5.5(b)** shows the λ-dependent $I_{ph}(t)$ characteristics. Upon irradiating with a 450 nm excitation, the transient shows the positive peak indicating hole extraction only across the perovskite/PEDOT:PSS interface. From 480 nm onwards, a negative peak appears which becomes significant as the λ increases. It is important to note that negative current appears even at these short λ, where absorption is maximum at the G-HOIP/PEDOT:PSS interface. This negative current corresponds to the free carriers that are generated and collected at the perovskite/P3HT interface as a result of charge/energy transfer from the lower-order quantum wells. This observation is correlated with TA profile (**Figure 5.2(d)**) and TA kinetics (**Figure 5.2(f)**) which indicates that in the first few picoseconds, for short-λ excitation, most of the excitons generated in lower order (higher bandgap) quantum

wells (near PEDOT:PSS/ITO) undergo energy and charge transfer to generate free carriers in the higher order (lower bandgap) quantum wells (near P3HT/Ag). In the device configuration, charge extraction across the selective contacts occurs in addition to energy/charge funneling to the higher order quantum wells[15, 20]. In our choice of a hole transporting layer, a small fraction of the carrier generation also occurs in the P3HT semiconducting layer[24]. These photogenerated carriers, due to the already decayed optical field in the G-HOIP layer, contribute only to the negative current[25].

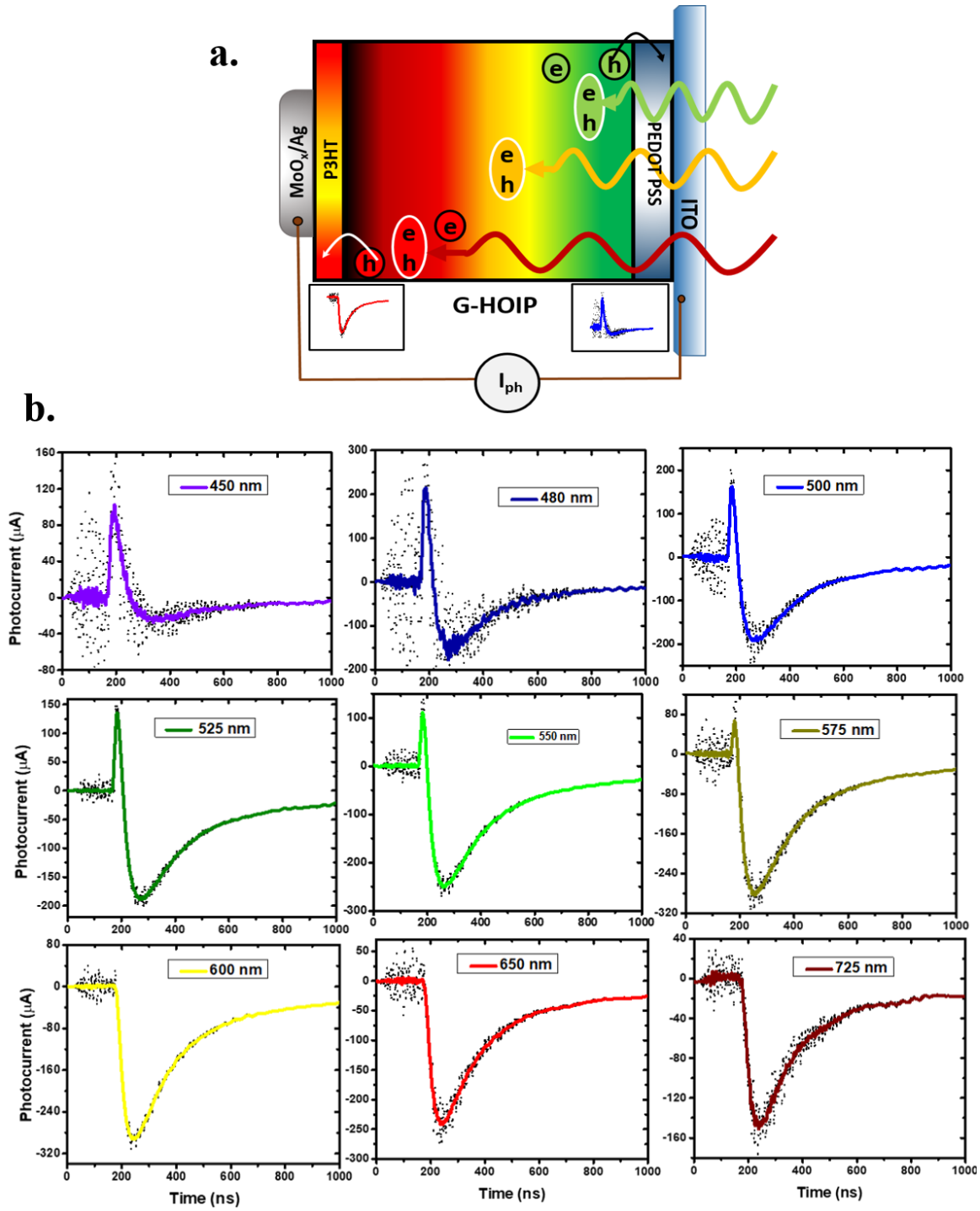

***Figure 5. 5**: **(a)** Schematic illustrating λ-dependent positive and negative currents in a symmetric hole-only device. Blue light generates and collects carriers at the PEDOT:PSS-perovskite interface giving rise to positive current while red light generates and collects carriers at perovskite-P3HT interface resulting in negative current. **(b)** $I_{ph}(t)$ profiles with the illumination of λ across the UV-Vis-NIR spectrum.*

Positive peaks are suppressed and negative peaks are enhanced upon increasing the λ of excitation. (Reprinted with permission from Ganesh, N., Shivanna R, Friend R. H. and Narayan. K. S "Wavelength-dependent charge carrier dynamics for single pixel color sensing using graded perovskite structures." Nano letters 19, no. 9 (2019): 6577-6584, Copyright (2019) American Chemical Society)

For $\lambda > 600$ nm, the transient $I_{ph}(t)$ exclusively exhibits a negative peak (**Figure 5.5(b)**), and for $\lambda < 450$ nm the transient $I_{ph}(t)$ exhibits a positive peak. In the window 450 nm $< \lambda <$ 600 nm, well-separated positive maxima and negative minima features are observed. Additionally, **Figure 5.6** shows that the λ-dependent $I_{ph}(t)$ profiles remain consistent over a range of excitation-intensity, although the component of the positive peak increases at a higher intensity. The magnitude of the maxima and minima can readily be used for color-sorting by noting the ratio of the corresponding amplitudes.

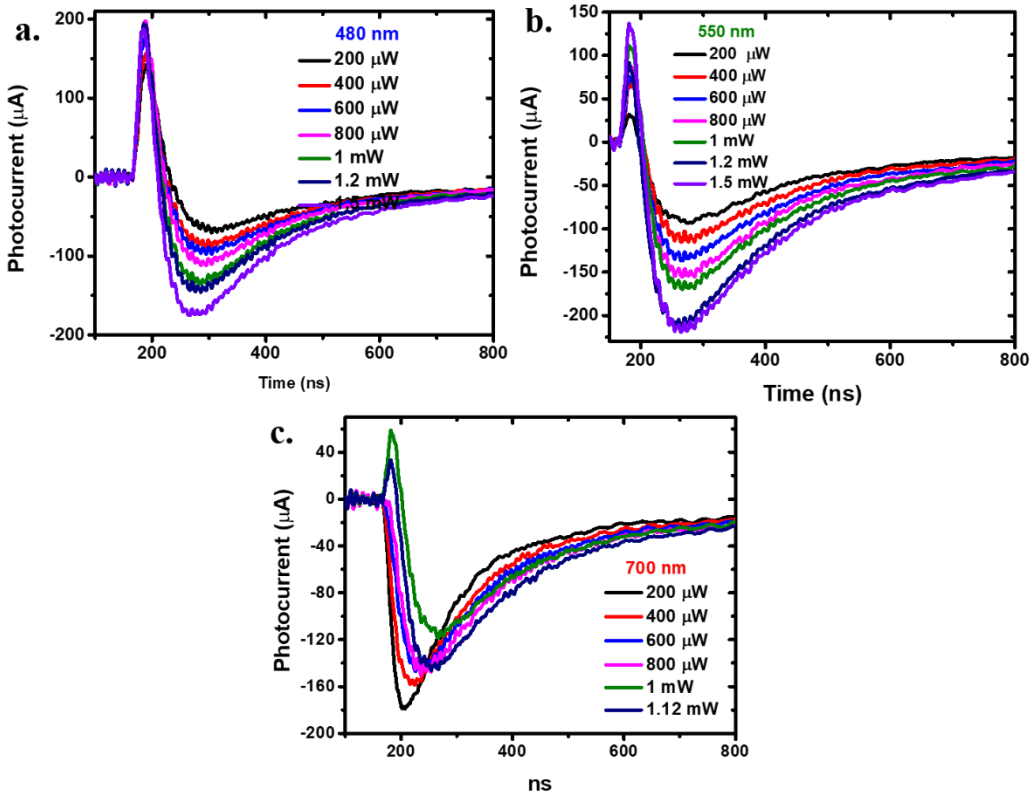

Figure 5. 6*: Ultrafast photocurrent on symmetric devices indicating intensity dependent photocurrent profile with illumination at* ***(a)*** *480 nm* ***(b)*** *550 nm and* ***(c)*** *700 nm. (Reprinted with permission from Ganesh, N., Shivanna R, Friend R. H. and Narayan. K. S "Wavelength-dependent charge carrier dynamics for single pixel color sensing using graded perovskite structures." Nano letters 19, no. 9 (2019): 6577-6584, Copyright (2019) American Chemical Society)*

5.3.3.2 Color-sensing scheme

The previous section describes the λ-dependent I_{ph} (t) characteristics, which can be used for color-sensing application. The resolution of wavelength identification can be further improved by analyzing: (i) initial slope of I_{ph}(t) upon photo-excitation and the (ii) derivative of I_{ph}(t) in the interval spanning I_{ph}^{max} and I_{ph}^{min}. This is illustrated schematically in **Figure 5.7(a)** and **(b)**, which shows λ-dependent normalized I_{ph}(t) profiles and their time-varying slope ($\frac{dI_{ph}(t)}{dt}$), respectively.

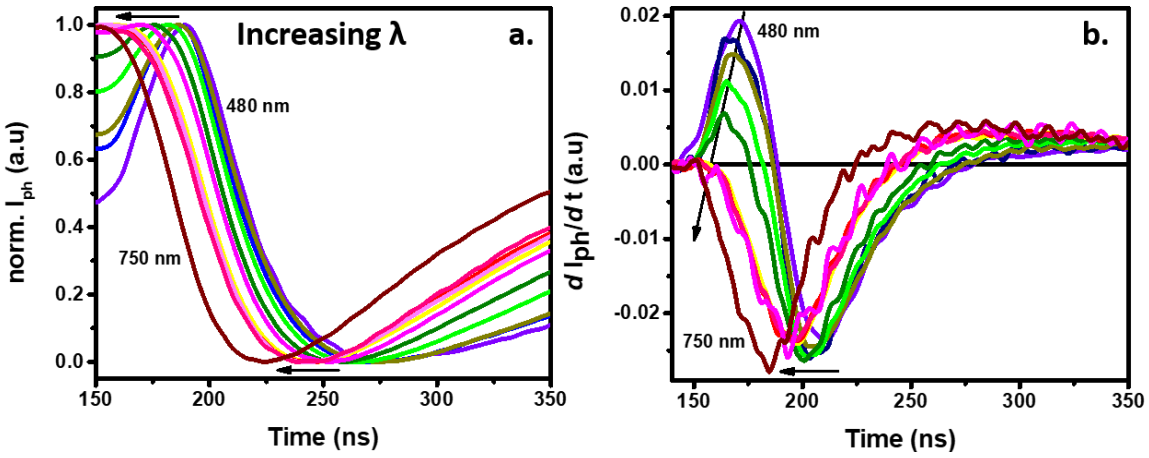

***Figure 5. 7**: **(a)** Photocurrent features (derived from **Figure 5.5(a)**), smoothed and normalized in the range [0, 1] show that the photocurrent minima appears earlier in case of longer wavelengths. **(b)** Slopes of photocurrent features showing an increased rate of charge extraction for lower wavelengths in the positive transients. The early arrival of I_{ph} minima is also reflected at the zero-crossing point.*

In principle, the resolution can be improved substantially with a precise algorithm. For example, **Figure 5.8(a)** shows a reasonable estimate of incident λ with a resolution of 10 nm, which was carried out by linear interpolation of $I_{ph}(t)$ based on experimentally extracted features from **Figure 5.5(b)**. This is further verified by a comparison of estimated $I_{ph}(t)$ with the experimentally obtained response. **Figure 5.8(b)** shows an excellent resemblance of the linearly interpolated $I_{ph}(t)$ profile with the experimentally obtained profile for incident 575 nm.

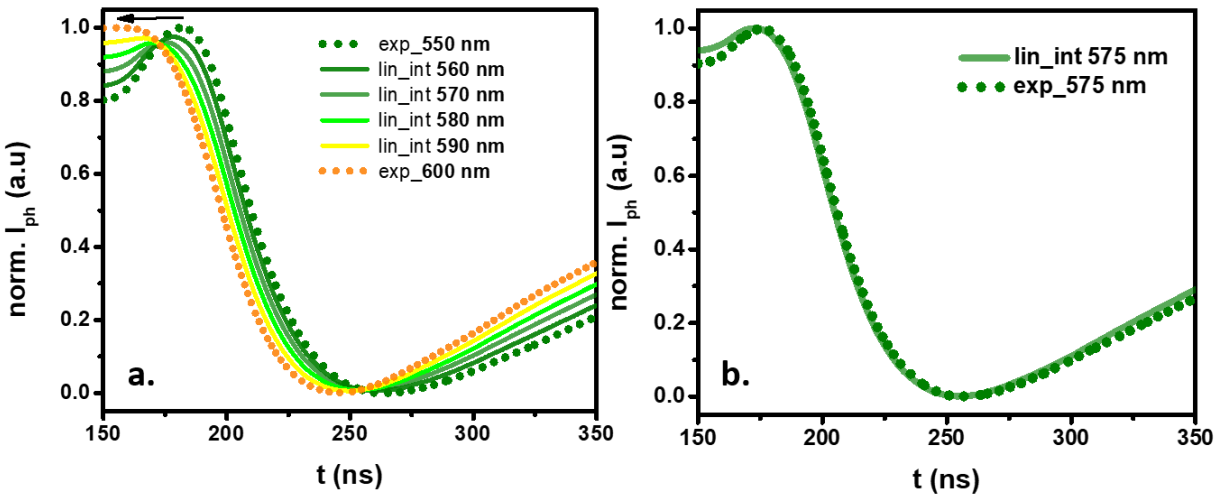

***Figure 5. 8**: **(a)** $I_{ph}(t)$ features (normalized in [0, 1]) determined by interpolation for λ in the interval between two experimentally acquired sets of data. $I_{ph}(t)$ were acquired at 550 nm and 600 nm. The intermediate features were obtained on linear interpolation. **(b)** The plot shows a good fit between the $I_{ph}(t)$ for 575 nm excitation and the feature obtained on interpolation.*

The key process here is the initiation of photogenerated-hole transfer processes from the interfacial region to the cathode (ITO side for incident blue-λ) and to the anode (Ag side for incident red-λ), accompanied by electron and hole transport within the bulk. The apparently symmetric responses $I_{ph}(t)$ of different polarity to the blue-λ and red-λ at short timescale is accompanied by a discernable asymmetry of $I_{ph}(t)$ at longer *t*. This difference in $I_{ph}(t)$ responses for blue-λ and red-λ primarily arises from the variation in the barriers[26] for the *e*/*h* transport in bulk. The gradient in the 2D/3D quantum structure and the differences in the potential landscape for *e*/*h* manifests as λ dependent $I_{ph}(t)$.

5.3.4 Color sensing with steady-state illumination

The reproducibility of the transient response to a single pulse is also evident in steady-state measurements. In this study, steady-state measurements involve periodic light

pulsing where the I_{ph} response is a measure of the long-term average of carrier generation and transport. The preservation of the characteristic λ-dependent I_{ph} features, in the absence of ultrafast lasers in the measurement set-up, extends the utility of these detectors. Parameters such as the λ dependent t_{peak} (corresponding to $I_{ph}^{max/min}$) observed in response to the single narrow pulse is now represented by the off-cycle decay features. The resolution for λ identification is controlled by measurement parameters (driving period and duty cycle). The following sections demonstrate a simple protocol, using which, chromatic sources can be identified within a reasonable error range using steady-state measurements. Since the response now does not contain the characteristic fast features of a single transient pulse, the features of the slower dynamic components of the cumulative response are utilized, which are preserved in the measurement frequency (ω) range.

5.3.4.1 Photo-response in Asymmetric devices

Figure 5.9(a) shows the photocurrent response in an asymmetric device along with the λ-dependent off-cycle features (**Figure 5.9(b)**). These measurements were studied using periodic monochromatic photo-excitation (LED, 10 kHz, 50 % duty cycle) at different λ: 460 nm (11.3 mW cm^{-2}), 530 nm (10.4 mW cm^{-2}), 630 nm (5.9 mW cm^{-2}) and 725 nm (6.5 mW cm^{-2}) covering the span of Vis-NIR region. In all the color responses that were studied, the photon flux for different λ was comparable (~ 2×10^{16} photons/cm^2). The off-cycle features can be modeled as the photocurrent response corresponding to an equivalent electrical circuit. The $I_{ph}(t)$ signal from the G-HOIP device indicates the presence of both resistive and capacitive components in the equivalent-circuit network[27]. The equivalent circuit description shown in **Figure 5.9(c)** provides a simplistic representation of the physical processes where, R_{ser}, R_{sh}, and R_{bulk}

are the series, shunt and bulk resistance respectively, and the 1 µA current source being equivalent to carrier photogeneration.

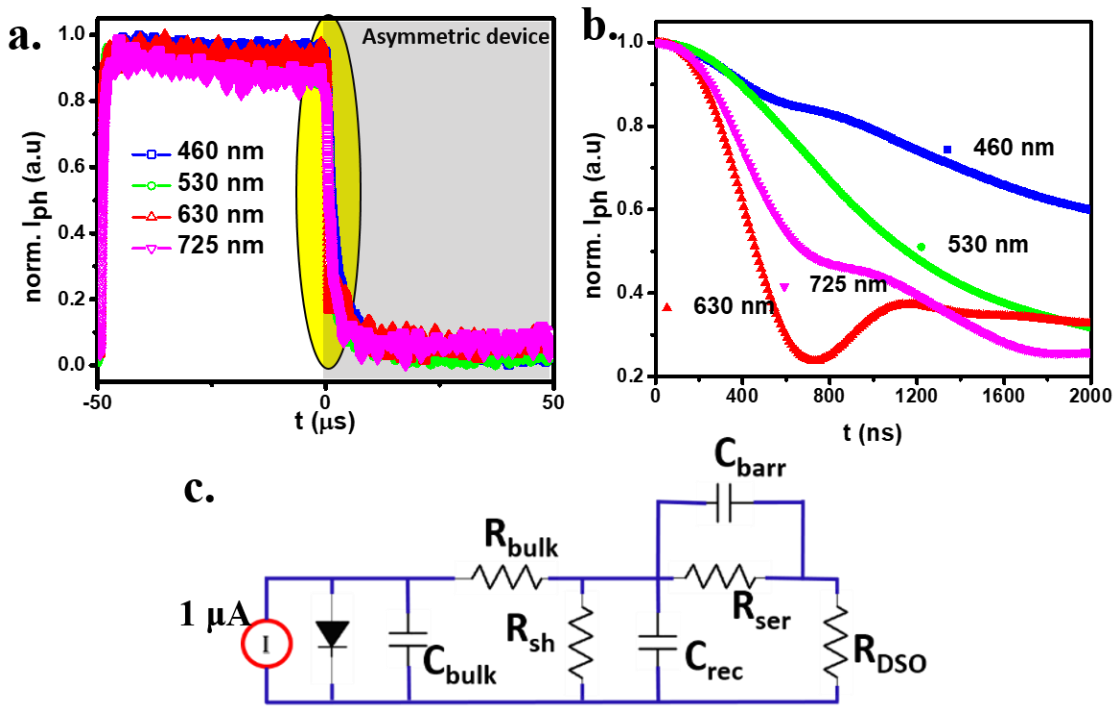

***Figure 5. 9**: **(a)** Pulsed response in an asymmetric device. The shaded region represents the light OFF-cycle part of the pulse. **(b)** λ-dependent off-cycle features on the asymmetric device. **(c)** Equivalent circuit diagram to model the photocurrent decay features obtained in (b). (Reprinted with permission from Ganesh, N., Shivanna R, Friend R. H. and Narayan. K. S "Wavelength-dependent charge carrier dynamics for single pixel color sensing using graded perovskite structures." Nano letters 19, no. 9 (2019): 6577-6584, Copyright (2019) American Chemical Society)*

In the perovskite solar cells, capacitive contributions to the I_{ph} have been reported [28-31]. To capture the respective network contributions of the observed photocurrent over a wide time scale[32, 33], the circuit simulation results were compared to the response in an

asymmetric device. It is additionally noted that these OFF-cycle features are maintained over a range of light-intensity, as shown in **Figure 5.10**.

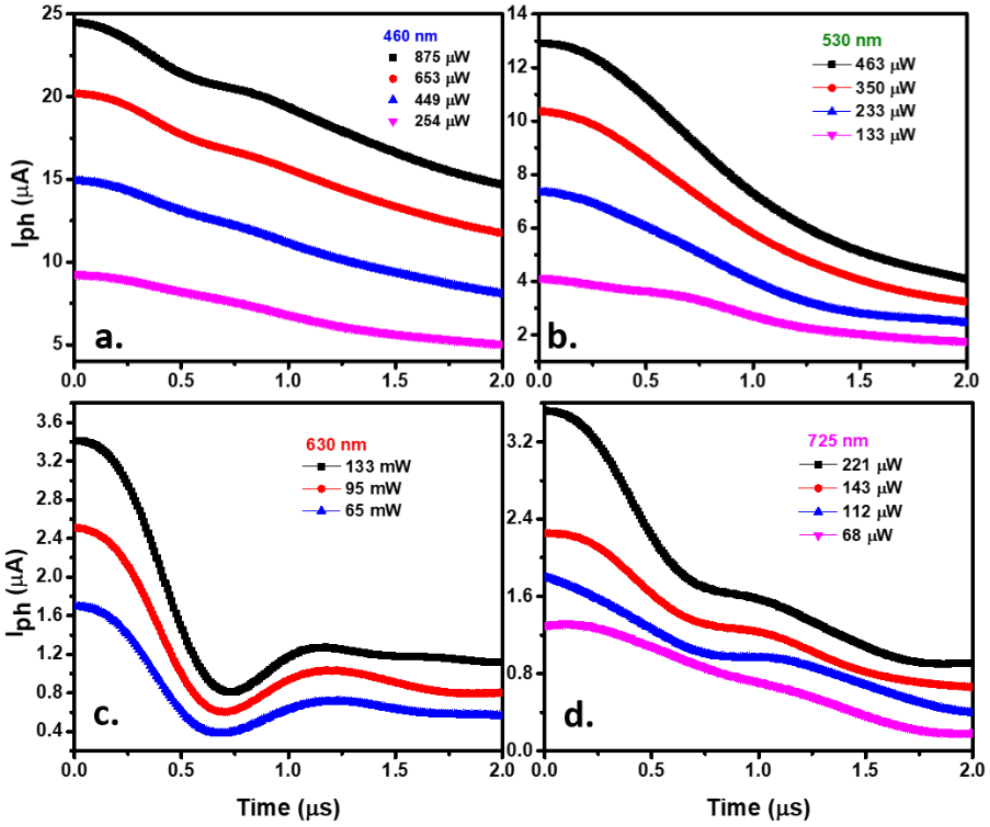

***Figure 5. 10**: OFF-pulse $I_{ph}(t)$ profiles upon steady-state pulsing illumination in **(a)** blue **(b)** green **(c)** red and **(d)** NIR region of the visible spectrum.*

5.3.4.2 Equivalent circuit representation of off-cycle features in asymmetric devices.

In a p-i-n perovskite solar cell, the device is generally modeled based on two capacitive contributions: recombination capacitance (C_{rec}) and total/bulk capacitance (C_{bulk})[29]. C_{rec} is the equivalent representation of carrier decay due to recombination in a device accompanied by a characteristic time constant namely the recombination lifetime. C_{bulk} is the net capacitance experienced by the photogenerated charge carriers during transport across the bulk (thickness) of the device layer and the interfacial regions. In the case of layered G-HOIP devices, the additional capacitive contribution associated

with the organic-linker in between the two quantum well layers also needs to be considered. This barrier capacitance (C_{barr}) acts as an accumulation center for the photogenerated carriers. These capacitive contributions have been included in the equivalent circuit depicted in **Figure 5.9(c).**

To study of contributions from each of the capacitive elements, the equivalent of light pulsing measurements was simulated using a circuit-simulation software, MultiSim. The time-varying light pulse was represented by a pulsed current source (**Figure 5.9(c)**). The simulation results in **Figure 5.11(a)**, **(b),** and **(c)** are the current across R_{DSO} (50 Ω input impedance of Digital Signal Oscilloscope, DSO) for variation in C_{bulk}, $C_{rec,}$ and C_{barr} respectively. From the representation given in **Figure 5.11(b)**, it is evident that the off-cycle features consist of 3 distinct time-scales:

(i) Fast-decaying timescale parameter: t_{decay}

(ii) Slow-decaying timescale parameter: t_{rec}

(iii) Timescale corresponding to reverse-current capacitive discharge: t_{dis}

The $I_{ph}(t)$ OFF-pulse response can be effectively modeled as a combination of the decay timescales unique to the temporal profile corresponding to the incident λ. However, for an accurate estimation of the carrier lifetimes involved in the λ-dependent trends, a detailed characterization of microstructure and the associated dynamics of the physical processes involved are needed.

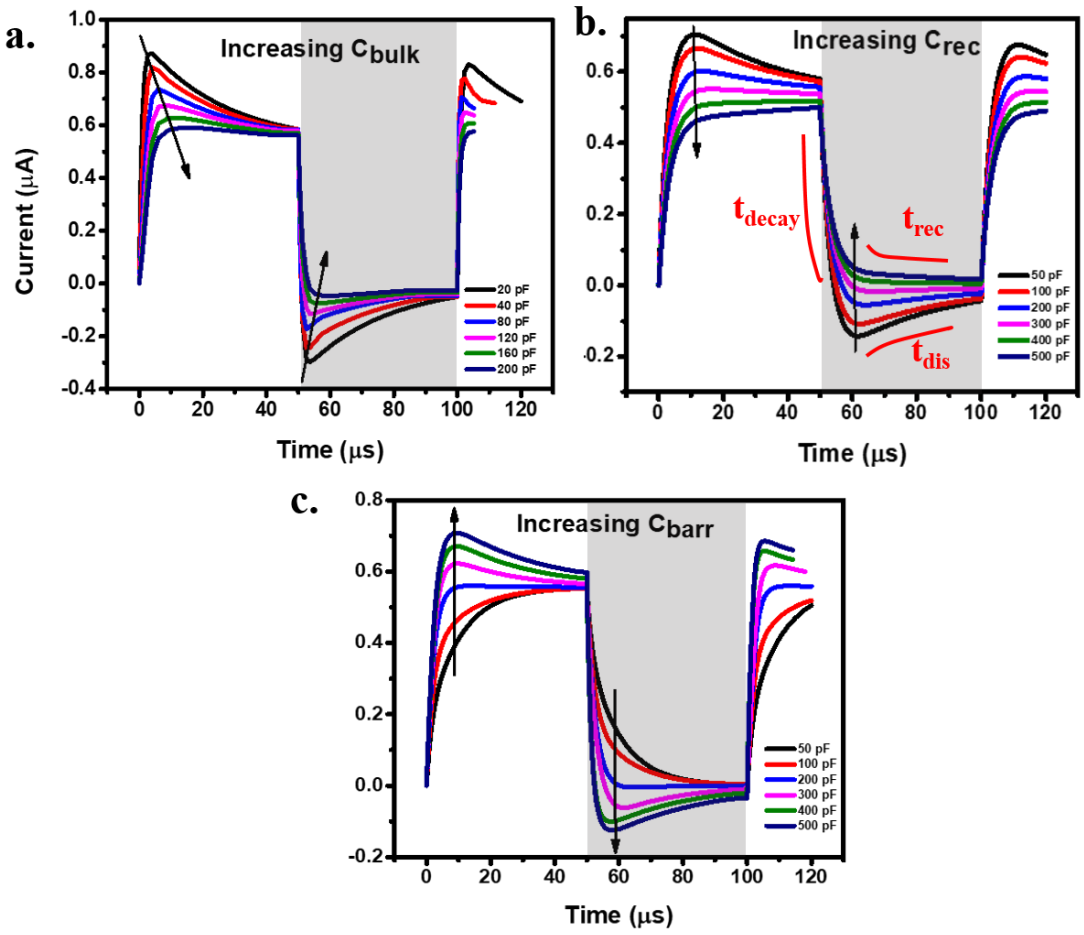

Figure 5. 11*:*(a) *Simulated current profiles for light pulsing operation measured across digital signal analyzer (R_{DSO}) in* ***Figure 5.9(c)*** *for varying C_{bulk},* ***(b)*** *C_{rec} and* ***(c)*** *C_{barr}. The shaded region represents the light OFF-cycle part of the pulse.*

5.3.4.3 Photo-response in symmetric devices

Prior to studying the photocurrent response in the symmetric graded bandgap device, photocurrent responses were measured on controlled symmetric devices, which consisted of pristine 3D perovskite in the active layer. The data in **Figure 5.12** shows the normalized photocurrent response on control symmetric devices which contains the prototypical $MAPbI_3$, in the following device configuration: ITO/PEDOT:PSS/3D-$MAPbI_3$/P3HT/Ag. This confirms the absence of λ-dependent current-reversal behavior at higher λ-excitations.

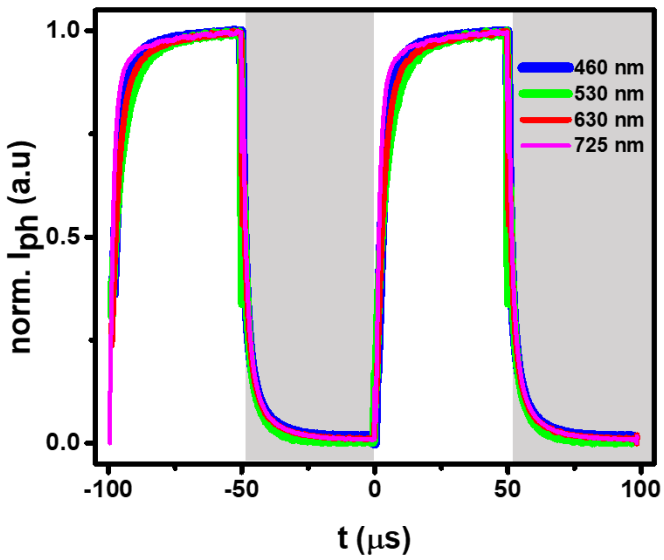

Figure 5. 12*: Steady-state light pulsing measurement of control (3-D) symmetric device in short-circuit mode, using a preamplifier and digital signal oscilloscope. The device configuration in this case was: ITO/PEDOT:PSS/3D-MAPbI$_3$/P3HT/Ag. The bright regions represent the ON part and the shaded regions represent the OFF part of the light pulse.*

On the other hand, the response of the symmetric device with graded perovskite in the active layer shows λ-dependent polarity reversal. **Figure 5.13(a)** and **(b)** shows the response of the symmetric device structure, with a graded band-gap in the active layer. After illuminating the light pulse, the off-cycle currents in **Figure 5.13(c)** were analyzed for photoresponse. Off-cycle current features correspond to initial I_{ph} decay in the off-cycle of light pulsing[34]. As expected, the blue and green illumination generates a positive I_{ph} while the red and nir light generate a negative I_{ph}, which is in agreement with results obtained from ultrafast transient measurements (**Figure 5.5(b)**). A closer look into the off-cycle $I_{ph}(t)$ in **Figure 5.13(c)** reveals decay features that are dependent on the incident wavelength. Additionally, the IPCE in **Figure 5.13(d)**

exhibits enhanced charge collection at either end (λ > 600 nm and λ < 450 nm) of the UV-Vis spectrum.

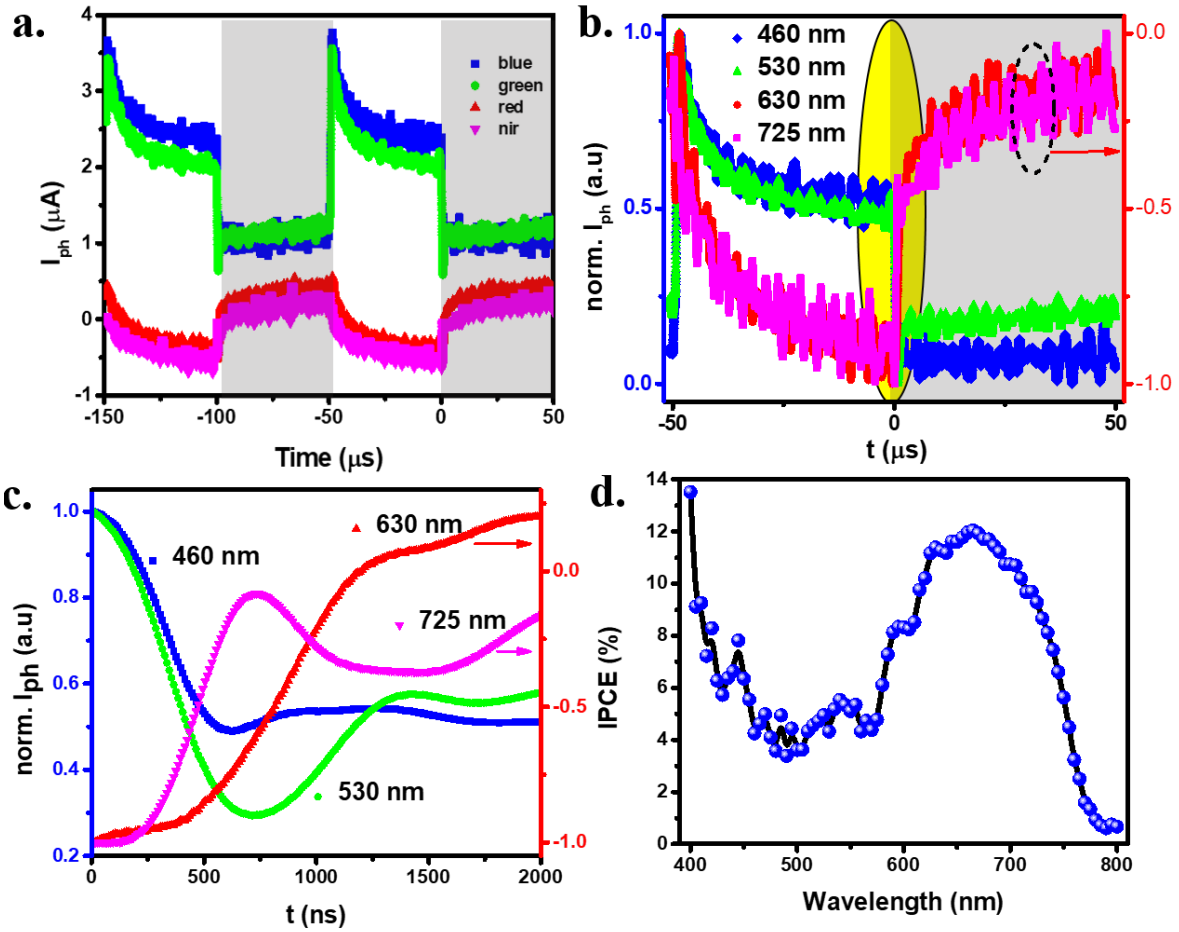

Figure 5. 13:(a) *Short-circuit current its* ***(b)*** *normalised plot measured on the symmetric hole only devices with light pulsing at 10 kHz, showing polarity reversal for long-λ illumination. The shaded region represents the light OFF-cycle part of the pulse. The yellow highlighted region represents the off-cycle features* ***(c)*** *showing I_{ph} decay at different λ of illumination.* ***(d)*** *IPCE of the symmetric hole only device across the spectrum. (Reprinted with permission from Ganesh, N., Shivanna R., Friend R. H. and Narayan K. S. "Wavelength-dependent charge carrier dynamics for single pixel color sensing using graded perovskite structures." Nano letters 19, no. 9 (2019): 6577-6584, Copyright (2019) American Chemical Society)*

The above observed λ-dependent polarity (in **Figure 5.13(c)**) is an added feature that can be utilized in addition to the OFF-cycle decay profiles discussed in the previous section. The simulated off-cycle I_{ph} behavior follows similar trends as seen in the case of an asymmetric device with only polarity being different. The analysis of these results can then yield a look-up table for the appropriate parameter required for predicting the incident λ across the entire visible spectral range. This method offers an alternative procedure for color sensing where the observed features are cumulative effects of dominant resistive pathways accompanied by the capacitive network.

5.3.5 Use of graded band-gap devices for spectral resolution

The characteristic $I_{ph}(t)$ response is utilized to extract the wavelength information using the graded band-gap device structures. Unlike the conventional method, where an array of color filters (RGB) is used to extract the wavelength information, a different approach towards this objective was previously pursued in our laboratory, which demonstrated the possibility of using a semiconducting polymer-electrolyte-based device structure for multicolor sensing[35, 36]. This color sensing method relied on an appropriate thickness of the active polymer layer in contact with a liquid-electrolyte layer which results in a characteristic polarity and temporal profile of the photocurrent signal in response to various incident colors[35, 36]. However, the detection scheme involved slow timescales (~ ms) due to the dominant presence of the Helmholtz capacitance layer and are more suited for bio-mimicking electrophysiological processes, particularly, human-vision characteristics [36]. The present approach permits the implementation of a temporal detection scheme for color sensing using graded-bandgap hybrid perovskite, without the presence of a Helmholtz layer and a liquid layer. Consequently, this single-pixel sensor has unique λ-dependent photocurrent profiles at

faster timescales (10 ns -100 ns), unique to spectrally pure excitation (FWHM < 10 nm).

A polychromatic excitation can be spectrally resolved using interesting application themes, incorporating the λ-dependent features of the photo-detector. Since the total lifecycle of the transient features which emerge and decay can be controlled to reside within 100 ns, sequence of light pulses of different λ incident at rates > 100 ns can be detected and spectrally resolved serially. In essence, time-resolved λ identification can be achieved by a single element HOIP photo-detector. The requirements for the light-pulses fall in the temporal range typically involved in emission from molecules with fluorescence and phosphorescence components. Conceptually, a polychromatic signal with temporally separated constituent λs, can be identified. **Figure 5.14** represents a schematic showing the capability of this technique for polychromatic signal detection using optical time-division multiplexing (OTDM)[37]. A polychromatic source is first de-multiplexed into various channels corresponding to the constituent λ. The mechanism of de-multiplexing can be carried out by many methods using prisms and GRIN (graded-index) lens [38-40]. Once the light is incident in these channels, an optical time delay is introduced into successive channels before they are multiplexed back into a single optical fiber[41]. The light incident on the single-pixel sensor generates a time series response which can be reconstructed to give the spectral information.

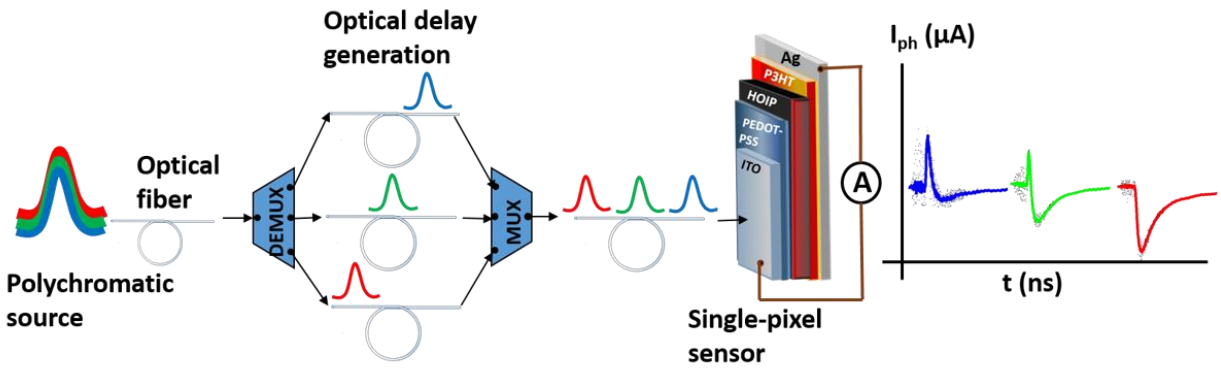

Figure 5. 14*: Schematic explaining the possibility of time-resolved wavelength identification by the single-pixel sensor using optical time division multiplexing (OTDM). (Reprinted with permission from Ganesh, N., Shivanna R, Friend R. H. and Narayan. K. S "Wavelength-dependent charge carrier dynamics for single pixel color sensing using graded perovskite structures." Nano letters 19, no. 9 (2019): 6577-6584. Copyright (2019) American Chemical Society)*

5.4 Conclusion

The hierarchical Ruddlesden-Popper hybrid perovskite featuring vertically graded bandgap devices are utilized to observe characteristic λ-dependent I_{ph} response due to the unique carrier generation profile in the thickness of the active layer. The symmetric electrode (hole only) device exhibited polarity reversal of photocurrent signal as the incident λ is spanned across the visible spectrum. In the case of transient single-pulse measurements, a spectrally pure incident λ, with an FWHM of < 10 nm, provides a unique $I_{ph}(t)$ feature which cannot be reconstructed by any other combination of λ response. In the case of multiple-photon excitation sources (comprising of different λ), the photocurrent response features are expected to deviate from a simplistic additive effect, since the charge dynamics are influenced by the potential landscape due to carriers generated in a different plane of the active layer. Further investigation in this

line of approach along with appropriate models should enable tailored detectors for multi-photon characterization.

Additionally, the observed fast I_{ph} response (~ 100's of ns) permits sequential detection of light pulses by a single pixel and opens up new applications. The resolution of the λ-identification, upon obtaining the $I_{ph}(t)$ feature, can be enhanced manifold using a suitable interpolation algorithm during spectral reconstruction. Further, a spatially patterned detector array with these features can in principle, be introduced in a optical microscopy setup to provide additional dynamic information, such as live-cell imaging studies. The electronic representation of light properties with minimal optical elements offers interesting design concepts in color capture and representations.

References

1. Wu D, *et al.* Welding Perovskite Nanowires for Stable, Sensitive, Flexible Photodetectors. *ACS nano* **14**, 2777-2787 (2020).
2. Zhao Q, *et al.* High efficiency perovskite quantum dot solar cells with charge separating heterostructure. *Nature communications* **10**, 1-8 (2019).
3. Kumar P, Ganesh N, Narayan K. Electrospun fibers containing emissive hybrid perovskite quantum dots. *ACS applied materials & interfaces* **11**, 24468-24477 (2019).
4. Kumar P, Muthu C, Nair VC, Narayan K. Quantum confinement effects in organic lead tribromide perovskite nanoparticles. *The Journal of Physical Chemistry C* **120**, 18333-18339 (2016).
5. Stoumpos CC, Kanatzidis MG. Halide Perovskites: Poor Man's High-Performance Semiconductors. *Advanced Materials* **28**, 5778-5793 (2016).
6. Raghavan CM, *et al.* Low-Threshold Lasing from 2D Homologous Organic–Inorganic Hybrid Ruddlesden–Popper Perovskite Single Crystals. *Nano letters* **18**, 3221-3228 (2018).
7. Cao DH, Stoumpos CC, Farha OK, Hupp JT, Kanatzidis MG. 2D homologous perovskites as light-absorbing materials for solar cell applications. *Journal of the American Chemical Society* **137**, 7843-7850 (2015).
8. Li MH, *et al.* Highly Efficient 2D/3D Hybrid Perovskite Solar Cells via Low-Pressure Vapor-Assisted Solution Process. *Advanced Materials* **30**, 1801401 (2018).
9. Qiao S, Feng K, Li Z, Fu G, Wang S. Ultrahigh, ultrafast and large response size visible-near-infrared optical position sensitive detectors based on CIGS structures. *Journal of Materials Chemistry C* **5**, 4915-4922 (2017).
10. Zhao B, *et al.* High-efficiency perovskite–polymer bulk heterostructure light-emitting diodes. *Nature Photonics* **12**, 783-789 (2018).
11. Tsai H, *et al.* High-efficiency two-dimensional Ruddlesden–Popper perovskite solar cells. *Nature* **536**, 312 (2016).
12. Cao DH, *et al.* Thin Films and Solar Cells Based on Semiconducting Two-Dimensional Ruddlesden–Popper (CH3 (CH2) 3NH3) 2 (CH3NH3) n− 1Sn n I3 n+ 1 Perovskites. *ACS Energy Letters* **2**, 982-990 (2017).
13. Hong X, Ishihara T, Nurmikko A. Dielectric confinement effect on excitons in PbI 4-based layered semiconductors. *Physical Review B* **45**, 6961 (1992).
14. Traore B, *et al.* Composite Nature of Layered Hybrid Perovskites: Assessment on Quantum and Dielectric Confinements and Band Alignment. *ACS nano* **12**, 3321-3332 (2018).
15. Liu J, Leng J, Wu K, Zhang J, Jin S. Observation of internal photoinduced electron and hole separation in hybrid two-dimentional perovskite films. *Journal of the American Chemical Society* **139**, 1432-1435 (2017).
16. Long M, *et al.* Interlayer Interaction Enhancement in Ruddlesden–Popper Perovskite Solar Cells toward High Efficiency and Phase Stability. *ACS Energy Letters* **4**, 1025-1033 (2019).
17. Hwang I, McNeill CR, Greenham NC. Drift-diffusion modeling of photocurrent transients in bulk heterojunction solar cells. *Journal of Applied Physics* **106**, 094506 (2009).
18. Li L, *et al.* Unraveling the growth of hierarchical Quasi-2D/3D perovskite and carrier dynamics. *The journal of physical chemistry letters* **9**, 1124-1132 (2018).

19. Quan LN, *et al.* Ligand-stabilized reduced-dimensionality perovskites. *Journal of the American Chemical Society* **138**, 2649-2655 (2016).
20. Qing J, *et al.* Aligned and Graded Type-II Ruddlesden–Popper Perovskite Films for Efficient Solar Cells. *Advanced Energy Materials*, 1800185 (2018).
21. Kamminga ME, *et al.* Confinement effects in low-dimensional lead iodide perovskite hybrids. *Chemistry of Materials* **28**, 4554-4562 (2016).
22. Chen Y, Sun Y, Peng J, Tang J, Zheng K, Liang Z. 2D Ruddlesden–Popper perovskites for optoelectronics. *Advanced Materials* **30**, 1703487 (2018).
23. Tsai H, *et al.* Stable Light-Emitting Diodes Using Phase-Pure Ruddlesden–Popper Layered Perovskites. *Advanced Materials* **30**, 1704217 (2018).
24. Kim Y, *et al.* A strong regioregularity effect in self-organizing conjugated polymer films and high-efficiency polythiophene: fullerene solar cells. In: *Materials For Sustainable Energy: A Collection of Peer-Reviewed Research and Review Articles from Nature Publishing Group* (ed^(eds). World Scientific (2011).
25. Conings B, Baeten L, De Dobbelaere C, D'Haen J, Manca J, Boyen HG. Perovskite-based hybrid solar cells exceeding 10% efficiency with high reproducibility using a thin film sandwich approach. *Advanced Materials* **26**, 2041-2046 (2014).
26. Chao L, Niu T, Xia Y, Ran X, Chen Y, Huang W. Efficient and Stable Low-Dimensional Ruddlesden–Popper Perovskite Solar Cells Enabled by Reducing Tunnel Barrier. *The journal of physical chemistry letters* **10**, 1173-1179 (2019).
27. Miller G, Ramirez J, Robinson D. A correlation method for semiconductor transient signal measurements. *Journal of Applied Physics* **46**, 2638-2644 (1975).
28. Almora O, Zarazua I, Mas-Marza E, Mora-Sero I, Bisquert J, Garcia-Belmonte G. Capacitive dark currents, hysteresis, and electrode polarization in lead halide perovskite solar cells. *The journal of physical chemistry letters* **6**, 1645-1652 (2015).
29. Pockett A, *et al.* Characterization of planar lead halide perovskite solar cells by impedance spectroscopy, open-circuit photovoltage decay, and intensity-modulated photovoltage/photocurrent spectroscopy. *The Journal of Physical Chemistry C* **119**, 3456-3465 (2015).
30. Guerrero A, *et al.* Properties of contact and bulk impedances in hybrid lead halide perovskite solar cells including inductive loop elements. *The Journal of Physical Chemistry C* **120**, 8023-8032 (2016).
31. Almora O, Aranda C, Mas-Marzá E, Garcia-Belmonte G. On Mott-Schottky analysis interpretation of capacitance measurements in organometal perovskite solar cells. *Applied Physics Letters* **109**, 173903 (2016).
32. Merten J, Asensi J, Voz C, Shah A, Platz R, Andreu J. Improved equivalent circuit and analytical model for amorphous silicon solar cells and modules. *IEEE Transactions on electron devices* **45**, 423-429 (1998).
33. Neamen DA. *Semiconductor physics and devices*. McGraw-Hill New York (1997).
34. Pierret RF. *Semiconductor device fundamentals*. Pearson Education India (1996).
35. Gautam V, Bag M, Narayan K. Single-pixel, single-layer polymer device as a tricolor sensor with signals mimicking natural photoreceptors. *Journal of the American Chemical Society* **133**, 17942-17949 (2011).

36. Gautam V, Bag M, Narayan K. Dynamics of bulk polymer heterostructure/electrolyte devices. *The Journal of Physical Chemistry Letters* **1**, 3277-3282 (2010).
37. Spirit DM, Ellis AD, Barnsley PE. Optical time division multiplexing: Systems and networks. *IEEE Communications Magazine* **32**, 56-62 (1994).
38. Metcalf B, Proviclakes J. High-capacity wavelength demultiplexer with a large-diameter GRIN rod lens. *Applied Optics* **21**, 794-796 (1982).
39. Huber DR. Optical demultiplexers with grating reflectors. (ed^(eds). Google Patents (1998).
40. Nishi I, Oguchi T, Kato K. Broad-passband-width optical filter for multi/demultiplexer using a diffraction grating and a retroreflector prism. *Electronics Letters* **21**, 423-424 (1985).
41. Tucker RS, Eisenstein G, Korotky SK. Optical time-division multiplexing for very high bit-rate transmission. *Journal of lightwave technology* **6**, 1737-1749 (1988).

Chapter 6: Summary and Future Directions

This thesis primarily involves the studies on photo-carrier transport in various device structures corresponding to different length scales, with hybrid perovskite as the active semiconductor. The spatial signatures of the photocurrent were studied as the device dimensions varied from ~ mm to ~ nm in size. Photophysical approaches, traditionally used for conventional semiconductors were employed.

In the $MAPbBr_3$ single-crystals with carrier-selective electrodes, the observed photocurrent was dominantly diffusive, with associated diffusion length scales. The introduction of light bias resulted in the reduction of this decay length indicating trap mediated transport. Intensity-dependent lifetime measurements provided further insights into the mechanism of band recombination and trap emission. These observations indicate that the sub-band-gap trap recombination influences carrier transport in the low-intensity excitation regime, while bimolecular recombination and transport dominate at high intensity.

In the next part of the thesis, transport characteristics were studied in the lateral MSM devices, for different interelectrode channel lengths. In contrast to the large length-scale crystal studies, the carrier transport in short-channel devices is significantly influenced by the electric field. The apparent observation of rectification-like behavior in this system is traced to originate due to the bias-direction dependent SCLC behavior. This cross-over from ohmic to SCLC behavior depends on the applied bias and the device channel length. Spatial potential mapping using KPFM studies revealed that the presence of a transport barrier at the Al-$MAPbI_3$ interface impedes the efficient injection of carriers. Moreover, the presence of an electric field in the bulk

indicates negligible screening due to the mobile ions in the lateral structures. Spatial photocurrent mapping in these devices using near field excitation revealed dominant recombination and charge separation zones. These devices displayed photodetector capabilities and demonstrate a fast light-switching response of ~ 12 ns.

The 2D position-sensitive detectors were fabricated by combining the lateral and sandwich architectures into a 5-terminal device geometry. The sensitivity of position detection in these devices was ~ 50 μV/mm. Position detection both in the x and the y axis allowed for applications such as a quadrant detector. Using this functionality, dynamic imaging of a light beam trajectory was demonstrated. Transient photocurrent measurements exhibit excitation-position dependent response time in the range ~ 1 μs. Such fast time scales allow for dynamic imaging with a photo signal sampling rate of ~ 1 MHz. The excitation-position dependent trends were understood in terms of equivalent circuit modeling, in combination with impedance spectroscopy measurements. This analysis reveals that the carrier transport is resistive and is influenced by the transit timescales of the photo carriers.

Effect of excitation-wavelength dependent photocarrier generation and transport were studied in graded bandgap 2D/3D perovskite structures. These studies were carried out both on bare films as well as in the devices. The wavelength-dependent dynamics were reflected in the transient photocurrent features. The contrast in the wavelength-dependent temporal photocurrent characteristics was further enhanced in symmetric device structures which demonstrated complete reversal of the photocurrent polarity as the wavelength of light was spanned across the visible region of the spectrum. This scheme of color sensing application was demonstrated both in ultrafast excitation regime as well as steady-state light illumination. Interesting possibilities

were proposed for resolving the spectral components of a polychromatic source using sequential wavelength determination using an optical delay generation.

Future Directions

Since the light bias-dependent studies reveal the effect of trap filling on the carrier diffusion lengths, further λ- and T- dependent studies may be useful to elucidate the nature of the traps and the associated activation energies. This approach will be useful to provide a complete picture relating to the defect tolerance in these systems.

The lateral MSM structure provides a device framework to separately study the transport of free carriers and mobile ions, especially under the influence of higher electric field and light soaking conditions. From the device perspective, this MSM serves as an initial step to the designing of efficient devices. Back contact solar cells offer a promising approach for further exploration. Besides, high-performance devices can be structured with further modifications to electrode deposition and interface engineering for high-speed operation (~ GHz).

The possibility of printing HOIP films offers the realization of large-area flexible PSDs. Thin layer single crystal growth, which has high bulk mobility can also be explored to improve the device responsivity.

In the single-pixel color sensors, the resolution of wavelength identification can be enhanced using a suitable interpolation algorithm during spectral reconstruction. Further, a spatially patterned detector array with λ-dependent response can be integrated into an optical microscopy to provide additional dynamic information, such as live-cell imaging studies. This approach towards the electronic representation of light properties, with minimal optical elements, offers interesting design concepts in color capture and image processing.

Appendix 1: Solution to transport equation based on drift-diffusion formalism.

Here the solution to the transport equation accounting for the combined effects of carrier drift and diffusion is presented. The modelling is specific to the scanning photocurrent experiments, where the point of carrier generation is assumed to be spatially separated from the point of carrier collection.

The 1-D transport equation for excess electrons is given as:

$$\frac{\partial \delta n}{\partial t} = D\frac{\partial^2 \delta n}{\partial x^2} + \mu E\frac{\partial \delta n}{\partial x} + G - \frac{\delta n}{\tau} \qquad \text{(A1.1)}$$

where, δn_0, E, D, G and τ represents the excess carrier density at the point of generation, electric field, diffusion coefficient, generation function and recombination lifetime, respectively. In the scanning photocurrent experiments, where we have a steady-state point generation of photo-carriers, the carrier generation function is given $G(x) = G_0\, \delta(x-x_0)$. Solving for 1D transport with carrier collection away from the point of generation ($x \neq x_0$), the equation reduces to the following:

$$D\frac{\partial^2 \delta n}{\partial x^2} + \mu E\frac{\partial \delta n}{\partial x} - \frac{\delta n}{\tau} = 0 \qquad \text{(A1.2)}$$

This second order homogeneous equation is of the form:

$$ay'' + by' + cy = 0 \qquad \text{(A1.3)}$$

Where $y = \delta n$ and $a = D$, $b = \mu E$ and $c = -1/\tau$;

The characteristic equation is of the form for (3) is of the form

$$a\lambda^2 + b\lambda + c = 0 \qquad \text{(A1.4)}$$

Where λ = (-b ± $\sqrt{(b^2 - 4ac)}$)/ 2a, and the solution is of the form

$$y = Aexp(\lambda_1 x) + B.\exp(\lambda_2 x \qquad \text{(A1.5)}$$

Here substituting the variable such that field – E is acting on electrons, we have:

$$\lambda_1 = \left(\frac{\mu E + \sqrt{\left(\mu^2 E^2 + \frac{4D}{\tau}\right)}}{2D} \right) \qquad \text{(A1.6)}$$

And

$$\lambda_2 = \left(\frac{\mu E - \sqrt{\left(\mu^2 E^2 + \frac{4D}{\tau}\right)}}{2D} \right) \qquad \text{(A1.7)}$$

Now the initial conditions for solution (A1.5) are $\delta n(x = 0) = \delta n_0 = aG_0\tau$, and $\delta n(x = \infty) = 0$. Using this we obtain coefficients A = 0 and B = δn_0.

Therefore we obtain the solution as:

$$\delta n(x) = \delta n_0 \exp\left\{ -\left(\frac{\sqrt{\left(\mu^2 E^2 + \frac{4D}{\tau}\right)} - \mu E}{2D} \right) x \right\} \qquad \text{(A1.8)}$$

A1.1 Carrier diffusion in the perovskite single crystal.

Using the carrier distribution function obtained in the above case, a comparative study of diffusion vs. drift effect on the carrier transport is presented. For the sake of simplicity, we consider the device parameters as follows: mobility μ = 100 cm^2V/s, lifetime τ = 100 ns, electric field E = 6 V/cm, an initial excess carrier concentration δn_0 = 1.8×10^{14} carriers/cm^3, and the diffusion coefficient $D = kT\mu/e$. The assumed values are in close agreement with the material parameters associated with the $MAPbBr_3$ single crystal. Using Eq. (A1.8), the spatial distribution profiles are given below to compare with and without the presence of an electric field.

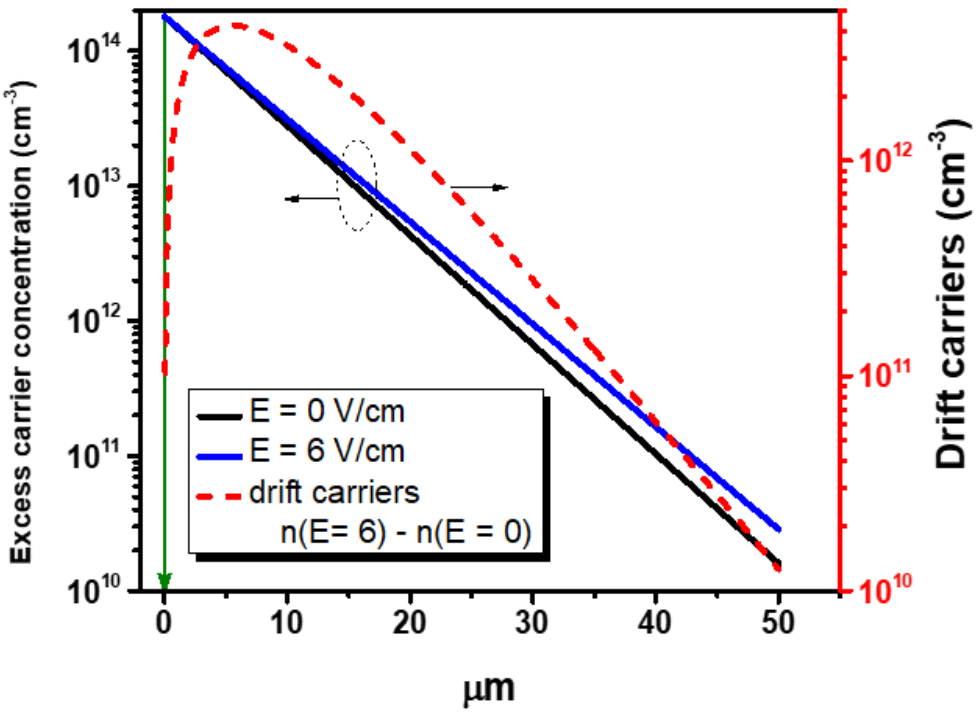

***Figure A1.1**: Comparison of carrier distribution profiles with and without the electric field.*

The black solid line represents the carrier distribution, n_{diff} as a result of carrier diffusion in the absence of an electric field. The solid blue line represents the carrier distribution in the presence of a finite electric field, E = 6 V/cm. It is seen that the electric field has

a marginal effect on carrier distribution profiles. Further, the calculated drift carrier concentration, which is considered as: $n_{drift} = n(E = 6\ V/cm) - n_{diff}$, is represented as the dashed red line. It is observed that the magnitude of is n_{drift} is at least an order of magnitude lower within the first 40 μm from the point of excitation. Experimentally this translates to a distance of ~ 40 μm from the electrode. Therefore the presence of a low electric field (6 V/cm) doesn't violate the condition that carrier diffusion is the dominant transport pathway and that $\mu E \frac{\partial \delta n}{\partial x} << Dn \frac{\partial^2 n}{\partial x^2}$. The photocurrent profiles that are observed corresponds to the dominant contribution of the carrier diffusion. The supposition that the extracted decay length is indicative of carrier diffusion and $L_d \propto L_{diff}$, holds reasonable.

Appendix 2: Influence of photon recycling on carrier diffusion

To study the effect of photon recycling on carrier diffusion, the carrier generation profile was simulated using the finite element method, accounting for photon recycling. The excess carrier diffusion and photon propagation upon point illumination at x=0 was simulated with finite element method using coupled equations.

$$n(x) = n_0 exp\left(-\frac{x}{L_{diff}}\right) + \gamma_{pp}(x).n_\alpha.\tau \quad \text{(A2.1)}$$

$$\gamma(x) = \frac{n(x).\varphi_{PL}}{\tau} + \gamma_{pp}(x)(1 - n_\alpha) \quad \text{(A2.2)}$$

Where n(x) and γ(x) is the excess carrier density and photon density at point x respectively. n_α is the ratio of reabsorbed photons of the total emitted photons. We consider the value n_α = 0.54 as given in the reference[1]. φ_{PL} is the internal luminescence efficiency of the sample and is given by Yamada et. al as[1]:

$$\varphi_{PL} = \frac{\tau_\infty - \tau_0}{\tau_\infty - n_\alpha.\tau_0} \quad \text{(A2.3)}$$

Where τ_∞ can be attributed to the monomolecular lifetime (~ 125 ns) and τ_0 is the lifetime under consideration for a given carrier density. Considering probe illumination at x = 0, the excess density is highest at x = 0 and then decays further away (shown in the black solid line in **Figure A2.1(c)**). Since the lifetime τ_0 is small for high carrier density, the φ_{PL} value is higher. **Figure A2.1(a)** shows the plot of φ_{PL} as a function of distance away from the point of excitation. In proportional to the carrier density, φ_{PL}

reduces away from the x=0. The photon recycling (PR) efficiency [1] given as $\upsilon_{PR} = n_{\alpha}.\varphi_{PL}$ follows the same trend as φ_{PL} (shown in **Figure A2.1(a)**). $\gamma_{PP}(x)$ is the photon density as a result of photon propagation from a previous emissive event. It can be written as:

$$\gamma_{PP}(x) = \gamma(x_{n-1}).\exp\left(\frac{-x}{L_{\alpha}}\right).f(\theta) \qquad \text{(A2.4)}$$

where $\gamma(x_{n-1})$ is the photon density from the previous iterative determination. $L\alpha = 1/\alpha$ is the photon propagation length. We consider an upper limit of $L\alpha$ = 10 µm for the case of 545 nm[2]. f(θ) is an additional angular function that indicates the fraction of isotropically emitted photons towards 1-D carrier diffusion. Here $\theta = \tan^{-1}(L_{\alpha}/x)$ is the angle subtended by the emission point, which is x distance away from the collection electrode. In finite element method given the small inter-iterative distance (~ 0.1 µm), i.e., $x << L_{\alpha}$, f(θ) ~ 0.5. This implies that over small distances, half the emitted photons propagate in one direction and the rest in the opposite direction. Additionally, γ (0) = αG_0 and $n_0 = \alpha G_0 \tau$.

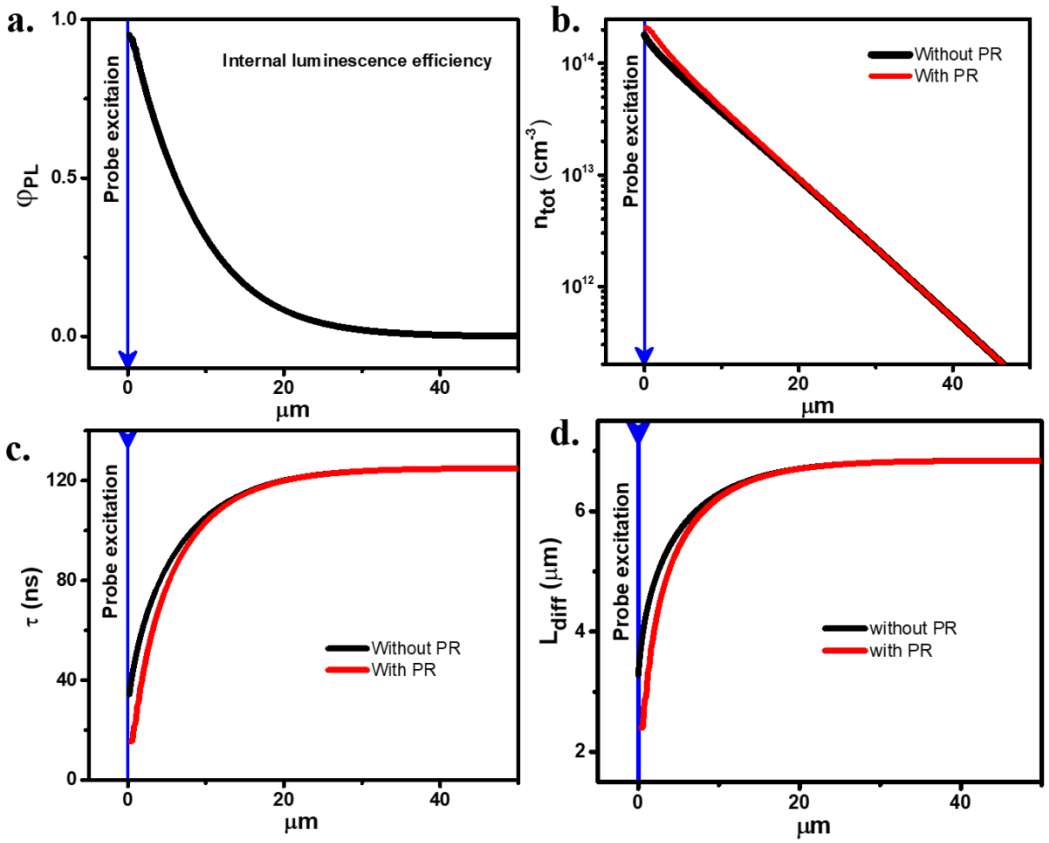

***Figure A2.1**: **(a)** Plot of φ_{PL} (internal luminescence efficiency) which depends on the background carrier density. Blue vertical lines in all the plots indicate the point of excitation. As the carriers diffuse away from x=0, the carrier density reduces resulting in a reduction of the lifetime (shown in **Figure 2.13(d)**). From **Equation A2.3**, φ_{PL} is high when the carrier lifetime is smaller. **(b)** The plot of excess carrier density profile shows a marginal increase considering photon recycling (PR). Consequently, due to the relative increase in the excess carrier density, the lifetime and diffusion length parameters show a marginal reduction as shown in **(c)** and **(d)** respectively.*

The simulated plot of excess carrier density with and without photon recycling is shown in **Figure 2.14(b)**. It can be observed that the change in the carrier density is minimal and close to the illumination point. Similarly, as shown in **Figure 2.14(c)** and **Figure 2.14(d)** the change in the lifetime and L_{diff} values is marginal.

References

1. Yamada T, Yamada Y, Nakaike Y, Wakamiya A, Kanemitsu Y. Photon emission and reabsorption processes in CH 3 NH 3 PbBr 3 single crystals revealed by time-resolved two-photon-excitation photoluminescence microscopy. *Physical Review Applied* **7**, 014001 (2017).
2. Wenger B, Nayak PK, Wen X, Kesava SV, Noel NK, Snaith HJ. Consolidation of the optoelectronic properties of CH 3 NH 3 PbBr 3 perovskite single crystals. *Nature communications* **8**, 1-10 (2017).

Appendix 3: Representation of the SCLC current

Figure. 3.5(b) (in the text) shows the plot of J' vs. V^2/l^3. J' corresponds to the SCLC dark current corrected for the ohmic contribution. For instance, **Figure A3.1** shows the log-log J(V) plot for a 4 μm channel device with positive bias. The profile indicates the dominant ohmic and SCLC regimes as a function of the function of applied bias. Here, the ohmic current is given as $J_{ohmic} = n_0 e\mu \frac{V}{L}$, and $J_{SCLC} = \frac{9}{8}\mu\theta\varepsilon_0\varepsilon_r \frac{V^2}{L^3}$ is given by the Mott-Gurney Law [1, 2]. The total mixed current can be represented as [3]:

$$J = J_{ohmic} + J_{sclc} \tag{A3.1}$$

To account for only the SCLC part of the observed current, at bias beyond the SCLC onset voltage, V', the SCLC current is given as:

$$J_{sclc} = J - J_{ohmic} \tag{A3.2}$$

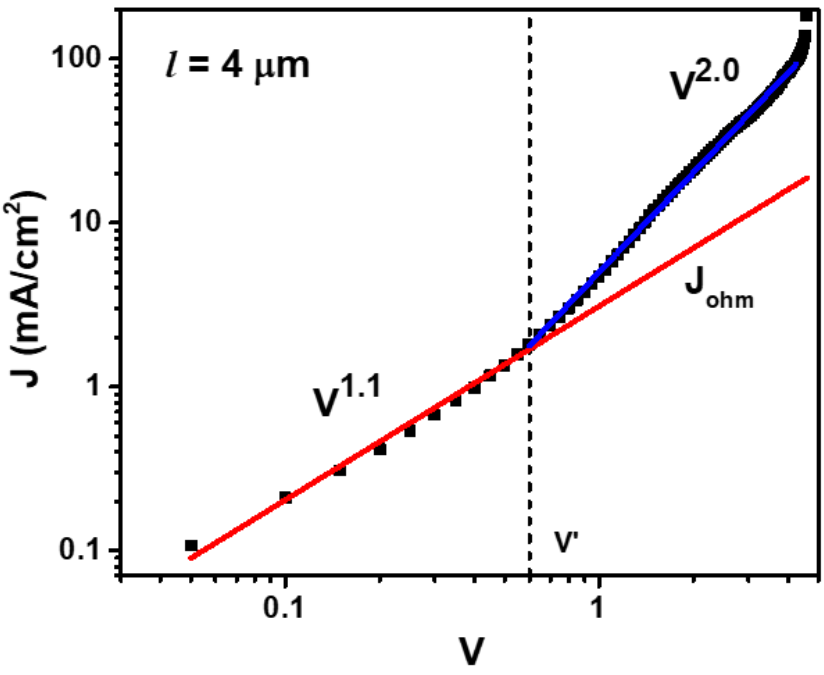

Figure. A3.1*: Log-log plot of the J(V) characteristics for positive bias sweep in a l = 4 μm asymmetric device. The plot shows distinct ohmic and SCLC behavior. The solid red line shows the baseline for the ohmic current.*

From the plot in **Figure A3.1**, the extrapolated red line corresponds to the J_{ohmic}, which is corrected, using **Equation A3.2**, to obtain the SCLC current, *J'*. It must be noted that the voltage represented in **Figure 3.5(b)** corresponds only to the SCLC voltage, i.e., V > V'.

References:

1. Mott N. GURNEY RW-Electronic processes in ionic crystals. (ed^(eds). Oxford University Press (1940).
2. Lampert MA, Mark P. *Current injection in solids*. Academic press (1970).
3. Röhr JA, MacKenzie RC. Analytical description of mixed ohmic and space-charge-limited conduction in single-carrier devices. *Journal of Applied Physics* **128**, 165701 (2020).

Appendix 4: Thickness uniformity of mixed-phase perovskite films

Large area uniformity of perovskite films is crucial for the position-sensitive detectors (PSD). To confirm the thickness-uniformity in $FA_{0.83}Cs_{0.17}Pb(I_{0.90}Br_{0.10})_3$ perovskite films, the perovskite layer thickness was probed at different points. Three locations were selected from the center to the edge of the film over a distance of ~ 2 cm. **Figure A4.1** below shows the perovskite film spin-coated on an ITO substrate (3 cm x 3 cm). Points marked as 1, 2 and 3 indicate the locations where the perovskite was removed using a razor blade to check for film thickness.

The thickness of the perovskite layer was probed using images acquired with a Keyence VK-X200 laser scanning confocal microscope. **Figures A4.1(b)**, **(c),** and **(d)** in the image above shows the thickness profile at sites 1,2 and 3, respectively. The perovskite thickness at the three locations was determined to be 645, 633 and 658 nm. The difference in the thickness estimates ranges within the roughness value (~ 36 nm) of the perovskite film. Additionally, care was taken to position the active area of the device to the center, away from the edge of the ITO substrate. This further ensures uniformity across the active device area.

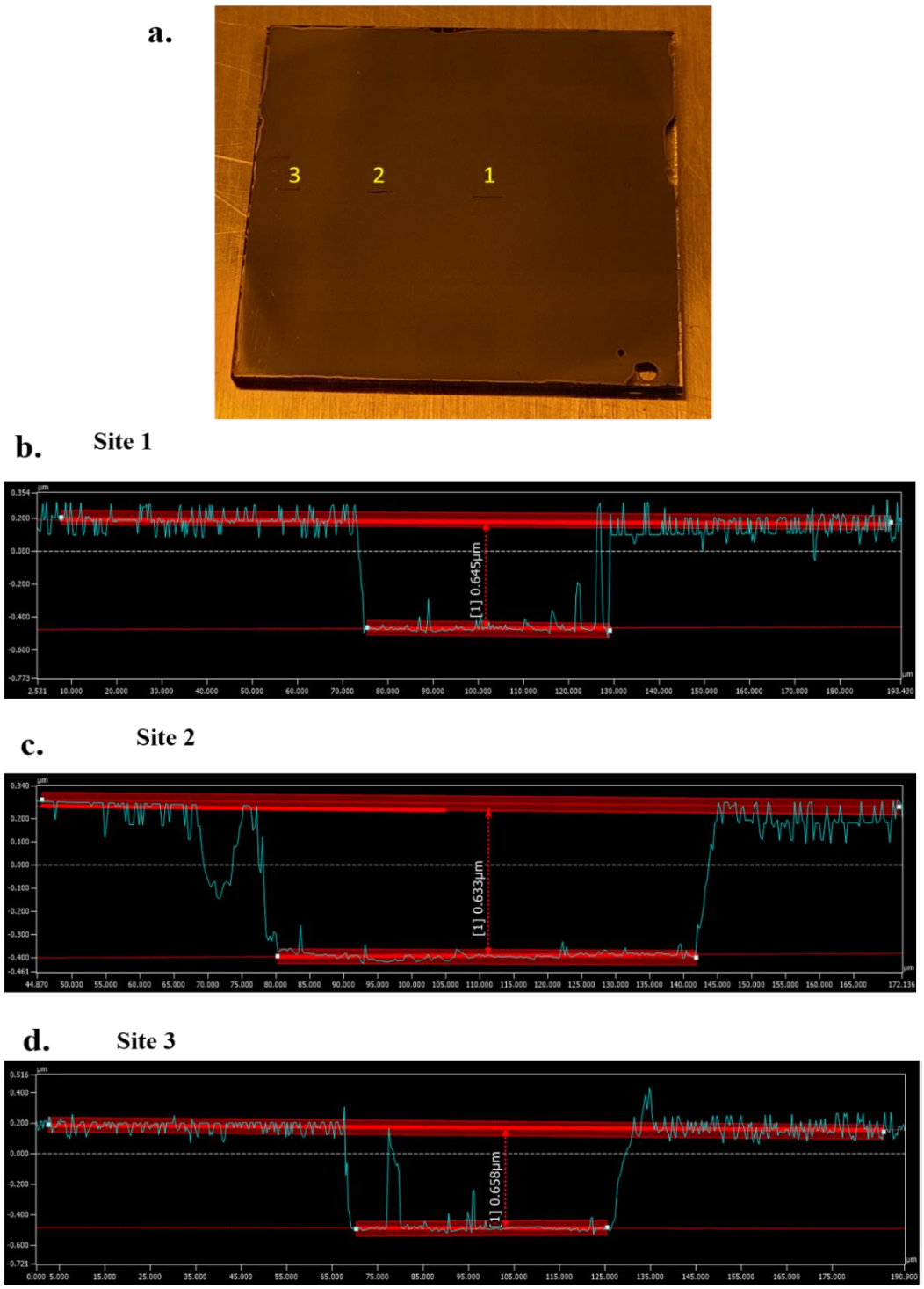

***Figure A4.1**: **(a)** Image of the perovskite film coated on ITO substrate (3 cm × 3 cm). Locations 1, 2 and 3 are the sites where the perovskite is removed with razor blade to probe the thickness. The thickness profile is imaged and determined to be **(b)** 645 nm at site 1, **(c)** 633 nm at site 2, and **(d)** 658 nm at site 3.*